Universitat
de les Illes Balears

DOCTORAL THESIS

2020

WAVEFORM MODELLING OF BINARY BLACK HOLES IN THE ADVANCED LIGO ERA

by

Cecilio García Quirós

Doctor by the Universitat de les Illes Balears

Universitat
de les Illes Balears

DOCTORAL THESIS

2020

Doctoral programme of physics

WAVEFORM MODELLING OF BINARY BLACK HOLES IN THE ADVANCED LIGO ERA

by

Cecilio García Quirós

Supervisors:
Sascha Husa & Alicia M. Sintes Olives

Tutor:
Carles Bona García

Doctor by the Universitat de les Illes Balears

WE, THE UNDERSIGNED DECLARE:

That the thesis

WAVEFORM MODELLING OF BINARY BLACK HOLES IN THE ADVANCED LIGO ERA,

presented by Cecilio García Quirós to obtain the doctoral degree, has been completed under the supervision of Dr. Alicia Magdalena Sintes Olives and Dr. Sascha Husa.

For all intents and purposes, we sign this document.

Palma de Mallorca,

Dr. Alicia Magdalena Sintes Olives

Dr. Sascha Husa

Mr. Cecilio García Quirós

"Why do we fall Bruce? So that we can learn that gravity rules the world."

Albert Wayne.

I dedicate the work of these four years to my grandparents:
Bernardino, María, Joaquín and Concha.

List of publications derived from this thesis

Main author publications:

1. Cecilio García-Quirós, Marta Colleoni, Sascha Husa, Héctor Estellés, Geraint Pratten, Antoni Ramos-Buades, Maite Mateu-Lucena, Rafel Jaume. *IMRPhenomXHM: A multi-mode frequency-domain model for the gravitational wave signal from non-precessing black-hole binaries.* arXiv:2001.10914 [gr-qc] (2020).

2. Cecilio García-Quirós, Sascha Husa, Maite Mateu-Lucena, Angela Borchers. *Accelerating the evaluation of inspiral-merger-ringdown waveforms with adapted grids.* arXiv:2001.10897 [gr-qc] (2020).

3. Geraint Pratten, Cecilio García-Quirós, Marta Colleoni, Antoni Ramos-Buades, Héctor Estellés, Maite Mateu-Lucena, Rafel Jaume, Maria Haney, David Keitel, Jonathan E. Thompson, Sascha Husa. *Let's twist again: computationally efficient models for the dominant and sub-dominant harmonic modes of precessing binary black holes.* arXiv:2004.06503 [gr-qc] (2020).

Other publications as co-author:

1. Lionel London, Sebastian Khan, Edward Fauchon-Jones, Cecilio García, Mark Hannam, Sascha Husa, Xisco Jiménez-Forteza, Chinmay Kalaghatgi, Frank Ohme, and Francesco Pannarale. *First Higher-Multipole Model of Gravitational Waves from Spinning and Coalescing Black-Hole Binaries.* Phys. Rev. Lett. 120, 161102 (2018).

2. Antoni Ramos-Buades, Sascha Husa, Geraint Pratten, Héctor Estellés, Cecilio García-Quirós, Maite Mateu-Lucena, Marta Colleoni, Rafel Jaume. First survey of spinning eccentric black hole mergers: Numerical relativity simulations, hybrid waveforms, and parameter estimation. Physical Review D 101, 083015 (2020).

3. Geraint Pratten, Sascha Husa, Cecilio García-Quirós, Marta Colleoni, Antoni Ramos-Buades, Héctor Estellés, Rafel Jaume. *Setting the cornerstone for the IMRPhenomX family of models for gravitational waves from compact binaries: The dominant harmonic for non-precessing quasi-circular black holes.* arXiv:2001.1142 [gr-qc] (2020).

4. Héctor Estellés, Antoni Ramos-Buades, Sascha Husa, Cecilio García-Quirós, Marta Colleoni, Leïla Haegel and Rafel Jaume. IMRPhenomTP: A phenomenological time domain model for dominant quadrupole gravitational wave signal of coalescing binary black holes. arXiv:2004.08302 [gr-qc] (2020).

5. I. Romero-Shaw et. al. *Bayesian inference for compact binary coalescences with BILBY: Validation and application to the first LIGO–Virgo gravitational-wave transient catalog.* arXiv:2006.00714 (2020).

During the last four years I have been a member of the LIGO Scientfic Collaboration, which in that time has published 40 scientific articles where I appear as a co-author.

Summary (in English)

The focus of this thesis is the development of accurate and computationally efficient waveform models for the description of the signal of non-precessing and precessing black-hole binary systems detected by the LIGO-Virgo detectors. Waveform models play a key role in the detection and parameter estimation of gravitational wave signals. The more accurate these models are, the more signals can be detected, but even more importantly, inaccuracies in the signal description will lead to systematic errors for the estimated parameters of the source. The models presented in this thesis include the description of several subdominant effects, which were not considered in the studies during the two first observation runs O1 and O2 of the LIGO-Virgo interferometers, but break degeneracies in the signal and generally improve the accuracy of parameter estimation. During the gap between the O2 and O3 runs several research groups have incorporated the most important subdominant harmonics into their models. However, we find that the models presented in this thesis improve the accuracy of several of these models and outperform in computational efficiency to all of them. The non-precessing model follows the standard strategy of the phenomenological models of calibrating an analytical ansatz to numerical relativity simulations. I produced a number of these simulations specifically for the calibration of the model placing them strategically in regions of the parameter space poorly populated. I also produced several waveforms in the extreme mass ratio (EMRI) limit extending the calibration region of the model from mass ratio 1 to 1000. On the other hand, the precessing model follows the standard technique of twisting-up a non-precessing model but extended in this case to a model with subdominant harmonics. The evaluation of the models is then accelerated by incorporating the interpolation technique of "multibanding", originally introduced by Vinciguerra et. al. I have extended this technique, adapted it to the two frequency domain models presented in this thesis, and formulated the technique in a way to make it applicable to any analytical frequency or time domain model.

Resumen (en español)

El objetivo de esta tesis es el desarrollo de modelos de forma de onda precisos y computacionalmente eficientes para la descripción de la señal de sistemas binarios de agujero negros sin precesión y con precesión detectados por los detectores LIGO-Virgo. Los modelos de forma de onda juegan un papel clave en la detección y estimación de parámetros de señales de ondas gravitacionales. Cuanto más precisos sean estos modelos, más señales se pueden detectar, pero aún más importante, las inexactitudes en la descripción de la señal conducirán a errores sistemáticos para los parámetros estimados de la fuente. Los modelos presentados en esta tesis incluyen la descripción de varios efectos subdomiantes, que no se consideraron en los estudios durante las dos primeras ejecuciones de observación O1 y O2 de los interferómetros LIGO-Virgo, pero rompen las degeneraciones en la señal y generalmente mejoran la precisión de la estimación de parámetros. Durante la brecha entre las ejecuciones de O2 y O3, varios grupos de investigación han incorporado los armónicos subdominantes más importantes en sus modelos, sin embargo, encontramos que los modelos presentados en esta tesis mejoran la precisión de varios de estos modelos y superan en eficiencia computacional a todos ellos. El modelo sin precesión sigue la estrategia estándar de los modelos fenomenológicos de calibración de una respuesta analítica a simulaciones de relatividad numérica. Produje varias de estas simulaciones específicamente para la calibración del modelo colocándolas estratégicamente en regiones del espacio de parámetros poco pobladas. También elaboré una serie de formas de onda en el límite de la relación de masa extrema que extiende la región de calibración del modelo desde la relación de masa 1 a 1000. Por otro lado, el modelo de precesión sigue la técnica estándar de "twisting-up" de un modelo sin precesión, pero se extiende en este caso a un modelo con armónicos subdominantes. La evaluación de los modelos es acelerada incorporando la técnica de interpolación de "multibanding", originalmente presentada por Vinciguerra et. al. He ampliado esta técnica, la he adaptado a los dos modelos de dominio de frecuencia presentados en esta tesis y he formulado la técnica de manera que sea aplicable a cualquier modelo analítico de frecuencia o dominio de tiempo.

Resum (en català)

L'objectiu d'aquesta tesi és el desenvolupament de models de forma d'ona precisos i computacionalment eficaços per a la descripció del senyal de sistemes binaris de forat negre no precessant i precessant detectats pels detectors LIGO-Virgo. Els models de forma d'ona tenen un paper clau en la detecció i l'estimació de paràmetres de senyals d'ona gravitacional. Com més precisos siguin aquests models, més senyals es poden detectar, però encara més important, les inexactituds en la descripció del senyal conduiran a errors sistemàtics per als paràmetres estimats de la font. Els models presentats en aquesta tesi inclouen la descripció de diversos efectes subdominants, que no es van considerar en els estudis durant els dos primers períodes d'observació O1 i O2 dels interferòmetres LIGO-Virgo, però trenquen degeneracions en el senyal i milloren generalment la precisió de l'estimació de paràmetres. Durant el període entre les execucions de O2 i O3, diversos grups de recerca han incorporat als seus models els harmònics subdominants més importants, no obstant trobem que els models presentats en aquesta tesi milloren la precisió de diversos d'aquests models i superen en eficiència computacional a tots ells. El model no precessant segueix l'estratègia estàndard dels models fenomenològics de calibració d'un ansatz analític a simulacions de relativitat numèrica. Vaig produir una sèrie d'aquestes simulacions específicament per a la calibració del model situant-les estratègicament en regions de l'espai de paràmetres mal poblats. També vaig produir diverses formes d'ona en el límit de la proporció massiva extrema que va ampliar la regió de calibració del model des de la relació de massa 1 a 1000. D'altra banda, el model precessant segueix la tècnica estàndard de retorçar un model no precessant, però estès en aquest cas a un model amb harmònics subdominants. L'avaluació dels models s'accelera després incorporant la tècnica d'interpolació de "multibanding", originalment introduïda per Vinciguerra et. al. He ampliat aquesta tècnica, l'he adaptat als dos models de domini de freqüència presentats en aquesta tesi i he formulat la tècnica per tal de fer-la aplicable a qualsevol model de domini de freqüència o analítica.

Acknowledgements

In first place I would like to express my sincere gratitude to my supervisors Prof. Sascha Husa and Prof. Alicia Sintes for their guidance, help and support during all these years. I am specially grateful and glad to have had the opportunity of living from inside one of the most exciting moments in the scientific community that has happened in times.

All these difficult four years have been more bearable thanks to the professional and personal support of all the members of the Phenom Cave at UIB: Marta Colleoni, Héctor Estellés, Rafel Jaume, Geraint Pratten and Maite Mateu. A special mention is required for my partner of PhD don Toni Ramos, who has been present from the very first to the very last day of this PhD and has been a continuous source of happiness, love and doubtless respect towards my person.

I am also very grateful to Prof. Vivien Raymond and all the members of the Gravity Exploration group at Cardiff University for their valuable lessons and hospitality during my stay there. I would like to thank specially to Dr. Lorenzo Aliello and Dr. Aldo Ejlli for their daily "kind" motivation and inspiration for starting writing this thesis. Also I would like to thank for their personal support to Jorge de Andrés and Dr. Xisco Jiménez who made more bearable my stay in Cardiff.

I recall also to some of my best friends in Mallorca during these years for their personal support and for the great time we have spent together: Tomeu, Aldara, Ángel, Konsta, Toni, Fernando, Leyre and Ángela. Finally, a special thanks to my family, parents and brother for trying to make me happy at any time I stay with them.

This work has been done as a member of the LIGO Scientific Collaboration and and the Institute of Applied Computing and Community Code (IAC3) of the University of the Balearic Islands. This work has been supported by the Spanish Ministry of Education and Professional Formation grants FPU15/01319 and EST18/00873. The author also acknowledges the support by the Govern de les Illes Balears through the Vicepresidència i Conselleria d'Innovació, Recerca i Turisme and the Direcció General de Política Universitària i Recerca with funds from the Tourist Stay Tax Law

ITS 2017-006 (PRD2018/24), the European Union FEDER funds and EU COST Actions CA18108, CA17137, CA16214, and CA16104, the Ministry of Science, Innovation and Universities and the Spanish Agencia Estatal de Investigación grantes FPA2016-76821-P, RED2018-102.661-T, RED2018-102.573-E, FPA2017-90566-REDC, FPA2017-90687-REDC, and the Generalitat Valenciana (PROMETEO/2.019/071). The author thankfully acknowledges the computer resources at MareNostrum and the technical support provided by Barcelona Supercomputing Center (BSC) through Grants No. AECT-2020-1-0025, AECT-2019-3-0020, AECT-2019-2-0010, AECT-2019-1-0022, AECT-2018-3-0017, AECT-2018-2-0022, AECT-2018-1-0009, AECT-2017-3-0013, AECT-2017-2-0017, AECT2017-1-0017, AECT-2016-3-0014, AECT2016-2-0009, from the Red Española de Supercomputación (RES) and PRACE (Grant No. 2015133131). BAM and Einstein Toolkit simulations were carried out on the BSC MareNostrum computer center under PRACE and RES allocations and on the FONER cluster at the University of the Balearic Islands.

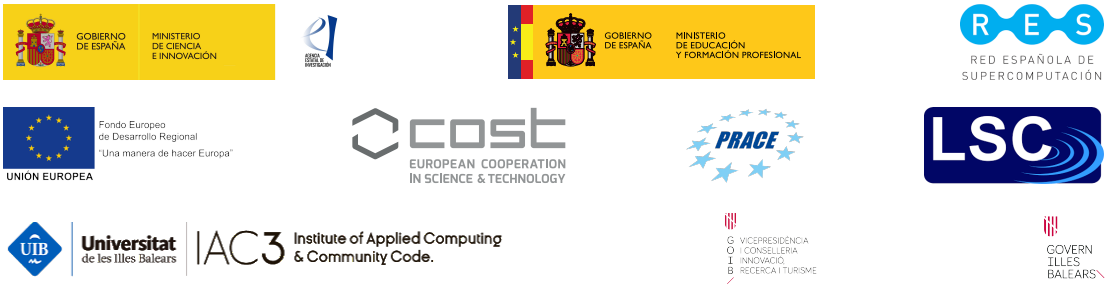

Contents

Preface **XII**

I Introductory notions **1**

1 Introduction to Gravitational Waves **2**
1.1 Introduction to GR . . . 2
1.2 Linearized Einstein field equations . . . 8
1.3 The Transverse-Traceless (TT) gauge . . . 11
1.4 Distortion of a ring of particles . . . 13
1.5 Quadrupole formula . . . 14
1.6 Quadrupole emission from binary systems in circular motion . . . 16
1.7 Quadrupole emission from rotating rigid bodies . . . 20

Bibliography **23**

2 Experiments and Data Analysis **26**
2.1 Gravitational Wave Detectors . . . 26
2.1.1 Resonant-mass detectors . . . 26
2.1.2 Ground-based Interferometers . . . 27
2.1.3 Spaced-based Interferometers . . . 33
2.2 Gravitational Wave Data Analysis . . . 34
2.2.1 Detector response . . . 34
2.2.2 Matched filtering . . . 36
2.2.3 Frequentist vs Bayesian statistics . . . 38
2.2.4 Parameter estimation . . . 40
2.2.4.1 Samplers . . . 41
2.3 Waveform approximants . . . 43
2.3.1 Post-Newtonian theory . . . 44
2.3.2 EOB models . . . 46
2.3.3 Phenom models . . . 47
2.3.4 Numerical Relativity . . . 49
2.3.5 The need for subdominant harmonics approximants . . . 52
2.3.6 Introducing the PhenomX family . . . 58

Bibliography **61**

II Original scientific results **72**

3 Modelling subdominant harmonics from non-precessing black-hole binaries: IMRPhenomXHM **73**
3.1 Introduction . . . 74
3.2 Preliminaries . . . 76
3.2.1 Conventions . . . 76
3.2.2 Perturbative waveform phenomenology: inspiral and ringdown . . . 78
3.2.3 Strategy for fitting our model to numerical data . . . 81
3.3 Calibration data set . . . 86
3.3.1 Numerical relativity waveforms . . . 87
3.3.2 Extrapolation to the test-mass limit . . . 88
3.4 Inspiral model . . . 88
3.4.1 Amplitude . . . 90
3.4.1.1 Default reconstruction . . . 90
3.4.1.2 Vetoes and non-default reconstruction . . . 91
3.4.2 Phase . . . 92
3.5 Intermediate model . . . 93
3.5.1 Amplitude . . . 95
3.5.1.1 Default reconstruction . . . 95
3.5.1.2 Extreme-mass-ratio reconstruction . . . 96
3.5.1.3 Vetoes and non-default reconstruction . . . 97
3.5.2 Phase . . . 98
3.6 Ringdown model . . . 101
3.6.1 Amplitude . . . 102
3.6.2 Phase . . . 104
3.6.2.1 Modes without mode-mixing . . . 104
3.6.2.2 Modes with mode-mixing . . . 105
3.7 Quality control . . . 107
3.7.1 Single Mode Matches . . . 107
3.7.2 Multi-Mode Matches . . . 108
3.7.3 Recoil . . . 111
3.7.4 Time-domain behaviour . . . 112
3.7.5 Parameter estimation: GW170729 . . . 113
3.7.6 NR injection study . . . 114
3.7.7 Computational cost . . . 115
3.8 Conclusions . . . 118

Appendices **122**
3.A Conversion from spheroidal to spherical-harmonic modes . . . 122
3.B Testing tetrad conventions . . . 123
3.C Notes on the implementation of the IMRPhenomXHM model in the LIGO Algorithms Library . . . 123
3.D Inspiral phase: higher-mode extension of IMRPhenomXAS . . . 127
3.E Fourier Domain Post-Newtonian amplitudes . . . 128

Bibliography **132**

4 Accelerating waveform model evaluation with adapted grids: Multibanding **142**
4.1 Introduction . . . 143
4.2 Algorithms . . . 145
4.2.1 Interpolation error . . . 145
4.2.1.1 Inspiral in the frequency domain . . . 146
4.2.1.2 Merger and ringdown in the frequency domain . . . 148
4.2.2 Efficient evaluation of complex exponentials . . . 151
4.2.3 Complete multibanding algorithm in the frequency domain . . . 151
4.2.3.1 Building the coarse frequency grid . . . 152
4.2.3.2 Evaluate the modes on the fine grid, with and without mode-mixing . . . 154
4.3 Results . . . 157
4.3.1 Computational performance . . . 157
4.3.2 Accuracy . . . 159
4.3.3 Parameter estimation . . . 163
4.4 Conclusions . . . 165

Bibliography **167**

5 Modelling precessing binary black holes for the subdominant harmonics: IMRPhenomXPHM **172**
5.1 Introduction . . . 173
5.2 Notation and Conventions . . . 176
5.3 Modelling Precessing Binaries . . . 178
5.3.1 The twisting construction in terms of Euler angles . . . 178
5.3.2 Gravitational-Wave Polarizations in the Frequency Domain . . . 179
5.4 Constructing the Model . . . 180
5.4.1 Post-Newtonian NNLO Euler Angles . . . 180
5.4.2 MSA Euler Angles . . . 183
5.4.3 Post-Newtonian Orbital Angular Momentum . . . 185
5.4.4 Modelling the Final State . . . 187
5.5 Model Performance and Validation . . . 191
5.5.1 Comparison of Euler angles with Numerical Relativity . . . 191
5.5.2 Time Domain Waveforms . . . 192
5.5.3 Match Calculations for Precessing Waveforms . . . 194
5.5.3.1 Matches Against SXS Numerical Relativity Simulations . . . 194
5.5.3.2 Matches Against other Models . . . 195
5.5.4 Multibanding and Euler Angles . . . 198
5.5.5 Benchmarking . . . 201
5.5.6 Parameter estimation . . . 204
5.5.6.1 GW150914 . . . 205
5.5.6.2 GW170729 . . . 205
5.5.6.3 Numerical relativity injections . . . 209
5.6 Conclusions . . . 212

Appendices **214**
5.A Wigner-d Matrices . . . 214

5.B Conventions for non-Precessing Modes . . . 217
5.C Frames Transformations and Polarization Basis . . . 218
5.D Choices of polarization vectors P and Q . . . 223
5.E Derivation of the frequency domain waveform . . . 224
5.F LALSuite Implementation . . . 226
5.G Post-Newtonian Results . . . 230
5.G.1 NNLO PN Euler Angles . . . 231
5.G.2 Orbital Angular Momentum . . . 232

Bibliography **232**

6 Conclusions **244**

Bibliography **249**

Abbreviations **252**

A Fourier domain polarizations in terms of individual modes **255**

B Permissions Chapter 3 **259**

C Permissions Chapter 4 **267**

D Permissions Chapter 5 **271**

Preface

Gravitational waves (GWs) were predicted by Albert Einstein in 1916 [1] as a solution to the equations of his theory of general relativity (GR), presented in 1915 [2]. They propagate as ripples in the fabric of space-time at the speed of light, and their interaction with matter is so weak that Einstein expected they will never be detected. Indeed, it required a hundred years of extraordinary technological and theoretical developments to be able to finally detect them. There was already some indirect evidence for the existence of GWs provided by the discovery of the Hulse-Taylor pulsar [3] which periastron advance was explained by the loss of energy in form of GWs. However, the first-ever direct detection of GWs was announced on 11 February 2016 by the LIGO-Virgo collaboration (LVC) which reported the detection of the event GW150914 [4], a stellar-mass black hole merger, confirming the existence of black holes and that they form binary systems [1]. This discovery constituted an extraordinary achievement not just for the LIGO and Virgo collaborations, but indeed for generations of scientists in the entire field of gravitational physics. However, far from this being the end of the research field, it marked the birth of a new kind of discipline, *GW astronomy*. This is a new way of observing the universe and gathering information from it. During millennia, humans relied on electromagnetic radiation to gather information about the universe, first using their naked eyes sensitive to this radiation and later, since Galileo Galilei, using telescopes. Now there exists a new channel that can provide information on events "invisible" to electromagnetic astronomy but also provide complementary information for events where electromagnetic and gravitational radiation are emitted. Electromagnetic and gravitational waves together with cosmic rays and neutrinos constitute a new multichannel kind of astronomy known as *multimessenger astronomy*.

One very active field of research is *waveform modelling* which undertakes to model the shape of the GWs as a function of the physical properties of the source according to the predictions of GR. As we will explain in more detail in chapter 2, having a theoretical prediction or *template* of how the morphology of the signal is key to extract physical

[1] Supermassive black holes mergers are also believed to occur during the merger of galaxies but no direct observation has been confirmed so far.

information from the detector data. So far, all the detections reported by LIGO-Virgo used simplified templates where only the dominant contribution of the signal was present. In a similar way to the electromagnetic case, the gravitational radiation can also be described as a multipole expansion where the dominant contribution, in this case, is the quadrupole one instead of the dipole one. The angular part is described by the spin weighted spherical harmonics (SWSH) of spin weight -2, denoted by ${}_{-2}Y_{lm}$:

$$h(t,\boldsymbol{\lambda},\iota,\phi) = h_+ - ih_\times = \sum_{l=2}^{\infty}\sum_{m=-l}^{l} h_{lm}(t,\boldsymbol{\lambda})\,{}_{-2}Y_{lm}\,(\iota,\phi). \tag{1}$$

The dominant contribution, also known as *quadrupolar* emission, includes only the $(l,|m|) = (2,2)$ modes. Here $\boldsymbol{\lambda}$ refers to the set of source parameters, in the case of binary systems consists of the masses and spin vectors of the two objects, the distance between the source and the observer, and in case there is a neutron star the equation of state EOS, and parameters relative to neutron stars. Note that a similar multipole-expansion, which starts with the dipole, is also a standard technique for electrodynamics. Multipole expansions are also often combined with expansions in $1/r$, where r is the distance to the source. Since here we are interested in the field at a very large distance from the source only the leading term in $1/r$ is considered. Analogously to massless scalar and electromagnetic fields, gravitational radiation decays with the inverse of the distance, and in the asymptotic region, the distance just acts as a scaling factor for the field. In the gravitational case, the total mass of the system appears also as a scale factor. The intrinsic parameters of the source, those which define the structure and shape of the waveform reduce then to the mass ratio $q = m_1/m_2$ and the spin vectors plus the tidal parameters in case of neutron stars. The angles ι and ϕ are also extrinsic parameters which locate the line of sight i.e. the position of the observer in the sky of the source. This decomposition is very convenient because it separates the angular dependence from the source parameters, in fact, it reminds us of the solution of the wave equation for a relativistic scalar field

$$\psi(t,r,\iota,\phi) = \frac{1}{r}\sum_{l=0}^{\infty}\sum_{m=-l}^{l} c_{lm}Y_{lm}(\iota,\phi). \tag{2}$$

Notice that in Eq. (1) the sum starts at $l = 2$, this means that in GR there exists neither monopole nor dipole gravitational radiation and this is why we start with the quadrupolar radiation. In the electromagnetic case, we recall that there is no monopole radiation due to the conservation of charge. In the gravitational case, the conservation of the energy-momentum tensor translates into the conservation of mass, linear and angular momentum. The first one is responsible to cancel the monopole while the other two cancel the "electric" and "magnetic" dipoles respectively. A common framework for

different types of spherical harmonics (for scalar, vector and tensor fields) is provided by the SWSH [5], which can be defined in terms of the Wigner d functions:

$$ {}_{-s}Y^{\ell m}(\iota,\phi) = (-1)^s \sqrt{\frac{2\ell+1}{4\pi}} d^{\ell}_{ms}(\iota) e^{im\phi} \tag{3} $$

where

$$ \begin{aligned} d^{\ell}_{ms}(\iota) =& \sqrt{(\ell+m)!(\ell-m)!(\ell+s)!(\ell-s)!} \\ & \times \sum_{k=k_i}^{k_f} \frac{(-1)^k \left(\sin\frac{\iota}{2}\right)^{2k+s-m} \left(\cos\frac{\iota}{2}\right)^{2\ell+m-s-2k}}{k!(\ell+m-k)!(\ell-s-k)!(s-m+k)!}. \end{aligned} \tag{4} $$

For the GWs, which correspond to symmetric trace-free tensors or spin-2 fields, the spin-weight is chosen as $s = -2$. When one starts to talk about subdominant harmonics Eq. (1) is the starting point, however, we will not present here such a derivation, but we point to an excellent work of Kidder [6] that presents this result in a clear and concise manner and refer to the relevant literature [7] for a more detailed discussion. A similar treatment can be found in Sec. 3.1 of [8]. In Sec. 3.5 of [9] the multipole expansion is also explained in detail although it does not explicitly relate it to the individual modes functions h_{lm}.

Equation (1) tells us that for modelling the GW signal we only have to model the individual functions h_{lm}. The main contribution of this thesis is to model some of these h_{lm} functions beyond the dominant $(2, \pm 2)$ modes both for non-precessing and precessing binary black hole systems. The inclusion of these *higher* or *subdominant spherical harmonics* provides a more accurate description of our templates of GW signals and allows us for better detection rates and better recovery of the source parameters. The subdominant modes are particularly important for edge-on systems i.e. with inclination near to $\pi/2$, as well as systems with very high mass and high mass ratio. All these systems will now be better understood thanks to the subdominant modes. Moreover, they help to disentangle the degeneracy between inclination and distance present in quadrupolar templates, enabling a more accurate recovery of the distance which is key for improving the measurement of the Hubble constant through GWs. This new way of measuring the Hubble constant could help to solve the current tensions existing between different measurement methods. For all these reasons we decided to develop a new waveform model that included subdominant modes and was at the same time accurate and fast to evaluate.

This thesis is divided into two main parts. In Part I I give a brief introduction and overview of the field. I start in Chapter 1 with a theoretical introduction of GWs, explaining how they arise from GR. In Chapter 2 I discuss how these waves are detected

on Earth and how physical information is extracted from the detector data through comparisons with theoretical templates, and also present some of the existing families of templates currently in use in GW data analysis. In Part II I present the original results derived from this thesis, which have lead to three papers submitted to peer-reviewed journals. Each paper is presented in a separate chapter, where I first summarize the work and results and indicate my contributions to the paper. More specifically, in Chapter 3 the non-precessing model with subdominant modes, IMRPhenomXHM, is presented. Then in Chapter 4 the technique of multibanding to accelerate the evaluation of waveform models by means of adapted grids is introduced, and in Chapter 5 the IMRPhenomXPHM model is presented, which is an extension of the two previous works to the more general systems of precessing black hole binaries. Finally, in Chapter 6 I summarize the main results, contributions and conclusions of this thesis as well as comment on opportunities to extend this research.

Bibliography

[1] A. Einstein. Näherungsweise integration der feldgleichungen der gravitation. *Sitzungsber Akad. Wiss.*, pages 688–696, 1916.

[2] A. Einstein. Die grundlage der allgemeinen relativitätstheorie. *Annalen der Physik*, 354:769–822, 1916.

[3] R. A. Hulse and J. H. Taylor. Discovery of a pulsar in a binary system. *Astrophysical Journal, Letters*, 195:L51–L53, January 1975. doi: 10.1086/181708.

[4] B. P. Abbott et al. Observation of gravitational waves from a binary black hole merger. *Phys. Rev. Lett.*, 116:061102, Feb 2016. doi: 10.1103/PhysRevLett.116.061102. URL https://link.aps.org/doi/10.1103/PhysRevLett.116.061102.

[5] J. N. Goldberg, A. J. Macfarlane, E. T. Newman, F. Rohrlich, and E. C. G. Sudarshan. Spin-s spherical harmonics and ð. *Journal of Mathematical Physics*, 8(11):2155–2161, 1967. doi: 10.1063/1.1705135. URL https://doi.org/10.1063/1.1705135.

[6] Lawrence E. Kidder. Using full information when computing modes of post-Newtonian waveforms from inspiralling compact binaries in circular orbit. *Phys. Rev. D*, 77:044016, Feb 2008. doi: 10.1103/PhysRevD.77.044016. URL https://link.aps.org/doi/10.1103/PhysRevD.77.044016.

[7] Kip S. Thorne. Multipole expansions of gravitational radiation. *Rev. Mod. Phys.*, 52:299–339, Apr 1980. doi: 10.1103/RevModPhys.52.299. URL https://link.aps.org/doi/10.1103/RevModPhys.52.299.

[8] Luc Blanchet. Gravitational Radiation from Post-Newtonian Sources and Inspiralling Compact Binaries. *Living Reviews in Relativity*, 17(1):2, 2014. ISSN 1433-8351. URL https://doi.org/10.12942/lrr-2014-2.

[9] Michele Maggiore. *Gravitational Waves. Volume 1: Theory and Experiments*. Oxford, 2008.

Part I

Introductory notions

Chapter 1

Introduction to Gravitational Waves

With the development of general relativity (GR), Einstein's theory passed to substitute replaced Newton's theory as the preferred theory of gravity. Although there exist several alternative theories which modify GR, none of them has been experimentally confirmed and only GR is considered as our modern theory of gravity. GR has allowed explaining several experimental observations that Newton's theory was not able to as the perihelion advance of Mercury [1, 2], the light deflection in presence of massive objects [3, 4], and recently the existence of gravitational waves (GWs) [5, 6]. In this chapter, we review some of the basic principles of GR, with special emphasis on discussing the GWs in the linearized theory, as well as the mechanism of different sources that produce them.

1.1 Introduction to GR

For almost two centuries and a half, since Isaac Newton announced his famous universal law of gravitation, the whole community of scientists had agreed and accepted that this description was indeed the correct theory of gravity. The traditional concept that gravity was an attractive force between two massive objects and that they create a "gravitational field" around them was so rooted in the minds of the scientists that practically nobody questioned its validity. However, in 1915 Albert Einstein defied the accepted paradigm and explained gravity not as a force between bodies but as the effect of the curvature of the *spacetime*. Einstein came to this conclusion after realizing that Newton's theory was incompatible with his theory of *special relativity* [7], which stated that any interaction can not propagate instantaneously, and after understanding the fundamental role of the *equivalence principle*. This was the birth of a new theory, the theory of GR [8], which combined gravity with Einstein's special relativity published in 1905. The two basic

postulates of special relativity are the principle of relativity and the invariance of the speed of light:

1. The laws of physics take the same form in all inertial frames of reference.
2. The speed of light in vacuum is the same for all inertial observers and is independent of the movement of the source.

The first postulate refers only to inertial frames, however, a freely falling observer in a gravitational field is not an inertial observer but rather an accelerated one. In GR, freely falling observers take the role of inertial observers by virtue of Einstein's formulation of the equivalence principle:

Freely falling observers in a gravitational field are locally equivalent to inertial observers.

Such a freely falling observer will see free-falling objects, in a sufficiently near region around him, moving at constant velocity (or being static if the initial velocity in this frame was zero), since these objects are subject to the same gravitational field and suffer the same acceleration. This is the same situation that an observer would face if he was at rest or moving at constant velocity (inertial observer). In fact, he is not able to distinguish the two situations, a freely falling observer is "locally" equivalent to an observer in absence of gravitational field.

Special relativity also introduced the concept of flat spacetime, a four-dimensional manifold which is the combination of the three-dimensional Euclidean space with time. All the physical events are described as spacetime points in this flat manifold, named as Minkowski spacetime. The distance between events can be measured through the Minkowski flat metric $\eta_{\mu\nu}$

$$ds^2 = \eta_{\mu\nu} dx^\mu dx^\nu, \qquad \eta_{\mu\nu} = diag(-1, 1, 1, 1), \tag{1.1}$$

where the repetition of indices denotes summation over those indices. In the following, Greek letters will denote indices spanning form 0 to 3, while Latin letters will stand for the spatial indices from 1 to 3. The symbol ds denotes the infinitesimal displacement between points (events) in the manifold. Note that the metric must be symmetric since swapping dx^μ and dx^ν must return the same result.

The equivalence principle involves that there exists a change of coordinates capable to eliminate the gravitational field in a small region that resembles the Minkowski spacetime. Due to the complexity of the gravitational field, this change of coordinates is different from point to point of the spacetime, which implies that this spacetime locally behaves as

Minkowski but globally it does not. This brings up the concept of curved manifolds. The metric, now called $g_{\mu\nu}$, is not uniform anymore through the manifold but it varies from point to point ($g_{\mu\nu}(x)$) and it represents a general symmetric tensor with 10 independent components. We will only consider manifolds where at any given point the flat tangent space corresponds to a Minkowski spacetime with a metric signature as in Eq. (1.1), i.e. a flat *Lorentzian* manifold.

The principle of relativity introduced before requires that the line element in the manifold $ds^2 = g_{\mu\nu}dx^\mu dx^\nu$ must be the same for all the observers. The generalization of the principle of relativity to accelerated observers leads to the concept of general covariance, which postulates that the spacetime structure is determined only by the metric tensor and tensors derived from it. The metric must remain invariant under any change of coordinate system $x^\alpha = f^\alpha(x'^\mu)$. Performing this transformation the coordinate displacement is

$$dx^\mu = \frac{\partial x^\mu}{\partial x'^\alpha} dx'^\alpha. \tag{1.2}$$

Introducing this into the definition (1.1) of ds^2 we have

$$ds^2 = g_{\mu\nu}\frac{\partial x^\mu}{\partial x'^\alpha}\frac{\partial x^\nu}{\partial x'^\beta}dx'^\alpha dx'^\beta, \tag{1.3}$$

and we see that to keep ds^2 invariant the metric $g_{\mu\nu}$ must transform as

$$g'_{\alpha\beta} = g_{\mu\nu}\frac{\partial x^\mu}{\partial x'^\alpha}\frac{\partial x^\nu}{\partial x'^\beta}, \tag{1.4}$$

so $g_{\mu\nu}$ transforms as a covariant tensor field under general coordinate transformations.

Let us consider now a vector field $\mathbf{A}$ defined in our 4 dimensional manifold. If the manifold is flat, the vector basis in which we describe $\mathbf{A}$ is the same in the whole manifold, and the derivative of $\mathbf{A}$ is given just by the derivative of its components. However, in curved manifolds the vector basis changes from point to point both in magnitude and in direction so the derivative applies both to the components and to the basis vectors:

$$\partial_\mu \mathbf{A} = (\partial_\mu A^\nu)\mathbf{e}_\nu + A^\nu(\partial_\mu \mathbf{e}_\nu). \tag{1.5}$$

The derivative of the basis vectors is used as a definition for the components of the *affine connection* $\Gamma^\lambda_{\mu\nu}$

$$\partial_\mu \mathbf{e}_\nu = \Gamma^\lambda_{\nu\mu}\mathbf{e}_\lambda. \tag{1.6}$$

We will use the affine connection to introduce the concept of a new derivative which takes into account the changes also in the basis vectors. This is known as the *covariant*

derivative and when applied to a vector field it takes the form

$$\nabla_\mu A^\nu := \partial_\mu A^\nu + \Gamma^\nu_{\lambda\mu} A^\lambda, \tag{1.7}$$

so now we can express $\partial_\mu \mathbf{A}$ as $\partial_\mu \mathbf{A} = (\nabla_\mu A^\nu)\mathbf{e}_\nu$. The covariant derivative is not exclusive of vector fields but can be defined also for tensor fields. For example, applied to the metric, which is a tensor of rank (2,0), we have

$$\nabla_\mu g^{\nu\rho} = \partial_\mu g^{\nu\rho} + \Gamma^\nu_{\mu\lambda} g^{\lambda\rho} + \Gamma^\rho_{\mu\lambda} g^{\nu\lambda}. \tag{1.8}$$

And for any generic tensor C of rank (m, n) the covariant derivative can be expressed from the partial derivative and the affine connection as

$$\begin{aligned} \nabla_\rho C^{\mu_1\ldots\mu_m}{}_{\nu_1\ldots\nu_n} &= \partial_\rho C^{\mu_1\ldots\mu_m}{}_{\nu_1\ldots\nu_n} \\ &+\Gamma^{\mu_1}_{\rho\lambda} C^{\lambda\mu_2\ldots\mu_m}{}_{\nu_1\ldots\nu_n} + \ldots + \Gamma^{\mu_m}_{\rho\lambda} C^{\mu_1\ldots\mu_{m-1}\lambda}{}_{\nu_1\ldots\nu_n} \\ &-\Gamma^\lambda_{\rho\nu_1} C^{\mu_1\ldots\mu_m}{}_{\lambda\nu_2\ldots\nu_n} - \ldots - \Gamma^\lambda_{\rho\nu_{n-1}} C^{\mu_1\ldots\mu_m}{}_{\nu_1\ldots\nu_{n-1}}. \end{aligned} \tag{1.9}$$

The covariant derivative allows us to define the concept of *parallel transport* of any vector. In a simplified manner, the parallel transport of a vector consists of transporting a vector from a point p in the manifold to a point q, but keeping all the information that the vector had in p. In general, this parallelly transported vector in q will not coincide with the vector in p since the manifold is curved and they belong to completely different tangent flat spacetimes. In mathematical language, a vector V^μ is parallel transported along a curve $x^\mu(\tau)$ if

$$\frac{dx^\mu(\tau)}{d\tau} \nabla_\mu V^\nu = 0. \tag{1.10}$$

Measuring how a vector changes under parallel transport along a closed curve provides a measure of "how much" curvature there is inside the curve. To measure the curvature at one point in the manifold we can define the curve given by an infinitesimal parallelogram with sides dx^μ and dx^ν. So we can compare the result of parallelly transporting a vector first through dx^μ and later dx^ν with transporting first through dx^ν and later through dx^μ. This is equivalent to compute the commutator of the covariant derivative $[\nabla_\mu, \nabla_\nu] = \nabla_\mu\nabla_\nu - \nabla_\nu\nabla_\mu$ of a vector. Inserting the expression for the covariant derivative (1.7) we have

$$[\nabla_\mu, \nabla_\nu] V^\lambda = R_{\mu\nu\rho}{}^\lambda V^\rho - U^\rho_{\mu\nu} \nabla_\rho V^\lambda, \tag{1.11}$$

where

$$R_{\mu\nu\rho}{}^\lambda = \partial_\mu \Gamma^\lambda_{\nu\rho} - \partial_\nu \Gamma^\lambda_{\mu\rho} + \Gamma^\lambda_{\mu\sigma}\Gamma^\sigma_{\nu\rho} - \Gamma^\lambda_{\nu\sigma}\Gamma^\sigma_{\mu\rho}, \tag{1.12}$$

$$U^\rho_{\mu\nu} = \Gamma^\rho_{\mu\nu} - \Gamma^\rho_{\nu\mu}. \tag{1.13}$$

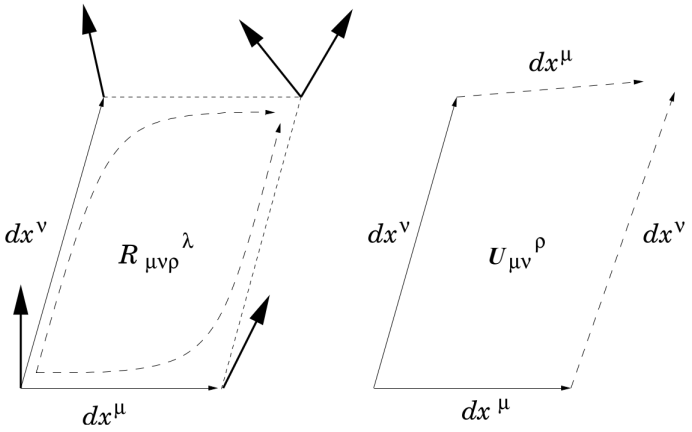

FIGURE 1.1: The Riemann tensor $R_{\mu\nu\rho}{}^{\lambda}$ measures the difference on a vector parallel transported through an infinitesimal parallelogram and it is a measurement of the curvature inside the parallelogram. The torsion tensor $T_{\mu\nu}{}^{\rho}$ measures if the parallel transport of dx^ν along dx^μ and the parallel transport of dx^μ along dx^ν produces a closed curve.

$R_{\mu\nu\rho}{}^{\lambda}$ is known as the *Riemann tensor* and measures the curvature enclosed by the parallelogram. $U^{\rho}_{\mu\nu}$ is the *torsion tensor*, the antisymmetric part of the connection and measures whether quadrilaterals close under parallel transport (see Fig. 1.1). In GR there is no observational evidence that the torsion tensor plays any role in nature so it is usually set to zero. There exists an alternative theory named Einstein–Cartan–Sciama–Kibble (ECSK) [9, 10] that includes torsion. Furthermore, in GR a unique connection is chosen, which can be defined in terms of the metric, consistent with the principle of general covariance. This connection is called the *Levi-Civita connection* and it satisfies two conditions:

1. Symmetry: $\Gamma^{\rho}_{\mu\nu} = \Gamma^{\rho}_{\nu\mu}$.
2. Compatibility with the metric: $\nabla_\mu g_{\nu\rho} = 0$.

The first condition cancels the torsion tensor and allows the scalar product of two vectors to be invariant under parallel transport. The second allows one to lower and raise indexes of a tensor inside a covariant derivative:

$$g_{\mu\nu}\nabla_\rho S^{\mu\nu} = \nabla_\rho(g_{\mu\nu}S^{\mu\nu}) = \nabla_\rho S^{\mu}{}_{\mu}. \tag{1.14}$$

With these properties, the connection is completely determined by the metric and its explicit dependence is specified by the *Christoffel symbols*

$$\Gamma^{\lambda}_{\mu\nu} = \frac{1}{2}g^{\lambda\sigma}\left(\partial_\mu g_{\sigma\nu} + \partial_\nu g_{\mu\lambda} - \partial_\lambda g_{\mu\nu}\right). \tag{1.15}$$

Consequently, the Riemann tensor also depends directly on the metric and it acquires extra symmetries which convert the *Ricci tensor* in the only independent contraction of the Riemann tensor:

$$R_{\mu\nu} = R_{\mu\lambda\nu}{}^{\lambda} = R_{\mu\lambda}{}^{\lambda}{}_{\nu} = R_{\mu\nu\lambda}{}^{\lambda} = \frac{1}{2}\left(\partial^{\rho}\partial_{\mu}g_{\nu\rho} + \partial^{\rho}\partial_{\nu}g_{\mu\rho} - \partial^{\rho}\partial_{\rho}g_{\mu\nu} - \partial_{\mu}\partial_{\nu}g\right). \quad (1.16)$$

The symbol g refers to the trace of $g_{\mu\nu}$. The *Ricci scalar* is the contraction of the Ricci tensor

$$R = g^{\mu\nu}R_{\mu\nu} = \partial^{\mu}\partial^{\nu}g_{\mu\nu} - \partial^{\mu}\partial_{\mu}g. \quad (1.17)$$

We now have all the elements to build the Einstein tensor $G_{\mu\nu}$

$$G_{\mu\nu} = R_{\mu\nu} - \frac{1}{2}g_{\mu\nu}R. \quad (1.18)$$

With the Levi-Civita connection it can be shown that the Riemann tensor satisfies

$$\nabla_{\sigma}R_{\mu\nu\rho\lambda} + \nabla_{\lambda}R_{\mu\nu\sigma\rho} + \nabla_{\rho}R_{\mu\nu\lambda\sigma} = 0, \quad (1.19)$$

and by contracting the two pair of indices we come to the conservation law for the Einstein tensor

$$\nabla_{\mu}\left[R_{\mu\nu} - \frac{1}{2}g_{\mu\nu}R\right] = \nabla_{\mu}G^{\mu\nu} = 0. \quad (1.20)$$

The trajectories that free test particles follows in the manifold are called *geodesics*. This curve satisfies that the tangent vector keeps parallel to itself under parallel transport through the curve, and also it turns out to be an extremal-length curve between two points. These two properties are satisfied thanks to the choice of the Levi-Civita connection, a general connection will not satisfy these two properties at the same time and there exists then a distinction between *affine* and *metric* geodesics respectively. Since the geometry is curved, a freely moving observer will feel an acceleration which is interpreted as the acceleration of "gravity". If the spacetime is flat a freely moving object follows a straight line with constant velocity, however, in a curve manifold straight lines become curves and the objects' velocity does not remain constant. In words of John Wheeler, "spacetime geometry tells matter how to move". The second part of his famous quote states that moreover, "matter tells spacetime how to curve". Indeed, it is well known that matter is the source of gravity, and if gravity is the result of the curvature of the spacetime matter must determine the geometry of the spacetime. In fact, not only matter must be a source of curvature but also energy, since they are equivalent according to Einstein's famous equation $E = mc^2$. The source of gravity is then the content of mass and energy which is described by the stress-energy tensor $T_{\mu\nu}$.

The Einstein's tensor and stress-energy tensor are related by a constant of proportionality:

$$G_{\mu\nu} = \kappa T_{\mu\nu}, \tag{1.21}$$

which establishes the intrinsic relation between geometry and matter. The constant of proportionality κ is obtained by imposing the Newtonian limit so we get the famous Einstein field equations,

$$G_{\mu\nu} = \frac{8\pi G}{c^4} T_{\mu\nu}. \tag{1.22}$$

1.2 Linearized Einstein field equations

In this section, we study how GWs emerge from Einstein's GR theory. The approach followed here is similar to Einstein's original calculation and relies on the "weak field approximation" which assumes that the background spacetime where the GWs propagate is flat, i.e. it is described by the Minkowski metric $\eta_{\mu\nu}$. Since we will measure the GWs on Earth, at a very large distance from the source, and with a weak local gravitational field, this is a good enough approximation. An illustration of the weakness of the gravitational field on Earth is provided by the extremely small slow-down of time between e.g. the surface of the Earth and a satellite. There are of course many other scenarios where the gravitational interaction overcomes the effect of other forces such as in our Sun or any other star, where gravity can compensate the pressure force emerging from the nuclear reactions that are being produced in the core. GWs arise naturally when the background metric of the flat spacetime $\eta_{\mu\nu}$ is influenced by small perturbations. The Einstein's field equations lead to a wave equation under this approximation. The full Einstein equations are given by

$$R_{\mu\nu} - \frac{1}{2} g_{\mu\nu} R = \frac{8\pi G}{c^4} T_{\mu\nu}. \tag{1.23}$$

We want to study how these equations transform under a perturbation of the flat metric:

$$g_{\mu\nu} = \eta_{\mu\nu} + h_{\mu\nu}, \qquad |h_{\mu\nu}| \ll 1 \tag{1.24}$$

and expand them only up to linear order in the perturbation $h_{\mu\nu}$. This requires recomputing the Christoffel symbols with the new perturbed metric, continue with the Riemann tensor and finally with the Ricci tensor and Ricci scalar. These calculations need the inverse metric in the contravariant form

$$g^{\mu\nu} = \eta^{\mu\nu} - h^{\mu\nu}, \tag{1.25}$$

which satisfies the inverse relation only in the linearized approximation since

$$(\eta_{\mu\nu} - h_{\mu\nu})\,(\eta^{\nu\sigma} - h^{\nu\sigma}) = \eta_\mu{}^\sigma - h_{\mu\sigma} + h_{\mu\sigma} + O(h^2) = \delta_\mu{}^\sigma + O(h^2). \tag{1.26}$$

Inserting this metric (1.24) in the expressions for the Christoffel symbols (1.15) leads to

$$\Gamma^\lambda_{\mu\nu} = \frac{1}{2}\eta^{\lambda\sigma}\left(\partial_\mu h_{\sigma\nu} + \partial_\nu h_{\mu\lambda} - \partial_\lambda h_{\mu\nu}\right). \tag{1.27}$$

Introducing them in the general expression for the Riemann tensor (1.12) we obtain the expression of the perturbed Riemann tensor

$$R_{\mu\nu\rho\lambda} = \frac{1}{2}\left(\partial_\nu\partial_\rho h_{\mu\lambda} + \partial_\mu\partial_\lambda h_{\nu\rho} - \partial_\mu\partial_\rho h_{\nu\lambda} - \partial_\nu\partial_\lambda h_{\mu\rho}\right). \tag{1.28}$$

The Ricci tensor and scalar are computed by contraction of the Riemann and Ricci tensors,

$$R_{\mu\nu} = \eta^{\rho\lambda}R_{\mu\rho\nu\lambda} = \frac{1}{2}\left(\partial^\lambda\partial_\nu h_{\mu\lambda} + \partial_\mu\partial^\rho h_{\rho\nu} - \partial_\mu\partial_\nu h^\lambda_\lambda - \partial^\lambda\partial_\lambda h_{\mu\nu}\right), \tag{1.29}$$

$$R = \eta^{\mu\nu}R_{\mu\nu} = \partial^\mu\partial^\nu h_{\mu\nu} - \partial_\mu\partial^\mu h^\nu_\nu. \tag{1.30}$$

Inserting (1.29) and (1.30) into (1.23), we obtain the linearized form of the Einstein field equations

$$\Box\bar{h}_{\mu\nu} + \eta_{\mu\nu}\partial^\rho\partial^\sigma\bar{h}_{\rho\sigma} - \partial^\rho\partial_\nu\bar{h}_{\mu\rho} - \partial^\rho\partial_\mu\bar{h}_{\nu\rho} = -\frac{16\pi G}{c^4}T_{\mu\nu}, \tag{1.31}$$

where we have introduced the symbol of the flat space d'Alembertian, $\Box = \eta_{\mu\nu}\partial^\mu\partial^\nu = \partial_\mu\partial^\mu$ and also the following notation

$$\bar{h}_{\mu\nu} = h_{\mu\nu} - \frac{1}{2}\eta_{\mu\nu}h, \qquad\qquad h = \eta^{\mu\nu}h_{\mu\nu} = h^\mu_\mu. \tag{1.32}$$

Eq. (1.31) does not exhibit yet the form of a wave equation. The next step in this direction is to fix the "gauge freedom". In GR there exists the freedom of choosing the reference system, such that the theory is covariant under any coordinate transformation

$$x^\mu \to x'^\mu(x). \tag{1.33}$$

For the sake of simplicity, we adopted coordinate systems where $|h_{\mu\nu}| \ll 1$ so that we do not have the same gauge freedom than GR but we keep a residual gauge symmetry given by

$$x^\mu \to x'^\mu = x^\mu + \xi^\mu(x), \tag{1.34}$$

where $\xi^\mu(x)$ is small. In order to confirm that this coordinate change is indeed a symmetry of the linearized theory let us investigate how the metric (1.24) behaves under this

change of coordinates

$$g_{\mu\nu}(x) \to g'_{\mu\nu}(x') = \eta_{\mu\nu} + h_{\mu\nu} - (\partial_\mu \xi_\nu + \partial_\nu \xi_\mu) + O(\partial\xi h) + O(\partial\xi\partial\xi) + O(\partial\xi\partial\xi h). \quad (1.35)$$

The flat space metric $\eta_{\mu\nu}$ does not change since it does not depend on x and restricting to linear order we can do the identification

$$h_{\mu\nu}(x) \to h'_{\mu\nu}(x') = h_{\mu\nu}(x) - (\partial_\mu \xi_\nu + \partial_\nu \xi_\mu). \quad (1.36)$$

Requiring that $|\partial_\mu \xi_\nu| \ll 1$ is about the same order of magnitude as $|h_{\mu\nu}|$, the condition that $|h'_{\mu\nu}| \ll 1$ is still preserved and therefore the requirements of a linearized theory are retained.

We can now use the gauge freedom for choosing ξ^μ to simplify the expression (1.31). The most appropriate choice is known as the *harmonic gauge* (or the De Donder gauge or also the Hilbert gauge) which is written as

$$\partial^\nu \bar{h}_{\mu\nu} = 0. \quad (1.37)$$

The above expression resembles the Lorentz gauge used in electromagnetism, $\partial_\mu A^\mu = 0$. We derive hereafter the expression for ξ_μ which satisfies this relation. Under the change of (1.34) the quantity $\bar{h}_{\mu\nu}$ transforms as

$$\bar{h}_{\mu\nu} \to \bar{h}'_{\mu\nu} = \bar{h}_{\mu\nu} - (\partial_\mu \xi_\nu - \partial_\nu \xi_\mu - \eta_{\mu\nu}\partial_\rho \xi^\rho), \quad (1.38)$$

finding the derivative of the above expression we obtain that the quantity in expression (1.37) transforms as

$$\partial^\nu \bar{h}_{\mu\nu} \to (\partial^\nu \bar{h}_{\mu\nu})' = \partial^\nu \bar{h}_{\mu\nu} - \partial^\nu \partial_\nu \xi_\mu. \quad (1.39)$$

So that the transformed quantity $(\partial^\nu \bar{h}_{\mu\nu})'$ also satisfies the gauge condition it is required that

$$\Box \xi_\mu = \partial^\nu h_{\mu\nu}. \quad (1.40)$$

There always exist solutions for ξ_μ which satisfy this relation which are given in terms of the Green's function of the d'Alembertian operator:

$$\xi_\mu(x) = \int d^4y \, G(x-y)\partial^\nu h_{\mu\nu}(y). \quad (1.41)$$

Now that we have demonstrated that the harmonic gauge is a perfectly valid choice of gauge we can insert it into (1.31) which cancels the last three terms of the left hand side

and leads to the familiar form of the wave equation:

$$\Box\bar{h}_{\mu\nu} = -\frac{16\pi G}{c^4}T_{\mu\nu}. \tag{1.42}$$

The symbol $\Box$ refers to the d'Alembertian operator in flat space $((-1/c^2)\partial_t^2, \partial_x^2, \partial_y^2, \partial_z^2)$ and Eq. (1.42) corresponds to a wave equation which propagates at the speed of light and that possesses $T_{\mu\nu}$ as source term. Performing the partial derivative ∂^μ of (1.42) and recalling that the harmonic gauge is satisfied, we obtain the following constraint

$$\partial^\mu T_{\mu\nu} = 0, \tag{1.43}$$

which is the condition of conservation of the energy-momentum tensor in linearized theory. In GR for a general curved metric the partial derivative is replaced by the covariant derivative, consistent with the "recipe" of translating physical laws in Minkowski spacetime to curved spacetimes by replacing the Minkowski metric with a general metric, and partial by covariant derivatives.

1.3 The Transverse-Traceless (TT) gauge

Once GWs are emitted they travel through the universe during millions of years at the speed of light until reaching the Earth and the detectors. At this point they are far outside the source so we can consider the source term equal to zero and the wave equation (in vacuum) simplifies to

$$\Box\bar{h}_{\mu\nu} = 0. \tag{1.44}$$

In this situation, it turns out that there exists an extra gauge freedom which allows us to clearly manifest the transversality of the wave and to make it traceless, i.e. $\bar{h} = 0$. Consider a similar transformation to (1.34), $x^\mu \to x^\mu + \epsilon^\mu$ (we just replaced ξ by ϵ to clarify that it is a different transformation) where the functions ϵ^μ now satisfy

$$\Box\epsilon_\mu = 0. \tag{1.45}$$

We already know that there exist always a solution for the former equation. In addition, this new transformation still satisfies the harmonic gauge $(\partial^\nu\bar{h}_{\mu\nu})' = 0$. Remember from (1.39) that

$$(\partial^\nu\bar{h}_{\mu\nu})' = \partial^\nu\bar{h}_{\mu\nu} - \Box\epsilon_\mu, \tag{1.46}$$

and from (1.38) we see that by choosing ϵ_μ we can impose certain conditions on $\bar{h}_{\mu\nu}$. Since there are 4 functions ϵ_μ to choose we can impose 4 conditions which for convenience

are

$$\bar{h} = 0, \qquad h^{0i} = 0. \tag{1.47}$$

The right hand expression implies that the temporal dependence of the wave appears only in their spatial components. It can be shown that these conditions together with the harmonic gauge translate into

$$h^{0\mu} = 0, \qquad h^i_i = 0, \qquad \partial^j h_{ij} = 0. \tag{1.48}$$

The imposition of the Lorentz gauge and the TT gauge restricts the original 10 degrees of freedom of our problem. Both gauge choices involve 4 conditions each one so only 2 degrees of freedom remain. These are identified by the *plus* and *cross polarizations*, denoted by h_+ and $h_\times$.

In the TT gauge, since $\bar{h} = 0$ we have that $\bar{h}_{\mu\nu} = h_{\mu\nu}$ and equation (1.44) admits plane wave solutions of the form

$$h^{TT}_{\mu\nu} = A_{\mu\nu} e^{ik_\rho x^\rho}, \tag{1.49}$$

where $k^\mu = (\omega/c, \mathbf{k})$ and $\mathbf{k}$ is the wave-vector, which indicates the direction of propagation. The third condition in (1.48) implies that the wave oscillates in the plane perpendicular to the direction of propagation. By selecting the z-axis as the direction of propagation we can write $h_{\mu\nu}$ in the TT gauge as

$$h^{TT}_{\mu\nu} = \begin{pmatrix} 0 & 0 & 0 & 0 \\ 0 & h_+ & h_\times & 0 \\ 0 & h_\times & -h_+ & 0 \\ 0 & 0 & 0 & 0 \end{pmatrix}_{\mu\nu} = \begin{pmatrix} 0 & 0 & 0 & 0 \\ 0 & A_+ & A_\times & 0 \\ 0 & A_\times & -A_+ & 0 \\ 0 & 0 & 0 & 0 \end{pmatrix}_{\mu\nu} e^{i\omega(t-z/c)}, \tag{1.50}$$

where we introduce the amplitudes $A_\times$ and A_+. A convenient way to transform to the TT gauge any given plane wave $h_{\mu\nu}$, which is already in the Lorentz gauge, is by means of the Lambda tensor $\Lambda_{ij,kl}$,

$$h^{TT}_{ij} = \Lambda_{ij,kl} h^{kl}. \tag{1.51}$$

The Lambda tensor is defined as

$$\Lambda_{ij,kl}(\hat{\mathbf{n}}) = P_{ik}P_{jl} - \frac{1}{2}P_{ij}P_{kl}, \qquad \text{with } P_{ij}(\hat{\mathbf{n}}) = \delta_{ij} - n_i n_j, \tag{1.52}$$

n^i are the components of the unitary vector in the direction of the line of sight from the source to the observer, which coincides with the direction of the wave vector, $\hat{\mathbf{n}} = \mathbf{k}/|\mathbf{k}|$.

1.4 Distortion of a ring of particles

Now that we have an explicit solution for the GWs travelling in vacuum we wonder how matter reacts to an incoming wave of such nature. We will study in this section what is the effect of a GW over a ring of free particles perpendicular to the incoming wave. Assuming that the separation between two of these test masses is small compared to the wavelength of the radiation, the equation of motion for the separation vector between these two masses x^μ is given by the geodesic deviation equation

$$\frac{d^2x^i}{dt^2} = -c^2 R_{0i0k} x^k. \tag{1.53}$$

Incorporating the expression for the Riemann tensor of (1.28) we have

$$\frac{d^2x^i}{dt^2} = \frac{1}{2}\ddot{h}_{ij}x^j, \tag{1.54}$$

where the two dots denote second derivative respect to time. The solution to this equation up to leading order in h_{ij} is expressed by

$$x^i(t) = x^i(0) + \frac{1}{2}h^{ik}(t)x_k(0) \tag{1.55}$$

or

$$x(t) = x_0 + \frac{1}{2}(h_+ x_0 + h_\times y_0), \qquad y(t) = y_0 + \frac{1}{2}(h_\times x_0 - h_+ y_0), \qquad z(t) = z_0. \tag{1.56}$$

To interpret more simply the motion described by the previous set of equations let us consider a case where only the h_+ mode is present. We find out that when h_+ increases the separation in the $x-$axis grows the separation in the y-axis must decrease, while when h_+ decreases the opposite behaviour occurs. So for an initial ring of particles, it can be seen that the circle is distorted into an ellipse given by

$$\left(\frac{x}{1+\frac{h_+}{2}}\right)^2 + \left(\frac{y}{1-\frac{h_+}{2}}\right)^2 = 1. \tag{1.57}$$

The ellipse transforms between the shapes shown in Fig. 1.2. Equivalently for a case where only the $h_\times$ mode is present the ellipse is given by

$$\left(\frac{x+y}{1+\frac{h_\times}{2}}\right)^2 + \left(\frac{x-y}{1-\frac{h_\times}{2}}\right)^2 = 1. \tag{1.58}$$

Notice that this ellipse is rotated by 45° with respect to the h_+ one. So the vibration mode of $h_\times$ is the same as for h_+ but rotated by 45°. In fact, we can justify this

by pointing out that under a general rotation of the angle ψ around the z-axis the polarizations transform in the following way (see e.g. section 11.1.7 in [11])

$$h'_+ = h_+ \cos 2\psi + h_\times \sin 2\psi, \qquad h'_\times = -h_+ \sin 2\psi + h_\times \cos 2\psi. \tag{1.59}$$

From above it can be seen that when the rotation is $\psi = 45°$ then $h'_+ = h_\times$ and $h'_\times = h_+$, so the polarizations are interchanged.

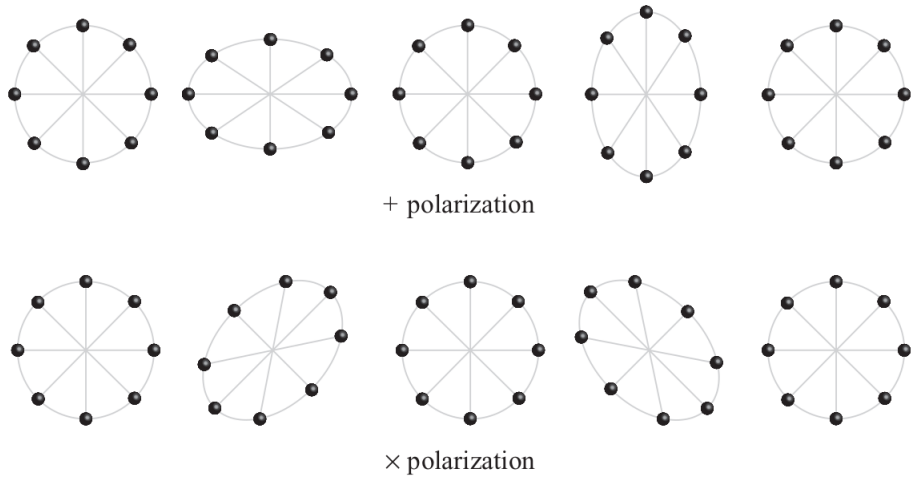

FIGURE 1.2: Distortion of a ring of free particles by the h_+ and $h_\times$ polarizations of a GW coming perpendicular to the paper. Image credits: [11].

1.5 Quadrupole formula

In the previous section, we have shown the effects of a passing GW on a ring of particles with no assumptions on the eventual sources that generate them. In this section, we will study how GWs are generated by matter sources by means of the quadrupole approximation. The quadrupole formula is an approximation to the GW emission that relies on two assumptions: the gravitational field produced by the source is weak, so the background metric can be taken as flat and the typical velocities inside the source are small compared to the speed of light. Under these assumptions the *quadrupole formula* is given by

$$\left[h_{ij}^{TT}(t, \mathbf{x})\right]_{\text{quad}} \equiv \frac{2G}{rc^4} \ddot{\mathcal{I}}_{ij}^{TT}(t - r/c), \tag{1.60}$$

where r is the distance to the source and $\mathcal{I}^{ij}$ is the *quadrupole moment* defined as

$$\mathcal{I}^{ij}(t) = \frac{1}{c^2} \int d^3x' T^{00} \left(t - \frac{r}{c}, \mathbf{x}'\right) x'^i x'^j. \tag{1.61}$$

The expression for the quadrupole formula was derived first by Einstein in 1916 [5] and corresponds to the first prediction of the existence of GWs (although they were already proposed by Henri Poincaré in 1905). Given its importance and the enormous and exciting results that came after that, we will dedicate a few paragraphs below to summarize how this formula is derived.

We start from the basic result of linearized theory (1.42)

$$\Box \bar{h}_{\mu\nu} = -\frac{16\pi G}{c^4} T_{\mu\nu}, \tag{1.62}$$

where $T_{\mu\nu}$ is linear in $h_{\mu\nu}$, and the Lorentz gauge $\partial^\mu \bar{h}_{\mu\nu} = 0$ is already applied. The solution to the above equation for a radiation problem, as it is for electromagnetism, is given in terms of the retarded Green's function,

$$\bar{h}_{\mu\nu}(t, \mathbf{x}) = \frac{4G}{c^4} \int d^3x' \frac{1}{|\mathbf{x} - \mathbf{x}'|} T_{\mu\nu} \left(t - \frac{|\mathbf{x} - \mathbf{x}'|}{c}, \mathbf{x}' \right). \tag{1.63}$$

The vector $\mathbf{x}$ indicates the position of the observer measured from the center of mass of the source, and $\mathbf{x}'$ refers to a particular point inside the source (see Fig. 1.3). We are

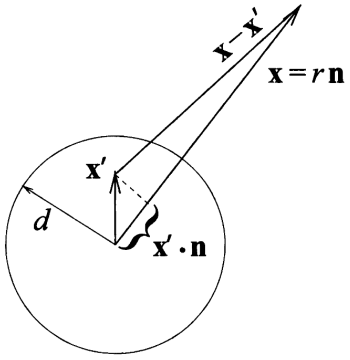

FIGURE 1.3: Illustration of the vectors and distances used in this section. $\mathbf{n}$ is the unitary vector in the line of sight, pointing in the direction from the center of mass of the source to the observer (where we want to compute the solution). d is the typical size of the source, it does not require that the source must be spherical. Image credits: [12].

interested in the solution far away from the source where we can impose the TT gauge and deem only the spatial components of $h_{\mu\nu}$. Also we consider the approximation that the distance to the source r is much larger than the typical size of the source d ($r \gg d$) so

$$|\mathbf{x} - \mathbf{x}'| = r - \mathbf{x}' \cdot \hat{\mathbf{n}} + O\left(\frac{d^2}{r}\right). \tag{1.64}$$

Inserting this into the TT gauge version of (1.63) we have

$$h_{ij}^{TT}(t, \mathbf{x}) = \frac{4G}{c^4} \Lambda_{ij,kl} \int d^3x' \frac{1}{r - \mathbf{x}' \cdot \hat{\mathbf{n}}} T^{kl} \left(t - \frac{r}{c} + \frac{\mathbf{x}' \cdot \hat{\mathbf{n}}}{c}, \mathbf{x}' \right), \tag{1.65}$$

when $r \gg d$ and so $r \gg |x' \cdot \hat{n}|$ we can factor out $1/r$ from the integral

$$h_{ij}^{TT}(t, \mathbf{x}) = \frac{4G}{r\, c^4} \Lambda_{ij,kl} \int d^3x'\, T^{kl} \left(t - \frac{r}{c} + \frac{\mathbf{x}' \cdot \hat{\mathbf{n}}}{c}, \mathbf{x}' \right). \tag{1.66}$$

Now we make use of the second assumption we mentioned at the beginning of this section, which was that the typical velocities inside the source are low compared to the speed of light. This allows us to make an expansion of $T_{ij}\left(t - \frac{r}{c} + \frac{\mathbf{x}' \cdot \hat{\mathbf{n}}}{c}, \mathbf{x}'\right)$ in powers of $1/c$ whose first element is given by $T_{ij}\left(t - \frac{r}{c}\right)$. Inserting this into expression (1.66) we get

$$h_{ij}^{TT}(t, \mathbf{x}) = \frac{4G}{r\, c^4} \Lambda_{ij,kl} \int d^3x'\, T^{kl} \left(t - \frac{r}{c}, \mathbf{x}' \right). \tag{1.67}$$

Making use of the conservation of the energy-momentum tensor $\partial^\mu T_{\mu\nu} = 0$ and integrating the right-hand side by parts twice we obtain

$$h_{ij}^{TT}(t, \mathbf{x}) = \frac{4G}{r\, c^4} \Lambda_{ij,kl} \partial_0 \partial_0 \int d^3x' \frac{1}{2} T^{00} \left(t - \frac{r}{c}, \mathbf{x}' \right) x'^k x'^l. \tag{1.68}$$

Remembering the definition of the quadrupole moment in (1.61) we see that finally, we have arrived at the expression for the quadrupole formula. In a low-velocity expansion of T^{00} the leading order is proportional to the energy density ρ and the square of the speed of light, so expression (1.68) turns into

$$h_{ij}^{TT}(t, \mathbf{x}) = \frac{2G}{r\, c^2} \Lambda_{ij,kl} \partial_0 \partial_0 \int d^3x'\, \rho \left(t - \frac{r}{c}, \mathbf{x}' \right) x'^k x'^l. \tag{1.69}$$

We can now obtain the $h_{+,\times}$ polarizations in a frame whose z-axis points toward the observer by performing the following projection

$$\begin{aligned} h_+ &= \frac{1}{2} \left(e_X^i e_X^j - e_Y^i e_Y^j \right) h_{ij} \\ h_\times &= \frac{1}{2} \left(e_X^i e_Y^j + e_Y^i e_X^j \right) h_{ij} \end{aligned} \tag{1.70}$$

The triad $\{\mathbf{e_X}, \mathbf{e_Y}, \mathbf{e_Z}\}$ defines the new frame whose z-axis coincides with the line of sight and is commonly known as the *wave frame*.

1.6 Quadrupole emission from binary systems in circular motion

We now focus on a special kind of source: binary systems where the source is composed of two compact objects that orbit around each other. These are the most likely sources of GWs to be detected by ground based detectors and are known as Compact Binary Coalescence (CBC) signals. In fact, CBC signals are the only ones detected so far by

the [6, 13–18]. The compact objects can be black holes or neutron stars so we can have binaries black holes (BBH), binaries neutron stars (BNS or a system with neutron star and a black hole (NSBH). In order to describe the GW emission of these systems, we will approximate the two compact objects by point-like particles so the energy density is given by

$$\rho(t, \mathbf{x}) = \sum_{i=1,2} m_i \delta(\mathbf{x} - \mathbf{x_i}), \tag{1.71}$$

where m_i are the masses of each object and $\mathbf{x_i}$ the positions of each one. We will choose a frame with origin at the center of mass of the system and whose z-axis is parallel to the orbital angular momentum so that the x-y plane is the orbital plane. For the moment we will assume that objects describe a circular motion and that the orbit does not shrink due to the emission of GWs. This is known as a circular "Newtonian" orbit. In this situation, the positions of the two particles are provided by

$$\mathbf{x_1} = \frac{m_2}{M}\mathbf{R}, \qquad \mathbf{x_2} = -\frac{m_1}{M}\mathbf{R}, \qquad \mathbf{R} = \mathbf{x_1} - \mathbf{x_2}, \tag{1.72}$$

where $M = m_1 + m_2$ and R is the radius of the orbit. Similarly, the velocities are written as

$$\mathbf{v_1} = \frac{m_2}{M}\mathbf{v}, \qquad \mathbf{v_2} = -\frac{m_1}{M}\mathbf{v}, \qquad \mathbf{v} = \mathbf{v_1} - \mathbf{v_2}. \tag{1.73}$$

In a circular orbit these expressions are simplified to

$$\mathbf{R}(t) = (R\cos(\omega_s t), R\sin(\omega_s t), 0), \tag{1.74}$$

$$\mathbf{v}(t) = (-R\omega_s \sin(\omega_s t), R\omega_s \cos(\omega_s t), 0), \tag{1.75}$$

with $\omega_s^2 = GM/R^3$. Substituting the above relative position and velocity into the quadrupole moment tensor of (1.61) we get that $\mathcal{I}^{ij} = \frac{m_1 m_2}{M} R^i R^j$. Taking out the second time derivative and inserting it into (1.60) we arrive at

$$h^{ij} = \frac{4G m_1 m_2}{rc^4}\left(v^i v^j - \frac{GM}{R^3} R^i R^j\right). \tag{1.76}$$

Finally, for an observer located at a sky position given by the polar angles (ι, φ) with respect to the source, the $h_{+,\times}$ polarizations are obtained by performing the projection of (1.70) with the set of vectors

$$\mathbf{e_X} = (\cos\iota\cos\varphi, \cos\iota\sin\varphi, -\sin\iota), \tag{1.77}$$

$$\mathbf{e_Y} = (-\sin\varphi, \cos\varphi, 0), \tag{1.78}$$

$$\mathbf{e_Z} = (\sin\iota\cos\varphi, \sin\iota\sin\varphi, \cos\iota), \tag{1.79}$$

where we have made the choice of putting $\mathbf{e_X}$ in the orbital plane. The final result is therefore

$$\begin{aligned} h_+(t) &= -\frac{4Gm_1m_2\omega_s^2R^2}{rc^4}\left(\frac{1+\cos^2\iota}{2}\right)\cos\left(2\omega_s(t-r/c)-2\varphi\right), \\ h_\times(t) &= -\frac{4Gm_1m_2\omega_s^2R^2}{rc^4}\cos\iota\sin\left(2\omega_s(t-r/c)-2\varphi\right). \end{aligned} \tag{1.80}$$

Note that in the quadrupole approximation, the GW emission frequency is twice the orbital frequency of the source, $\omega_{gw} = 2\omega_s$. If in the above expressions we eliminate R in favour of ω_s, substitute $t_{ret} = t - r/c$ and rearrange terms we obtain

$$\begin{aligned} h_+(t) &= \frac{4}{r}\left(\frac{G\mathcal{M}_c}{c^2}\right)^{5/3}\left(\frac{\omega_{gw}}{2c}\right)^{2/3}\left(\frac{1+\cos^2\iota}{2}\right)\cos\left(\omega_{gw}t_{ret}-2\varphi\right), \\ h_\times(t) &= \frac{4}{r}\left(\frac{G\mathcal{M}_c}{c^2}\right)^{5/3}\left(\frac{\omega_{gw}}{2c}\right)^{2/3}\cos\iota\cos\left(\omega_{gw}t_{ret}-2\varphi\right). \end{aligned} \tag{1.81}$$

We have also introduced the *chirp mass*

$$\mathcal{M}_c = \frac{(m_1m_2)^{3/5}}{(m_1+m_2)^{1/5}}, \tag{1.82}$$

which is the only intrinsic quantity the waves depend on at the zero-order approximation. The power emitted in form of GWs per solid angle is computed as

$$\frac{dP}{d\Omega} = \frac{r^2c^3}{16\pi G}\langle\dot{h}_+^2+\dot{h}_+^2\rangle \tag{1.83}$$

where $\langle\rangle$ means averaged over several cycles such that $\langle\cos^2(\omega_{gw}t)\rangle = \langle\sin^2(\omega_{gw}t)\rangle = 1/2$. Incorporating expressions (1.81) and integrating over the sphere the total power radiated is

$$P_{GW} = \frac{32c^5}{5G}\left(\frac{G\mathcal{M}_c\omega_{gw}}{2c^3}\right)^{10/3}. \tag{1.84}$$

Now we consider the more realistic case where the loss of energy emitted in form of GWs indeed affects the orbit. Then the radius of the orbit and the frequency ω_s are no longer constant. As the orbit loses energy, the orbit shrinks, R decreases and consequently ω_s increases, however, this provokes that the emission of GWs is even higher, so there is a runaway process until eventually the two objects merge and the emission stops. To keep using the approximation of circular orbits we need to request that the radial velocity $\dot{R}$ is much smaller than the tangential one $R\omega_s$. This, together with the *adiabatic* approximation, which assumes that energy loss is negligible over one orbit, lead to $\dot{\omega}_s \ll$

ω_s^2. With these approximations the energy of the orbit at any given time is

$$E_{orbit} = -\frac{Gm_1m_2}{2R(t)} = -\left(\frac{G^2\mathcal{M}_c^5\omega_{gw}^2(t)}{32}\right)^{1/3}. \tag{1.85}$$

Since the loss of energy in the orbit must correspond to the radiated energy in form of GWs, the radiated power P_{GW} of (1.84) is equal to $-dE_{orbit}/dt$. By equating these two quantities we get an equation for ω_{gw} for any given time:

$$\dot{\omega}_{gw} = \frac{12}{5}2^{1/3}\left(\frac{G\mathcal{M}_c}{c^3}\right)^{5/3}\omega_{gw}^{11/3}. \tag{1.86}$$

This equation can be integrated from an arbitrary time t to the time of coalescence i.e. the time t_{coal} when the two bodies merge. Introducing a new variable for the time to coalescence, $\tau = t_{coal} - t$, we have

$$\omega_{gw}(\tau) = \left(\frac{5}{128\tau}\right)^{3/8}\left(\frac{G\mathcal{M}_c}{c^3}\right)^{-5/8}. \tag{1.87}$$

Note that the frequency diverges for $\tau = 0$ since at the coalescence time the two bodies merge and the orbital frequency is no longer defined. Now that we have the time dependence of the frequency we could also obtain the time dependence of the radius of the orbit. With these two quantities, and following the same procedure that we used for obtaining the expressions (1.81) we could derive the expressions for the polarizations. However, since we use the approximations of quasi-circular and adiabatic orbits ($\dot{\omega}_s \ll \omega_s^2$) the only required changes to (1.81) are replacing ω_{gw} by $\omega_{gw}(t)$ and substitute $\omega_{gw}t$ by

$$\Phi(t) = \int_{t_0}^{t}\omega_{gw}(t')dt'. \tag{1.88}$$

The polarizations are then given by

$$h_+(t) = \frac{4}{r}\left(\frac{G\mathcal{M}_c}{c^2}\right)^{5/3}\left(\frac{\omega_{gw}(t_{ret})}{2c}\right)^{2/3}\left(\frac{1+\cos^2\iota}{2}\right)\cos\left(\Phi(t_{ret}) - 2\varphi\right), \tag{1.89}$$

$$h_\times(t) = \frac{4}{r}\left(\frac{G\mathcal{M}_c}{c^2}\right)^{5/3}\left(\frac{\omega_{gw}(t_{ret})}{2c}\right)^{2/3}\cos\iota\cos\left(\Phi(t_{ret}) - 2\varphi\right). \tag{1.90}$$

Notice that there exists the freedom to choose the origin of time, shifting the waveform by a constant time does not introduce any change in the shape of the waveform so the parameter t_0 is an arbitrary choice. We could take the coalescence time as our reference time and perform the integral of ω_{gw} to get

$$\Phi(\tau) = -2\left(\frac{5G\mathcal{M}_c}{c^3}\right)^{-5/8}\tau^{5/8} + \Phi_0 \tag{1.91}$$

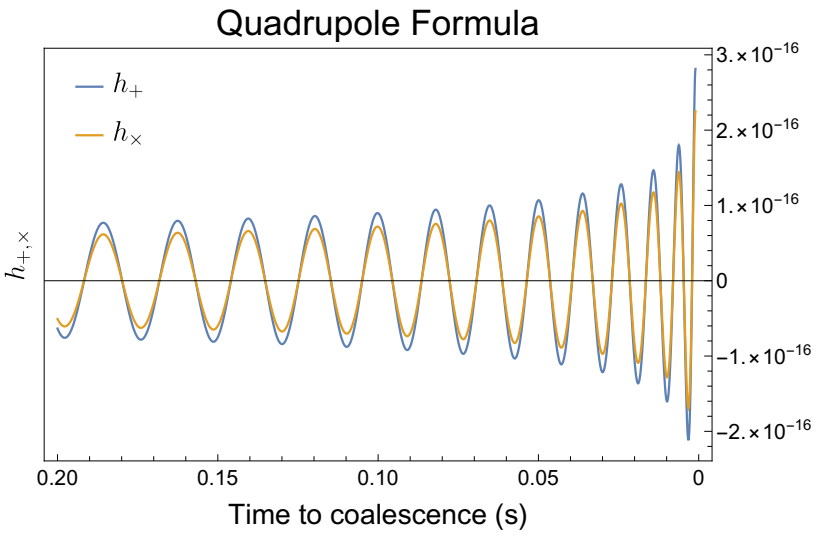

FIGURE 1.4: h_+, $h_\times$ polarizations as predicted by the quadrupole formula for a binary system of masses $m_1 = 30M_\odot$, $m_2 = 20M_\odot$ at distance 1 Mpc from the observer and inclination $\pi/3$.

with Φ_0 the phase at the coalescence time. Finally, the polarizations of the quadrupole emission of a binary system of point particles in terms of the coalescence time would be

$$h_+(t) = \frac{4}{r}\left(\frac{G\mathcal{M}_c}{c^2}\right)^{5/4}\left(\frac{5}{c\tau_{ret}}\right)^{1/4}\left(\frac{1+\cos^2\iota}{2}\right)\cos\left(\Phi(\tau_{ret})-2\varphi\right), \tag{1.92}$$

$$h_\times(t) = \frac{4}{r}\left(\frac{G\mathcal{M}_c}{c^2}\right)^{5/4}\left(\frac{5}{c\tau_{ret}}\right)^{1/4}\cos\iota\cos\left(\Phi(\tau_{ret})-2\varphi\right). \tag{1.93}$$

From the above formulas we see that when the binary approaches the time of coalescence, both amplitude and frequency grow rapidly, this is known as the *chirp* of the GW. In Fig. 1.4 we show a simple example waveform as predicted by the quadrupole formula where we can see the characteristic chirp.

1.7 Quadrupole emission from rotating rigid bodies

An isolated rigid object can also emit GWs if it spins and if it is not spherically symmetric. This is the case of isolated neutron stars. Two main scenarios may occur: the object rotates around one of its principal axes (or symmetry axes) or it rotates around a generic axis, what translates into a motion of precession. We saw in section 1.5 that the main quantity that describes the GW emission is the quadrupole moment, given by

$$\mathcal{I}^{ij} = \int d^3x\rho(\mathbf{x})(r^2\delta^{ij} - x^i x^j). \tag{1.94}$$

This is a hermitian matrix and therefore it can always be diagonalized. The frame where $\mathcal{I}^{ij}$ is diagonal is formed by its principal axes x'_i. This is a frame that rotates with the body and it is also called as the "body frame". The eigenvalues are given by

$$\mathcal{I}_1 = \int d^3x' \rho(\mathbf{x}')(x_2'^2 + x_3'^2), \tag{1.95}$$

$$\mathcal{I}_2 = \int d^3x' \rho(\mathbf{x}')(x_1'^2 + x_3'^2), \tag{1.96}$$

$$\mathcal{I}_3 = \int d^3x' \rho(\mathbf{x}')(x_1'^2 + x_2'^2). \tag{1.97}$$

In the case that the rigid object is an ellipsoid of semiaxes a, b, c the eigenvalues transform to

$$\mathcal{I}_1 = \frac{m}{5}(b^2 + c^2), \tag{1.98}$$

$$\mathcal{I}_2 = \frac{m}{5}(a^2 + c^2), \tag{1.99}$$

$$\mathcal{I}_3 = \frac{m}{5}(a^2 + b^2). \tag{1.100}$$

The angular momentum and energy of a rotating object with angular frequency ω is given in terms of the quadrupole moment as

$$J_i = \mathcal{I}_{ij}\omega^j, \qquad E = \frac{1}{2}\mathcal{I}_{ij}\omega^i\omega^j. \tag{1.101}$$

Notice that in general the axis of rotation $\hat{\omega}$ and the direction of the total angular momentum will not be the same unless the object is spherically symmetric or the rotation happens around one of the principal axes. Let us consider now first the case where the rotation occurs around one of the principal axes, let say around the x'_3 axis. Previously we computed the components of the quadrupole moment in the body frame $\mathcal{I}_{ij} = \mathrm{diag}(\mathcal{I}_1, \mathcal{I}_2, \mathcal{I}_3)$ but for obtaining the GW emission we need the components $\mathcal{I}_{ij}$ in the "static" frame which are time-dependent. These two frames are related by a rotation of angle ωt around the axis $x_3 = x'_3$. Therefore the quadrupole moment in these two frames is related by

$$\mathcal{I} = \mathbf{R}^T(\omega t)\mathcal{I}'\,\mathbf{R}(\omega t), \tag{1.102}$$

where

$$\mathbf{R}(\omega t) = \begin{pmatrix} \cos\omega t & \sin\omega t & 0 \\ -\sin\omega t & \cos\omega t & 0 \\ 0 & 0 & 1 \end{pmatrix}. \tag{1.103}$$

The only non-vanishing components of the quadrupole moments, written in terms of the eigenvalues ($\mathcal{I}_1$, $\mathcal{I}_2$ and $\mathcal{I}_3$), are then

$$\mathcal{I}_{11} = \frac{\mathcal{I}_1 + \mathcal{I}_2}{2} + \frac{\mathcal{I}_1 - \mathcal{I}_2}{2}\cos 2\omega t, \tag{1.104}$$

$$\mathcal{I}_{12} = \frac{\mathcal{I}_1 - \mathcal{I}_2}{2}\sin 2\omega t, \tag{1.105}$$

$$\mathcal{I}_{22} = \frac{\mathcal{I}_1 + \mathcal{I}_2}{2} - \frac{\mathcal{I}_1 - \mathcal{I}_2}{2}\cos 2\omega t, \tag{1.106}$$

$$\mathcal{I}_{33} = \mathcal{I}_3. \tag{1.107}$$

Once we have the quadrupole moment components, the polarizations of the GWs emitted are given by

$$h_+ = \frac{4G\omega^2}{rc^4}(\mathcal{I}_1 - \mathcal{I}_2)\frac{1+\cos^2\iota}{2}\cos 2\omega t, \tag{1.108}$$

$$h_\times = \frac{4G\omega^2}{rc^4}(\mathcal{I}_1 - \mathcal{I}_2)\cos^2\iota \sin 2\omega t. \tag{1.109}$$

The angular dependence of the GW emission of this system is the same as for the binary case, and also the GW frequency is twice the orbital one. The ellipticity is typically defined as $\epsilon \equiv \frac{\mathcal{I}_1 - \mathcal{I}_2}{\mathcal{I}_3}$ which together with the GW frequency $f_{gw} = 4\pi\omega$ allows us to express the polarizations in terms of a constant amplitude $h_0 = \frac{4G\omega^2 I_3 f_{gw}^2}{rc^4}\epsilon$,

$$h_+ = h_0 \frac{1+\cos^2\iota}{2}\cos 2\pi f_{\mathrm{gw}} t, \tag{1.110}$$

$$h_\times = h_0 \cos\iota \sin 2\pi f_{\mathrm{gw}} t. \tag{1.111}$$

Notice that according to the expression of h_0, faster rotating objects produce stronger signals and therefore they are more likely to be detected. Computing the power emitted by GWs and equating it to the energy loss by the system, as we did in 1.6, we get an equation for the frequency dependence given by

$$\dot{\omega} = -\frac{32G}{5c^5}\epsilon^2 \mathcal{I}_3 \omega^5. \tag{1.112}$$

Experimental measurements [19–24] of this decay rate indicate that dependence is not with the fifth power of the orbital frequency but with a power between 2 or 3. This suggests that the GW emission is not the main mechanism by which neutron stars lose energy and there must be other mechanisms of electromagnetic nature that must dominate.

In a general situation, the rotation of the body does not happen around one of the principal axes and the object describes an additional movement of precession. Now the rotation that relates the inertial frame with the body frame is not just a 2D rotation as

before but and Euler rotation with three angles. In the general case of triaxial bodies, these three angles will be time-dependent and the body suffers a complicated precessional movement around the axis of the total angular momentum. In the special case in which the object is axisymmetric, only the second of the Euler angles is time-dependent, so the frequency vector $\hat{\omega}$ precesses around the axis x_3' so it rotates in the plane (x_1', x_2'). The precessional movement of the body introduces a "new" frequency of GW emission which translates in a modulation of the amplitude of the signal. Finally, we would like to recall that all this description assumed that the body is rigid, but in reality, neutron stars are much more sophisticated objects, and their interior is usually described by an unknown EOS i.e. as a fluid body with an elastic crust.

Bibliography

[1] Albert Einstein. Erklärung der Perihelbewegung des Merkur aus der allgemeinen Relativitätstheorie. *Sitzungsberichte der Königlich Preußischen Akademie der Wissenschaften (Berlin*, pages 831–839, January 1915.

[2] U. Le Verrier. Lettre de m. le verrier à m. faye sur la théorie de mercure et sur le mouvement du périhélie de cette planète. Comptes rendus hebdomadaires des séances de l'Académie des sciences, 1859.

[3] A. Einstein. Über den einfluß der schwerkraft auf die ausbreitung des lichtes. *Annalen der Physik*, 340(10):898–908, 1911. doi: 10.1002/andp.19113401005. URL https://onlinelibrary.wiley.com/doi/abs/10.1002/andp.19113401005.

[4] Frank Watson Dyson, Arthur Stanley Eddington, and C. Davidson. A determination of the deflection of light by the sun's gravitational field, from observations made at the total eclipse of may 29, 1919. *Philosophical Transactions of the Royal Society of London. Series A, Containing Papers of a Mathematical or Physical Character*, 220(571-581):291–333, 1920. doi: 10.1098/rsta.1920.0009. URL https://royalsocietypublishing.org/doi/abs/10.1098/rsta.1920.0009.

[5] A. Einstein. Näherungsweise integration der feldgleichungen der gravitation. *Sitzungsber Akad. Wiss.*, pages 688–696, 1916.

[6] B. P. Abbott et al. Observation of gravitational waves from a binary black hole merger. *Phys. Rev. Lett.*, 116:061102, Feb 2016. doi: 10.1103/PhysRevLett.116.061102. URL https://link.aps.org/doi/10.1103/PhysRevLett.116.061102.

[7] A. Einstein. Zur elektrodynamik bewegter körper. *Annalen der Physik*, pages 891–921, 1905.

[8] A. Einstein. Die grundlage der allgemeinen relativitätstheorie. *Annalen der Physik*, 354:769–822, 1916.

[9] Élie Cartan. Sur les variétés à connexion affine et la théorie de la relativité généralisée (première partie). *Annales scientifiques de l'École Normale Supérieure*, 3e série, 40:325–412, 1923. doi: 10.24033/asens.751. URL http://www.numdam.org/item/ASENS_1923_3_40__325_0.

[10] Élie Cartan. Sur les variétés à connexion affine, et la théorie de la relativité généralisée (première partie) (suite). *Annales scientifiques de l'École Normale Supérieure*, 3e série, 41:1–25, 1924. doi: 10.24033/asens.753. URL http://www.numdam.org/item/ASENS_1924_3_41__1_0.

[11] Clifford M. Will Eric Poisson. *Gravity. Newtonian, Post-Newtonian, Relativistic.* Cambridge, 2014.

[12] Michele Maggiore. *Gravitational Waves. Volume 1: Theory and Experiments.* Oxford, 2008.

[13] B. P. Abbott et al. Gw151226: Observation of gravitational waves from a 22-solar-mass binary black hole coalescence. *Phys. Rev. Lett.*, 116:241103, Jun 2016. doi: 10.1103/PhysRevLett.116.241103. URL https://link.aps.org/doi/10.1103/PhysRevLett.116.241103.

[14] B. P. Abbott et al. Gw170104: Observation of a 50-solar-mass binary black hole coalescence at redshift 0.2. *Phys. Rev. Lett.*, 118:221101, Jun 2017. doi: 10.1103/PhysRevLett.118.221101. URL https://link.aps.org/doi/10.1103/PhysRevLett.118.221101.

[15] B. P. Abbott et al. Gw170814: A three-detector observation of gravitational waves from a binary black hole coalescence. *Phys. Rev. Lett.*, 119:141101, Oct 2017. doi: 10.1103/PhysRevLett.119.141101. URL https://link.aps.org/doi/10.1103/PhysRevLett.119.141101.

[16] B. P. Abbott et al. Gw170817: Observation of gravitational waves from a binary neutron star inspiral. *Phys. Rev. Lett.*, 119:161101, Oct 2017. doi: 10.1103/PhysRevLett.119.161101. URL https://link.aps.org/doi/10.1103/PhysRevLett.119.161101.

[17] B. P. Abbott et al. GW170608: Observation of a 19 solar-mass binary black hole coalescence. *The Astrophysical Journal*, 851(2):L35, dec 2017. doi: 10.3847/2041-8213/aa9f0c. URL https://doi.org/10.3847%2F2041-8213%2Faa9f0c.

[18] B. P. Abbott, R. Abbott, T. D. Abbott, S. Abraham, F. Acernese, K. Ackley, C. Adams, R. X. Adhikari, V. B. Adya, C. Affeldt, and et al. Gw190425: Observation of a compact binary coalescence with total mass $\sim$ 3.4 $m_{\odot}$. *The Astrophysical Journal*, 892(1):L3, Mar 2020. ISSN 2041-8213. doi: 10.3847/2041-8213/ab75f5. URL http://dx.doi.org/10.3847/2041-8213/ab75f5.

[19] Nadja Magalhaes, Thaysa Miranda, and Carlos Frajuca. Predicting ranges for pulsars' braking indices. *Astrophysical Journal*, 755, 08 2012. doi: 10.1088/0004-637X/755/1/54.

[20] E. J. Groth. Timing of the Crab Pulsar III. The Slowing Down and the Nature of the Random Process. *Astrophysical Journal, Supplement*, 29:453–465, November 1975. doi: 10.1086/190354.

[21] Andrew G. Lyne, Robert S. Pritchard, Francis Graham-Smith, and Fernando Rossi Camilo. Very low braking index for the vela pulsar. *Nature*, 381:497–498, 1996.

[22] V. M. Kaspi, R. N. Manchester, B. Siegman, S. Johnston, and A. G. Lyne. On the Spin-down of PSR B1509-58. *Astrophysical Journal, Letters*, 422:L83, February 1994. doi: 10.1086/187218.

[23] R. N. Manchester and B. A. Peterson. A Braking Index for PSR 0540-69. *Astrophysical Journal, Letters*, 342:L23, July 1989. doi: 10.1086/185475.

[24] H O de Oliveira, R M Marinho, and N S Maglhaes. Stellar structures and the enigma of pulsars rotation frequency decay. *Journal of Physics: Conference Series*, 630:012059, jul 2015. doi: 10.1088/1742-6596/630/1/012059. URL https://doi.org/10.1088%2F1742-6596%2F630%2F1%2F012059.

Chapter 2

Experiments and Data Analysis

The GWs detected by the LIGO-Virgo detectors were produced by the collision of black holes or neutron stars which occurred even before the human species existed and have been travelling through the universe since then. The detection of gravitational waves constitutes the most accurate measurement of displacement carried out in the human history, and it is equivalent to be able to detect a displacement thousand of times smaller than the size of a proton. In this chapter we will discuss how these tiny vibrations of the spacetime can be registered by a detector and how the data is analyzed in order to infer the properties of the source which emitted them.

2.1 Gravitational Wave Detectors

We start the discussion from the experimental point of view. We will review the two main approaches historically adopted to detect gravitational waves. First, we discuss the resonant-mass detectors that despite not having detected any signal were the first experiments ever proposed and built for this purpose. Then we will pass to the LIGO-style interferometer detectors which performed the very first gravitational wave detection. Finally, we will discuss the current projects to send the interferometers to the space which will allow us to detect the abundance of signals that are suppressed by terrestrial noise sources.

2.1.1 Resonant-mass detectors

The first attempt for direct detection of gravitational waves dates from the 1960s when Joseph Weber introduced the concept and built the first resonant bar detector. The idea consisted in that a gravitational wave passing through a massive bar, of few meters long

and a few tons of weight, vibrates if the frequency of the wave is close to the resonant frequency of the bar. These detectors operate in a quite narrow frequency band around 30 Hz, but they can reach higher frequencies $10^3 - 10^4$ Hz where the interferometers can not operate due to the shot noise of the photons. The resonant bars are typically composed of an alloy of aluminium but can also be made of niobium, silicon or sapphire. The typical variations in the length of the bar due to a passing GW are of the order $\Delta L/L \sim 10^{-19} - 10^{-18}$, so it is extremely important to control the thermal noise of the bar which is the most important source of the noise. To achieve that, the bars have to be cryogenically cooled down to temperatures around 0.1-6 K. The temperature will depend on the detector, for example, the ultra-cryogenic detector NAUTILUS using ^{3}He-^{4}He was able to reach a temperature as low as 0.1 K [1]. The current resonant detectors can reach sensitives in the amplitude of a GW of the order $h \sim 4 \cdot 10^{-19}$. They have a theoretical limit for $h \sim 10^{-21}$ [2, 3] given by the Heisenberg uncertainty principle which complicates reaching better sensitivities. That is the reason why the main experimental focus moved to the interferometers, with a much lower bound. There exist however some proposed methods to circumvent the quantum limit utilizing *quantum non-demolition* techniques [4, 2, 3].

2.1.2 Ground-based Interferometers

In section 1.4 we saw that the interaction of a gravitational wave with matter produces the stretching of one direction and the squeezing of the orthogonal one. This behaviour inspired scientists to use laser interferometry as a novel tool to detect gravitational waves. The basic idea of this approach consists in the classic Michelson interferometer (see Fig. 2.1), where a laser beam is split in two beams that travel in perpendicular directions, then each one is reflected by a suspended mirror at the end of their paths and they recombine and interfere in a photodetector. If the distance (or optical path) travelled by the two beams is the same, their interference will be destructive since one of the beams acquires an extra phase of π in the beam splitter. However, since the mirrors are freely suspended, a passing gravitational wave can stretch one arm while squeezing the other one, so the relative optical paths change and now the two beams interfere in a constructive manner producing a readout power in the photodetector. One can express this in a mathematical language considering the electric field of each beam at the time when they recombine after travelling twice the length of their arms,

$$E_1 = -\frac{1}{2} E_0 e^{-i2\pi f_L + 2ik_L L_1}, \qquad E_2 = \frac{1}{2} E_0 e^{-i2\pi f_L + 2ik_L L_2} \tag{2.1}$$

where k_l, f_L are the wavenumber and frequency of the laser beam and the factors one half come from the reflection and transmission factors in the beam splitter and the mirrors.

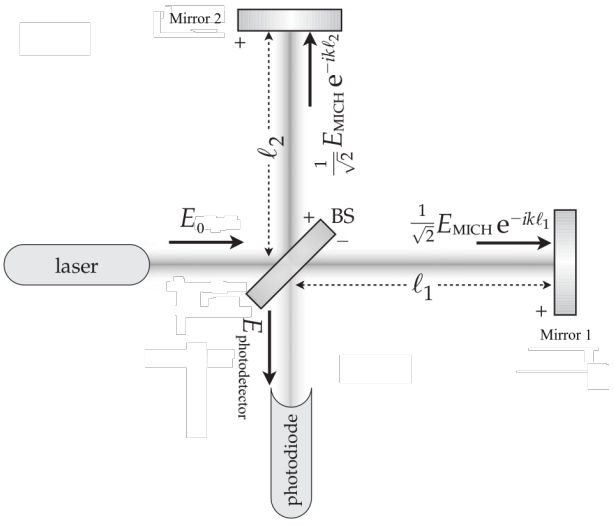

FIGURE 2.1: Optical distribution of a Michelson interferometer. Image credits: modified version of [5].

The combined electric field reaching the photodetector is the sum $E_1 + E_2$ and the power measured can be expressed as

$$|E_{\mathrm{photodetector}}|^2 = E_0^2 \sin^2 \left[k_l (L_2 - L_1)\right]. \tag{2.2}$$

This conceptual approach to detect gravitational waves was first introduced in 1963 by Gertsenshtein and Pustovoit in [6], while the first small prototype was built by Robert Forward in 1971 who after 150 hours of observation with his 8.5 m arms interferometer reported "an absence of significant correlation between the interferometer and several Weber bars detector" i.e. lack of evidence of GWs detection.

The construction of "initial LIGO" started in late 1994 and ended in 1997, it consisted of two interferometers of 4km length, one in Hanford (Washington) and the second one in Livingston (Louisiana). The LIGO detectors combined periods of operation with subsequent upgrades until September 2015 when they detected the first gravitational wave signal. As mentioned before, the LIGO interferometers are much more sophisticated than the original Michelson ones. Let us now discuss some of the improvements needed. First, in the Michelson interferometer the gravitational wave induces a change in the length of the arms given by $h = \Delta L/L$, the minimum variation ΔL that an interferometer can measure is limited by the wavelength of the laser $\Delta L \sim \lambda_{\mathrm{laser}}$. So with a kilometre based interferometer and with an infrared laser, we have that the metric perturbation we can measure is of the order

$$h = \frac{\Delta L}{L} \sim \frac{\lambda_{\mathrm{laser}}}{L} \sim \frac{10^{-6} m}{10^{3} m} = 10^{-9}. \tag{2.3}$$

The metric perturbation that we are targeting is however of the order $h \sim 10^{-21}$ so further improvement is needed. The most evident upgrade would be to augment the length of the arms of the detector. This can be achieved by building longer arms which at some point becomes technically and financially prohibitive, however, the effective length that the light travels can be increased without building longer arms by forcing the light to do several traversals in the arms before letting it interfere in the photodetector. This can be achieved with the installation of "Fabry-Perot cavities" halfway of each arm where the light bounces several times before exiting the cavity such that the effective path travelled is larger than the length of the arm $L_{\text{eff}} > L$. This method can degrade the sensitivity of the detector and the effective length L_{eff} has an approximate limit given by the order of magnitude of the wavelength of the gravitational wave we want to measure $L_{\text{eff}} \sim \lambda_{GW}$. Our ground-based detectors are more sensitive to frequencies ~ 300 Hz which correspond to $\lambda_{GW} \sim 1000$ km, therefore the strain we can measure is

$$h \sim \frac{\Delta L}{L_{\text{eff}}} \sim \frac{\lambda_{\text{laser}}}{\lambda_{GW}} \sim \frac{10^{-6}m}{10^{6}m} \sim 10^{-12}. \tag{2.4}$$

Several orders of magnitude of improvement are still needed. Previously, we assumed that the change of optical path which can be measured is of the order of λ_{laser} but this can be refined by considering that the variation in the amount of light that the photodetector measures in a given period of time τ follows a Poisson process. For a large number of photons $\Delta N_{\text{photons}} \sim N_{\text{photons}}^{1/2}$ and the minimum optical path measurable is

$$\Delta L \sim \frac{N_{\text{photons}}^{1/2}}{N_{\text{photons}}} \lambda_{\text{laser}}. \tag{2.5}$$

The period of time τ for which we can collect photons is of the order of the period of the gravitational wave signal so the number of photons can be written as

$$N_{\text{photons}} = \frac{P_{\text{laser}}}{E_{\text{photon}}} \tau = \frac{P_{\text{laser}}}{hc/\lambda_{\text{laser}}} \tau \sim \frac{P_{\text{laser}}}{hc/\lambda_{\text{laser}}} \frac{1}{f_{GW}}. \tag{2.6}$$

Inserting this in (2.4) and substituting for the typical values employed before and for $P_{\text{laser}} = 1W$ we obtain

$$h \sim \frac{\Delta L}{L_{\text{eff}}} \sim \frac{\lambda_{\text{laser}}}{N_{\text{photons}}^{1/2} \lambda_{GW}} \sim \left(\frac{\lambda_{\text{laser}} hc^2}{P_{\text{laser}} \lambda_{\text{GW}}^3} \right)^{1/2} = 10^{-20}. \tag{2.7}$$

There exist further upgrades that can be applied to improve the sensitivity such as the technique of *power recycling*. This consists in taking the light that escapes in the direction of the laser by transmission in the beam splitter when the two beams are recombined and injected it again in the interferometer. A similar technique exists for the light leaving the interferometer in the direction of the photodetector called in this case *signal recycling*.

These techniques allow us to reach the desired theoretical sensitivity of $h \sim 10^{-21}$,

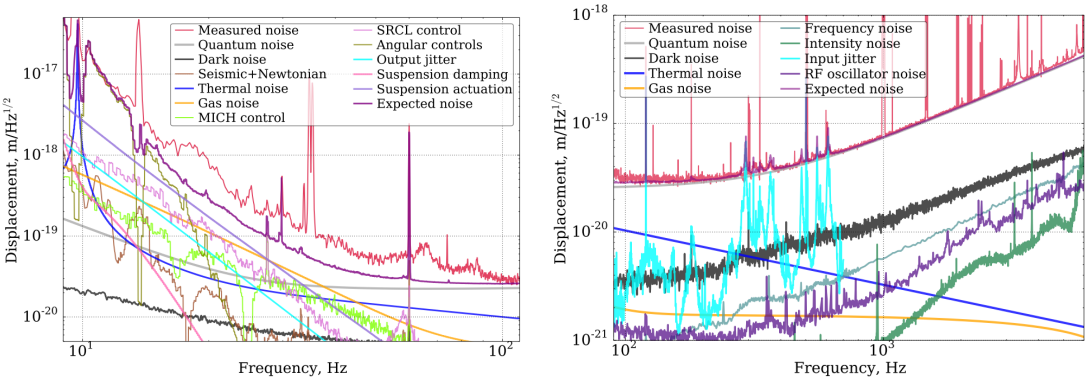

FIGURE 2.2: Left panel shows the noise curves for the Livingston observatory in the low frequency regime while right panel displays the noise contribution of the Hanford observatory for the high frequency regime. The sum of all the contributions provides the sensitivity curve of the detector shown in Fig. 2.3. Image credits: [7].

however there are many different sources of noise that intervene in the performance of the detector and degrade its sensitivity. These sources are usually classified as: shot noise, radiation pressure, seismic and Newtonian noise and thermal noise. We briefly discuss each of them hereafter.

- **Shot noise**: due to the quantum character of the light we can not detect continuous variations in the power measured by the photodetector. There exists an amount of power lost by the counting error governed by the Poisson distribution which for high power lasers translates into a Gaussian process with standard deviation $\Delta N_{\text{photon}} = N_{\text{photon}}^{1/2}$. The larger the number of photons, the lower the relative error $(\Delta N/N)$ becomes. This is achieved by increasing the power of the laser and by using the power and signal recycling methods discussed before.

- **Radiation pressure**: when the power of the laser increases, the pressure that the light impinges on the mirrors becomes more important and can provoke minuscule displacements in the mirrors. If the power of the laser were constant then it would be simple to counter the effect by applying an equivalent force in the opposite direction, however since the power follows a gaussian process the vibrations of the mirror are stochastic and difficult to compensate. An approach to tackle the competing effect of the shot noise and radiation pressure is through the squeezing of the light [8] which has been recently incorporated to the LIGO detectors [9]. This technique creates pairs of photons that are quantum-mechanically entangled and therefore their time of arrival at the detector is correlated, what reduces the width of the time distribution and the uncertainty in the variation of the power of the laser.

- **Seismic and Newtonian noise**: the mirrors can not only be displaced by a passing gravitational wave but also by any environmental activity like earthquakes, local traffic, planes, even the ring of a telephone in the operations office of the detectors. Another source of noise is when the gravitational field of the Earth changes, for example due to turbulence in the atmosphere what can affect the test masses of the interferometer. This is known as Newtonian noise or gravity gradient noise and can not be eliminated. The dominant source of noise is however the seismic one and it can be mitigated by hanging the mirrors from a set of pendulums in cascade.

- **Thermal noise**: it is produced by the inherent motion of the atoms of any macroscopic object with a certain temperature. It affects both the mirrors and the suspension system. To reduce these oscillations, materials with low mechanical dissipation factors are employed.

There exist several more sources of noise with a contribution to different frequency ranges. In Fig. 2.2 we show all the noise sources as a function of the frequency, the sum of all them provides the so-called noise curve or power spectral density function $S_n(f)$. This curve is not constant over time since the noise sources are time-dependent, consequently, it is of key importance to monitor the state of this curve to carry out the data analysis studies as we will see in Sec. 2.2.2. An example noise curve (sensitivity curve) for the LIGO detectors is shown in Fig. 2.3.

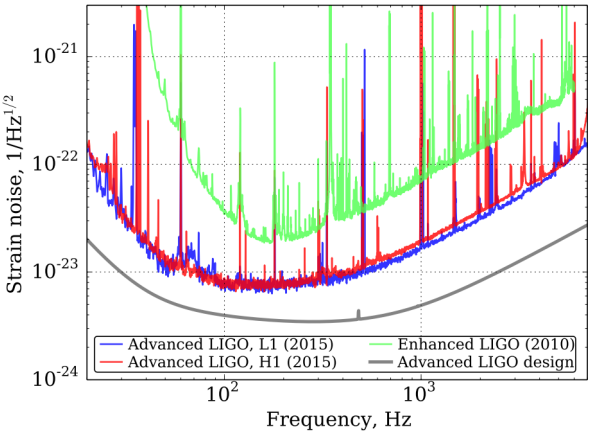

FIGURE 2.3: Strain sensitivity curves for Hanford (H1) and Livingston (L1) (red and blue respectively) during the first observation run O1 when the first detection happened, together with the curves of the initial detectors at the end of the final data collection run S6 (green curve) and the design sensitivity of Advanced LIGO (grey curve). Image credits: [7].

Additionally to the LIGO detectors, there exist others ground-based interferometers which belong to the net of detectors hunting gravitational waves:

- Virgo. It is built in Cascina, Italy. The detector arms are 3 km long, the sensitivity is in general slightly lower than for LIGO although for some particular frequencies it is higher. The incorporation of Virgo to the gravitational wave network is key to improve the sky location of the source when there is no electromagnetic (EM) counterpart since a third detector allows one to triangulate the position of the source much more accurately (see discussion in Sec. 2.2.1). The first joint detection with LIGO was GW170814 on 14 August 2017.

- KAGRA. Located in the Japanese region of Gifu, it is built underground in the Kamioka mine. It has two arms of 3km length and uses cryogenic mirrors. Its design sensitivity is similar to the LIGO one and its first observation run started on 25 February 2020.

- GEO600. Located near Hannover, Germany. It consists in a Michelson interferometer with arms 600 m long where the beam performs two traversals so the effective length is 1200 m. Its frequency range is much shorter than the Advanced LIGO/Virgo (50-1500 Hz) and its sensitivity is orders of magnitude inferior, so typically it has been used to develop and test the technology that is later installed in LIGO. However, due to its better sensitivity at high frequencies, it has also been involved in the search for high-frequency events, in particular galactic supernovae, within the framework of the Astrowatch program, which has been running between LIGO-Virgo observation runs to ensure that gravitational wave signals from galactic supernovae events will not be missed.

- LIGO-India. It is a project to duplicate the Hanford detector in India. It was approved 'in principle' by the cabinet of the Indian Prime Minister just 6 days after the first detection was announced on 11 February 2016. The project is designed to be identical to the LIGO detector but operated by an Indian team. The estimates to be operative are placed in 2024.

The initial and advanced stages of the LIGO-Virgo detectors constitute the first and second generation of gravitational wave detectors respectively. Nevertheless, there exist additional proposals and plans to build the "third-generation detectors" which will improve substantially the designed sensitivity of the current second generation. The two main projects planned for the next generation are:

- Einstein Telescope. This is a European project [10] that aims to build, instead of a traditional L-shaped interferometer, a triangular shaped one with arms of 10 km longitude, and located underground. The new shape allows a single detector to be able of measuring the polarization of the gravitational wave, while for the L-shape at least two detectors are needed. The lower cutoff frequency is targeted at 1 Hz.

- Cosmic Explorer. It is a project of the United States [11] with a similar desig as the LIGO detectors but with arms 10 times longer, 40 km each. This will increase the amplitude of the signals that can be observed without increasing the noise, however the lower cutoff will remain around the 10 Hz.

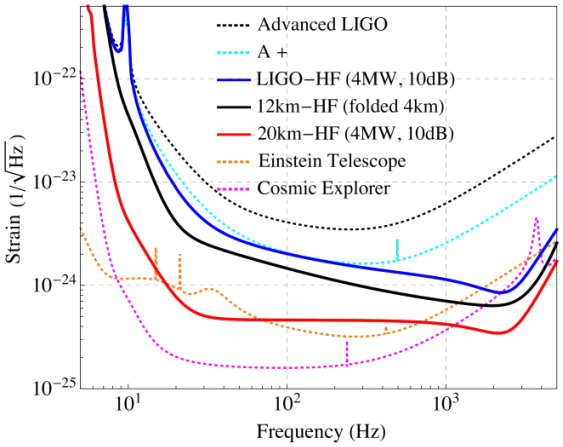

FIGURE 2.4: Sensitivity curves for third-generation ground-based interferometers. Image credits: [12].

In Fig. 2.4 one can see the theoretical sensitivity curves of these two third-generation detectors compared to the current Advanced LIGO one plus next upgrades of LIGO and some hypothetical detectors of length 12 and 20 km.

2.1.3 Spaced-based Interferometers

The seismic and Newtonian noise form the main impediment for ground-based detectors to reach frequencies below 10 Hz. However, an abundance of very interesting gravitational wave sources lays below this cutoff frequency in the band of mHz, such as supermassive black holes and extreme mass ratio (EMR) binaries (see Fig. 2.5). To access these sources the detector must go to space where these noise sources are much more weakened. This is the main goal of the Laser Interferometer Space Antenna (LISA) mission lead by the European Space Agency (ESA). The project [13] aims to send three space crafts into space, which would be separated 2.5 million kilometres from each one forming a triangular shape and orbiting the sun (see Fig. 2.5). The test masses would be free-falling inside each spacecraft and connected by a laser beam which travels from one spacecraft to the other through space. The scientific and technological challenges of this mission are extraordinary notorious, for that reason the ESA decided to launch first the LISA Pathfinder mission which would test all the technology required for LISA and the viability of such mission. After the great success of the LISA Pathfinder results [14] in 2017, the ESA gave clearance for the LISA mission to be launched for the 2030s.

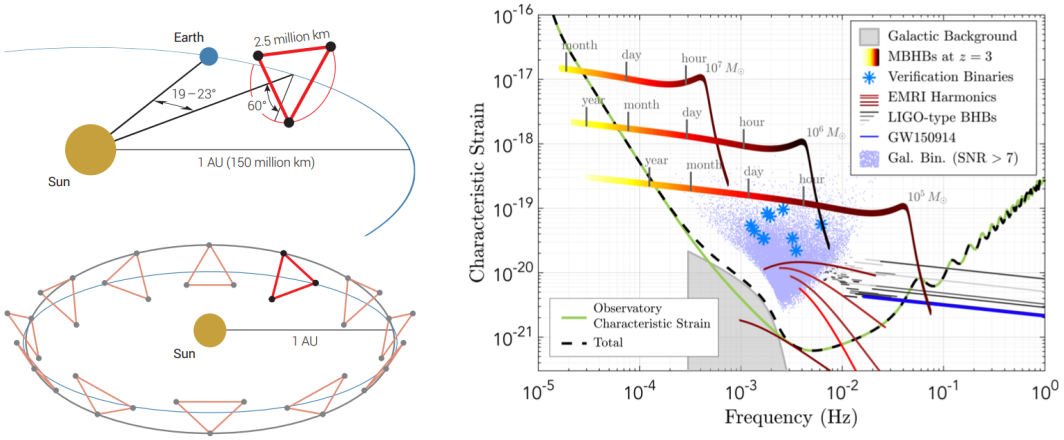

FIGURE 2.5: Left: Illustration of the orbit of LISA around the Sun following the Earth. Right: sensitivity curve of LISA together with the Fourier domain amplitude of several gravitational wave events expected to exist in that frequency regime. The blue line represents the first detection of gravitational waves by LIGO GW150914, here we see the early inspiral while LIGO detected the final merger. Image credits: [13].

2.2 Gravitational Wave Data Analysis

When a gravitational wave reaches the arms of the detector a time series of the relative displacement of the arms is recorded. We saw in the previous section that there exist several non-astrophysical sources that can also produce displacements of the mirrors which act as noise for the GW measurement. If the signal is loud enough it will stand out from the noise and be observable to the naked eye (after some filtering) as it happened for the first event GW150914. However, the standard situation is that the signal is buried in the noise. The main focus of the following sections is to discuss the techniques to dig out the signal from the noise and to infer the source parameters from the detector data.

2.2.1 Detector response

The incoming gravitational wave $h_{ij}(t)$ to the detector is a tensorial quantity, but the response of the detector is rather a scalar quantity $h(t)$, which in the case of interferometers represents the relative difference between the lengths of the two arms as a function of time. The response of the detector can be expressed then as

$$h(t) = D^{ij} h_{ij}(t), \tag{2.8}$$

where D is the *detector tensor*, a constant tensor which depends on the geometry of the detector. Inverting the expressions in (1.70) we can express the tensorial components in

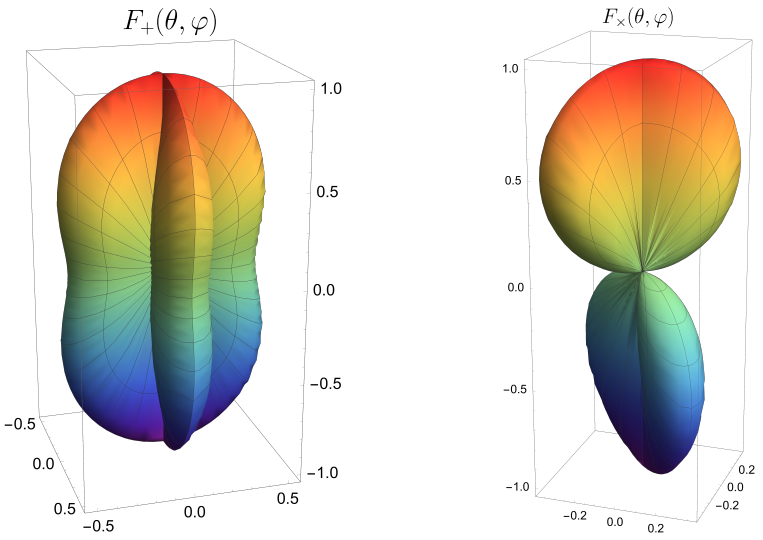

FIGURE 2.6: Angular distribution of the antenna patterns for an interferometric detector.

terms of the gravitational wave polarizations $h_{+,\times}$ and the *polarization tensors*

$$\begin{aligned} e^{+}_{ij}(\hat{\mathbf{n}}) &= \left(e^i_X e^j_X - e^i_Y e^j_Y\right), \\ e^{\times}_{ij}(\hat{\mathbf{n}}) &= \left(e^i_X e^j_Y + e^i_Y e^j_X\right). \end{aligned} \tag{2.9}$$

The vector $\hat{\mathbf{n}} = (\theta, \phi)$ represents the direction of the incoming wave measured from the detector frame. Hence, the detector response in terms of the polarizations can be written as

$$h(t) = \sum_{A=+,\times} D^{ij} e^A_{ij}(\hat{\mathbf{n}}) h_A(t). \tag{2.10}$$

It is common to define the *antenna patterns* or *detector pattern functions* $F_A(\hat{\mathbf{n}}) = D^{ij} e^A_{ij}(\hat{\mathbf{n}})$ and express the detector response as

$$h(t) = h_+(t) F_+(\theta, \phi) + h_\times(t) F_\times(\theta, \phi). \tag{2.11}$$

In the case of interferometric detectors and under the assumption that the wavelength is much larger than the detector size, the angular dependence of the antenna patterns is given by

$$F_+(\theta, \phi) = \frac{1}{2}\left(1 + \cos^2\theta\right)\cos 2\phi, \tag{2.12}$$

$$F_\times(\theta, \phi) = \cos\theta \sin 2\phi. \tag{2.13}$$

Notice that in general, the gravitational wave detector is omnidirectional, i.e. it can record signals coming from any direction. This is in clear contrast to the traditional EM telescopes which need to point to a particular direction and is more similar to typical

radio antennas. There are, however, according to equation (2.12), some blind spots for the interferometric detector. For example, the directions $\phi = \pi/4, 3\pi/4, 5\pi/4, 7\pi/4)$ are blind to the h_+ polarization ($F_+ = 0$) since the GW produces the same displacement in the two arms. For the $h_\times$ polarizations the directions correspond to $\phi = 0, \pi/2, \pi, 3\pi/2$. In Fig. 2.6 we represent the angular distribution of the two antenna patterns and all these blind spots can be easily observed. In fact, with only one detector we are only sensitive to measure one of the two polarizations. The detector only returns an output $h(t)$ however there are four unknown quantities in the problem: the two polarizations $h_{+,\times}$ and the sky location (θ, ϕ). With two detectors we need a coincident signal in both of them so we would have as output the two strains from each detector $h_1(t)$, $h_2(t)$ and the time delay of the signal from one detector to the other. This is not yet enough to solve the problem of 4 unknown quantities. This is the reason why the sky location that the LIGO detectors reported in the first observations were rather poor. With a third detector we instead have 5 variables at our disposal, the three strains in each detector and two independent time delays, therefore now the triangulation is much more accurate. Consequently, the incorporation of Virgo to the detector network improved significantly the sky location of the subsequent events. Fig. 2.7 displays the global antenna factor for three different detector networks

$$F^2 = \sum_{A=\text{detects.}} (F_+^A)^2 + (F_\times^A)^2. \tag{2.14}$$

Blue regions in the figure represent the blind spots of the network. It can be observed how Virgo dramatically improves the sky coverage. With six detectors the coverage is practically uniform and there are no blind spots. A good measurement of the sky location is key for the observation of events with a multi-messenger counterpart, because it allows us to point, in particular EM telescopes, towards a small region of the sky and thus increase the chances of discovering an EM counterpart, and possibly identifying the host galaxy.

2.2.2 Matched filtering

Due to the extremely minuscule variations that gravitational waves produce in the arms of the detector the instrument needs to be extraordinarily precise. This provokes that not only gravitational waves are registered but also any environmental disturbance which produces deviations in the mirrors of the interferometer. The output of the detector $s(t)$ will be therefore the sum of the noise of the detector $n(t)$ together with the gravitational wave signal $h(t)$

$$s(t) = n(t) + h(t). \tag{2.15}$$

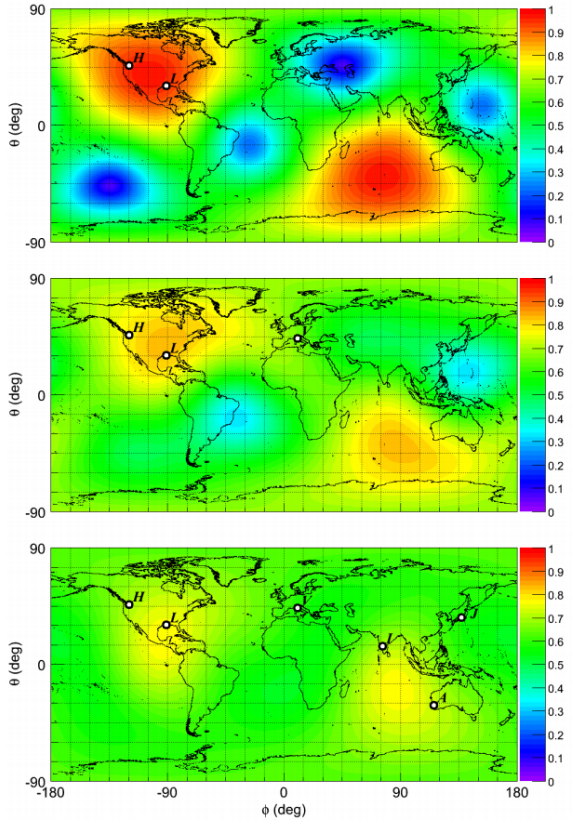

FIGURE 2.7: Network antenna pattern distributions as a function of latitude (θ) and longitude ϕ for three different detector networks: Hanford-Livingston (top), Hanford-Livingston-Virgo (middle) and the incorporation to the previous network of KAGRA, LIGO-India and a hypothetical detector in Australia. Image credits: [15].

It is evident that when the signal is louder than the noise $|h(t)| > |n(t)|$ we are in a position of claiming a gravitational wave detection. However, with the current sensitivity of the detectors the situation is rather the opposite and $|h(t)| \ll |n(t)|$. The technique of *matched filtering* allows us to dig inside the noise and extract the GW signal. The basic quantity that assets if there exists a GW signal is the signal-to-noise ratio (SNR or ρ), when this quantity is above a certain threshold we can assert GW detection. The SNR is defined hereafter.

Firstly, let us define the Power Spectral Density (PSD) $S_n(f)$ as

$$\langle \tilde{n}^*(f)\tilde{n}(f')\rangle = \delta(f - f')\frac{1}{2}S_n(f). \tag{2.16}$$

This quantity describes the noise curve of the detector. Here $\langle\rangle$ represents *ensemble average*; it is an average over possible states or "realizations" of the system. If we had several instruments to make the same measurement the average would be over all these instruments. Since for now, we are considering just one single GW detector, we dispose of just one instrument, whose state changes in time due to environmental fluctuations.

Then the ensemble average translates into a time average. The time average over a time interval T is considered as one realization, and the next one is another time T' average sufficiently separated from the previous realization.

We also introduce the inner product (known as Wiener scalar product) between two real time series $a(t)$, $b(t)$ as

$$(a|b) \equiv \int_{-\infty}^{\infty} df \frac{\tilde{a}^*(f)\tilde{b}(f) + \tilde{a}(f)\tilde{b}^*(f)}{S_n(f)} = 2Re \int_{-\infty}^{\infty} df \frac{\tilde{a}^*(f)\tilde{b}(f)}{S_n(f)} = 4 \int_0^{\infty} df \frac{\tilde{a}^*(f)\tilde{b}(f)}{S_n(f)}. \tag{2.17}$$

In the last step we have utilized that for real time series $\tilde{a}(f) = \tilde{a}^*(-f)$ and that $S_n(f) = S_n(-f)$. This inner product is normalized such that $\langle (n|n) \rangle = 1$ and possesses the property $\langle (a|n)(n|b) \rangle = (a|b)$. Given a model template h the SNR is defined as

$$\text{SNR} = \frac{(h|s)}{\sqrt{\langle (h|n)(n|h) \rangle}} = \frac{(h|s)}{\sqrt{(h|h)}}. \tag{2.18}$$

The higher the SNR the more probable is that a gravitational wave signal similar to h is present in the data.

2.2.3 Frequentist vs Bayesian statistics

When physicists perform an experimental measurement of a particular physical parameter we always use statistical reasoning to indicate our belief that the measurement is correct and how close it is to the true value. We use the concept of probability to refer to this belief, and typically a confidence interval is provided with the measurement, i.e. we believe that the true value of the physical parameter lays within this interval and our degree of belief is given by the probability value. There are two main approaches to describe the probability: the Frequentist and the Bayesian approaches [16–18] which share some properties. Let us consider a set S with subsets A, B, ..., then the probability P satisfies the Kolmogorov axioms [19]:

1. For every subset in S: $P(A) \geq 0$
2. For disjoint subsets ($A \cap B = 0$): $P(A \cup B) = P(A) + P(B)$
3. P(S) = 1

We can also define the conditional probability, i.e. the probability of A given B as

$$P(A|B) = \frac{P(A \cap B)}{P(B)}. \tag{2.19}$$

The main difference between the two approaches is the interpretation of the subsets. For a frequentist, the subsets are the outcomes of a particular experiment which can be repeated under the same conditions. $P(A)$ is the probability to obtain A when we perform the experiment, more formally, when the experiment is repeated an infinite number of times. $P(A)$ is the frequency of occurrences of A in all these infinite repetitions. In this framework, it is meaningful to talk about the probability of obtaining some data given some hypothesis or theory $P(data|hypothesis)$. However, it is not meaningful to talk about the probability of a particular hypothesis, since it is not a repeatable experiment. But in the Bayesian framework, since the subsets are not the result of a repeatable experiment, it is meaningful to talk about the probability of the hypothesis or a theory. This is related to the probability of the data through the *Bayes' theorem*:

$$P(A|B) = \frac{P(B|A)P(A)}{P(B)}, \tag{2.20}$$

where we have used $A = hypothesis$ and $B = data$. The left-hand side term is called the *posterior* probability and it represents our degree of belief that the hypothesis is true in the presence of the current data. The term $P(data|hypothesis)$ is the *likelihood* function which is obtained by experimental measurements. This term modifies P(hypothesis) which is the *prior* probability and describes our state of knowledge about the truth of the hypothesis before having analyzed the data. This prior probability is given by the assumptions we make about the observable we want to measure. For example, if we want to measure the mass of a star we would set the probability of the hypothesis to zero for negative masses because we already know, previously to any experiment, that the mass has to be positive. We can incorporate into the prior any information that we already know about the star, e.g. if we know that our star has a low temperature but high luminosity, the Hetzspring-Russel diagram tells us that the star is a red supergiant, so in this case we can give to our mass prior a higher probability for the masses of supergiant stars. Finally, the term P(data) is a normalization constant, the probability of obtaining the data without assuming any hypothesis. This terms is quite important for applications like *model selection* and receives the name of *evidence*.

Another important result derived from the axioms of probability is the concept of *marginalization*, expressed mathematically as,

$$P(A) = \int P(A, B)dB. \tag{2.21}$$

Marginalization allows us to get rid of the *nuisance* parameters, i.e. parameters that enter the analysis, but we are not interested in studying them. Let us consider the case of a binary coalescence where we measure the mass of the primary black hole and we

have a hypothesis for the mass of the secondary black hole. The hypothesis over the second black hole could be that its value lies in a particular mass interval. However when we marginalize over the mass of the secondary black hole we are integrating over all its possible values, we are not assuming any hypothesis about this parameter, the prior information is removed and there exists a larger uncertainty in the problem. Therefore, the posterior for the primary black hole will be broader since we now have "less" information. Then the posterior represents what is our best estimate for the mass of the first black hole when we do not know anything about the second.

In many fields in astronomy, we can not repeat the experiment as many times as we want and we do not have any control over the conditions for which it happens. The events are those given by nature and they are rather infrequent compared to for example particle accelerator experiments where the scientists have control over the experiment and can repeat it as many times as they want. For that reason, in GWs data analysis, the natural framework to work with is the Bayesian one.

2.2.4 Parameter estimation

Parameter estimation PE studies which are the properties of the source which produced the gravitational wave signal recorded by the detectors by assigning a probability to each of them. Each source parameter is assigned a posterior distribution whose maximum value provides the best estimate for this parameter. The probability of a signal being present in the data is given by $P(\mathcal{H}|s)$ where $\mathcal{H}$ is the hypothesis that a signal is present. For a binary coalescence signal, the morphology of the waveform depends on multiple parameters such as the masses of the objects, the distance to the source, its orientation, etc. We encode all these parameters with the notation $\boldsymbol{\lambda} = \{\lambda_1, \lambda_2, ...\}$. The hypothesis is now parameterized by $\boldsymbol{\lambda}$ and its probability is $P(\mathcal{H}_{\boldsymbol{\lambda}}|s)$. The source parameters $\boldsymbol{\lambda}$ that are more likely to have produced the signal s, are those which maximize the probability $P(\mathcal{H}_{\boldsymbol{\lambda}}|s)$. The following set of equations needs to be solved

$$\frac{\partial}{\partial \lambda_i} P(\mathcal{H}_{\boldsymbol{\lambda}}|s)\bigg|_{\boldsymbol{\lambda}=\boldsymbol{\lambda}_{max}} = 0. \tag{2.22}$$

The hypothesis $\mathcal{H}_{\boldsymbol{\lambda}}$ represents that the output data from the detector s is the composition of a particular noise realization and a GW signal with parameters $\boldsymbol{\lambda}$,

$$s(t) = n(t) + h(t; \boldsymbol{\lambda}). \tag{2.23}$$

Under the assumption of Gaussian noise the distribution for the noise is

$$P(n) = N e^{-\frac{1}{2}\int_{-\infty}^{\infty} df \frac{|\tilde{n}(f)|^2}{S_n(f)/2}}, \tag{2.24}$$

where N is a normalization constant. Recalling the inner product defined in (2.17) we have

$$P(n) = Ne^{-(n|n)/4}. \tag{2.25}$$

Assuming that there is a signal present in the output of the detector (i.e. that $s = n + h(\boldsymbol{\lambda})$)), the probability above is equivalent to the likelihood function Λ of having measured s given a signal $h(\boldsymbol{\lambda})$. The likelihood can be obtained by inserting $n = s - h(\boldsymbol{\lambda})$ into equation (2.25),

$$\Lambda(s|\lambda) = Ne^{\frac{1}{2}(h(\boldsymbol{\lambda})|s) - \frac{1}{4}(h(\boldsymbol{\lambda})|h(\boldsymbol{\lambda})) - \frac{1}{4}(s|s)}. \tag{2.26}$$

The term $(s|s)$ can be reabsorbed in the normalization factor N since it is constant and does not depend on the parameters $\boldsymbol{\lambda}$. By introducing the prior distribution $\pi(\boldsymbol{\lambda})$ we obtain the posterior probability,

$$P(\boldsymbol{\lambda}|s) = N\pi(\boldsymbol{\lambda})e^{\frac{1}{2}(h(\boldsymbol{\lambda})|s) - \frac{1}{4}(h(\boldsymbol{\lambda})|h(\boldsymbol{\lambda}))}. \tag{2.27}$$

In the case when the prior probability is flat the maximization of the posterior probability and the likelihood are the same. For this case, it can be shown that the set of values that maximizes the likelihood $\boldsymbol{\lambda}_{max}$ coincides with the set of parameters that gives the highest signal-to-noise ratio in the matched filtering.

2.2.4.1 Samplers

In the preceding section, we saw that the problem of PE consists in calculating the posterior distribution of the parameters $\boldsymbol{\lambda}$. In the case of a binary coalescence system, there are 15 parameters which are given by the masses of the two black holes, the two spin vectors of each object (6 components), the distance from the observer to the source, two angles that locate the position of the observer in the sky of the source (which enters in the SWSH functions), two angles that locate the sky position of the source in the detector frame (which enters in the antenna pattern functions), the reference time at which the signal enters in the detector bandwidth and the polarization angle which determines the axes with respect the $h_{+,\times}$ polarizations are defined. Our best estimate of the parameters of the source is given by the parameters that maximize the posterior distribution. To carry out this study it is necessary a prediction of the GW signal for a given set of parameters $\boldsymbol{\lambda}$ and this is represented by $h(\boldsymbol{\lambda})$. The waveform approximants provide this prediction, we discuss some of the most widely used approximants in Sec. 2.3. The accuracy of the approximant and the kind of physics that describes have a great impact on the parameters and the properties of the source that can be inferred.

In PE we are interested in finding the posterior distribution of each parameter and its maximum value. Naively one could try brute force and make a discrete grid in the parameter space, evaluate the posterior for each point and then search for the maximum. However, due to large dimensionality of the problem (15 dimensions), this rapidly becomes prohibitive, e.g. just by sampling each parameter in 10 points we would lead with 10^{15} evaluations. The alternative solution is to use a stochastic sampler. The two most common categories are the Markov Chain Monte-Carlo [20, 21] and nested sampling [22]. Both algorithms "sample" the parameter space, not in a uniform way as done previously, but starting from some initial guesses and drawing a path which converges to the maximum value of the posterior distribution. In the next two sections, we describe some of the peculiarities of each algorithm.

Markow Chain Monte-Carlo

Markow Chain Monte-Carlo (MCMC) algorithms [20, 21] start by distributing a set of initial guesses randomly across parameter space, then each one carries out a random walk through parameter space (known as a "chain"), distributing samples proportionally to the desired posterior distribution. To generate the next random step of the chain we require a proposal for the density function $Q(\boldsymbol{\lambda}'|\boldsymbol{\lambda})$ to generate the new sample $\boldsymbol{\lambda}'$ which depends only in the current sample $\boldsymbol{\lambda}$. The new proposal is then accepted and added to the chain with a probability $p = min(1, \alpha)$ where

$$\alpha = \frac{Q(\boldsymbol{\lambda}|\boldsymbol{\lambda}')P(h(\boldsymbol{\lambda}'|s))}{Q(\boldsymbol{\lambda}'|\boldsymbol{\lambda})P(h(\boldsymbol{\lambda}|s)}. \tag{2.28}$$

The MCMC algorithm suffers from an initial period known as "burn-in" when the samples added to the chain highly depend on the initial guesses where the algorithm starts from. Once this period is overcome the algorithm passes to a steady phase and the samples can start to be accumulated. The algorithm produces new samples and enlarges the length of the chains until a convergence criterion is satisfied. A commonly employed criterion is the Gelman-Rubin convergence diagnostic [23, 24], which analyzes the difference between multiple Markov chains. The convergence is assessed comparing the estimated variance between chains and within chains for each model parameter. Small differences between these variances indicate convergence.

Nested sampling

The nested sampling algorithm [22] starts by populating the parameter space with a set of "live points" according to the prior distribution. Then, at each iteration, the live point with the lowest likelihood is removed from the list (it becomes a "dead point") and it is replaced with a new point that has got a higher likelihood than the removed one. A visualization of this iterative procedure is shown in Fig. 2.8. This procedure is repeated

until a stopping condition is satisfied. One of the conditions most commonly used in gravitational waves PE is that the loop continues until $L_{max}X_i/Z_i > e^{0.1}$, where L_{max} is the maximum likelihood that has been obtained so far, Z_i is the current estimate of the total evidence and X_i is the prior mass or fraction of the prior volume inside the current contour line. Opposite to the MCMC algorithm, the posterior samples do not accumulate linearly in time nor is the algorithm straightforward parallelizable.

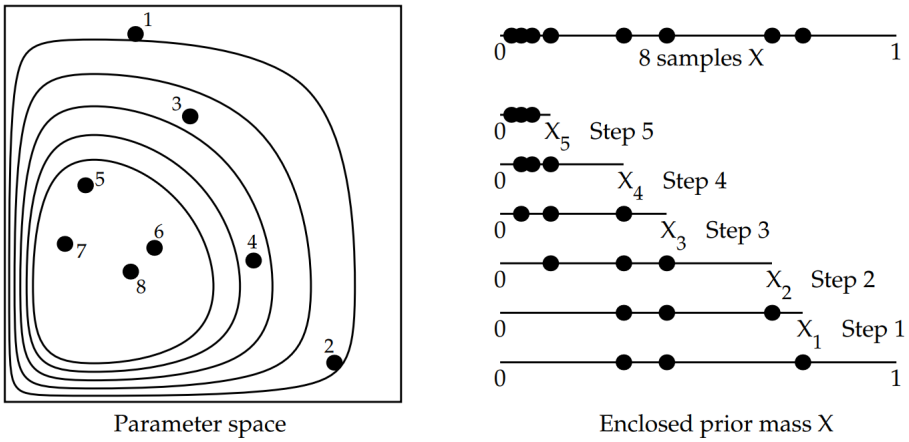

FIGURE 2.8: Representation of the nested sampling algorithm through 5 iterations for a set of three live points. Image credits: [22].

2.3 Waveform approximants

In the previous section, we studied the crucial role that waveform templates play in order to discover gravitational wave signals buried into the noise of the detector and how to extract the physical information about the sources that produced such events. There exist different approaches to produce these templates, they can be analytical, numerical or combine both techniques. These approaches are known as waveform *approximants*. Different approximants can describe different physics and are usually valid for a restricted region of the parameter space or for a determined frequency range. For example, Post-Newtonian (PN) theory was the first approach to describe the gravitational wave signal and it is only valid for the inspiral regime where the two bodies are distant. During the merger, the two bodies are much closer and the strong field interactions control the dynamics so the full Einstein equations need to be solved. Nowadays this is only possible by means of numerical techniques known as Numerical Relativity (NR) and powerful supercomputers. As we will see, these two approaches (PN theory and NR) are combined by other families of approximants such as the Effective One Body (EOB) and Phenom to produce accurate waveforms for the whole frequency regime: inspiral, merger and ringdown (IMR). The field of waveform modelling is nowadays very active and continuously

more advanced, more accurate and more efficient models come to light pushed forward by the improvements on the sensitivities of the detectors and what facilitates the detection of more challenging events and therefore more complicated physics. Now we will review some of the most important families of waveform approximants.

2.3.1 Post-Newtonian theory

In section 1.6, we discussed the generation of gravitational waves by sources moving in a flat spacetime, i.e. we assumed that the sources that produce this gravitational wave emission do not contribute significantly to the curvature of spacetime in the near-field region. We carried out an expansion in powers of v/c to compute the gravitational wave emission and took the leading order given by the Einstein quadrupole formula. In this section, we want to consider the more realistic case where the binary system contributes to curve the spacetime and it is not flat anymore. Now we will not be able to describe the dynamics of the system using Newtonian gravity rather we will need the PN formalism. The two basic assumptions of the PN theory are, first, slowly moving sources, this is the same requirement we had for the linearized theory and it means that $v/c \ll 1$, a result for relativistic objects requires then very high orders in the (v/c) expansion. Second, the sources must be weakly self-gravitating, i.e. the curvature they introduce in the spacetime is not "too strong". Therefore the PN formalism will be only valid when the two objects are sufficiently separated from each other, this corresponds to the inspiral part of the coalescence. However, near the merger, where the two objects are close, the fields are much stronger and the PN formalism is not valid anymore. In order to describe this regime, we will need to solve the full Einstein equations with the methods of NR. It is out of the scope of this section to present a complete derivation of the PN formalism and we will just indicate some basic results. There exist several approaches to perform the PN expansion namely the Direct Integration of the Relaxed Einstein equations (DIRE) [25–27], the multipolar expansion of the source potential of Blanchet and Damour [28], the effective field theory formalism [29] and the Hamiltonian formulation [30]. The PN formalism has allowed us to compute the GWs emission including several subdominant harmonics up to 3.5 PN order for non-spinning binary systems and up to 2PN order for spinning ones. This formalism permits as well to solve the dynamic equations of the system. The equation of motion up to 3.5 PN order is given by

$$\frac{dv^i}{dt} = -\frac{Gm}{r^2}\left[(1+\mathcal{A})\frac{x^i}{r} + \mathcal{B}v^i\right] + \mathcal{O}\left(\frac{1}{c^8}\right), \tag{2.29}$$

where the coefficients $\mathcal{A}$ and $\mathcal{B}$ can be found in Eqs. 220a, 220b of [28]. For quasi-circular orbits, the expression can be simplified to

$$\frac{dv^i}{dt} = -\omega_s^2 x^i - \zeta v^i, \tag{2.30}$$

where

$$\omega_s^2 = \frac{GM}{r^3}\left\{1 + (-3+\eta)\gamma + \left(6 + \frac{41}{4}\eta\right)\gamma^2\right. \tag{2.31}$$

$$\left. + \left[-10 + \left(22\log(r/r'_0) - \frac{75707}{840} + \frac{41}{64}\pi^2\right)\eta + \frac{19}{2}\eta^2 + \eta^3\right]\gamma^3\right\} \tag{2.32}$$

$$+ \mathcal{O}\left(\frac{1}{c^8}\right), \tag{2.33}$$

$$\zeta = \frac{32}{5}\frac{G^3M^3\eta}{c^5r^4} + \mathcal{O}\left(\frac{1}{c^7}\right), \tag{2.34}$$

and

$$\gamma \equiv \frac{GM}{rc^2}, \tag{2.35}$$

Eq. (2.31) represents an extension of Kepler's law since it relates the orbital frequency with the radius of the orbit. If we rewrite these expressions in terms of the PN expansion parameter

$$x = \left(\frac{GM\omega_s}{c^3}\right)^{2/3}, \tag{2.36}$$

it can be shown that the energy of the orbit is then given by

$$E_{orbit} = -\frac{\eta Mc^2 x}{2}\left\{1 + \left(-\frac{3}{4} - \frac{1}{12}\eta\right)x + \left(-\frac{27}{8} + \frac{19}{8}\eta - \frac{1}{24}\eta^2\right)x^2\right. \tag{2.37}$$

$$\left. + \left[-\frac{675}{64} + \left(\frac{34445}{576} - \frac{205}{96}\pi^2\right)\eta - \frac{155}{96}\eta^2 - \frac{35}{5184}\eta^3\right]x^3\right\} \tag{2.38}$$

$$+ \mathcal{O}\left(\frac{1}{c^8}\right). \tag{2.39}$$

Similarly to the procedure followed in Sec. 1.6, we equate the energy loss of the orbit to the power emitted in form of gravitational waves P_{GW} which in this case is given by Eq. 314 in [28]. This provides an equation from where one can attain the solution of the orbital phase ϕ as a function of the PN expansion parameter x, see Eq. 318 in [28]. The expression for the orbital phase evolution can be plugged into the $h_{+,\times}$ polarizations obtaining the final result displayed in [28] through equations 320-323. All the results so far correspond to a binary system without spins i.e. neither of the two objects rotate around themselves. For a general case of spinning objects, the procedure is essentially the same, but now the expressions for the energy of the orbit and the power

emitted include terms related with the spins in addition to the already discussed non-spinning terms. The new spinning terms appear at higher PN orders [31, 32] so they are a subdominant effect. The final result depends on how the equation of the energy and flux is expanded, different expansions can change significantly the behaviour of the approximant for high frequencies. No expansion is always better behaved than the rest, so each one will be more suitable for different parts of the parameter space. Some of these variants are the `TaylorT1`, `TaylorT2`, `TaylorT3`, `TaylorT4` or `TaylorEt` approximants. A Fourier domain approximant can be obtained by performing the Stationary-Phase-Approximation (SPA). This is an analytical approximation for the integral of the Fourier transform and it assumes that the phase slowly changes with the frequency, which is true only in the inspiral and it breaks down for high frequencies. The result is the `TaylorF2` approximant which has been widely used in the calibration of phenomenological models for the inspiral part (see Section 2.3.3 for more details). For a review of the technical details of how each approximant is built see [33].

2.3.2 EOB models

A second approach to the description of gravitational wave emission in the two-body problem is the effective-one-body (EOB) [34–38], which employs results from PN theory. These results are not expressed in their original "Taylor expanded" form (i.e. as a polynomial in v) but in a resummed manner as a non-polynomial function of v. This enables to incorporate some non-perturbative aspects of the exact result. The basic pillars for the EOB formalism comprise an expression for the conservative part of the dynamics of the two black holes, a description for the radiation-reaction part and finally a description of the gravitational wave generated by the system. The equations of the dynamics can be solved numerically and its new resummed form allows one to transcend the inspiral phase, and reach the plunge phase where PN is not valid. The ringdown part is attached using results from perturbation theory, resulting in a complete inspiral-merger-ringdown (IMR) waveform. The EOB approach is known to be more accurate than PN theory but still, it dephases respect to the "exact" solution in the merger. By comparing with the "exact" solutions given by NR one can perform a fit of the yet unknown higher PN coefficients and use them to solve the dynamics equations. The EOB models calibrated to NR are called "EOBNR" models and there exist an abundance of different versions depending on which features of the waveform are described and which NR data set is used for the calibration. The versions that are currently being more widely utilized are SEOBNRv4 [39] which describes the dominant $(2, 2)$ mode of non-precessing system, SEOBNRv4HM [40] includes the higher modes. Equivalently, for precessing systems, we have SEOBNRv4P and SEOBNRv4PHM. There exist also some work to include

the effect of eccentric orbits in the EOB formalism [41]. Although EOB models are more accurate than PN and much faster to compute than an NR simulation, they are still computationally very expensive for carrying out PE studies, where millions of waveforms have to be evaluated. The Reduced Order Models (ROM) [42, 43] are typically the accepted solution for this problem. They are simplified representations in the Fourier domain of the more complex time-domain EOB model. Building these models can be computationally very expensive and accumulate important amounts of data, but once they are built they can be evaluated rapidly at the cost of only losing a small fraction of accuracy.

2.3.3 Phenom models

The Phenom models are an alternative approach which solves some of the main drawbacks of the EOB models, namely their complexity and their high computational cost. The Phenom or phenomenological models [44–47] are analytical models built already in the Fourier domain based on closed-form expressions which are functions of the parameters of the binary system under study. Their evaluation is therefore very rapid and since they are already in the Fourier domain they do not have to be Fourier transformed during the PE studies. The core idea of the Phenom models consists in employing a phenomenological ansatz which is calibrated to NR simulations. Since the main contribution of the present thesis is to develop two new Phenom models, let us explain in more detail the basic procedure they are based on:

- First, we need a data set of NR simulations against which we will calibrate our model. The NR simulations are typically short and do not contain the early inspiral part of the waveform. In order to the model be valid for low frequencies we need to calibrate to longer waveforms. To this end we build the *hybrid* waveforms, by "glueing" the early inspiral described by an EOB waveform to the NR waveform. These hybrids are transformed to the Fourier domain and constitute the data set the model is calibrated to. The larger the number of hybrids in the dataset and the more they span the parameter space, the more reliable and valid the model will be.

- Once in the Fourier domain, we propose ansatzes for the amplitude and for the phase of the waveform. These ansatzes are chosen as piecewise functions adapted to the morphology of the waveform in each frequency region. For example, in the inspiral, an ansatz based on PN theory is used, where higher-order and yet unknown PN coefficients are calibrated to NR. We call the calibration of the ansatz

to a hybrid waveform the *direct fit*, and we perform this fit for the whole dataset of hybrid waveforms at our disposal.

- For each hybrid waveform, we obtain a set of fitted coefficients. Each of these coefficients is now fitted across parameter space as a function of the intrinsic parameters, i.e. symmetric mass ratio and two spin components in the case of non-precessing systems. For this 3-dimensional fit, we follow the hierarchical fitting procedure developed in [48].

- To obtain the final waveform or "reconstruct" the model we follow the backward direction. First, we evaluate the parameter space fitted coefficients for the case under study, then plug these coefficients into the phenomenological ansatzes, which depend on the frequency, and finally evaluate that ansatz for all the required frequency points.

- Once we have evaluated the amplitude and phase in the desired frequency array the waveform is computed by performing the operation $h(f) = A(f)e^{i\phi(f)}$ for each frequency point.

The main bottleneck in the evaluation of phenomenological models is in the evaluation of trigonometric functions that appear in the ringdown part as well as the evaluation of the complex exponential of the final waveform. Both of these issues are addressed in chapter 4. Due to the good performance of the Phenom models, a number of them have been developed recently. Each version incorporating different features and physics of the waveform. In Table 2.1 we summarize some of the current models as well as compare to the new-born PhenomX family models to which this thesis has contributed.

Physics	Old Phenom	PhenomX family
22-mode only	PhenomD [49]	PhenomXAS [50]
higher modes	PhenomHM [51]	PhenomXHM [52]
Precessing 22 mode	PhenomPv2 [53] (Pv3)[54]	PhenomXP [55]
Precessing and higher modes	PhenomPv3HM [54]	PhenomXPHM [55]
22-mode only + tidal corrections	PhenomD_NRTidal(v2) [56]	-
Precessing 22 mode + tidal corrections	PhenomPv2_NRTidal(v2) [56]	-
Neutron Star Black Hole	PhenomNSBH [57]	-

TABLE 2.1: Summary of current Phenom models.

2.3.4 Numerical Relativity

Until the present day, the only way to solve the two-body problem in the strong field regime of general relativity is by solving the Einstein equations numerically in a computer. This is not an easy task even nowadays, solving these equations for the last few orbits of the evolution can take weeks in the most modern supercomputers. The first attempts to perform NR simulations started in the 1960s [58, 59], and in the 1970s head-on collisions started to be studied [60–64]. However, the simulation of two orbiting objects dodged all the daunting efforts until 2005-2006 when finally several independent groups could simulate the last few orbits of a binary black hole system [65–67] (see Fig. 2.9). The task was indeed extremely complicated since, before fixing the gauge, Einstein's equations consist of 10 coupled non-linear second order differential equations, one for each component of the metric $g_{\mu\nu}$. Let us now outline how the problem was solved. First, the covariant Einstein equations are reformulated as an initial value problem. This requires to break four-dimensional covariance by distinguishing a time coordinate. The most common way of doing this is to choose the three-dimensional hypersurfaces that correspond to constant time as spatial surfaces. Such a hypersurface will then also be chosen to define the initial data. Rewriting the Einstein equations in a form that is adapted to a description of spacetime in terms of evolving three-dimensional spatial hypersurfaces is known as 3+1 formulation. The resulting equations are often referred to as the "ADM" equations, where ADM stands for Arnowitt, Deser and Misner, who derived such a formulation in the context of a Hamiltonian description of general relativity [68] (see [69, 70] for earlier work on 3+1 decompositions). In NR the ADM equations are typically used in their reformulation by York [71]. We start by splitting the metric into a temporal and a spatial part,

$$ds^2 = (-\alpha^2 + \beta_i\beta^i)(cdt)^2 + 2\beta_i dt dx^i + \gamma_{ij} dx^i dx^j. \tag{2.40}$$

The quantities α and β^i are known as the *lapse function* and *shift vector* which parameterize the choice of coordinate gauge. Nevertheless, for a numerical code, the choice of a suitable gauge is key to prevent the code to find the singularities of the black holes and provoke non-assigned numbers that finally lead to the crash of the code. With the decomposition in (2.40) we foliate the spacetime with a set of 3-dimensional hypersurfaces Σ_t which are parameterized by the coordinate t. The lapse function α establishes the step size in proper time between the hypersurfaces. On the other hand, the shift vector β_i describes how the coordinates x^i on a slice Σ_t relate to the coordinates in the next slice Σ_{t+dt}. The dynamical variable here is the *spatial metric* γ_{ij} which measures the distances on a particular slide. Another very important variable is the so-called *extrinsic curvature* $K_{\mu\nu}$ which describes how the 3-dimensional slice is embedded in the 4-dimensional

spacetime. It is defined in terms of the unit normal vector to the hypersurface n_μ,

$$K_{\mu\nu} = -(\delta^\rho_\mu + n^\rho n_\mu)\nabla_\rho n_\nu. \tag{2.41}$$

The system of equations to solve consists of two evolution equations and two constraints. There is an evolution equation for the spatial metric γ_{ij} and another for the extrinsic curvature K_{ij}:

$$\partial_t \gamma_{ij} = -2\alpha K_{ij} + \bar{\nabla}_i \beta_j + \bar{\nabla}_j \beta_i, \tag{2.42}$$

$$\partial_t K_{ij} = \alpha \left[R_{ij} + K K_{ij} - 2K_{ik}K^k_j \right] + \beta^k \partial_k K_{ij} + K_{ik}\partial_j \beta^k + K_{kj}\partial_i \beta^k \tag{2.43}$$

$$- 8\phi\alpha(S_{ij} - \frac{1}{2}\gamma_{ij}(S - \rho)). \tag{2.44}$$

The constraint equations are given by a constraint in the Hamiltonian and another in the momentum:

$$R + K^2 - K_{ij}K^{ij} = 16\pi\rho, \tag{2.45}$$

$$\bar{\nabla}_j (K^{ij} - \gamma^{ij} K) = 8\phi S^i. \tag{2.46}$$

Here we have introduced the matter source terms

$$\rho = n_a n_b T^{ab}, \qquad S^i = -\gamma^{ij} n^a T_{aj}, \qquad S_{ij} = \gamma_{ia}\gamma_{jb} T^{ab}, \qquad S = \gamma^{ij} S_{ij}, \tag{2.47}$$

and the symbol $\bar{\nabla}_i$ refers to the covariant derivative associated with γ_{ij}.

This formulation of the ADM equations is not adequate for an unconstrained numerical evolution of the initial data. The evolution equations are at best (depending on the coordinate gauge) weakly hyperbolic and the initial value problem is ill-posed. This will lead the evolution to violate the Hamiltonian and momentum constraints and will typically end in the crash of the code. New formulations are required to transform the problem into a well-posed one. Some of these successful formulations are the Baumgarte-Shapiro-Shibata-Nakamura (BSSN) formulation [72, 73], the Z4 formulation [74–77], one based on the generalization of harmonic coordinates [65] and a constrained formulation [78, 79]. We will quickly review the BSSN formalism since it is the basis of the BAM code [80] which has contributed to this thesis with several NR simulations.

In the BSSN formalism, the spatial metric is decomposed in terms of a conformal variable ϕ,

$$\gamma_{ij} = e^{4\phi}\bar{\gamma}_{ij}. \tag{2.48}$$

The extrinsic curvature is also decomposed in its trace and traceless part,

$$K_{ij} = e^{4\phi}\tilde{A}_{ij} + \frac{1}{3}\gamma_{ij}K. \tag{2.49}$$

The Hamiltonian constraint now becomes

$$\bar{\gamma}^{ij}\bar{\nabla}_i\bar{\nabla}_j e^{\phi} - \frac{e^{\phi}}{8}\bar{R} + \frac{e^{5\phi}}{8}\tilde{A}_{ij}\tilde{A}^{ij} - \frac{e^{5\phi}}{12}K^2 + 2\pi e^{5\phi}\rho, \tag{2.50}$$

while the momentum constraint transforms to

$$0 = \bar{\nabla}_j\left(e^{6\phi}\tilde{A}^{ji}\right) - \frac{2}{3}e^{6\phi}\bar{\nabla}^i K - 8\pi e^{6\phi}S^i. \tag{2.51}$$

The evolution equation of the spatial metric γ_{ij} splits into two equations,

$$\begin{aligned}\partial_t\phi &= -\tfrac{1}{6}\alpha K + \beta^i\partial_i\phi + \tfrac{1}{6}\partial_i\beta^i \\ \partial_t\bar{\gamma}_{ij} &= -2\alpha\tilde{A}_{ij} + \beta^k\partial_k\bar{\gamma}_{ij} + \bar{\gamma}_{ik}\partial_j\beta^k + \bar{\gamma}_{kj}\partial_i\beta^k - \tfrac{2}{3}\bar{\gamma}_{ij}\partial_k\beta^k,\end{aligned} \tag{2.52}$$

On the other hand, the evolution equation for the extrinsic curvature splits into

$$\partial_t K = -\gamma^{ij}\nabla_j\nabla_i\alpha + \alpha\left(\tilde{A}_{ij}\tilde{A}^{ij} + \frac{1}{3}K^2\right) + 4\pi\alpha(\rho + S) + \beta^i\partial_i K \tag{2.53}$$

$$\partial_t\tilde{A}_{ij} = e^{-4\phi}\left(-\left(\nabla_i\nabla_j\alpha\right)^{TF} + \alpha\left(R^{TF}_{ij} - 8\pi S^{TF}_{ij}\right)\right) + \alpha\left(K\tilde{A}_{ij} - 2\tilde{A}_{il}\tilde{A}^l_j\right) \tag{2.54}$$

$$+ \beta^k\partial_k\tilde{A}_{ij} + \tilde{A}_{ik}\partial_j\beta^k + \tilde{A}_{kj}\partial_i\beta^k - \frac{2}{3}\tilde{A}_{ij}\partial_k\beta^k. \tag{2.55}$$

The superscript TF means trace-free so it refers to the tensor without the trace. Also, it has been introduced an auxiliary conformal connection used in the covariant derivatives $\bar{\nabla}$ defined by

$$\bar{\Gamma}^i := \bar{\gamma}^{jk}\bar{\Gamma}^i_{jk} = -\partial_j\bar{\gamma}^{ij}, \tag{2.56}$$

where $\tilde{\Gamma}^i_{jk}$ are the Christoffel symbols for the conformal metric $\bar{\gamma}_{ij}$. These objects satisfy their own evolution equations

$$\partial_t\bar{\Gamma}^i = -2\tilde{A}^{ij}\partial_j\alpha + 2\alpha\left(\bar{\Gamma}^i_{jk}\tilde{A}^{kj} - \frac{2}{3}\bar{\gamma}^{ij}\partial_j K - 8\pi\bar{\gamma}^{ij}S_j + 6\tilde{A}^{ij}\partial_j\phi\right) \tag{2.57}$$

$$+ \beta^j\partial_j\bar{\Gamma}^i - \bar{\Gamma}^j\partial_j\beta^i + \frac{2}{3}\bar{\Gamma}^i\partial_j\beta^j + \frac{1}{3}\bar{\gamma}^{li}\partial_l\partial_j\beta^j + \bar{\gamma}^{lj}\partial_j\partial_l\beta^i. \tag{2.58}$$

To complete the system of evolution equations we need to define the evolution equations for the gauge variables. This is also a gauge choice and depends on the specific spacetime to be evolved. For example, in BAM, the lapse and shift are evolved through the *1+log* lapse condition[82], which is a special case of the Bona-Massó family of gauge conditions

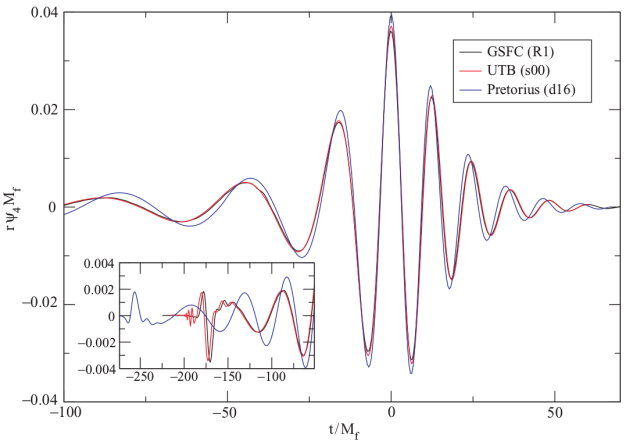

FIGURE 2.9: Comparison of the three first NR simulations obtained by three independent research groups: Pretorious [65], Goddar Space Flight Center (GSFC) [66] and University of Texas [67]. Image credits: [81].

[83], and the *gamma-freezing* [84] shift conditions

$$\partial_0 \alpha = -2\alpha K \quad , \quad \partial_0 \beta^i = \frac{3}{4} B^i \quad , \quad \partial_0 B^i = \partial_0 \tilde{\Gamma}^i - \bar{\eta} B^i, \tag{2.59}$$

where $\partial_0 = \partial_t - \beta^i \partial_i$, B^i is an auxiliary vector which improves the constraints at the initial location of the punctures, and $\bar{\eta}$ is the gamma-freezing damping parameter which controls the growth of the horizons [85].

2.3.5 The need for subdominant harmonics approximants

We discuss now how the subdominant harmonics affect the anatomy of the waveform, which is their impact on the detection and PE studies of gravitational waves events and why they need to be included in the templates.

There are three main parameters that enhance the importance of the subdominant harmonics: the inclination of the orbit (i.e. the angle between the angular momentum of the binary and the line of sight), the mass ratio and the total mass of the system. We will discuss hereafter each one separately. For simplicity, we will focus the discussion on waveforms of non-precessing binaries. In this situation there exists an equatorial symmetry which relates the gravitational wave signal in the range of inclination $\iota = (0, \pi/2)$ with the range $\iota = (\pi/2, \pi)$ given by

$$h(t, \iota) = h^*(t, \pi - \iota). \tag{2.60}$$

This can be used to establish a relation between the positive and the negative (l, m) modes

$$h_{lm}(t) = (-1)^l h^*_{l-m}(t). \tag{2.61}$$

The effect of the inclusion of the subdominant harmonics as a function of the inclination is shown in Fig. 2.10. We see in this figure how the anatomy of the waveform with subdominant harmonics changes respect to the quadrupolar one when the inclination tends to $\pi/2$. For the $(2, \pm 2)$-only case, the peaks and nodes of the waveforms are all aligned while for the case with subdominant harmonics there is a dephasing between peaks and nodes due to the different relative phases between modes. Let us justify why this misalignment is more pronounced when inclination tends to $\pi/2$. In Eq. (1)

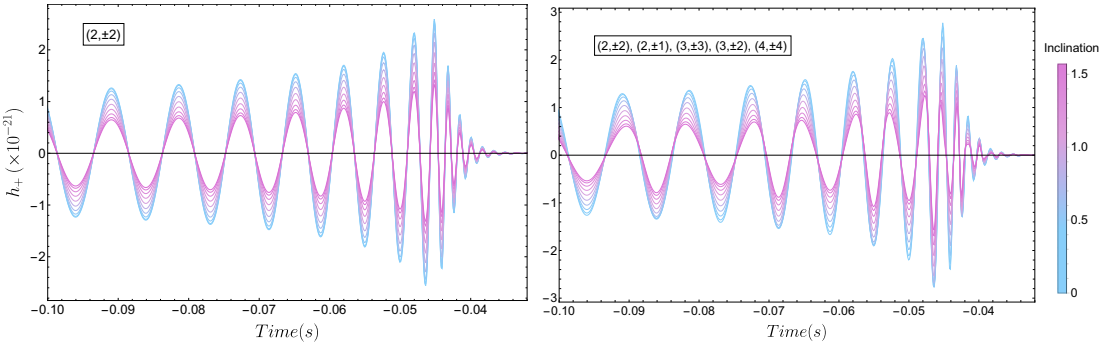

FIGURE 2.10: Effect of the inclination in a waveform with only the dominant part (left) and with subdominant harmonics (right). The inclination is varied from 0 to $\pi/2$, due to the equatorial symmetry the second quadrant $(\pi/2, \pi)$ is equivalent.

we already saw that the individual h_{lm} do not have any angular dependence, which is captured by the spin-2 weighted spherical harmonics. In Fig. 2.11 we show the angular distribution of these spherical harmonics for the strongest modes. The reference system of these plots corresponds to the source frame of the binary system so they represent the emission of each mode a function of the location of the observer in the sky of the source. Note that all the plots show an equatorial symmetry, in fact, the half above the equator corresponds to the spherical harmonic with $m > 0$ while the half below corresponds to the $m < 0$. The modes with $m = \pm 2$ are the only ones which do not vanish for inclination $0(\pi)$ (face-on/off systems). None of them vanishes for inclination $\pi/2$ (edge-on systems) although the contribution of the $Y_{2\pm2}$ mode is minimal here and lower than for other modes. Consequently, even when the individual mode h_{lm} is weaker than the dominant h_{22} ($|h_{lm}| < |h_{22}|$) the spherical harmonic amplifies the relative relevance of the subdominant mode in the total signal. In Fig. 2.12 we represent the amplitude of the spherical harmonics as a function of the inclination and see how indeed the amplitude of the SWSH of subdominant harmonics becomes more relevant than the one for the $(2, 2)$ mode when the inclination tends to $\pi/2$.

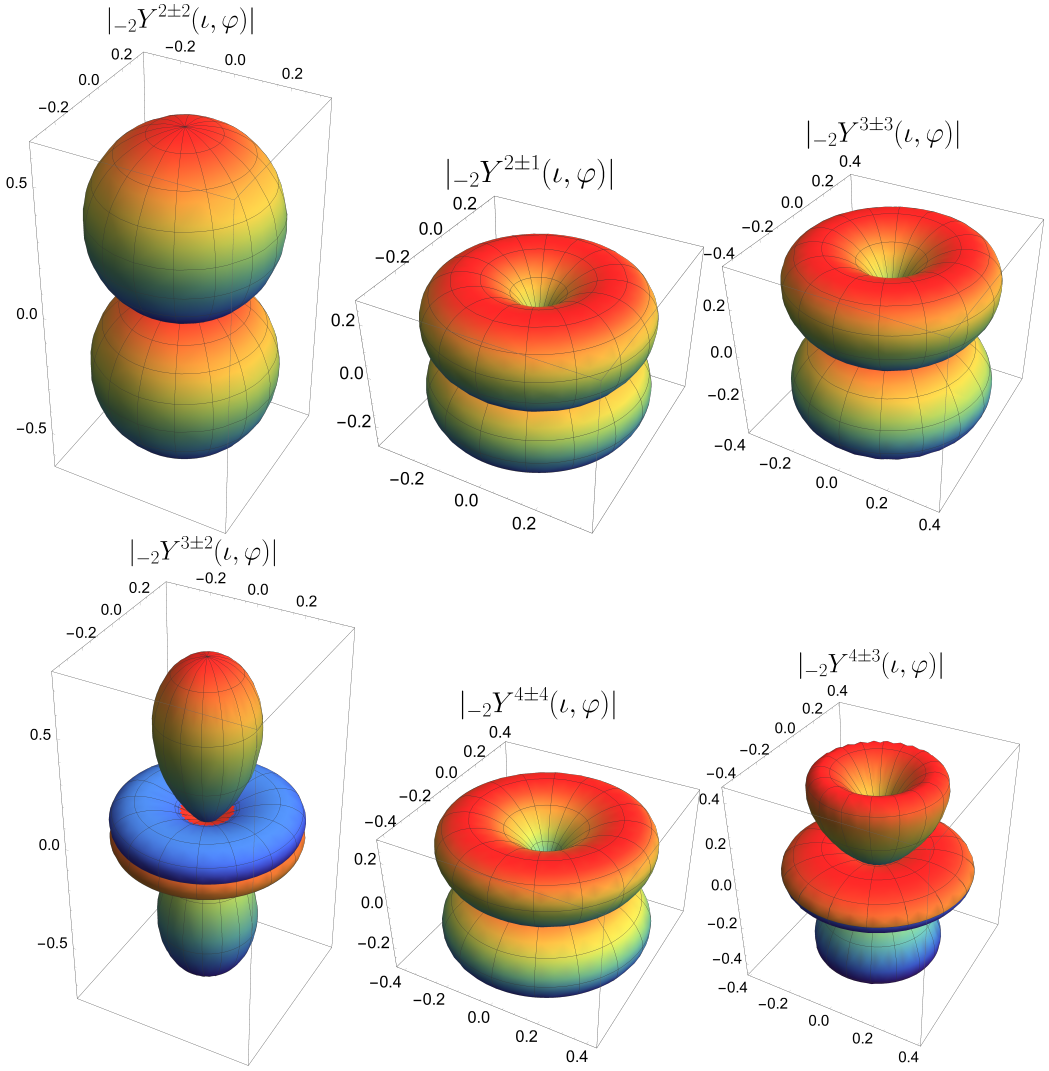

FIGURE 2.11: Angular dependence of the amplitude of the spin-2 weighted spherical harmonics. This gives an idea of the power emitted in each direction by every individual mode.

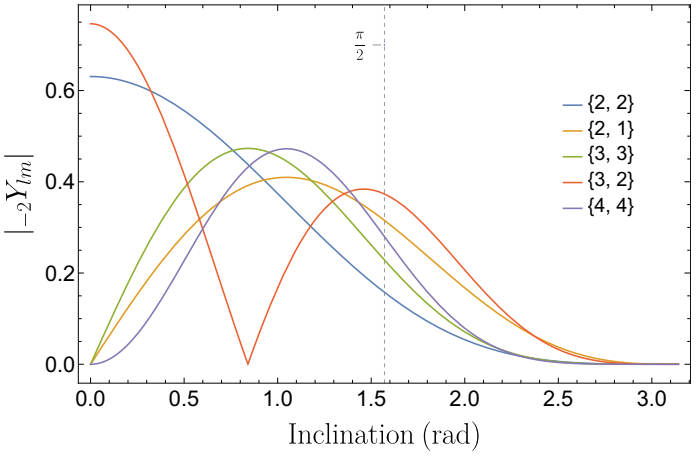

FIGURE 2.12: Dependence of the amplitude of the spin-2 weighted spherical harmonics with the inclination. The negative modes would show the same dependence but mirror reflected respect $\pi/2$ (due to the equatorial symmetry).

We pass now to justify why the higher modes are more important for systems with higher total mass. We already mentioned in the Preface that the mass of the system is just a scale factor which does not modify the morphology of the waveform, i.e. there is no enhancement of the emission of subdominant modes for high masses, then what does it mean that the higher modes are more relevant for high masses? The reason is that our gravitational wave detectors have a particular frequency band where they are more sensitive and for high masses, the part of the waveform that appears in this frequency band is the ringdown, where several subdominant modes can be stronger than the dominant $(2, \pm 2)$ modes. In Fig. 2.13 we represent the Fourier domain amplitude of several modes together with the noise curves for two different masses. When using geometrical units ($G = c = 1$) the shift in frequencies happens for the noise curve instead of for the waveforms, which are shifted when using units of Hz for the frequencies. We see how several modes reach higher frequencies than the $(2, \pm 2)$ and therefore become to be the dominant modes. The reason why different modes reach different frequencies is that they rotate at different rates. During the inspiral, the phase of each mode scales approximately with m the orbital phase, $\phi_{lm} \approx m\phi_{orb}$, according to this the $(4, \pm 4)$ mode will be the fastest rotating and therefore reach higher frequencies than the rest. Then we have the $(3, \pm 3)$ and later the $(2, \pm 2)$ and $(3, \pm 2)$ which approximately reach a similar frequency since they have the same m and finally the $(2, \pm 1)$ are the slowest ones and reach lower frequencies. The plot shows how for high masses the region where the $(3, \pm 3)$ and $(4, \pm 4)$ become dominant appears above the noise curve, therefore their contribution becomes more important.

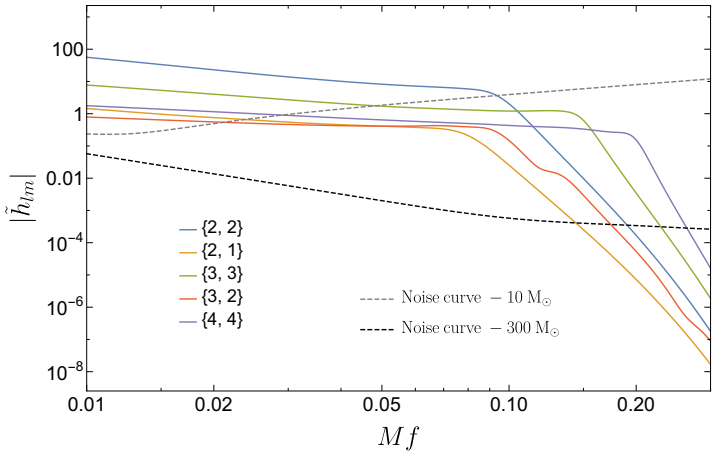

FIGURE 2.13: Frequency domain amplitude of several individual $\tilde{h}_{lm}$ modes and noise/sensitivity curves for two different total masses of the system.

Finally, we have the effect of the mass ratio. Looking at the leading order PN contribution of each mode we see that the relative strength of the subdominant harmonics with respect to the $(2, \pm 2)$ modes increases with the mass ratio. One way to explain this is that the asymmetry of the system enhances the emission of subdominant harmonics. In

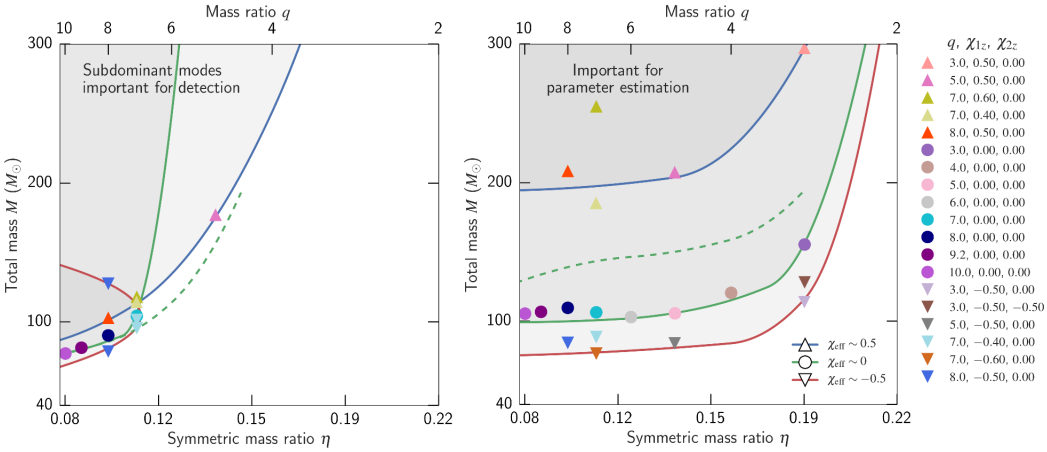

FIGURE 2.14: Regions of the parameter space where subdominant harmonics templates are important for detection (left) and PE (right). Image credits: [86].

Fig. 2.11 we saw that the emission of the $(2, \pm 2)$ modes have a quadrupolar shape, but an asymmetric system with mass ratio larger than one would be difficult to produce such symmetric emission and therefore subdominant harmonics should also be emitted. The opposite is also true, the more symmetric the system is, the smaller the contribution of higher harmonics is, in particular the odd modes (odd m) cancel for systems of two identical black holes. This happens because the odd modes introduce a minus sign when the system is rotated an angle π but if the two black holes are identical this is equivalent to not having rotated the system, so a number equal to its negative must be zero. For systems with equal mass black holes but different spins the odd modes are not zero but several leading orders of the PN expansion cancel and only the higher spinning PN orders contribute so the odd modes are in these cases very weak.

Now we wonder if the subdominant harmonics really need to be taken into account when analyzing the data from the detectors, do we need templates able to describe the subdominant contribution or is it enough to use quadrupolar ones? There are several studies that quantify how the neglection of subdominant harmonics in our templates affects the detection rates and the PE biases [86, 87]. A summary of the region of parameter space where there exists an important loss of detection rate and biases for PE is found in Fig. 2.14.

Of special relevance for PE is the degeneracy between the distance and inclination that the subdominant harmonics break. In a quadrupolar-only template, the inclination and distance are degenerated because they appear as a multiplicative factor of the oscillatory part of the waveform. However, in a waveform with subdominant harmonics, the inclination appears in a different functional form in every term of the expansion in spherical harmonics, this separation permits the PE algorithm to be able to infer each parameter

much more accurately. Fig. 2.15 displays an example of how this degeneracy is broken with the use of subdominant harmonics approximants, the example is taken from a recently published event by the LVC a high mass ratio [88].

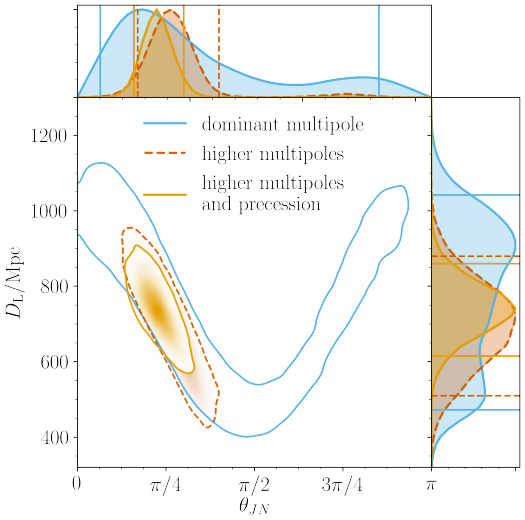

FIGURE 2.15: Posterior distribution for the luminosity distance D_L and inclination θ_{JN} (angle between total angular momentum and line of sight) of GW190412. Image credits: discovery paper of GW190412 [88].

During the observation runs O1 and O2 of the LIGO-Virgo detectors, only events with mass ratio close to one were found so the subdominant harmonics did not play an important role and only quadrupolar templates were needed for the analysis [89]. However, with the upgrade in the detectors and the improvement in sensitivity, the spacetime volume with detectable sources will be significantly increased and many more events are expected to be observed, some of them will lay in the regions where subdominant harmonics are important. This has turned out to be already true during the first weeks of the O3 observation run when the GW190412 event [88] was detected. It consisted of a binary black hole system with the most asymmetric masses detected so far: $\sim 30M_\odot$ and $\sim 8M_\odot$ respectively. The study of this event finds strong evidence for GW emission beyond the quadrupolar leading order. There exist always the question of how many subdominant harmonics must be included in order to have an accurate template. This is highly dependent on the accuracy requirements of the analysis under study, for GW190412 the most important subdominant modes are found to be the $(3, \pm 3)$ modes, which are those with the highest SNR. Although the mass ratio of this system is significantly different from all previous detections, the study shows that "it is consistent with the population model of stellar binary black holes inferred from the first two observing runs". The analysis of this kind of new events is really complex as it is evidenced by the delay of approximately one year between the detection and publication of such an event. One of the reasons for this delay is that the waveform models employed for the analysis were not computationally efficient and the PE runs could last up to several weeks. Providing computationally

efficient waveform models which include the subdominant effects can decrease this time to several days, therefore these models are of special importance and haste. The two new waveform models together with the acceleration technique presented in part II of this thesis constitute the first release of waveform models for general black hole binaries of the PhenomX waveform family. Their computational efficiency and their flexibility to test different waveform settings permit to perform complex and robust PE analyses in a very brief time scale. Therefore they appear as a very efficient solution to solve the current challenges in the analysis of present and future gravitational wave events.

2.3.6 Introducing the PhenomX family

The PhenomX family models constitute a new series of waveform models which involves an upgrade of the previous phenom models in order to satisfy the demand of accuracy and computational efficiency required for the upcoming observations runs of the Advanced LIGO-Virgo detectors. The previous phenom models IMRPhenomD and IMRPhenomPv2 have been widely used by the collaboration for the analysis of the events during the O1 and O2 observations runs. The model IMRPhenomHM [51] was the first approximant including higher modes by performing an approximate mapping of the $(2, 2)$ waveform given by IMRPhenomD. IMRPhenomPv3HM extends IMRPhenomHM by including precession effects.

In this section, we discuss the cornerstone of the PhenomX family, based on the IMRPhenomXAS model [50] which describes the $(2, 2)$ mode of non-precessing systems and implies the upgrade of the IMRPhenomD model. In Part II we discuss in detail the extension of IMRPhenomXAS to subdominant harmonics and precession which provides a natural upgrade of the IMRPhenomHM, IMRPhenomPv2, and IMRPhenomPv3HM models.

IMRPhenomXAS follows a similar calibration strategy to IMRPhenomD, it is fully calibrated in amplitude and phase to NR simulations. The main difference with IMRPhenomD is the extensive NR dataset employed for the calibration, IMRPhenomD was calibrated against 19 NR waveforms while IMRPhenomXAS employs 460 simulations (see Fig. 2.16 for the parameter space distribution), and incorporates EMR waveforms up to mass ratio 1000. A second major improvement is the accurate treatment of unequal spin effects for the hierarchical parameter space fits. The implementation of the model in LALSuite [90] follows a modular philosophy, allowing for swift updates of the parameter space fits and switches between PN approximants among other features.

The updated calibration entails a significant improvement in the accuracy of the model. The match $\mathcal{M}$ is a quantity that measures how similar two waveforms are and it is

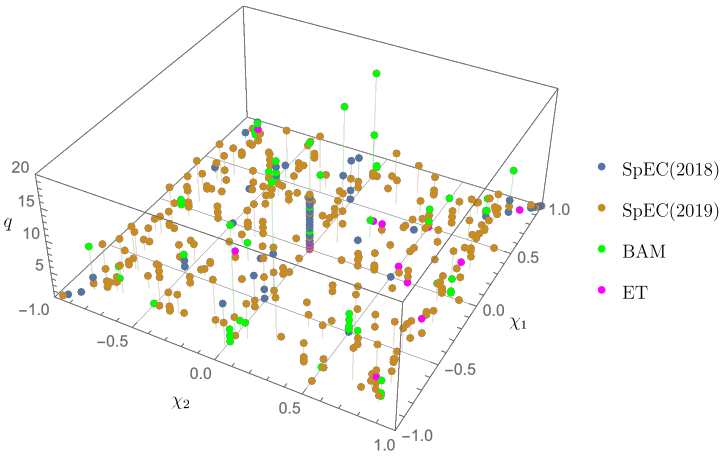

FIGURE 2.16: The mass ratio and spins for the NR waveforms used in the calibration of IMRPHENOMXAS. SXS simulations are shown in blue ([91]) and orange ([92]), BAM simulations in green and Einstein Toolkit simulations in pink. Image credits [50].

defined through the inner product of (2.17) although the integral's limits are now over a finite frequency range (f_{min}, f_{max}). The match is usually optimized over time and phase shifts between the two waveforms since these quantities do not affect the physics of the waveform

$$\mathcal{M} = \max_{t_0,\phi_0} \frac{(h_1|h_2)}{\sqrt{(h_1|h_1)}\sqrt{(h_2|h_2)}} \tag{2.62}$$

The mismatch is defined as $1 - \mathcal{M}$, the lower the mismatch, the more similar the two waveforms are. Mismatches of IMRPHENOMXAS and IMRPHENOMD against the hybrid waveforms used for the calibration are shown in Fig. 2.17. We see a dramatic decrease in the mismatch by 1 to 2 orders of magnitude across the parameter space. This figure presents mismatches against NRHYBSUR3DQ8 [93], the NR hybrid surrogate valid up to a mass ratio $q = 8$ and spins $\chi_{1,2} = \pm 0.8$. The matches are computed at random points in the parameter space, including points that are not used in the calibration to construct IMRPHENOMXAS. Here we see that IMRPHENOMXAS offers a significant improvement in accuracy in comparison to IMRPHENOMD or SEOBNRV4.

The improvement in accuracy is also transferred to PE studies. Fig. 2.18 presents several 1D posterior distributions of an injection with NRHybSur3dq8. IMRPHENOMXAS demonstrates excellent recovery of the injected parameters with significantly smaller biases and tighter posteriors than those exhibited by IMRPHENOMD.

In the subsequent part of this thesis, we use IMRPHENOMXAS as a cornerstone to build waveform models that include subdominant harmonics and precession effects. First, we present IMRPHENOMXHM which follows the strategy of calibrating the model to NR simulations and solves the inaccuracies of IMRPHENOMHM due to the usage of the approximate mapping, which breaks at high frequency, and allows for a description of the

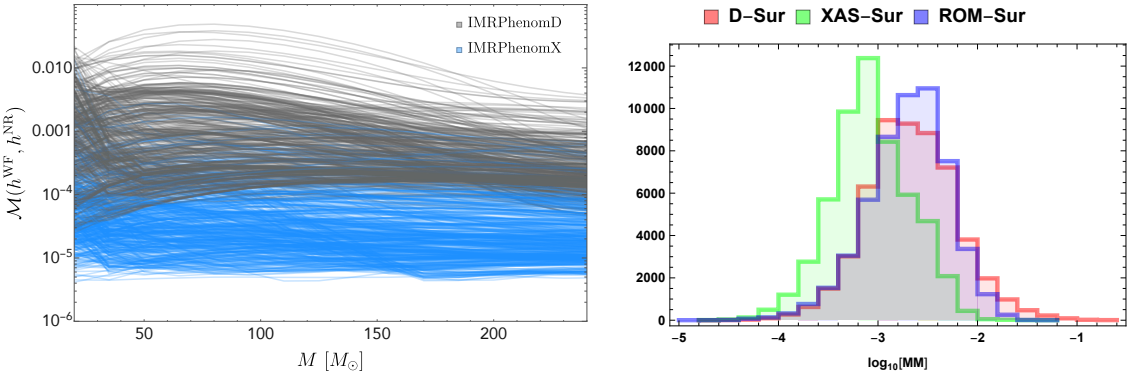

FIGURE 2.17: Left panel: Mismatches for IMRPHENOMXAS (blue) and IMRPHENOMD (grey) against all SXS NR hybrids. We use the Advanced LIGO design sensitivity PSD and a lower frequency cutoff of 20Hz. Right panel: Mismatches for IMRPHENOMXAS (green), IMRPHENOMD (red) and SEOBNRv4 (blue) against NRHybSur3dq8. Image credits: [50].

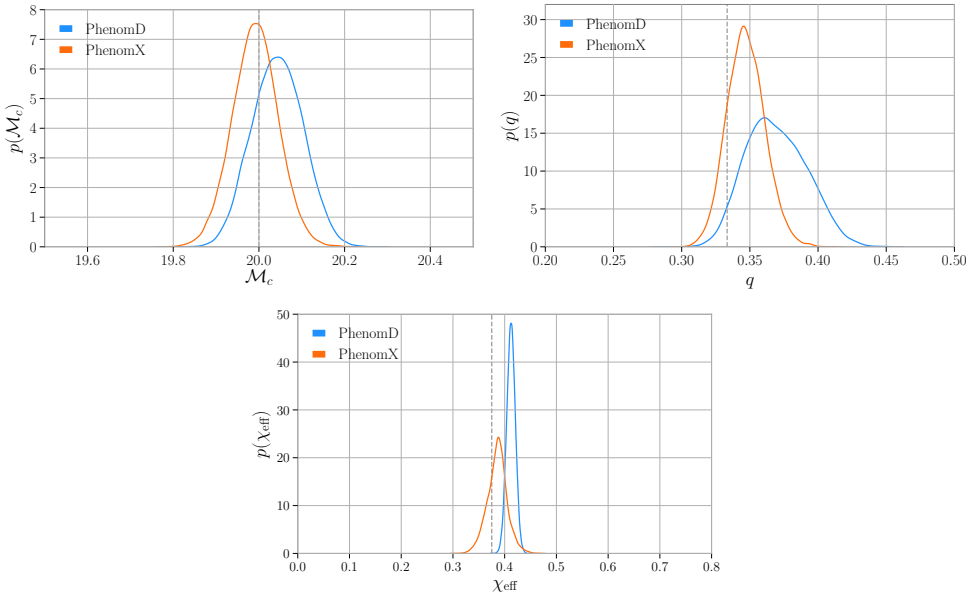

FIGURE 2.18: 1D posterior distributions for the chirp mass $\mathcal{M}_c$, mass ratio q and effective spin $\chi_{\rm eff}$ as recovered by IMRPHENOMXAS and IMRPHENOMD against an injected NRHybSur3dq8 waveform. The dashed line denotes the injected values. Image credits: [50].

mode-mixing present in the $(3, \pm 2)$ modes. IMRPHENOMXHM follows the same modular philosophy of IMRPHENOMXAS and besides permits to recover IMRPHENOMXAS when only the $(2, \pm 2)$ modes are activated. A derivation of how the multimode polarizations are computed in terms of the individual modes in the Fourier domain for IMRPHENOMXHM is presented in appendix A. Second, we apply the technique of multibanding to IMRPHENOMXHM, which introduces a significant improvement in the computational efficiency of the model, outperforming to the rest of the homologous models. Finally, we incorporate the effect of precession to IMRPHENOMXAS and IMRPHENOMXHM obtaining the precessing models IMRPHENOMXP and IMRPHENOMXPHM respectively.

The former is again attained as a subset of the version with higher modes IMRPhenomXPHM when only the $(2, \pm 2)$ modes, in this case in the co-precessing frame, are activated. An extension of the multibanding technique is incorporated into IMRPhenomXPHM, which demonstrates a significant improvement in performance respect to IMRPhenomPv3HM and the highest computationally efficiency of all the existing precessing models. All these characteristics provide the PhenomX family with the potential to become one of the main-stay models used in the analysis of every gravitational wave event for binary black holes, observed by the current LIGO and Virgo detectors, and any future GW detector to be built.

Bibliography

[1] P. Astone and et. al. Cumulative analysis of the association between the data of the gravitational wave detectors NAUTILUS and EXPLORER and the gamma ray bursts detected by BATSE and BeppoSAX. *Phys. Rev. D*, 71:042001, Feb 2005. doi: 10.1103/PhysRevD.71.042001. URL https://link.aps.org/doi/10.1103/PhysRevD.71.042001.

[2] Michael E. Tobar, Eugene N. Ivanov, and David G. Blair. Parametric transducers for the advanced cryogenic resonant-mass gravitational wave detectors. *General Relativity and Gravitation*, 32(9):1799–1821, Sep 2000. ISSN 1572-9532. doi: 10.1023/A:1001932614183. URL https://doi.org/10.1023/A:1001932614183.

[3] Odylio Denys Aguiar. Past, present and future of the resonant-mass gravitational wave detectors. *Research in Astronomy and Astrophysics*, 11(1):1–42, dec 2010. doi: 10.1088/1674-4527/11/1/001. URL https://doi.org/10.1088%2F1674-4527%2F11%2F1%2F001.

[4] V.D. Sandberg M. Zimmerman K.S. Thorne, C.M. Caves and R.W.P. Drever. *The quantum limit for gravitational wave detectors and methods of circumventing it in Sources of Gravitational Radiation*. Cambridge University Press, 1979.

[5] Warren G. Anderson Jolien D.E. Creighton. *Gravitational-Wave Physics and Astronomy*. WILEY-VCH, 2011.

[6] V. I. Pustovoit M. E. Gertsenshtein. On the detection of low frequency gravitational waves. *Journal of Experimental and Theoretical Physics*, 16:605, 1963.

[7] D. V. Martynov and et. al. Sensitivity of the Advanced LIGO detectors at the beginning of gravitational wave astronomy. *Phys. Rev. D*, 93:112004, Jun 2016. doi: 10.1103/PhysRevD.93.112004. URL https://link.aps.org/doi/10.1103/PhysRevD.93.112004.

[8] J. Abadie, et. al., and The LIGO Scientific Collaboration. A gravitational wave observatory operating beyond the quantum shot-noise limit. *Nature Physics*, 7(12): 962–965, 2011. ISSN 1745-2481. doi: 10.1038/nphys2083. URL https://doi.org/10.1038/nphys2083.

[9] J. Aasi and et. al. Enhanced sensitivity of the LIGO gravitational wave detector by using squeezed states of light. *Nature Photonics*, 7(8):613–619, 2013. ISSN 1749-4893. doi: 10.1038/nphoton.2013.177. URL https://doi.org/10.1038/nphoton.2013.177.

[10] Lead by Michele Punturo. Einstein gravitational wave Telescope. Conceptual Design Study., 2011. URL http://www.et-gw.eu/index.php/etdsdocument.

[11] David Reitze et al. Cosmic Explorer: The U.S. Contribution to Gravitational-Wave Astronomy beyond LIGO. *Bull. Am. Astron. Soc.*, 51:035, 2019.

[12] Denis Martynov, Haixing Miao, Huan Yang, Francisco Hernandez Vivanco, Eric Thrane, Rory Smith, Paul Lasky, William E. East, et al. Exploring the sensitivity of gravitational wave detectors to neutron star physics. *Phys. Rev. D*, 99:102004, May 2019. doi: 10.1103/PhysRevD.99.102004. URL https://link.aps.org/doi/10.1103/PhysRevD.99.102004.

[13] Lead by Karsten Danzmann. Laser Interferometer Space Antenna. A proposal in response to the ESA call for L3 mission concepts, 2017. URL https://www.elisascience.org/files/publications/LISA_L3_20170120.pdf.

[14] M. Armano and et. al. Beyond the Required LISA Free-Fall Performance: New LISA Pathfinder Results down to 20 μHz. *Phys. Rev. Lett.*, 120:061101, Feb 2018. doi: 10.1103/PhysRevLett.120.061101. URL https://link.aps.org/doi/10.1103/PhysRevLett.120.061101.

[15] Nils Andersson, John Baker, Krzystof Belczynski, Sebastiano Bernuzzi, Emanuele Berti, Laura Cadonati, Pablo Cerdá-Durán, James Clark, Marc Favata, et al. The transient gravitational-wave sky. *Classical and Quantum Gravity*, 30(19):193002, sep 2013. doi: 10.1088/0264-9381/30/19/193002. URL https://doi.org/10.1088%2F0264-9381%2F30%2F19%2F193002.

[16] E. T. Jaynes. *Probability Theory. The Logic of Science.* Cambridge University Press, 2003. ISBN 0521592712.

[17] R. J. Barlow. *Statistics. A Guide to the Use of Statistical Methods in the Physical Sciences.* John Wiley & Sons, 1989. ISBN 0471922943.

[18] D. S. Sivia. *Data Analysis. A bayesain tutorial.* Oxford University Press, 2006. ISBN 0198568322.

[19] Andrey Kolmogorov. *Foundations of the theory of probability.* Chelsea Publishing Company., 1933.

[20] M.N. Rosenbluth A.H. Teller N. Metropolis, A.W. Rosenbluth. Equation of state calculations by fast computing machines. *The Journal of Chemical Physics*, 21:1087, 1953.

[21] W. K. Hastings. Monte carlo sampling methods using markov chains and their applications. *Biometrika*, 57:97–109, 1970.

[22] J. Skilling. Nested sampling. *AIP Conference Proceedings*, 735:395, 2004.

[23] Andrew Gelman and Donald B. Rubin. Inference from iterative simulation using multiple sequences. *Statist. Sci.*, 7(4):457–472, 11 1992. doi: 10.1214/ss/1177011136. URL https://doi.org/10.1214/ss/1177011136.

[24] Stephen P. Brooks and Andrew Gelman. General methods for monitoring convergence of iterative simulations. *Journal of Computational and Graphical Statistics*, 7(4):434–455, 1998. doi: 10.1080/10618600.1998.10474787. URL https://www.tandfonline.com/doi/abs/10.1080/10618600.1998.10474787.

[25] Clifford M. Will and Alan G. Wiseman. Gravitational radiation from compact binary systems: Gravitational waveforms and energy loss to second post-newtonian order. *Physical Review D*, 54(8):4813–4848, Oct 1996. ISSN 1089-4918. doi: 10.1103/physrevd.54.4813. URL http://dx.doi.org/10.1103/PhysRevD.54.4813.

[26] Michael E. Pati and Clifford M. Will. Post-newtonian gravitational radiation and equations of motion via direct integration of the relaxed einstein equations: Foundations. *Physical Review D*, 62(12), Nov 2000. ISSN 1089-4918. doi: 10.1103/physrevd.62.124015. URL http://dx.doi.org/10.1103/PhysRevD.62.124015.

[27] Michael E. Pati and Clifford M. Will. Post-newtonian gravitational radiation and equations of motion via direct integration of the relaxed einstein equations. ii. two-body equations of motion to second post-newtonian order, and radiation reaction to 3.5 post-newtonian order. *Physical Review D*, 65(10), Apr 2002. ISSN 1089-4918. doi: 10.1103/physrevd.65.104008. URL http://dx.doi.org/10.1103/PhysRevD.65.104008.

[28] Luc Blanchet. Gravitational Radiation from Post-Newtonian Sources and Inspiralling Compact Binaries. *Living Reviews in Relativity*, 17(1):2, 2014. ISSN 1433-8351. URL https://doi.org/10.12942/lrr-2014-2.

[29] Michele Levi. Effective field theories of post-newtonian gravity: A comprehensive review, 2018.

[30] Gerhard Schäfer and Piotr Jaranowski. Hamiltonian formulation of general relativity and post-newtonian dynamics of compact binaries. *Living Reviews in Relativity*, 21 (1):7, Aug 2018. ISSN 1433-8351. doi: 10.1007/s41114-018-0016-5. URL https://doi.org/10.1007/s41114-018-0016-5.

[31] K. G. Arun, Alessandra Buonanno, Guillaume Faye, and Evan Ochsner. Higher-order spin effects in the amplitude and phase of gravitational waveforms emitted by inspiraling compact binaries: Ready-to-use gravitational waveforms. *Phys. Rev. D*, 79:104023, May 2009. doi: 10.1103/PhysRevD.79.104023. URL https://link.aps.org/doi/10.1103/PhysRevD.79.104023.

[32] Alessandra Buonanno, Guillaume Faye, and Tanja Hinderer. Spin effects on gravitational waves from inspiraling compact binaries at second post-newtonian order. *Phys. Rev. D*, 87:044009, Feb 2013. doi: 10.1103/PhysRevD.87.044009. URL https://link.aps.org/doi/10.1103/PhysRevD.87.044009.

[33] Alessandra Buonanno, Bala R. Iyer, Evan Ochsner, Yi Pan, and B. S. Sathyaprakash. Comparison of post-newtonian templates for compact binary inspiral signals in gravitational-wave detectors. *Phys. Rev. D*, 80:084043, Oct 2009. doi: 10.1103/PhysRevD.80.084043. URL https://link.aps.org/doi/10.1103/PhysRevD.80.084043.

[34] A. Buonanno and T. Damour. Effective one-body approach to general relativistic two-body dynamics. *Phys. Rev. D*, 59:084006, Mar 1999. doi: 10.1103/PhysRevD.59.084006. URL https://link.aps.org/doi/10.1103/PhysRevD.59.084006.

[35] Alessandra Buonanno and Thibault Damour. Transition from inspiral to plunge in binary black hole coalescences. *Phys. Rev. D*, 62:064015, Aug 2000. doi: 10.1103/PhysRevD.62.064015. URL https://link.aps.org/doi/10.1103/PhysRevD.62.064015.

[36] Thibault Damour, Piotr Jaranowski, and Gerhard Schäfer. Determination of the last stable orbit for circular general relativistic binaries at the third post-newtonian approximation. *Phys. Rev. D*, 62:084011, Sep 2000. doi: 10.1103/PhysRevD.62.084011. URL https://link.aps.org/doi/10.1103/PhysRevD.62.084011.

[37] Thibault Damour. Coalescence of two spinning black holes: An effective one-body approach. *Phys. Rev. D*, 64:124013, Nov 2001. doi: 10.1103/PhysRevD.64.124013. URL https://link.aps.org/doi/10.1103/PhysRevD.64.124013.

[38] Alessandra Buonanno, Yanbei Chen, and Thibault Damour. Transition from inspiral to plunge in precessing binaries of spinning black holes. *Phys. Rev. D*, 74:104005, Nov 2006. doi: 10.1103/PhysRevD.74.104005. URL https://link.aps.org/doi/10.1103/PhysRevD.74.104005.

[39] Alejandro Bohé, Lijing Shao, Andrea Taracchini, Alessandra Buonanno, Stanislav Babak, Ian W. Harry, Ian Hinder, Serguei Ossokine, Michael Pürrer, Vivien Raymond, Tony Chu, Heather Fong, Prayush Kumar, Harald P. Pfeiffer, Michael Boyle, Daniel A. Hemberger, Lawrence E. Kidder, Geoffrey Lovelace, Mark A. Scheel, and Béla Szilágyi. Improved effective-one-body model of spinning, nonprecessing binary black holes for the era of gravitational-wave astrophysics with advanced detectors. *Phys. Rev. D*, 95:044028, Feb 2017. doi: 10.1103/PhysRevD.95.044028. URL https://link.aps.org/doi/10.1103/PhysRevD.95.044028.

[40] Roberto Cotesta, Alessandra Buonanno, Alejandro Bohé, Andrea Taracchini, Ian Hinder, and Serguei Ossokine. Enriching the symphony of gravitational waves from binary black holes by tuning higher harmonics. *Phys. Rev. D*, 98:084028, Oct 2018. doi: 10.1103/PhysRevD.98.084028. URL https://link.aps.org/doi/10.1103/PhysRevD.98.084028.

[41] Zhoujian Cao and Wen-Biao Han. Waveform model for an eccentric binary black hole based on the effective-one-body-numerical-relativity formalism. *Phys. Rev. D*, 96:044028, Aug 2017. doi: 10.1103/PhysRevD.96.044028. URL https://link.aps.org/doi/10.1103/PhysRevD.96.044028.

[42] Michael Pürrer. Frequency domain reduced order model of aligned-spin effective-one-body waveforms with generic mass ratios and spins. *Phys. Rev. D*, 93:064041, Mar 2016. doi: 10.1103/PhysRevD.93.064041. URL https://link.aps.org/doi/10.1103/PhysRevD.93.064041.

[43] Roberto Cotesta, Sylvain Marsat, and Michael Pürrer. Frequency domain reduced order model of aligned-spin effective-one-body waveforms with higher-order modes, 2020.

[44] P. Ajith, M. Hannam, S. Husa, Y. Chen, B. Brügmann, N. Dorband, D. Müller, F. Ohme, D. Pollney, C. Reisswig, L. Santamaría, and J. Seiler. Inspiral-Merger-Ringdown Waveforms for Black-Hole Binaries with Nonprecessing Spins. *Phys. Rev. Lett.*, 106:241101, Jun 2011. doi: 10.1103/PhysRevLett.106.241101. URL https://link.aps.org/doi/10.1103/PhysRevLett.106.241101.

[45] P Ajith, S Babak, Y Chen, M Hewitson, B Krishnan, J T Whelan, B Brügmann, P Diener, J Gonzalez, M Hannam, S Husa, M Koppitz, D Pollney, L Rezzolla,

L Santamaría, A M Sintes, U Sperhake, and J Thornburg. A phenomenological template family for black-hole coalescence waveforms. *Classical and Quantum Gravity*, 24(19):S689–S699, sep 2007. doi: 10.1088/0264-9381/24/19/s31. URL https://doi.org/10.1088%2F0264-9381%2F24%2F19%2Fs31.

[46] P. Ajith, S. Babak, Y. Chen, M. Hewitson, B. Krishnan, A. M. Sintes, J. T. Whelan, B. Brügmann, P. Diener, N. Dorband, J. Gonzalez, M. Hannam, S. Husa, D. Pollney, L. Rezzolla, L. Santamaría, U. Sperhake, and J. Thornburg. Erratum: Template bank for gravitational waveforms from coalescing binary black holes: Nonspinning binaries [Phys. Rev. DPRVDAQ1550-7998 77, 104017 (2008)]. *Phys. Rev. D*, 79: 129901, Jun 2009. doi: 10.1103/PhysRevD.79.129901. URL https://link.aps.org/doi/10.1103/PhysRevD.79.129901.

[47] L. Santamaría, F. Ohme, P. Ajith, B. Brügmann, N. Dorband, M. Hannam, S. Husa, P. Mösta, D. Pollney, C. Reisswig, E. L. Robinson, J. Seiler, and B. Krishnan. Matching post-Newtonian and numerical relativity waveforms: Systematic errors and a new phenomenological model for nonprecessing black hole binaries. *Phys. Rev. D*, 82:064016, Sep 2010. doi: 10.1103/PhysRevD.82.064016. URL https://link.aps.org/doi/10.1103/PhysRevD.82.064016.

[48] Xisco Jiménez-Forteza, David Keitel, Sascha Husa, Mark Hannam, Sebastian Khan, and Michael Pürrer. Hierarchical data-driven approach to fitting numerical relativity data for nonprecessing binary black holes with an application to final spin and radiated energy. *Phys. Rev. D*, 95:064024, Mar 2017. doi: 10.1103/PhysRevD.95.064024. URL https://link.aps.org/doi/10.1103/PhysRevD.95.064024.

[49] Sebastian Khan, Sascha Husa, Mark Hannam, Frank Ohme, Michael Pürrer, Xisco Jiménez Forteza, and Alejandro Bohé. Frequency-domain gravitational waves from nonprecessing black-hole binaries. II. A phenomenological model for the advanced detector era. *Phys. Rev. D*, 93:044007, Feb 2016. doi: 10.1103/PhysRevD.93.044007. URL https://link.aps.org/doi/10.1103/PhysRevD.93.044007.

[50] Geraint Pratten, Sascha Husa, Cecilio García-Quirós, Marta Colleoni, Antoni Ramos-Buades, Héctor Estellés, and Rafel Jaume. Setting the cornerstone for the IMRPhenomX family of models for gravitational waves from compact binaries: The dominant harmonic for non-precessing quasi-circular black holes. *ArXiv:2001.11412*, 2020.

[51] Lionel London, Sebastian Khan, Edward Fauchon-Jones, Cecilio García, Mark Hannam, Sascha Husa, Xisco Jiménez-Forteza, Chinmay Kalaghatgi, Frank Ohme, and Francesco Pannarale. First Higher-Multipole Model of Gravitational Waves from Spinning and Coalescing Black-Hole Binaries. *Phys. Rev. Lett.*, 120:161102, Apr

2018. doi: 10.1103/PhysRevLett.120.161102. URL https://link.aps.org/doi/10.1103/PhysRevLett.120.161102.

[52] Cecilio García-Quirós, Marta Colleoni, Sascha Husa, Héctor Estellés, Geraint Pratten, Antoni Ramos-Buades, Maite Mateu-Lucena, and Rafel Jaume. IMRPhenomXHM: A multi-mode frequency-domain model for the gravitational wave signal from non-precessing black-hole binaries, 2020.

[53] Mark Hannam, Patricia Schmidt, Alejandro Bohé, Leïla Haegel, Sascha Husa, Frank Ohme, Geraint Pratten, and Michael Pürrer. Simple model of complete precessing black-hole-binary gravitational waveforms. *Phys. Rev. Lett.*, 113:151101, Oct 2014. doi: 10.1103/PhysRevLett.113.151101. URL https://link.aps.org/doi/10.1103/PhysRevLett.113.151101.

[54] Sebastian Khan, Frank Ohme, Katerina Chatziioannou, and Mark Hannam. Including higher order multipoles in gravitational-wave models for precessing binary black holes. *Phys. Rev. D*, 101:024056, Jan 2020. doi: 10.1103/PhysRevD.101.024056. URL https://link.aps.org/doi/10.1103/PhysRevD.101.024056.

[55] Geraint Pratten, Cecilio García-Quirós, Marta Colleoni, Antoni Ramos-Buades, Héctor Estellés, Maite Mateu-Lucena, Rafel Jaume, Maria Haney, David Keitel, Jonathan E. Thompson, and Sascha Husa. Let's twist again: computationally efficient models for the dominant and sub-dominant harmonic modes of precessing binary black holes. *ArXiv: 2004.06503*, 2020.

[56] Tim Dietrich, Sebastian Khan, Reetika Dudi, Shasvath J. Kapadia, Prayush Kumar, Alessandro Nagar, Frank Ohme, et al. Matter imprints in waveform models for neutron star binaries: Tidal and self-spin effects. *Phys. Rev. D*, 99:024029, Jan 2019. doi: 10.1103/PhysRevD.99.024029. URL https://link.aps.org/doi/10.1103/PhysRevD.99.024029.

[57] Jonathan E. Thompson, Edward Fauchon-Jones, Sebastian Khan, Elisa Nitoglia, Francesco Pannarale, Tim Dietrich, and Mark Hannam. Modeling the gravitational wave signature of neutron star black hole coalescences: PhenomNSBH, 2020.

[58] Dieter R. Brill and Richard W. Lindquist. Interaction energy in geometrostatics. *Phys. Rev.*, 131:471–476, Jul 1963. doi: 10.1103/PhysRev.131.471. URL https://link.aps.org/doi/10.1103/PhysRev.131.471.

[59] Susan G Hahn and Richard W Lindquist. The two-body problem in geometrodynamics. *Annals of Physics*, 29(2):304 – 331, 1964. ISSN 0003-4916. doi: https://doi.org/10.1016/0003-4916(64)90223-4. URL http://www.sciencedirect.com/science/article/pii/0003491664902234.

[60] Larry Smarr. *The Structure of General Relativity with a Numerical Example.* PhD thesis, University of Texas, Austin, 1975.

[61] Larry Smarr. Space-times generated by computers: Black holes with gravitational radiation*. *Annals of the New York Academy of Sciences*, 302(1):569–604, 1977. doi: 10.1111/j.1749-6632.1977.tb37076.x. URL https://nyaspubs.onlinelibrary.wiley.com/doi/abs/10.1111/j.1749-6632.1977.tb37076.x.

[62] Douglas M. Eardley and Larry Smarr. Time functions in numerical relativity: Marginally bound dust collapse. *Phys. Rev. D*, 19:2239–2259, Apr 1979. doi: 10.1103/PhysRevD.19.2239. URL https://link.aps.org/doi/10.1103/PhysRevD.19.2239.

[63] Peter Anninos, David Hobill, Edward Seidel, Larry Smarr, and Wai-Mo Suen. Collision of two black holes. *Phys. Rev. Lett.*, 71:2851–2854, Nov 1993. doi: 10.1103/PhysRevLett.71.2851. URL https://link.aps.org/doi/10.1103/PhysRevLett.71.2851.

[64] Peter Anninos, Joan Massó, Edward Seidel, Wai-Mo Suen, and John Towns. Three-dimensional numerical relativity: The evolution of black holes. *Phys. Rev. D*, 52:2059–2082, Aug 1995. doi: 10.1103/PhysRevD.52.2059. URL https://link.aps.org/doi/10.1103/PhysRevD.52.2059.

[65] Frans Pretorius. Evolution of Binary Black-Hole Spacetimes. *Phys. Rev. Lett.*, 95:121101, Sep 2005. doi: 10.1103/PhysRevLett.95.121101. URL https://link.aps.org/doi/10.1103/PhysRevLett.95.121101.

[66] John G. Baker, Joan Centrella, Dae-Il Choi, Michael Koppitz, James R. van Meter, and M. Coleman Miller. Getting a Kick Out of Numerical Relativity. *The Astrophysical Journal*, 653(2):L93–L96, dec 2006. doi: 10.1086/510448. URL https://doi.org/10.1086%2F510448.

[67] M. Campanelli, C. O. Lousto, P. Marronetti, and Y. Zlochower. Accurate Evolutions of Orbiting Black-Hole Binaries without Excision. *Phys. Rev. Lett.*, 96:111101, Mar 2006. doi: 10.1103/PhysRevLett.96.111101. URL https://link.aps.org/doi/10.1103/PhysRevLett.96.111101.

[68] Richard Arnowitt, Stanley Deser, and Charles W. Misner. Republication of: The dynamics of general relativity. *General Relativity and Gravitation*, 40(9):1997–2027, 2008. ISSN 1572-9532. doi: 10.1007/s10714-008-0661-1. URL https://doi.org/10.1007/s10714-008-0661-1.

[69] Georges Darmois. *Les équations de la gravitation einsteinienne*. Number 25 in Mémorial des sciences mathématiques. Gauthier-Villars, 1927. URL http://www.numdam.org/item/MSM_1927__25__1_0.

[70] André Lichnerowicz. L'intégration des équations de la gravitation relativiste et le problème des n corps. *Journal de Mathématiques pures et appliquées*, 23:37–63, 1944.

[71] James W. York. *Kinematics and dynamics of general relativity in Sources of Gravitational Radiation*. Cambridge University Press, 1979.

[72] Masaru Shibata and Takashi Nakamura. Evolution of three-dimensional gravitational waves: Harmonic slicing case. *Phys. Rev. D*, 52:5428–5444, Nov 1995. doi: 10.1103/PhysRevD.52.5428. URL https://link.aps.org/doi/10.1103/PhysRevD.52.5428.

[73] Thomas W. Baumgarte and Stuart L. Shapiro. Numerical integration of einstein's field equations. *Phys. Rev. D*, 59:024007, Dec 1998. doi: 10.1103/PhysRevD.59.024007. URL https://link.aps.org/doi/10.1103/PhysRevD.59.024007.

[74] C. Bona, T. Ledvinka, C. Palenzuela, and M. Žáček. General-covariant evolution formalism for numerical relativity. *Phys. Rev. D*, 67:104005, May 2003. doi: 10.1103/PhysRevD.67.104005. URL https://link.aps.org/doi/10.1103/PhysRevD.67.104005.

[75] Carsten Gundlach, Gioel Calabrese, Ian Hinder, and José M Martín-García. Constraint damping in the z4 formulation and harmonic gauge. *Classical and Quantum Gravity*, 22(17):3767–3773, aug 2005. doi: 10.1088/0264-9381/22/17/025. URL https://doi.org/10.1088%2F0264-9381%2F22%2F17%2F025.

[76] Sebastiano Bernuzzi and David Hilditch. Constraint violation in free evolution schemes: Comparing the bssnok formulation with a conformal decomposition of the z4 formulation. *Phys. Rev. D*, 81:084003, Apr 2010. doi: 10.1103/PhysRevD.81.084003. URL https://link.aps.org/doi/10.1103/PhysRevD.81.084003.

[77] Daniela Alic, Carles Bona-Casas, Carles Bona, Luciano Rezzolla, and Carlos Palenzuela. Conformal and covariant formulation of the z4 system with constraint-violation damping. *Phys. Rev. D*, 85:064040, Mar 2012. doi: 10.1103/PhysRevD.85.064040. URL https://link.aps.org/doi/10.1103/PhysRevD.85.064040.

[78] Isabel Cordero-Carrión, Pablo Cerdá-Durán, and José María Ibáñez. Dynamical spacetimes and gravitational radiation in a fully constrained formulation. *Journal of Physics: Conference Series*, 228:012055, may 2010. doi: 10.1088/1742-6596/228/1/012055. URL https://doi.org/10.1088%2F1742-6596%2F228%2F1%2F012055.

[79] Silvano Bonazzola, Eric Gourgoulhon, Philippe Grandclément, and Jérôme Novak. Constrained scheme for the einstein equations based on the dirac gauge and spherical coordinates. *Phys. Rev. D*, 70:104007, Nov 2004. doi: 10.1103/PhysRevD.70.104007. URL https://link.aps.org/doi/10.1103/PhysRevD.70.104007.

[80] Bernd Brügmann, José A. González, Mark Hannam, Sascha Husa, Ulrich Sperhake, and Wolfgang Tichy. Calibration of moving puncture simulations. *Phys. Rev. D*, 77:024027, Jan 2008. doi: 10.1103/PhysRevD.77.024027. URL https://link.aps.org/doi/10.1103/PhysRevD.77.024027.

[81] Stuart L. Shapiro Thomas W. Baumgarte. *Numerical Relativity. Solving Einstein's Equations on the Computer*. Cambridge, 2010.

[82] C. Bona, J. Massó, E. Seidel, and J. Stela. First order hyperbolic formalism for numerical relativity. *Phys. Rev. D*, 56:3405–3415, Sep 1997. doi: 10.1103/PhysRevD.56.3405. URL https://link.aps.org/doi/10.1103/PhysRevD.56.3405.

[83] A. Arbona, C. Bona, J. Massó, and J. Stela. Robust evolution system for numerical relativity. *Phys. Rev. D*, 60:104014, Oct 1999. doi: 10.1103/PhysRevD.60.104014. URL https://link.aps.org/doi/10.1103/PhysRevD.60.104014.

[84] Miguel Alcubierre, Bernd Brügmann, Peter Diener, Michael Koppitz, Denis Pollney, Edward Seidel, and Ryoji Takahashi. Gauge conditions for long-term numerical black hole evolutions without excision. *Phys. Rev. D*, 67:084023, Apr 2003. doi: 10.1103/PhysRevD.67.084023. URL https://link.aps.org/doi/10.1103/PhysRevD.67.084023.

[85] Miguel Alcubierre, Bernd Brügmann, Peter Diener, Michael Koppitz, Denis Pollney, Edward Seidel, and Ryoji Takahashi. Gauge conditions for long-term numerical black hole evolutions without excision. *Phys. Rev. D*, 67:084023, Apr 2003. doi: 10.1103/PhysRevD.67.084023. URL https://link.aps.org/doi/10.1103/PhysRevD.67.084023.

[86] Vijay Varma and Parameswaran Ajith. Effects of nonquadrupole modes in the detection and parameter estimation of black hole binaries with nonprecessing spins. *Phys. Rev. D*, 96:124024, Dec 2017. doi: 10.1103/PhysRevD.96.124024. URL https://link.aps.org/doi/10.1103/PhysRevD.96.124024.

[87] Juan Calderón Bustillo, Sascha Husa, Alicia M. Sintes, and Michael Pürrer. Impact of gravitational radiation higher order modes on single aligned-spin gravitational wave searches for binary black holes. *Phys. Rev. D*, 93:084019, Apr 2016. doi: 10.1103/PhysRevD.93.084019. URL https://link.aps.org/doi/10.1103/PhysRevD.93.084019.

[88] The LIGO Scientific Collaboration and the Virgo Collaboration. GW190412: Observation of a Binary-Black-Hole Coalescence with Asymmetric Masses. *ArXiv: 2004.08342*, 2020.

[89] B P Abbott et. al. Effects of waveform model systematics on the interpretation of GW150914. *Classical and Quantum Gravity*, 34(10):104002, apr 2017. doi: 10.1088/1361-6382/aa6854. URL https://doi.org/10.1088%2F1361-6382%2Faa6854.

[90] LIGO Scientific Collaboration. LIGO Algorithm Library - LALSuite. free software (GPL), 2018.

[91] Abdul H. Mroué, Mark A. Scheel, Bela Szilagyi, Harald P. Pfeiffer, Michael Boyle, et al. A catalog of 174 binary black-hole simulations for gravitational-wave astronomy. *Phys.Rev.Lett.*, 111:241104, 2013. doi: 10.1103/PhysRevLett.111.241104.

[92] Michael Boyle et al. The SXS Collaboration catalog of binary black hole simulations. *Class. Quant. Grav.*, 36(19):195006, 2019. doi: 10.1088/1361-6382/ab34e2.

[93] Vijay Varma, Scott E. Field, Mark A. Scheel, Jonathan Blackman, Lawrence E. Kidder, and Harald P. Pfeiffer. Surrogate model of hybridized numerical relativity binary black hole waveforms. *Physical Review D*, 99(6), Mar 2019. ISSN 2470-0029. doi: 10.1103/physrevd.99.064045. URL http://dx.doi.org/10.1103/PhysRevD.99.064045.

Part II

Original scientific results

Chapter 3

Modelling subdominant harmonics from non-precessing black-hole binaries: IMRPhenomXHM

This chapter presents the article:

- *IMRPhenomXHM: A multi-mode frequency-domain model for the gravitational wave signal from non-precessing black-hole binaries.* Cecilio García-Quirós, Marta Colleoni, Sascha Husa, Héctor Estellés, Geraint Pratten, Antoni Ramos-Buades, Maite Mateu-Lucena, Rafel Jaume. arXiv:2001.10914 [gr-qc] (2020),

which has been also submitted for peer review to Physical Review D.

Abstract

We present the IMRPhenomXHM frequency domain phenomenological waveform model for the inspiral, merger and ringdown of quasi-circular non-precessing black hole binaries. The model extends the IMRPhenomXAS waveform model [1], which describes the dominant quadrupole modes $\ell = |m| = 2$, to the harmonics $(\ell, |m|) = (2, 1), (3, 3), (3, 2), (4, 4)$, and includes mode mixing effects for the $(3, 2)$ spherical harmonic. IMRPhenomXHM is calibrated against hybrid waveforms, which match an inspiral phase described by the EOB model and PN amplitudes for the subdominant harmonics to NR waveforms and numerical solutions to the perturbative Teukolsky equation for large mass ratios up to 1000. A computationally efficient implementation of the model is available as part of the LSC Algorithm Library Suite [2].

3.1 Introduction

Frequency domain phenomenological waveform models for compact binary coalescence, such as [3–6] have become a standard tool for gravitational wave data analysis [7, 8]. These models describe the amplitude and phase of spherical harmonic modes in terms of piecewise closed-form expressions. The low computational cost to evaluate these models makes them particularly valuable for applications in Bayesian inference [9, 10], which typically requires millions of waveform evaluations to accurately determine the posterior distribution of the source properties measured in observations, such as the mass, arrival time, or sky location.

Until recently the modelling of the gravitational wave signal from such systems, and consequently gravitational wave data analysis, have focused on the dominant $\ell = |m| = 2$ harmonics. For high masses or high mass ratios this leads however to a significant loss of detection rate [11–13], systematic bias in the source parameters (see e.g. [14, 11, 15–18]), and implies a degeneracy between distance and inclination of the binary system. As the sensitivity of gravitational wave detectors increases, accurate and computationally efficient waveform models that include subdominant harmonics are required in order to not limit the scientific scope of gravitational wave astronomy.

Recently both time domain and frequency domain IMR models have been extended to sub-dominant spherical harmonics, i.e. modes other than the $(2, \pm 2)$ modes: In the time domain this has been done in the context of the EOB approach [19], however, EOB models are computationally expensive and usually a ROM model is constructed to accelerate evaluation [20, 21] (see however [22] for an analytical method to accelerate the inspiral). Furthermore, the NRHybSur3dq8 surrogate model [23] has been directly built from hybrid waveforms, but is restricted to mass ratios up to eight. For a precessing surrogate model, calibrated to NR waveforms, see [24]. Fast frequency domain models have previously been developed for the non-spinning sub-space [25, 26], and for spinning black holes through an approximate map from the $(2, 2)$ harmonic to general harmonics as described in [6], which presented the IMRPhenomHM model, which is publicly available as part of the LIGO Algorithm Library Suite (LALSuite) [2]. This approximate map is based on the approximate scaling behaviour of the subdominant harmonics with respect to the $(2, 2)$ mode, the IMRPhenomHM model is thus only calibrated to numerical data for the $(2, 2)$ mode. This information from numerical waveforms enters through the IMRPhenomD model, which is calibrated to NR waveforms up to mass ratio $q = 18$.

Here we present the first frequency domain model for the inspiral, merger and ringdown of spinning black hole binaries, which calibrates subdominant harmonics to a set of numerical waveforms for spinning black holes, instead of using an approximate map as

IMRPhenomHM. For the $(2, \pm 2)$ modes the model is identical to IMRPhenomXAS [1], which presents a thorough update of the IMRPhenomD model, extends it to extreme mass ratios, drops the approximation of reducing the two spin parameters of the black holes to effective spin parameters, and replaces ad-hoc fitting procedures by the hierarchical method presented in [27].

Our modelling approach largely follows our work on IMRPhenomXAS, with some adaptions to the phenomenology of subdominant modes, as first summarized in Sec. 3.2. As for IMRPhenomXAS we construct closed-form expressions for the amplitude and phase of each spherical harmonic mode in three frequency regimes, which correspond to the inspiral, ringdown, and an intermediate regime. In the inspiral and ringdown the model can be based on the perturbative frameworks of PN theory [28] and black hole perturbation theory [29]. The intermediate regime, which models the highly dynamical and strong field transition between the physics of the inspiral and ringdown still eludes a perturbative treatment. An essential goal of frequency domain phenomenological waveform models is computational efficiency. To this end, an accompanying paper [30] presents techniques to further accelerate the model evaluation following [31].

We model the complete observable signal, from the inspiral phase to the merger and ringdown to the remnant Kerr black hole, but we restrict our work to the quasi-circular (i.e. non-eccentric) and non-precessing part of the parameter space of astrophysical black hole binaries in general relativity, which is 3D and given by mass ratio $q = m_1/m_2 \geq 1$ and the dimensionless spin components χ_i of the two black holes which are orthogonal to the preserved orbital plane,

$$\chi_i = \frac{\vec{S}_i \cdot \vec{L}}{m_i^2 \, |\vec{L}|}, \tag{3.1}$$

where $\vec{S}_{1,2}$ are the spins (intrinsic angular momenta) of the two individual black holes, $\vec{L}$ is the orbital angular momentum, and $m_{1,2}$ are the masses of the two black holes. We also define the total mass $M = m_1 + m_2$, and the symmetric mass ratio $\eta = m_1 m_2 / M^2$. An approximate map from the non-precessing to the precessing parameter space [32, 4, 33] can then be used to extend the model to include the leading precession effects.

The paper is organized as follows. In Sec. 3.2 we collect some preliminaries: our conventions, notes on waveform phenomenology which motivate our modelling approach, and a brief description of our plan of fitting numerical data. In Sec. 3.3 we briefly describe our input data set of hybrid waveforms, and the underlying NR and perturbative Teukolsky waveforms. The construction of our model is discussed in Secs. 3.4-3.6 for the inspiral, intermediate region, and ringdown respectively. The accuracy of the model is evaluated in Sec. 3.7, and we conclude with a summary and discussion in Sec. 3.8. Appendix 3.A discusses the conversion from spheroidal to spherical-harmonic modes. In appendix 3.B

we describe our method to test tetrad conventions in multi-mode waveforms. Some technical details of our LALSuite [2] implementation are presented in appendix 3.C. Details regarding the rescaling of the inspiral phase are presented in appendix 3.D, and appendix 3.E summarizes PN results on the Fourier domain amplitude.

3.2 Preliminaries

3.2.1 Conventions

Our waveform conventions are consistent with those chosen for the IMRPhenomXAS model in [1] and our catalogue of multi-mode hybrid waveforms [34], which we introduce in Sec. 3.3. We use a standard spherical coordinate system (r, θ, ϕ) and spherical harmonics $Y^{-2}_{\ell m}$ of spin-weight -2 (see e.g. [35]). The black holes orbit in the plane $\theta = \pi/2$. Due to the absence of spin-precession the spacetime geometry exhibits equatorial symmetry, i.e. the northern hemisphere $\theta < \pi/2$ is isometric to the southern hemisphere $\theta > \pi/2$, and in consequence the same holds for the gravitational-wave signal.

The gravitational-wave strain h depends on an inertial time coordinate t, the angles θ, ϕ in the sky of the source, and the source parameters (η, χ_1, χ_2). We can write the strain in terms of the polarizations as $h = h_+(t, \theta, \varphi) - i\, h_\times\,(t, \theta, \varphi)$, or decompose it into spherical harmonic modes $h_{\ell m}$ as

$$h(t, \theta, \varphi) = \sum_{\ell=2, m=-\ell}^{4, \ell} h_{\ell m}\,(t)\ {}_{-2}Y_{\ell m}(\theta, \varphi). \tag{3.2}$$

The split into polarizations (i.e. into the real and imaginary parts of the time domain complex gravitational wave strain) is ambiguous due to the freedom to perform tetrad rotations, which corresponds to the freedom to choose an arbitrary overall phase factor. As discussed in detail in [36, 34] and in appendix 3.B, only two inequivalent choices are consistent with equatorial symmetry, and for simplicity we adopt the convention that for large separations (i.e. at low frequency) the time domain phases satisfy

$$\Phi_{\ell m} \approx \frac{m}{2}\Phi_{22}. \tag{3.3}$$

This differs from the convention of Blanchet et al. [37] by overall factors of $(-1)(-\imath)^m$ in front of the $h_{\ell m}$ modes. In appendix 3.B we discuss how to test a given waveform model for the tetrad convention that is used.

The equatorial symmetry of non-precessing binaries implies

$$h_{\ell m}(t) = (-1)^{\ell} h^*_{\ell -m}(t), \tag{3.4}$$

it is thus sufficient to model just one spherical harmonic for each value of $|m|$.

We adopt the conventions of the LIGO Algorithms Library [2] for the Fourier transform,

$$\tilde{h}(f) = \int_{-\infty}^{\infty} h(t)\, e^{-i\, 2\pi f t}\, dt. \tag{3.5}$$

With these conventions the time domain relations between modes (3.4) that express equatorial symmetry can be converted to the Fourier domain, where they read

$$\tilde{h}_{\ell m}(f) = (-1)^{\ell} \tilde{h}^*_{\ell -m}(-f). \tag{3.6}$$

The definitions above then also imply that $\tilde{h}_{\ell m}(f)$ (with $m > 0$) is concentrated in the negative frequency domain and $\tilde{h}_{\ell -m}(f)$ in the positive frequency domain. For the inspiral, this can be checked against the stationary phase approximation (SPA), see e.g. [38].

As we construct our model in the frequency domain, it is convenient to model $\tilde{h}_{\ell -m}$, which is non-zero for positive frequencies. The mode $\tilde{h}_{\ell m}$, defined for negative frequencies, can then be computed from (3.6). We model the Fourier amplitudes $A_{\ell m}(f > 0)$, which are non-negative functions for positive frequencies, and zero otherwise, and the Fourier domain phases $\Phi_{\ell m}(f > 0)$, defined by

$$\tilde{h}_{\ell -m}(f) = A_{\ell m}(f)\, e^{-i \Phi_{\ell m}(f)}. \tag{3.7}$$

The contribution to the gravitational wave polarizations of *both* positive and negative modes and for positive frequencies is then given by

$$\tilde{h}_{+}(f) = \frac{1}{2} \left(Y_{\ell -m} + (-1)^{\ell} Y^*_{\ell m} \right) \tilde{h}_{\ell -m}(f), \tag{3.8}$$

$$\tilde{h}_{\times}(f) = \frac{i}{2} \left(Y_{\ell -m} - (-1)^{\ell} Y^*_{\ell m} \right) \tilde{h}_{\ell -m}(f). \tag{3.9}$$

If we are only interested in the contribution of just one mode for positive frequencies then the polarizations read as:

$$\tilde{h}^{\ell,m}_{+}(f) = \frac{1}{2} (-1)^{\ell} Y^*_{\ell m} \tilde{h}_{\ell -m}(f), \tag{3.10}$$

$$\tilde{h}^{\ell,m}_{\times}(f) = -\frac{i}{2} (-1)^{\ell} Y^*_{\ell m} \tilde{h}_{\ell -m}(f), \tag{3.11}$$

$$\tilde{h}_{+}^{l,-m}(f) = \frac{1}{2} Y_{\ell -m} \tilde{h}_{\ell -m}(f), \tag{3.12}$$

$$\tilde{h}_{\times}^{l,-m}(f) = \frac{i}{2} Y_{\ell -m} \tilde{h}_{\ell -m}(f). \tag{3.13}$$

For the $\ell = 2, \pm 2$ modes these equations correspond to our IMRPhenomXAS model [1].

In appendix 3.C we discuss conventions which are specific to our LALSuite implementation, in particular how to specify a global rotation, and the time of coalescence.

3.2.2 Perturbative waveform phenomenology: inspiral and ringdown

The phenomenology of the oscillating subdominant modes $|m| > 0$ is largely similar to the dominant modes $\ell = |m| = 2$, which has been discussed in detail in [39, 1] - with some important exceptions that lead to both simplifications and complications when modelling these modes, as opposed to modelling $\ell = |m| = 2$.

The main simplification is that at low frequencies PN theory, combined with the stationary phase approximation, predicts an approximate relation between the phases $\Phi_{\ell m}$ of different harmonics, which with our choice of tetrad takes the simple form of eq. (3.3). This approximation is not exact, and becomes less accurate for higher frequencies. We have studied this in detail in [36, 34], and in [34] we find that for comparable mass binaries we can neglect the error of the approximation (3.3) before a binary system reaches its minimal energy circular orbit (MECO) as defined in [40]. As in our IMRPhenomXAS model, we will use the MECO to guide the choice of transition frequency between the inspiral and intermediate frequency regions. In the mass ratio range where we have NR data ($q \leq 18$) it is thus not necessary to model the inspiral phase, but we can use the scaling relation (3.3), as has been done in [6].

For the time domain amplitude, approximate scaling relations have been discussed in [41, 42], and in the frequency domain they have been used in the IMRPhenomHM model [6]. Unlike for the phase, however, even in the inspiral the errors are too large for our purposes, and we will need to model the amplitude for each spherical harmonic in a similar way as for IMRPhenomXAS, including in the inspiral.

Rotations in the orbital plane by an angle φ transform the spherical harmonic modes as

$$h_{\ell m} \to h_{\ell m} e^{im\varphi}. \tag{3.14}$$

Interchange of the two black holes thus corresponds to a rotation by $\varphi = \pi$, and modes with odd m vanish for equal black hole systems. A problem can arise in regions of the parameter space where the amplitude is close to zero, even in the inspiral, as discussed

in [19, 34]: For black holes with very similar masses, the amplitude can be very small, with the sign depending on the mass ratio, spins, and the frequency – which can lead to sign changes with frequency. In such cases the amplitude does become oscillatory, and the approximate relation (3.3) can not be expected to be satisfied. This happens in particular for the $(2, \pm 1)$ modes. We do not currently model the amplitude oscillations, and thus for a certain region of parameter space our model does not properly capture the correct waveform phenomenology. This region does depend on the frequency, but roughly corresponds to very similar masses and anti-aligned spins, for a particular example for the $(2, \pm 1)$ modes see Fig. 3.1. However, as phenomenon happens precisely when the amplitude of the $(2, \pm 1)$ modes is very small, this is not expected to be a significant effect for the current generation of detectors.

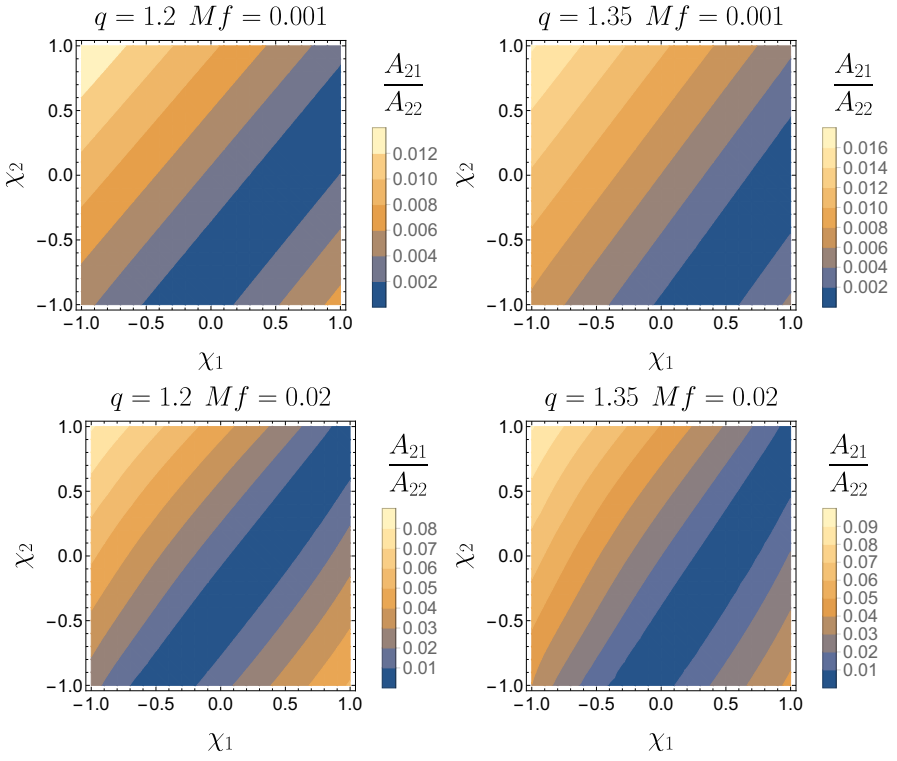

FIGURE 3.1: Relative amplitude of the $(2, 1)$ mode respect to the $(2, 2)$ mode as a function of the spins. The top row shows the amplitude ratio for a frequency of $Mf = 0.001$ while the bottom one shows it for $Mf = 0.02$. Left-side panels refer to a $q = 1.2$ binary and right-side ones to a $q = 1.35$ one. There exists a region (blue diagonal) where the amplitude of the $(2, 1)$ mode tends to zero. This diagonal moves toward the bottom-right corner of the plot as one increases the mass ratio and typically disappears for $q \gtrsim 2$.

During the inspiral and merger, gravitational wave emission is dominated by the direct emission due to the binary dynamics. As the final black hole relaxes toward a stationary Kerr black hole, the gravitational wave emission is eventually dominated by a superposition of quasinormal modes before the late time polynomial tail falloff sets in (for an overview see e.g. [43, 29]). As is common in waveform modelling targeting applications

in GW data analysis, we neglect the late-time power-law tail falloff, and focus our description of the ringdown on the quasinormal mode (QNM) emission, where the strain can be written as a sum of exponentially damped oscillations,

$$h(t,\theta,\varphi) \approx \sum_{\ell mn} a_{\ell mn} e^{i(\omega_{\ell mn} t)+\phi_{\ell mn}} {}_{-2}Y_{\ell m}(\theta,\phi), \tag{3.15}$$

where the complex frequencies $\omega_{\ell mn}$ are functions of the black hole spin and mass and their real and imaginary parts define the ringdown and damping frequencies as

$$f^{\ell m}_{ring} = \mathrm{Re}(\omega_{\ell m}), \qquad f^{\ell m}_{damp} = |\mathrm{Im}(\omega_{\ell m})|. \tag{3.16}$$

The functions ${}_{-2}Y_{\ell m}(\theta,\phi)$ are the *spheroidal* harmonics of spin weight -2 [44, 45]. The amplitude parameters $a_{\ell mn}$ and phase offsets $\phi_{\ell mn}$ will in general have to be fitted to NR data.

It has long been known that representing the spheroidal harmonic ringdown modes can result in *mode mixing* for modes with approximately the same real part of the ringdown frequency $\omega_{\ell mn}$ [46]. This happens in particular for modes with the same value of m, where then values with larger ℓ are much weaker, and do not show the usual exponential amplitude drop, but a more complicated phenomenology. In our case this happens for the $(3,2)$ mode. In this work we will model mixing only between two modes, specifically the $(3,2)$ with the $(2,2)$, as these are the two most strongly coupled modes (the coupling of the $(3,2)$ mode to other $m=2$ modes is in fact suppressed). While for the modes that do not show mixing it is sufficient to model their spherical harmonics, for the $(3,2)$ we will model the spheroidal harmonic, and then transform to the spherical harmonic basis, as discussed in Sec. 3.6. For a recent non-spinning model of mode-mixing see [26].

A key challenge of accurately modeling multi-mode waveforms is to preserve the relative time and phase difference between the individual modes, say as measured at the peaks of the modes. In the frequency domain time shifts are encoded in a phase term that is linear in frequency: the Fourier transformation of a time shifted function $h_\tau = h(t-\tau)$ will be given by $\tilde{h}_\tau = \tilde{h} e^{-i2\pi f\tau}$. In GW data analysis the quality of a model is typically evaluated in terms of how well two waveforms match, up to time shifts and global rotations, e.g. in terms of match integrals. Adding a linear term in the phase leaves such match integrals invariant. In order to improve the conditioning of the model calibration it has thus been common for phenomenological frequency domain models to subtract the linear part in frequency before calibrating the model to improve the conditioning of numerical fits, and then add back a linear in frequency term at the end, which approximately aligns the waveforms in time, e.g. by approximately aligning the amplitude peak at a certain time. This strategy has also been followed in our construction of the IMRPhenomXAS

model, i.e. for the $\ell = |m| = 2$ modes, whereas for the other modes we directly model a given alignment in time.

More specifically, our strategy of aligning the different spherical harmonic modes in time and phase has been the following: our hybrid waveforms are aligned in time and phase such that the peak of the $\ell = |m| = 2$ modes of ψ_4 in the time domain is located at $t = 0$, and the corresponding phase $\Phi_{22}(\psi_4, t = 0) = 0$, which corresponds to a time $\Delta t = 500M$ before the end of the waveform. For modes with odd m this leaves an ambiguity of a phase shift by multiples of π. We do not use the odd-m modes of the numerical waveforms to resolve this ambiguity in order not to depend on the poor quality of many odd-m data sets, and simply require a smooth transition of the inspiral phase into the merger-ringdown. This ambiguity in the phase will be harmless, as the relative phases among the modes can be unambiguously fixed using PN prescriptions, as we will explain in Subsec. 3.4.2 below. Our subdominant modes are calibrated to agree with this alignment of our hybrid waveforms. The $\ell = |m| = 2$ mode is aligned a posteriori to the same alignment, similar to what has been done in previous phenomenological frequency domain models. A difference here is that this a posteriori time alignment is achieved via an additional parameter space fit.

3.2.3 Strategy for fitting our model to numerical data

As discussed above, following IMRPhenomXAS our model is constructed in terms of closed-form expressions for the frequency domain amplitude and phase of spherical or spheroidal harmonic modes, which are each split into three frequency regimes. We will refer to a model for the amplitude or phase for one of the frequency regimes as a *partial model*. We thus need to construct a total of six partial models for each mode. For the inspiral phase, we can use the scaling relation (3.3) for comparable masses, and only need to model the extreme mass ratio case. For each of the six partial models the ansatz will be formulated in terms of some coefficients, which for example in the inspiral will be the pseudo-PN coefficients that correspond to yet unknown higher PN orders.

We thus employ two levels of fits to our input numerical data: First, for each waveform in our hybrid data set we perform fits of the six partial models for each mode to the data. This yields a set of coefficients for each mode, quantity (amplitude or phase), and frequency interval. We call this first level the direct fit of the model to our data. Second, we fit each coefficient across the 3D parameter space of mass ratio and component spins. We call this second level the parameter space fit. In the direct fit we usually collect redundant information: such as the model coefficients, values and derivatives at certain frequencies, and other quantities. This redundancy provides for some freedom when

reconstructing the model waveform after the parameter space fits. We make extensive use of this freedom when tuning our model, while the final model uses a particular reconstruction, which is what will be described below.

Fitting the coefficients of a particular partial model across the parameter space may not turn out to be a well-conditioned procedure, e.g. for the inspiral the pseudo PN coefficients have alternating signs, the PN series converges slowly, and different sets of PN coefficients can yield very similar functions. We will thus sometimes transform the set of coefficients we need to model to an alternative representation, in particular collocation points, following [39, 3, 1]. In this approach, one constructs fits for the values of the amplitude and phase at specific frequency nodes. The coefficients of the phenomenological ansätze are then obtained by solving linear systems that take such values as input. This method has been adopted to avoid fitting directly the phenomenological coefficients, which would result in a worse conditioned problem. We thus fit the values or derivatives at certain frequencies, and use the freedom in reconstructing the final phase or amplitude in tuning the model as mentioned above.

In order to perform the 3D parameter space fits in symmetric mass ratio η and the two black-hole spins $\chi_{1,2}$ we use the hierarchical fitting procedure described in [27], which we have also used for the underlying IMRPhenomXAS model. The goal of this procedure is to avoid both underfitting and overfitting our data set. In order to simplify the problem we split the 3D problem into a hierarchy of lower dimensional fits to some particular subsets of all data points. For each lower dimensional problem it is significantly easier to choose an ansatz that avoids underfitting and overfitting, and finally we combine the lower-dimensional fits into the full 3D fit and check the global quality of the fit. In order to check fit quality we compute residuals and compute the RMS error, and we employ different information criteria to penalize models with more parameters as discussed in [27] as an approximation to a full Bayesian analysis.

As a first step of our hierarchical procedure we perform a 1-dimensional fit for non-spinning subspace, choosing the symmetric mass ratio η as the independent variable. We can then identify two further natural one-dimensional problems: First, for the extreme mass ratio case we can neglect the spin of the smaller black hole, and consider the mass ratio as a scaling parameter, and we thus consider a one-dimensional problem in terms of the spin of the larger hole. Second, at fixed mass ratio we can fix a relation between the spins. For quantities such as the final spin and mass, or the coefficients of the IMRPhenomXAS model for the $(2, 2)$ mode, it has been natural to consider equal black holes, e.g. equal mass and equal spin for this one-dimensional problem.

It is then useful to express the results for the one-dimensional spin fits in terms of a suitably chosen effective spin, such as

$$\chi_{\rm eff} = \frac{m_1\chi_1 + m_2\chi_2}{m_1 + m_2}, \tag{3.17}$$

which is typically measured in PE (see e.g. [8]), and which has also been the choice in the early phenomenological waveform models IMRPhenomB [47] and IMRPhenomC [48]. A judicious choice of effective spin parameter can minimize the errors when approximating functions of the 3D parameter space by functions of η and effective spin, and can be sufficient for many applications, since spin-differences are a sub-dominant effect. For IMRPhenomD [39, 3] two effective spin parameters have been used: For the inspiral calibration to hybrid waveforms (3.17) has been augmented by extra terms motivated by PN theory [49]

$$\chi_{PN} = \chi_{\rm eff} - \frac{38\eta}{113}(\chi_1 + \chi_2) \tag{3.18}$$

The final spin and mass, and thus the ringdown frequency have been fit to numerical data in terms of the rescaled total angular momentum of the two black holes

$$\hat{S} = \frac{m_1^2\chi_1 + m_2^2\chi_2}{m_1^2 + m_2^2}. \tag{3.19}$$

We model the dominant spin-contributions to the amplitude as functions of χ_{PN} during the inspiral and as functions of $\hat{S}$ during the merger-ringdown. For the phase inspiral we use the scaling relation (3.3) for comparable masses, such that a phase inspiral calibration is only necessary for large mass ratios, which we treat in the same way as other phase coefficients, where we again use $\hat{S}$. We will denote a generic effective spin parameter by χ in general equations involving the effective spin, implying that this refers either to χ_{PN} or $\hat{S}$ as appropriate.

We thus perform three one-dimensional fits, one for the non-spinning sub-space (depending on η), one for equal black holes (depending on χ), and one for extreme mass ratios (again depending on χ). Then a 2D ansatz depending on η and χ is built such that it reduces to the 1D fits for those particular cases. The 2D fit is then performed for all data points and from it we get the best-fit function of η and χ minimizing the sum of squared residuals.

In order to extend the hierarchical method to the full 3D parameter space, a second spin parameter needs to be chosen, which incorporates spin difference effects. For small spin difference effects, we can simply choose

$$\Delta\chi = \chi_1 - \chi_2 \tag{3.20}$$

without worrying about a particular mass-weighting of the spins, since differences in mass-weighting could be absorbed into higher order terms. The spin difference effects are then modelled with a function $f_{\Delta\chi}(\eta)$ as a term

$$f_{\Delta\chi}(\eta)\Delta\chi, \tag{3.21}$$

and the modelling of small spin difference effects is reduced to the 1-dimensional problem of fitting a function of η. Note that this is reminiscent of the structure of PN expansions (see for instance [50]), where spin-difference effects are usually described in terms of the anti-symmetric spin combination $\chi_a = (\chi_1 - \chi_2)/2$. For larger spin difference effects, we will however need higher order terms, and in [27] a term quadratic in $\Delta\chi$ and a term proportional to $\chi\,\Delta\chi$ were included, and again these terms can be modelled as one-dimensional problems in terms of functions of η.

Extensions to this procedure are needed to model the behaviour of sub-dominant modes, in particular for the $(3,2)$ mode and for odd m modes. For the $(3,2)$, we need to model mode mixing in the ringdown, as discussed briefly above, and in detail in Sec. 3.6. While this requires a transformation from spheroidal to spherical harmonics, it does not directly affect our strategy for carrying out the direct fits and the parameter space fits. For odd m modes, changes are required due to the change of sign in the amplitude when rotating by an angle of π, see eq. (3.14), corresponding to interchanging the two black holes. For even m modes, rotations by π correspond to the identity, and as for IMRPhenomXAS it is natural to work with non-negative gravitational-waveform amplitudes. For odd m modes however, restricting the amplitude to positive values will make it a non-smooth function in the two-dimensional spin parameter space, where the amplitude $A_{\ell m}(f)$, as defined through Eq. (3.7), corresponds to the absolute value of a function that can change sign.

This can be best understood by plotting the values of the amplitude at a collocation point as a function of the two black holes' spins, for a given mass ratio (see Fig. 3.2). It can be seen that the two-dimensional data in the spin parameter space exhibit a crease along a line which corresponds to a vanishing amplitude. For equal masses, this line appears for equal spin systems, as shown in the top panel. In order to work with smooth surfaces, we allow the amplitude to take negative values when fitting our numerical data. Such sign flips occur at the level of the full gravitational-wave strain and we choose to fold them into the amplitude for mere convenience, to simplify the fitting procedure. Since we require our reconstructed amplitudes to be non-negative functions, we then take the absolute value of the fits, whenever we allow such sign flips (see Eq. (3.7) and discussion therein). Notice that, for sufficiently large mass ratios, the spin dependence of the sign

of the phase can be neglected, we thus choose which part of the crease we flip in sign to be consistent with the behaviour for higher mass ratios data.

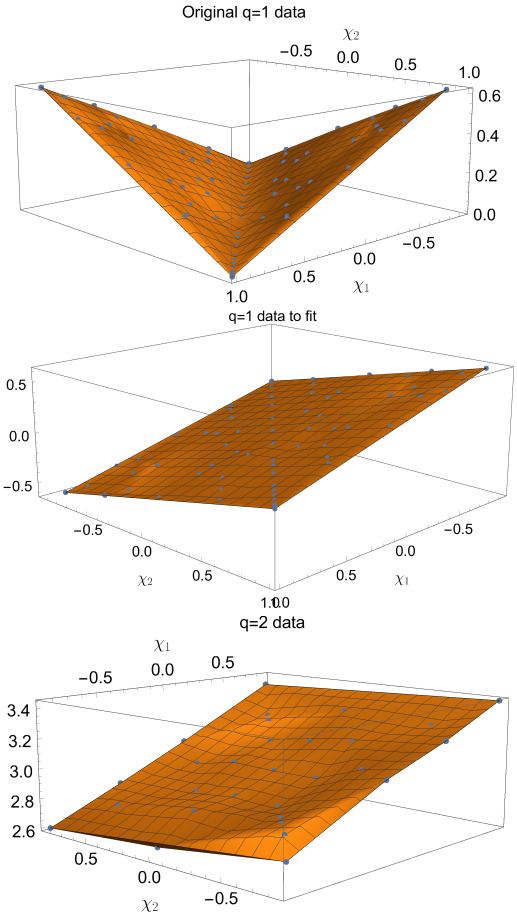

FIGURE 3.2: Example of how the amplitude data set is modified for the parameter space fit. The data shown correspond to the first intermediate collocation point of the $(3, 3)$ mode. One of the leaves of the original $q = 1$ data (top plot) is flipped in sign so we get a flat surface that is easier to fit (intermediate plot). The leaf to be flipped is chosen such that the final behaviour is consistent with the data for other mass ratios, e.g. mass ratio 2 (bottom plot). After the fit we take the absolute value of the final fit to return back positive amplitude.

When modelling the amplitude of odd m modes we can not use equal masses as one of our one-dimensional fitting problems, since the amplitude vanishes there, and instead we use a different mass ratio, typically $q = 3$. Applying appropriate boundary conditions for equal black hole systems is then essentially straightforward – we simply demand that the amplitude vanishes. Setting appropriate boundary values for odd mode phases for equal black hole is however a complicated problem, since the phase will in general not vanish as one takes the limit toward the boundary. The numerical data typically become very noisy and inaccurate for modes with very small amplitude, and thus one can not in general expect to model odd m modes for close-to-equal black holes with small relative errors. When building a parameter space ansatz for odd mode amplitudes we are adding

a minus sign when exchanging the spins, the non-spinning and effective-spin parts of the ansatz must be manifestly set to zero because they pick up a minus sign when exchanging the black holes, while at the same time they are invariant by symmetry. We implement this by adding a multiplicating factor $\sqrt{1-4\eta}$ that cancels these parts for equal mass systems. The even modes behave in the opposite way: since when exchanging the two spins they remain the same, it is the spin-difference part which has to vanish because it would introduce a minus sign.

3.3 Calibration data set

Our input data set coincides with the data we have used for the IMRPhenomXAS model [1], and comprises a total of 504 waveforms: 466 for comparable masses (with $1 \leq q \leq 18$) and 38 for extreme mass-ratios (with $q = \{200, 1000\}$). These waveforms are "hybrids", constructed by appropriately gluing a computationally inexpensive inspiral waveform to a computationally expensive waveform, which covers the late inspiral, merger and ringdown (IMR). For comparable masses, the $\ell = |m|$ inspiral is taken from the SEOBNRv4 model [51], and the subdominant modes are constructed from the phase of the $\ell = |m|$ mode and PN amplitudes as described in [34] along with other details of our hybridization procedure. The IMR part of the waveform is taken from NR simulations summarized below.

For extreme mass ratios the IMR part is taken from numerical solutions of the perturbative Teukolsky equation, and the inspiral part is taken from a consistent EOB description, as discussed below in Sec. 3.3.2.

Due to the poor quality of many of the NR waveforms, and the fact that our extreme mass ratio waveforms are only approximate perturbative solutions, we do not use all of the waveforms of our input data set for the calibration of all the quantities we need to model across the parameter space. Already for IMRPhenomXAS (see [1]) we had to carefully select outliers, which lacked sufficient quality for model calibration. Higher-modes waveforms are typically even noisier and more prone to exhibit pathological features than the dominant quadrupolar ones. This can result in a large number of outliers in the parameter space fits, which can introduce unphysical oscillations in the fit surfaces. To attenuate this problem, we developed a system of annotations that stores relevant information about the quality of all the waveforms in the calibration set. A careful analysis of data quality is needed, separately for each quantity that we fit, such as the value of the amplitude (phase) at a given collocation point for each particular mode. We will not document these procedures in detail, instead, we will discuss outliers in Sec. 3.7, where we evaluate the quality of our model by comparing to the original hybrid data.

We will see that this comparison has less stringent quality criteria: pathologies which prohibit the use of a some waveform accurate fit for a particular coefficient may in the end not significantly contribute to the waveform mismatch. We will thus only discuss those waveforms which we excluded from the model evaluation, because of doubts in their quality.

3.3.1 Numerical relativity waveforms

The NR simulations used in this work were produced using three different codes to solve the Einstein equations: for the amplitude calibration we used 186 waveforms [52] from the public SXS collaboration catalog, as of 2018 [53] obtained with the Spectral Einstein Code (SpEC) [54], 95 waveforms [39, 27] obtained with the BAM code [55, 56], and 16 waveforms from simulations we have performed with the Einstein Toolkit (ET) [57] code. After the release of the latest SXS collaboration catalog [58], we extended the data set to include 355 SpEC simulations, and updated the parameter space fits for the phase accordingly. We chose not to update the amplitude fits, as their recalibration was expected to have a smaller effect on the overall quality of the model waveforms. The parameters of our waveform catalogue are visualized in Fig. 3.3. Note that to the same set of (η, χ_1, χ_2) can correspond multiple NR waveforms: this allows to compare at the same point in parameter space different resolutions and/or numerical codes and it is therefore important for data-quality considerations. A detailed list of the waveforms we have used can be found in our paper on the hybrid data set [34].

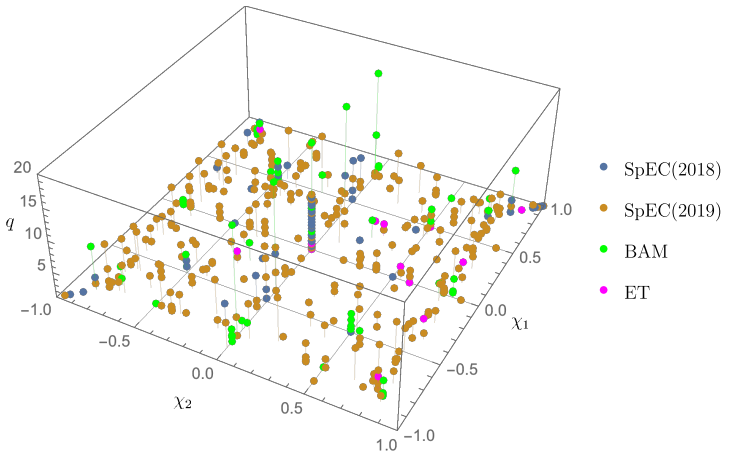

FIGURE 3.3: The mass ratios and Kerr parameters are shown for the comparable mass cases in our waveform catalogue, indicating the NR codes used to carry out the simulations.

3.3.2 Extrapolation to the test-mass limit

Due to the computational cost of high mass-ratio simulations, our catalogue of NR waveforms extends only up to $q = 18$, which would leave the test-particle limit of our model poorly constrained. Here, following [59], we chose to pin down the large-q boundary of the parameter space using EMR waveforms. We produced two sets of such waveforms, one with $q = 200$ and the other with $q = 10^3$. The spin on the primary spans the interval $[-0.9, 0.9]$ in uniform steps of 0.1, while the secondary is assumed to be non-spinning. The waveforms in the calibration set were generated by hybridizing a longer inspiral EOB waveform with a shorter numerical waveform computed using the code of Ref. [60]. The code solves the 2+1 Teukolsky equations for perturbations that can be freely specified by the user. In our case the gravitational perturbation was sourced by a particle governed by an EOB dynamics, with radiation-reaction effects included up to 6PN order for all the multipoles modelled in this work [61]. The EOB and Teukolsky waveforms, being both extracted at future null infinity, can be consistently hybridized, following the same hybridization routine used for comparable-mass cases.

3.4 Inspiral model

In the inspiral region we work under the assumption that the SPA approximation (see e.g. [38] and our discussion in the context of IMRPhenomXAS [1]) is valid. The frequency domain strain of each mode will therefore take the form

$$\tilde{h}_{\ell m}(f) = A_{\ell m}\sqrt{\frac{2\pi}{m\ddot{\phi}}}e^{i(2\pi f t_c - \phi_{\ell m} - \pi/4 + \psi_0)} := A^{\rm SPA}_{\ell m} e^{i\Psi_{\ell m}}, \tag{3.22}$$

where t_c is a time shift parameter, $\ddot{\phi}$ is the second derivative respect to time of the orbital phase (expressed as a function of the frequency), ψ_0 is an overall phase factor that depends on the choice of tetrad conventions and

$$A^{\rm SPA}_{\ell m} := A_{\ell m}\sqrt{\frac{2\pi}{m\ddot{\phi}}}, \tag{3.23}$$

$$\Psi_{\ell m} := 2\pi f t_c - \phi_{\ell m} - \pi/4 + \psi_0. \tag{3.24}$$

Notice that, in our tetrad-convention, $\psi_0 = \pi$ (see Eq. (3.3) and discussion therein).

Furthermore, we will assume that we can work within the PN framework, and that we can model currently unknown higher-order terms in the PN expansions with NR-calibrated coefficients. Let us stress that in IMRPhenomXHM the phase and amplitude

are treated in different ways: while the latter is fully calibrated to NR, the former is built with a reduced amount of calibration, as we will explain below.

Following the approach taken in IMRPhenomXAS, we set the end of the inspiral region around the frequency of the MECO. For the amplitude, the default end-frequency of the inspiral is taken to be:

$$f^{\ell m}_{\rm Ins} = \frac{m}{2}\left(f^{22}_{\rm MECO}\,\epsilon^{\ell m}_{\rm Ins}(\eta,\chi_{eff}) + |f^{22}_{\rm ISCO} - f^{22}_{\rm MECO}|\,\delta^{\ell m}_{\rm Ins}(\eta,\chi_{eff})\right), \tag{3.25}$$

where $f^{22}_{\rm ISCO}$ and $f^{22}_{\rm MECO}$ are the gravitational-wave frequency of the 22-mode evaluated at the ISCO (innermost stable circular orbit) and MECO respectively. The mode-specific expressions for the functions $\delta^{\ell m}_{\rm Ins}$ and $\epsilon^{\ell m}_{\rm Ins}$ are given in Tab. 3.1. In the large-mass-ratio regime, the transition frequency of Eq. (3.25) is replaced by that of a local maximum in the amplitude of ψ_4, as we explain in Subsec. 3.5.1.2 below.

While the fully NR-calibrated amplitude requires careful tuning of the above transition frequencies, we find that for the phase we can simply set $f^{\ell m}_{\rm Ins} = \frac{m}{2} f^{22}_{\rm MECO}$.

The start frequencies of our hybrid waveforms [34] are set up such that $Mf \geq 0.001453 m/2$ for comparable masses, and $Mf \geq 0.001872\, m/2$ for extreme-mass-ratio waveforms (depending on the spherical harmonic index m). We start the amplitude calibration at a higher minimum frequency of $f_{\rm min} = 0.002\, m/2$ to avoid contamination from Fourier transform artefacts. Note that a higher cutoff frequency was chosen for IMRPhenomXAS due to the higher accuracy requirements in that case. For the phase, only a small and simple (linear) correction term (3.31) is calibrated, and the same minimum frequency cutoff is applied in this case.

Table 3.1: Explicit expressions for the coefficients $\delta^{\ell m}_{\rm Ins}$ and $\epsilon^{\ell m}_{\rm Ins}$ entering the inspiral cutting frequencies of the amplitude reconstruction, according to the notation of Eq. (3.25). $f^{\ell m}_{ring}$ is the fundamental quasi-normal mode frequency of the (ℓ, m) mode.

	Amplitude	
(ℓm)	$\delta^{\ell m}_{\rm Ins}$	$\epsilon^{\ell m}_{\rm Ins}$
21	$\left(3/4 - 0.235\,\chi_{\rm eff} - 5/6\,\chi^2_{\rm eff}\right)$	1
33	$\left(3/4 - 0.235\,\chi_{\rm eff} - 5/6\,\chi_{\rm eff}\right)$	1
32	$\left(3/4 - 0.235\,\lvert\chi_{\rm eff}\rvert\right)\frac{f^{32}_{ring}}{f^{32}_{ring}}$	$\frac{f^{32}_{ring}}{f^{22}_{ring}}$
44	$\left(3/4 - 0.235\,\chi_{\rm eff}\right)$	1

3.4.1 Amplitude

In the inspiral region, the amplitude ansatz of IMRPhenomXHM augments a PN expansion with terms up to 3PN oder with three NR-calibrated coefficients, which correspond to higher-order PN terms. A 3PN-order expansion for the Fourier domain amplitudes is computed in [50]. However, some of these expressions exhibit significant discrepancies with our numerical data and with analogous expressions we derived independently. The authors of [50] acknowledged a mistake in their derivation and agreed with our results. We gather the correct 3PN-order Fourier domain amplitudes in appendix 3.E and advise the reader to use the expressions reported there.

At low frequency, the leading order PN behavior of the Fourier amplitude of the $(2,2)$ mode is

$$A^0_{22} := \pi\sqrt{\frac{2\eta}{3}}\,(\pi f)^{-7/6}\,, \tag{3.26}$$

while the higher modes present milder divergences. Such a divergent behaviour is expected to negatively impact the conditioning of our amplitude fits. Therefore, we do not model the SPA amplitudes directly, but similarly to IMRPhenomXAS we rather work with the quantities

$$\mathcal{H}_{\ell m} := \frac{|A^{\rm SPA}_{\ell m}|}{A^0_{22}}, \tag{3.27}$$

which are non-negative by construction and non-divergent in the limit $f \to 0$.

3.4.1.1 Default reconstruction

Currently the highest known PN-term in the expansion of the $\mathcal{H}_{\ell m}$ is proportional to f^2. In order to model currently unknown higher-order effects, we introduce up to three pseudo-PN terms $\{\alpha, \beta, \gamma\}$ that depend only on the intrinsic parameters of the source, i.e. mass ratio and spins. The ansatz employed for the inspiral amplitude is given by

$$\mathcal{H}_{\ell m}(f) = \frac{|A^{PN}_{\ell m}(f)|}{A^0_{22}(f)} + \alpha\left(\frac{f}{f^{\rm Ins}_{\ell m}}\right)^{\frac{7}{3}} + \beta\left(\frac{f}{f^{\rm Ins}_{\ell m}}\right)^{\frac{8}{3}} + \gamma\left(\frac{f}{f^{\rm Ins}_{\ell m}}\right)^{\frac{9}{3}}. \tag{3.28}$$

Following [3], we do not perform parameter space fits of $\{\alpha, \beta, \gamma\}$. Instead, we compute parameter space fits of the hybrids' amplitudes evaluated at three equispaced frequencies $\left[0.5\, f^{\rm Ins}_{\ell m}, 0.75\, f^{\rm Ins}_{\ell m}, f^{\rm Ins}_{\ell m}\right]$, which we refer to as "collocation points".

We require that the reconstructed inspiral amplitude go through the three collocation points given by the parameter space fits. This yields a system of three equations that can

be solved to obtain the values for $\{\alpha, \beta, \gamma\}$. We observe however, that in some regions of parameter space this leads to oscillatory behaviour of the reconstructed amplitude for the $(2, 1)$ and $(3, 2)$ modes, and a lower order polynomial, calibrated to a smaller number of collocation points, gives more robust results. This problem arises in regions of the parameter space where the model is poorly constrained due to the lack of NR simulations, such as in cases with very high positive spins (where in addition the correct functional form is rather simple and a higher order polynomial is not required), and where the amplitude of the waveform is very small (see e.g. Fig. 3.1). For this reason we apply a series of vetoes that remove collocation points and allow for a smooth reconstruction, as discussed next.

3.4.1.2 Vetoes and non-default reconstruction

The removal of a collocation point implies the modification of the ansatz used in the reconstruction. For each collocation point removed, we set to zero one of the coefficients of the pseudo-PN terms, starting from the highest order one. The removal of the three collocation points would lead us to an ansatz without any pseudo-PN term.

For the $(2, 1)$ mode, when $q < 8$ we remove the collocation points which gives a Fourier domain amplitude $|\tilde{h}_{21}|$ below 0.2 (in geometric units), which is a typical value for the ringdown for comparable masses. Furthermore, we check whether the amplitude values at the three collocation points form a monotonic sequence, otherwise we remove the middle point to avoid oscillatory behaviour.

For the $(3, 2)$ mode we drop the middle collocation point if it is not consistent with monotonic behaviour. In addition, for this mode we have isolated two particular regions of the parameter space where we drop collocation points from our reconstruction due to the poor quality of the reconstruction. The first one is given by $q > 2.5$, $\chi_1 < -0.9$, $\chi_2 < -0.9$, where we do not use any of the collocation points and just reconstruct with the PN ansatz. The second is given by $q > 2.5$, $\chi_1 < -0.6$, $\chi_2 > 0$ where we just remove the highest frequency collocation point. For the 33 mode we remove the last collocation point in the region $q \in (1, 1.2)$, $\chi_1 < -0.1$, $\chi_2 > 0$.

In the future we will revisit this problem when recalibrating the amplitude against the recently released new SXS catalogue of NR simulations [58], which we expect to mitigate some of the issues we observe.

3.4.2 Phase

For the inspiral phase, we start from the consideration that, with good accuracy, the NR data satisfy the relation [36],

$$\phi_{\ell m}(f) \approx \frac{m}{2}\phi_{22}\left(\frac{2}{m}f\right). \tag{3.29}$$

As discussed above, our amplitude fits return a real quantity, but one must be mindful that the PN expansions of the $A^{\rm SPA}_{\ell m}$ are, in general, complex (see, for instance, [28, 50]). For each mode, we re-expand to linear order in the frequency the quantities

$$\Lambda^{PN}_{\ell m} = \arctan\left(\Im(A^{PN}_{\ell m})/\Re(A^{PN}_{\ell m})\right). \tag{3.30}$$

We evaluated the quantity $\Delta\phi^{\rm Ins}_{\ell m} := \phi_{\ell m}(f) - \frac{m}{2}\phi_{22}(2/mf)$ for all the hybrids in our catalogue and found that

$$\Delta\phi^{\rm Ins}_{\ell m} \approx \Lambda^{PN}_{\ell m} \tag{3.31}$$

In Fig. 3.4 we show the behaviour of this approximation for an example case of comparable mass ratio, as compared to the result obtained from the hybrids.

The accuracy of the above approximation tends to degrade for high-mass ratios, high-spins configurations and the PN relative phases are recovered only at sufficiently low frequencies, as illustrated in Fig. 3.5. Therefore, we compute parameter space fits to capture the leading order behaviour of each $\Delta\phi^{\rm Ins}_{\ell m}$, and use them to build our final inspiral ansatz in the extreme-mass ratio regime.

Based on the above discussion, we express the inspiral phase of each multipole as

$$\phi_{\ell m}(f) = \frac{m}{2}\phi^{X}_{22}(2/mf) + \Lambda_{\ell m}(f) + d\phi^{\rm Ins}_{\ell m} f + \phi^{\rm Ins}_{\ell m}, \tag{3.32}$$

where ϕ^{X}_{22} is the quadrupole phase reconstructed with IMRPhenomXAS, whose coefficients need to be rescaled as detailed in appendix 3.D, and

$$\Lambda_{\ell m} = \begin{cases} \Lambda^{PN}_{\ell m} & \text{if } q < 100 \\ \\ \Lambda^{fit}_{\ell m} & \text{if } q \geq 100 \end{cases} \tag{3.33}$$

The constant $d\phi^{\rm Ins}_{\ell m}$ in Eq. (3.32) is determined by continuity with the intermediate-region ansatz.

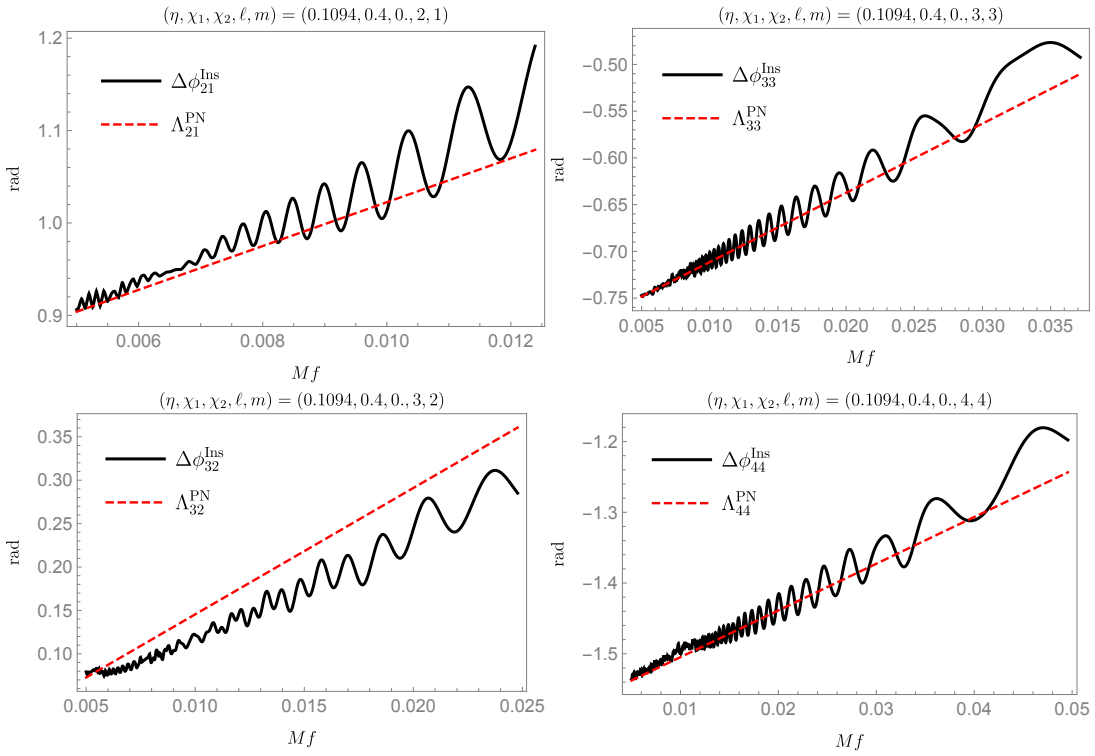

FIGURE 3.4: We compare the quantities $\Lambda^{PN}_{\ell m}$ defined in Eq. (3.30) (red dashed lines), with the $\Delta\phi^{\rm Ins}_{\ell m}$ computed from a Fourier transformed hybrid waveform with parameters $(\eta, \chi_1, \chi_2) = \{0.1094, 0.4, 0\}$ (black solid lines). Each plot is truncated around the end of the inspiral region corresponding to the selected mode.

Once a smooth phase derivative, defined with respect to the Fourier variable f, has been reconstructed, the remaining constant, $\phi^{\rm Ins}_{\ell m}$, is fixed by requiring that, at low frequencies, one has

$$\lim_{f\to 0}\left(\Psi_{\ell m} - \frac{m}{2}\Psi_{22}\right) = \frac{3}{4}\pi\left(1 - \frac{m}{2}\right), \tag{3.34}$$

which follows from Eq. (3.24) and from our choice of tetrad convention (see also (3.3).

3.5 Intermediate model

The intermediate region connects the inspiral regime to the ringdown. It is the only region where IMRPhenomXHM is fully calibrated, both in amplitude and phase. While for the amplitude this is the last region to be attached to the rest of the reconstruction, for the phase this is the central piece of the model, to which inspiral and ringdown phase derivatives will be smoothly attached. Physically, this implies that, in IMRPhenomXHM, the relative time-shifts among different modes are entirely calibrated around merger. We have found that a good practical way of testing whether time shifts are

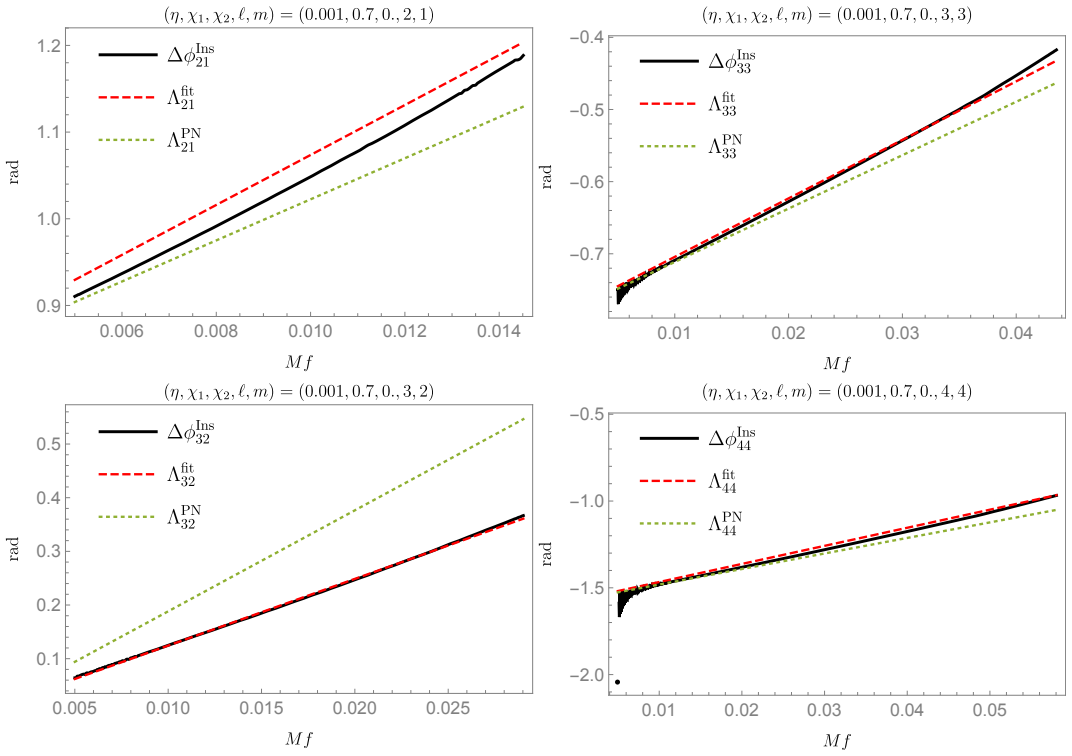

FIGURE 3.5: We compare the quantities $\Lambda_{\ell m}^{PN}$ defined in Eq. (3.30) (red dashed lines), with the $\Delta\phi_{\ell m}^{\rm Ins}$ computed from a hybrid Fourier domain waveform with parameters $(\eta, \chi_1, \chi_2) = \{0.001, 0.7, 0.\}$ (black solid lines). Red dashed lines denote our parameter space fits (corresponding to the $\Lambda_{\ell m}^{\rm fit}$ of Eq. (3.33)), while dotted green lines the corresponding analytical PN approximations. Each plot is truncated around the end of the inspiral region corresponding to the selected mode.

consistent between modes is to compute the recoil of the merger remnant, which is also of astrophysical interest, and which we discuss in Sec. 3.7.3.

The intermediate region covers the range of frequencies

$$f \in \left[f_{\rm Ins}^{\ell m}, f_{RD}^{\ell m}\right], \tag{3.35}$$

where the inspiral cutting frequencies $f_{\rm Ins}^{\ell m}$ are those of Eq. (3.25) and the ringdown cutting frequencies are defined as:

$$f_{RD}^{\ell m} = \delta_{RD}^{\ell m} f_{ring}^{\ell m} + \epsilon_{RD}^{\ell m}. \tag{3.36}$$

In the above equation, $f_{ring}^{\ell m}$ is the fundamental quasi-normal mode (QNM) frequency of the (ℓ, m) mode and the default coefficients $\delta_{RD}^{\ell m}, \epsilon_{RD}^{\ell m}$ are given in Tab. 3.2. We have computed fits for the real and imaginary parts of the QNMs as a function of the final dimensionless spin, based on publicly available data [62], see also [63]. Notice that, in the $(3, 2)$ reconstruction, high-mass, high-spin cases require an adjustment of the default

cutting frequencies, as we explain in Subsecs. 3.5.1 and 3.5.2 below.

The rationale behind our choice of cutting frequencies is simple: in general, the QNM frequencies $f^{\ell m}_{\rm ring}$ mark the onset of the ringdown region and it is therefore natural to terminate our intermediate region slightly before those. This does not apply to the $(3,2)$ mode, where, due to mode-mixing, new features appear in the waveforms already around $f \approx f^{22}_{\rm ring} < f^{32}_{\rm ring}$.

In the following subsections, we will describe in more detail our choice of ansätze and collocation points, based on the specific features of our numerical waveforms in the intermediate region.

TABLE 3.2: Choices for the coefficients $\delta^{\ell m}_{RD}$ and $\epsilon^{\ell m}_{RD}$ entering the default ringdown cutting frequencies in Eq. (3.36). $f^{\ell m}_{damp}$ is the quasi-normal mode damping frequency of the (ℓ, m) mode.

	Amplitude		Phase	
(ℓm)	$\delta^{\ell m}_{RD}$	$\epsilon^{\ell m}_{RD}$	$\delta^{\ell m}_{RD}$	$\epsilon^{\ell m}_{RD}$
21	0.75	0	1	$-f^{21}_{damp}$
33	0.95	0	1	$-f^{33}_{damp}$
32	0	f^{22}_{ring}	0	$f^{22}_{ring} - 0.5 f^{22}_{damp}$
44	0.9	0	1	$-f^{44}_{damp}$

3.5.1 Amplitude

3.5.1.1 Default reconstruction

In the intermediate frequency regime we model the amplitude with the inverse of a fifth-order polynomial as

$$\frac{A^{\rm Inter}_{\ell m}}{A_0} = \frac{1}{\delta_0 + \delta_1 f + \delta_2 f^2 + \delta_3 f^3 + \delta_4 f^4 + \delta_5 f^5}, \tag{3.37}$$

where $A_0 = \pi\sqrt{\frac{2\eta}{3}}$. This function has six free parameters, which are determined by imposing the value of the amplitude at two collocation points, together with four boundary conditions (two on the amplitude itself, and two on its first derivative), so that the final IMR amplitude is a C^1 function. We use two collocation points at the equally spaced frequencies $f^{\ell m}_{\rm Int_1} = f^{\ell m}_{\rm Ins} + (f^{\ell m}_{\rm RD} - f^{\ell m}_{\rm Ins})/3$ and $f^{\ell m}_{\rm Int_2} = f^{\ell m}_{\rm Ins} + 2/3(f^{\ell m}_{\rm RD} - f^{\ell m}_{\rm Ins})$.

TABLE 3.3: Conditions imposed to determine the parameters of the fifth-order polynomial used in the default intermediate amplitude reconstruction, see Eq. (3.37).

Collocation Points	Value	Derivative
$f_1 = f_{\rm Ins}^{\ell m}$	$v_1 = A_{\ell m}^{\rm Inter}(f_1)/A_0$	$d_1 = (A_{\ell m}^{\rm Inter}/A_0)'(f_1)$
$f_2 = f_{\rm Ins}^{\ell m} + (f_{\rm RD}^{\ell m} - f_{\rm Ins}^{\ell m})/3$	$v_2 = A_{\ell m}^{\rm Inter}(f_2)/A_0$	
$f_3 = f_{\rm Ins}^{\ell m} + 2(f_{\rm RD}^{\ell m} - f_{\rm Ins}^{\ell m})/3$	$v_3 = A_{\ell m}^{\rm Inter}(f_3)/A_0$	
$f_4 = f_{\rm RD}^{\ell m}$	$v_4 = A_{\ell m}^{\rm Inter}(f_4)/A_0$	$d_2 = (A_{\ell m}^{\rm Inter}/A_0)'(f_4)$

3.5.1.2 Extreme-mass-ratio reconstruction

For the EMR regime we refine the model to adapt to the steep amplitude drop at the end of the inspiral part, which is associated with the sharp transition from inspiral to plunge for extreme mass ratios. As one would expect, this drop is deeper for very negative spins. We find that the ansatz of Eq. (3.37) is not suited to this regime and we introduce a pre-intermediate region that ranges from the inspiral cutting frequency up to the frequency of the first collocation point. We add an extra collocation point at the frequency $f_{\rm Int_0}^{\ell m} = f_{\rm Ins}^{\ell m} + (f_{\rm Int_1}^{\ell m} - f_{\rm Ins}^{\ell m})/3$, where we calibrate the value of the amplitude and its derivative. We then use the inverse of a fourth order polynomial to model the amplitude in this new region. The five free coefficients of the polynomial are specified by imposing the conditions listed in Tab. 3.4.

TABLE 3.4: Conditions imposed to determine the parameters of the fourth-order polynomial used in the pre-intermediate region of the EMR amplitude reconstruction.

Collocation Points	Value	Derivative
$f_1 = f_{\rm Ins}^{\ell m}$	$v_1 = A_{\ell m}^{\rm Inter}(f_1)/A_0$	$d_1 = (A_{\ell m}^{\rm Inter}/A_0)'(f_1)$
$f_2 = f_{\rm Ins}^{\ell m} + (f_{\rm Int_1}^{\ell m} - f_{\rm Ins}^{\ell m})/3$	$v_2 = A_{\ell m}^{\rm Inter}(f_2)/A_0$	$d_2 = (A_{\ell m}^{\rm Inter}/A_0)'(f_2)$
$f_3 = f_{\rm Int_1}^{\ell m}$	$v_3 = A_{\ell m}^{\rm Inter}(f_3)/A_0$	

We then apply the default reconstruction procedure in the region $f \in [f_{\rm Int_0}^{\ell m}, f_{\rm RD}^{\ell m}]$, imposing the conditions listed in Tab. 3.3, with the replacement $f_{\rm Ins}^{\ell m} \to f_{\rm Int_0}^{\ell m}$.

The two calibration regions are shown in Fig. 3.6, where have shaded the pre-intermediate region in red and the intermediate one in blue. We find it convenient to terminate the inspiral region just before the amplitude drop. Therefore, we replace the cutting frequency of Eq. (3.25) with that of a local maximum in the amplitude of ψ_4, which always precedes the drop (see Fig. 3.6). We carried out a fit over the EMR parameter space of the frequency at which this maximum occurs and used it to replace the default inspiral cutting frequency when $q > 70$.

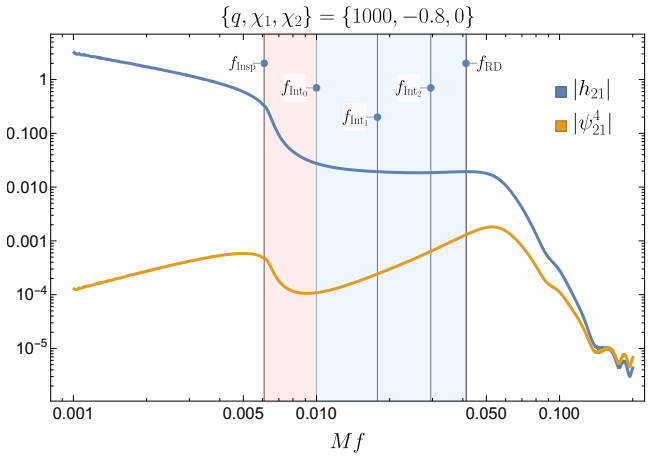

FIGURE 3.6: $(2,1)$ Fourier domain amplitude of an EMR waveform. The strain amplitude shows a deep drop after the inspiral. This feature is preceded by a local maximum in the amplitude of ψ_4. The red-shaded area corresponds to the pre-intermediate region mentioned in the text, where the amplitude is reconstructed using a fourth-order polynomial. The blue-shaded area corresponds to the intermediate region, where the default reconstruction procedure applies.

3.5.1.3 Vetoes and non-default reconstruction

While for comparable masses the ansatz of Eq. (3.37) is well suited to model the intermediate amplitude, in other regions of the parameter space modelling errors can result in a zero-crossing of the fifth order polynomial. We resolve this problem using a strategy akin to that of Subsec. 3.4.1.2 above, i.e. by removing collocation points and switching to a lower order polynomial, the minimum order being one. The regions of the parameter space affected are typically those where the amplitude is very small, or the high-spin regime. We have also isolated some regions where, due to the poor quality of the reconstruction, we drop both intermediate collocation points. This system of vetoes is summarized in Tab. 3.6.

We describe now in more detail the adjustments made to the default reconstruction procedure mode-by-mode. A summary of the rules applied can be found in Tab. 3.5.

For the $(2,1)$ mode, we remove the intermediate collocation points at which the strain Fourier domain amplitude $|\tilde{h}_{21}|$ is below 0.2. This happens when the $(2,1)$ amplitude is very small and in consequence the current accuracy of the parameter space fits is not sufficient. The advantage is that for those cases the $(2,1)$ mode does not contribute significantly to the total waveform and we can afford to simplify the reconstruction. It can be seen from Fig. 3.1 that the ratio between the $(2,1)$ and $(2,2)$ amplitude is in some cases well below 1%. If the amplitude at the ringdown cutting frequency is below a threshold of 0.01, we remove the two intermediate collocation points. If the intermediate collocation points have passed these preliminary tests, we check whether they form a

monotonic sequence, and if not we remove $f^{\ell m}_{\rm Int_2}$. Finally, we apply the parameter space vetoes indicated in Tab. 3.6.

For the $(3,2)$ mode, we require that the amplitude at the ringdown cutting frequency is above the same threshold applied to the $(2,1)$ mode. If this condition is not satisfied, we remove the two intermediate collocation points. If it is, we check whether the collocation points form a monotonic sequence. If not, we drop $f^{\ell m}_{\rm Int_2}$. Finally, we apply our set of parameter space vetoes.

The $(3,3)$ and $(4,4)$ modes are typically less problematic. However, we find that in the high-spin, high-mass-ratio region ($q > 7$, $\chi_1 > 0.95$) the inspiral is very long and there is a sharp transition to the ringdown, without a specific merger signature. For that reason we remove the two intermediate collocation points and connect inspiral and ringdown with a third-order polynomial. Once again, we apply the vetoes of Tab. 3.6.

After applying all the mode-specific vetoes, we check whether the denominator of our polynomial ansatz ever crosses zero in the frequency range of the intermediate region. If so, we lower the order of the polynomial by iteratively relaxing the boundary conditions until we obtain a well-defined ansatz.

TABLE 3.5: Summary of the sanity checks used in the intermediate amplitude reconstruction. The vetoes are sorted in order of application. The coefficient a_λ will be presented in Eq. (3.42).

Veto description	Applied to modes	Region where applied	Collocation point removed
Amplitude at $f^{\ell m}_{\rm Int_{1,2}} < 0.2$	21	$q < 8$	$f^{\ell m}_{\rm Int_{1,2}}$
Amplitude at $f^{\ell m}_{RD} < 0.01$	21	Always	$f^{\ell m}_{\rm Int_1}$ & $f^{\ell m}_{\rm Int_2}$
	32		$f^{\ell m}_{\rm Int_1}$, $f^{\ell m}_{\rm Int_2}$ & derivatives at boundaries
Monotonicity (if $f^{\ell m}_{\rm Int_1}$ and $f^{\ell m}_{\rm Int_2}$ have passed the previous checks)	21, 32	Always	$f^{\ell m}_{\rm Int_2}$
a_λ badly behaved	33, 44	$q > 7, \chi_1 > 0.95$	$f^{\ell m}_{\rm Int_1}$ & $f^{\ell m}_{\rm Int_2}$
parameter space vetoes	21, 33, 32, 44	see Tab. 3.6	$f^{\ell m}_{\rm Int_1}$ & $f^{\ell m}_{\rm Int_2}$
Check that the denominator of the resulting ansatz does not cross zero, if so remove derivatives at boundaries			

3.5.2 Phase

In the intermediate region our most general ansatz for the phase-derivative of each mode reads:

$$\frac{d\phi^{\rm Int}_{\ell m}}{df} = a^{\ell m}_\lambda \frac{f^{\ell m}_{\rm damp}}{(f^{\ell m}_{\rm damp})^2 + (f - f^{\ell m}_{\rm ring})^2} + \sum_{k=0}^{4} \frac{a^{\ell m}_k}{f^k}. \tag{3.38}$$

For the modes that do not show significant mode-mixing, namely $(2,1), (3,3), (4,4)$, we set $a^{\ell m}_3 = 0$ and retain all the remaining coefficients. This was done for consistency

TABLE 3.6: parameter space regions where the two intermediate collocation points at $f_{\rm Int_1}$ and $f_{\rm Int_2}$ are removed. "Still alive" means if the collocation point has not been removed yet by the previous vetoes.

(ℓm)	Region	Veto applied if
21	$\eta < 0.23$ & $\chi_1 > 0.7$ & $\chi_2 < -0.5$	Always
	$q > 40$ & $\chi_1 > 0.9$	$f^{\ell m}_{\rm Int_{1,2}}$ still alive
33	$q > 40$ & $\chi_1 > 0.9$	$f^{\ell m}_{\rm Int_{1,2}}$ still alive
32	$q > 2.5$ & $\chi_1 < -0.6$ & $\chi_2 > 0$	Always
	$\chi_1 < -0.9$ & $\chi_2 < -0.9$	Always
	$q > 40$ & $\chi_1 > 0.9$	$f^{\ell m}_{\rm Int_{1,2}}$ still alive
44	$q > 40$ & $\chi_1 > 0.9$	$f^{\ell m}_{\rm Int_{1,2}}$ still alive

with the IMRPHENOMXAS model (see Subsec. VII B. of [1]). For these modes, we do not impose any boundary condition, which leaves us with a total of five free coefficients, which we determine by solving the linear system

$$\frac{d\phi^{\rm Int}_{\ell m}}{df}(f^i_{\ell m}) = \mathcal{F}^i_{\ell m}, \quad i \in [1,5]\,. \tag{3.39}$$

In the above equation, $f^i_{\ell m}$ are the frequencies of the intermediate-region collocation points, and $\mathcal{F}^i_{\ell m}$ are the values of the phase-derivative evaluated at each $f^i_{\ell m}$, as reconstructed through our parameter space fits.

In the reconstruction of the $(3,2)$ mode, we allow a^{32}_3 to be non-zero: this extra degree of freedom allows to have better control on the effects caused by mode-mixing (see Fig. 3.7). In this case only, we impose two boundary conditions coming from the ringdown-region, where the $(3,2)$ phase is also fully calibrated [1]. We determine the six free coefficients of Eq. (3.38) by solving the system

$$\begin{aligned}
\frac{d\phi^{\rm Int}_{32}}{df}(f^i_{32}) &= \mathcal{F}^i_{32}, \quad i \in [1,4]\,,\\
\frac{d\phi^{\rm Int}_{32}}{df}(f^{32}_{RD}) &= \frac{d\phi^{\rm RD}_{32}}{df}(f^{32}_{RD}),\\
\frac{d^2\phi^{\rm Int}_{32}}{df}(f^{32}_{RD}) &= \frac{d^2\phi^{\rm RD}_{32}}{df}(f^{32}_{RD}).
\end{aligned} \tag{3.40}$$

The explicit expressions for the frequencies of our intermediate-region collocation points are given in Tab. 3.7. These values result from taking a mixture of equidistant and

[1] Notice that, when mode-mixing is absent, the ringdown is built through an appropriate rescaling of the quadrupole's phase and does not contain any information about the physical relative time-shifts among the modes.

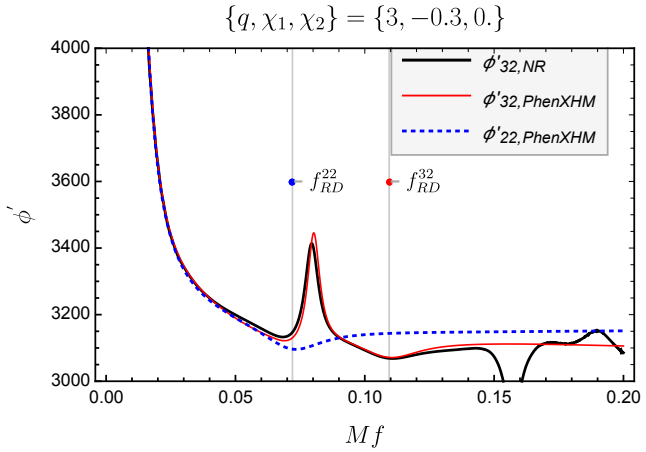

FIGURE 3.7: The plot shows the phase derivatives of the $(3,2)$ mode of a Fourier domain hybrid waveform with parameters $(q, \chi_1, \chi_2) = \{3, -0.3, 0.\}$, compared with the reconstructed $(2,2)$ and $(3,2)$ modes. The $(3,2)$ phase derivative does not show the usual fall-off in the ringdown region, due to mode-mixing with the $(2,2)$.

Gauss-Chebyshev nodes in the interval $\left[\beta(\eta) f^{\ell m}_{\rm Ins}, f^{\ell m}_{End}\right]$, where

$$f^{\ell m}_{End} = \begin{cases} f^{\ell m}_{\rm ring} & \text{if } (\ell, m) \neq (3,2) \\ \\ f^{22}_{\rm ring} - 0.5 f^{22}_{\rm damp} & \text{if } (\ell, m) = (3,2) \end{cases}$$

and $\beta(\eta)$ is a monotonically decreasing function of η that shifts forward the frequency of the first collocation points for small η, thus reducing the steepness of the parameter space fit surfaces in this limit, chosen here as $\beta(\eta) := (1. + 0.001(0.25/\eta - 1))$.

TABLE 3.7: Frequencies of the collocation points used in the reconstruction of the intermediate phase derivative.

	Collocation point frequencies
$f^1_{\ell m}$	$\beta(\eta) f^{\ell m}_{\rm Ins}$
$f^2_{\ell m}$	$\frac{1}{4}\left(\left(\sqrt{3}+2\right)\beta(\eta) f^{\ell m}_{\rm Ins} - \left(\sqrt{3}-2\right) f^{\ell m}_{\rm End}\right)$
$f^3_{\ell m}$	$\frac{1}{4}(f^{\ell m}_{\rm End} + 3\beta(\eta) f^{\ell m}_{\rm Ins})$
$f^4_{\ell m}$	$\frac{1}{2}(f^{\ell m}_{\rm End} + \beta(\eta) f^{\ell m}_{\rm Ins})$
$f^5_{\ell m}$	$\frac{1}{4}(3 f^{\ell m}_{\rm End} + \beta(\eta) f^{\ell m}_{\rm Ins})$
$f^6_{\ell m}$	$\frac{1}{8}(7 f^{\ell m}_{\rm End} + \beta(\eta) f^{\ell m}_{\rm Ins})$

We find it convenient to model one more collocation point than what is strictly needed, in order to add some flexibility to the calibration. Our standard choice of collocation

points can result in a badly-behaved reconstruction in regions of the parameter space where we have fewer calibration waveforms, such as the high spin and/or low-η regime. In such cases, we drop one of the collocation points close to inspiral, where the phase derivative has a steeper slope and is harder to model accurately, and replace it with a point in the flatter near-ringdown region, as we illustrate in Fig. 3.8.

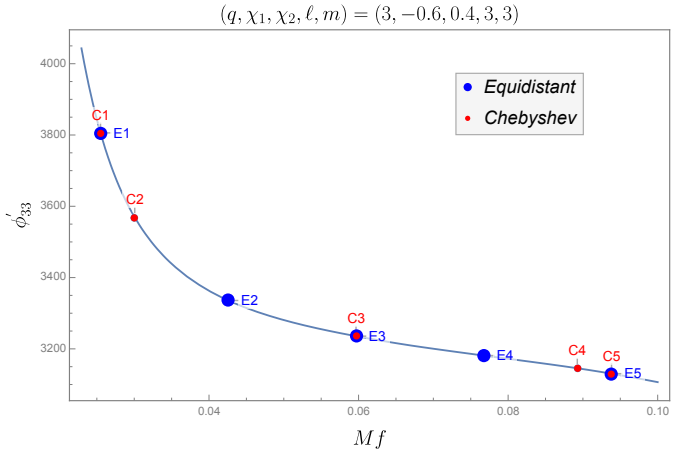

FIGURE 3.8: We compare two different sets of collocation points in the intermediate region of the $(3, 3)$ phase-derivative. Gauss-Chebyshev nodes are marked in red, while equidistant nodes are marked in blue. We compute parameter space fits of the phase-derivative evaluated at the points $[\text{C1}, \text{C2}, \text{E2}, \text{E3}, \text{E4}, \text{E5}]$. The default set of collocation points is $[\text{C1}, \text{C2}, \text{E2}, \text{E3}, \text{E5}]$; in regions with fewer calibration waveforms, we switch to the subset $[\text{C1}, \text{C2}, \text{E3}, \text{E4}, \text{E5}]$, which contains more points close to the ringdown. Here, the phase-derivative becomes flatter and our parameter space fits are more robust.

3.6 Ringdown model

The ringdown region covers the frequency range

$$Mf \in \left[f_{\rm RD}^{\ell m}, 0.3\right], \tag{3.41}$$

where $f_{\rm RD}^{\ell m}$ was defined in Eq. (3.36).

In IMRPhenomXHM, the modes $(2, 1), (3, 3), (4, 4)$ have a fully calibrated amplitude, while their phase is built by appropriately rescaling the quadrupole's phase, along the lines of IMRPhenomHM.

When mode-mixing visibly affects the ringdown waveform (i.e. in the $(3, 2)$ mode reconstruction), the model is instead fully calibrated to NR. In this case, the key observation is that the signal is much simpler when expressed in terms of spin-weighted spheroidal harmonics, as we illustrate in Figs. 3.9 and 3.10. This can be traced back to the fact that the Teukolsky equation is fully separable only in a basis of spheroidal harmonics, and not in a spherical-harmonic one [64].

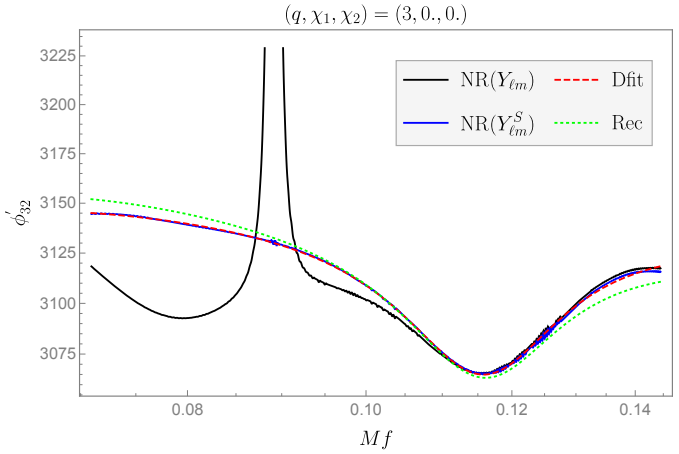

FIGURE 3.9: The phase derivative of the $(3, 2)$ mode can exhibit sharp features when plotted in the original spherical-harmonic basis (black solid line). However, the same signal written in terms of spheroidal harmonics is much simpler (blue solid line) and amenable to be fitted with the same ansatz used in IMRPHENOMXAS and IMRPHENOMD. Red and green lines mark the direct fit to the data and the final reconstruction.

Under the simplifying assumption that the $(3, 2)$ mode interacts only with the $(2, 2)$-mode, the spherical-harmonic strains can be projected onto a spheroidal-harmonic basis by means of a simple linear transformation, which we describe in App. 3.A. We reconstruct amplitude and phase of the signal in a spheroidal-harmonic basis and then transform the full waveform back into the original basis. After doing so, the ringdown reconstruction can be smoothly connected to the inspiral-merger waveform.

In the following subsections, we provide further details about the ansätze used in this region.

3.6.1 Amplitude

The ansatz we adopt is similar to the one used in IMRPHENOMXAS:

$$\frac{A^{\ell m}_{RD}}{A^{22}_{0}} = \frac{1}{f^{\frac{1}{12}}} \frac{|a_\lambda| \, f^{\ell m}_{damp} \, \sigma}{\left(f - f^{\ell m}_{ring}\right)^2 + \left(f^{\ell m}_{damp} \, \sigma\right)^2} e^{-\frac{\left(f - f^{\ell m}_{ring}\right) \lambda}{f^{\ell m}_{damp} \sigma}}, \tag{3.42}$$

except for the factor $f^{-1/12}$ used here for historical reasons and for the replacement of the $(2, 2)$ ringdown and damping frequencies with those of the corresponding (ℓ, m) mode. This ansatz is used for all the modes calibrated in the model. Notice, however, that for the $(3, 2)$ mode the ansatz is fitted to the data expressed in a spheroidal-harmonic basis, see Fig. 3.10.

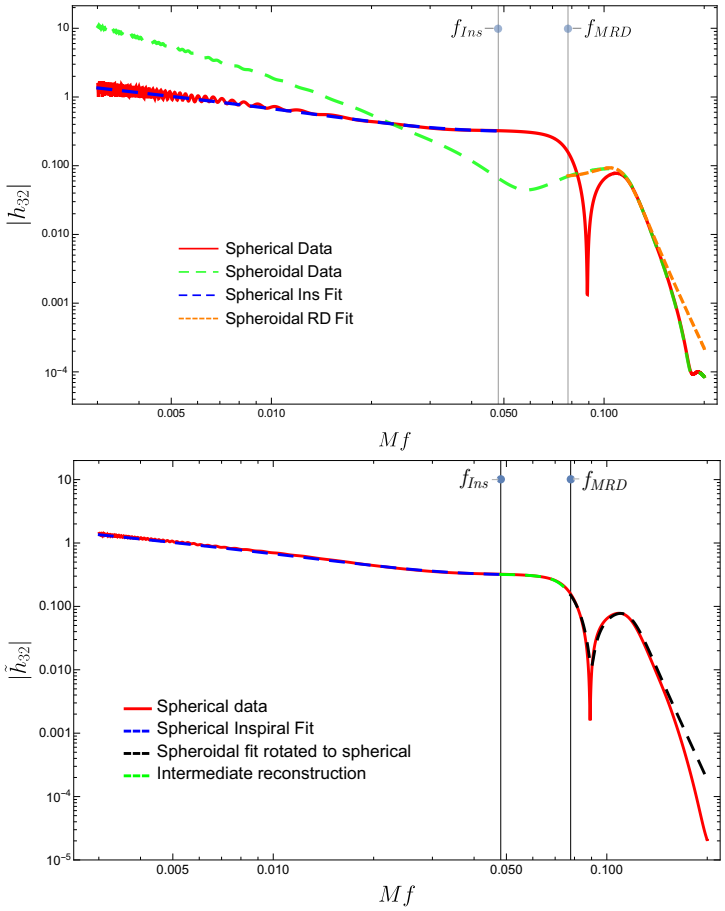

FIGURE 3.10: Top: The amplitude of the (3,2) mode expressed in a *spherical* (red) and *spheroidal* (green) basis for a $\{q, \chi_1, \chi_2\} = \{3, 0, 0\}$ case. The latter can be easily fitted using the ansatz (3.42) (orange curve). The inspiral portion of the amplitude is fitted in a spherical-harmonic basis (blue dashed line), therefore the ringdown waveform must be transformed back to the original basis before being smoothly attached to the rest of the model. Bottom: NR data and final reconstruction in spherical-harmonics for the same case plotted in the top panel. The black line is the transformation to a spherical-harmonic basis of the orange curve in the top plot (which is computed instead in a spheroidal-harmonic basis) . The green line is a smooth connection between the inspiral and ringdown fits (blue and black lines respectively) that goes through the two collocation points in the intermediate region.

We first fit the free coefficients $\{a_\lambda, \lambda, \sigma\}$ to NR data in a "primary" direct fit and then perform a parameter space fit of each coefficient for every mode. We find that the coefficient σ shows a very small dynamic range for the modes $(3,3)$, $(3,2)$ and $(4,4)$, and we thus take it as a constant. We then perform a "secondary" direct fit where we redo the direct fits using the constant values for σ shown in Tab. 3.8. Finally we repeat the parameter space fits for a_λ and λ.

The final reconstruction of the amplitude through inspiral, merger and ringdown for the modes without mixing can be seen in Fig. 3.11.

TABLE 3.8: Mode-specific values for the parameter σ appearing in Eq. (3.42). In the final model σ is taken to be fixed across parameter space except for the 21 mode. Here we show these fixed values, which correspond to an average across the parameter space of the values obtained through direct fits where σ is not specified a priori.

Mode	σ value
33	1.3
32	1.33
44	1.33

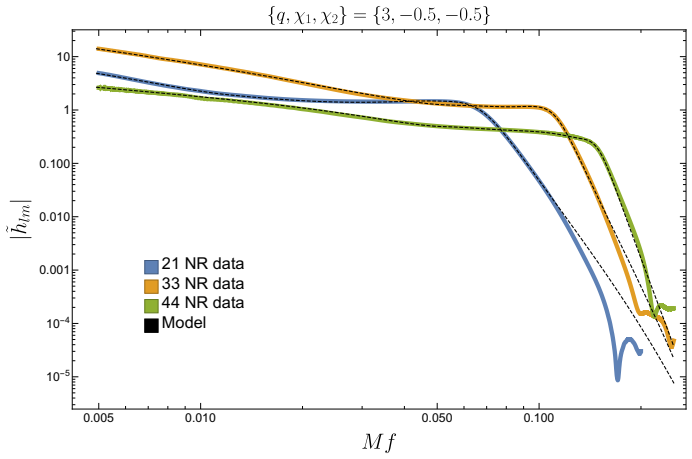

FIGURE 3.11: Comparison between the NR data and the final model for the amplitude of three modes for a system with $\{q, \chi_1, \chi_2\} = \{3, 0, 0\}$.

3.6.2 Phase

3.6.2.1 Modes without mode-mixing

To model the $(2,1), (3,3), (4,4)$ modes, for which mode-mixing is negligible, we rescale a simplified reconstruction of the quadrupole's ringdown phase, much in the spirit of IMRPHENOMHM.

Our ansatz for the phase-derivatives in this case reads:

$$\frac{d\phi^{\rm RD}_{\ell m}}{df} = \alpha_2^{\ell m} \frac{(f^{\ell m}_{ring})^2}{f^2} + \alpha_\lambda^{\ell m} \frac{f^{\ell m}_{\rm damp}}{(f^{\ell m}_{\rm damp})^2 + (f - f^{\ell m}_{ring})^2} + d\phi^{\ell m}_{\rm RD}, \tag{3.43}$$

which, integrated, gives:

$$\phi^{\rm RD}_{\ell m} = -\alpha_2^{\ell m} \frac{(f^{\ell m}_{ring})^2}{f} + \alpha_\lambda^{\ell m} \tan^{-1}\left(\frac{f - f^{\ell m}_{ring}}{f^{\ell m}_{\rm damp}}\right) + d\phi^{\ell m}_{\rm RD} f + \phi^{\ell m}_{\rm RD}, \tag{3.44}$$

We first compute parameter space fits of the quantities α_λ^{22} and α_2^{22} and rescale them to obtain their higher-modes counterparts. We set

$$\begin{aligned}\alpha_\lambda^{\ell m} &= \alpha_\lambda^{22},\\ \alpha_2^{\ell m} &= w_{\ell m}\frac{f_{\rm damp}^{22}}{f_{\rm damp}^{\ell m}}\alpha_2^{22},\end{aligned} \tag{3.45}$$

where $w_{\ell m}$ are some constants, which only depend on ℓ, m and not on the intrinsic parameters of the binary. We verified that the above equalities hold, albeit approximately, for the parameters of the direct fits to each mode's phase derivative.

The shifts $d\phi_{\rm RD}^{\ell m}$ and $\phi_{\rm RD}^{\ell m}$ are fixed by requiring a smooth connection to the intermediate-region reconstruction.

3.6.2.2 Modes with mode-mixing

As we outlined at the beginning of this section, the morphology of the $(3,2)$ mode ringdown signal is significantly affected by mode-mixing. In this case, we first build a reconstruction of the phase derivative in a spheroidal-harmonics base, using the ansatz below

$$\frac{d\phi_{32,S}}{df} = \frac{\alpha_2^{32}}{f^2} + \frac{\alpha_4^{32}}{f^4} + \alpha_\lambda^{32}\frac{f_{\rm damp}^{32}}{(f_{\rm damp}^{32})^2 + (f - f_{ring}^{32})^2} + d\phi_{\rm RD}^{32}. \tag{3.46}$$

Integrating the above equation, one obtains

$$\phi_{32,S} = -\frac{\alpha_2^{32}}{f} - \frac{\alpha_4^{32}}{3f^3} + \alpha_\lambda^{32}\tan^{-1}\left(\frac{f - f_{ring}^{32}}{f_{damp}^{32}}\right) + d\phi_{\rm RD}^{32} f + \phi_{\rm RD}^{32}, \tag{3.47}$$

where the subscript S is a reminder that we are now working in a spheroidal-harmonic basis. The four free coefficients of Eq. (3.46) are determined by solving the linear system

$$\frac{d\phi_{32,S}^{\rm RD}}{df}(f_{32}^i) = \mathcal{G}_{32}^i, \qquad i \in [1,4]\,, \tag{3.48}$$

where $\mathcal{G}_{32}^i$ are some parameter space fits of the value of the phase derivative, evaluated at four collocation points $f_{RD}^i, i \in [1,4]$, given in Tab. 3.9.

One must ensure that $\phi_{32,S}$ has the correct relative time and phase shift with respect to the $(2,2)$ mode that is being used, or else the transformation back to the original spherical-harmonic basis will produce an incorrect result. Therefore, we compute two

TABLE 3.9: Frequencies of the collocation points used in the reconstruction of the $(3,2)$ mode phase derivative.

Collocation points for $\phi'_{32,S}$	
f^1_{32}	$f^{22}_{\rm ring}$
f^2_{32}	$f^{32}_{\rm ring} - 3/2 f^{32}_{\rm damp}$
f^3_{32}	$f^{32}_{\rm ring} - 1/2 f^{32}_{\rm damp}$
f^4_{32}	$f^{32}_{\rm ring} + 1/2 f^{32}_{\rm damp}$

extra fits

$$\Delta T_{32,S} = \phi'_{32,S}(f_0) - \phi'_{22}(f_0) \tag{3.49}$$

$$\Delta \phi_{32,S} = \phi_{32,S}(f_1) - \phi_{22}(f_1), \tag{3.50}$$

at some suitable reference frequencies f_0, f_1 in the ringdown region, and use them to correctly align our spheroidal-harmonic reconstruction to the quadrupole's phase given by IMRPHENOMXAS.

In Fig. 3.12 we plot the $(3,2)$ mode of a hybrid waveform built from the SXS simulation SXS:BBH:0271 and show the corresponding time-domain reconstructions resulting from IMRPHENOMXHM and IMRPHENOMHM. The plot shows that our model can better capture the effects of mode-mixing on the ringdown waveform.

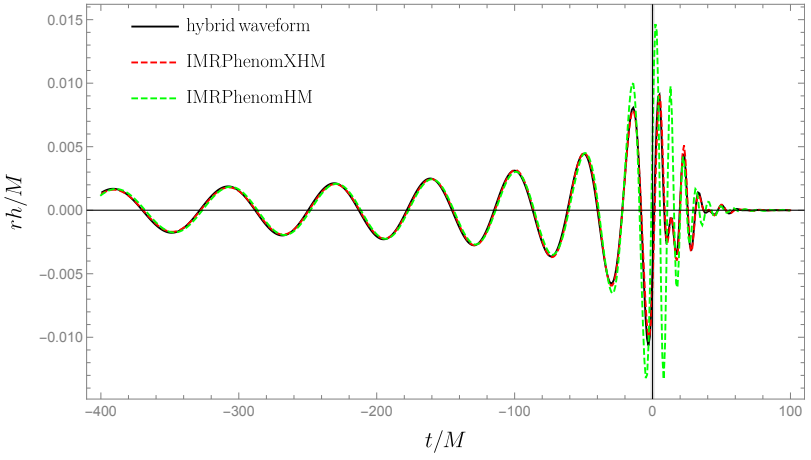

FIGURE 3.12: The plot shows the last few cycles of a hybrid $(3,2)$ mode waveform built hybridizing the SXS simulation SXS:BBH:0271 with SEOBNRv4 (black solid line), together with the corresponding IMRPHENOMXHM and IMRPHENOMHM reconstructions (red and green dashed lines respectively). The (22) modes of all waveforms have been previously time-shifted so that their amplitudes peak at $t = 0$.

3.7 Quality control

3.7.1 Single Mode Matches

To quantify the agreement between two single-mode waveforms (reals in time domain) we use the standard definition of the inner product (see e.g. [65]),

$$\langle h_1, h_2 \rangle = 4Re \int_{f_{min}}^{f_{max}} \frac{\tilde{h_1}(f)\, \tilde{h_2^*}(f)}{S_n(f)}, \tag{3.51}$$

where $S_n(f)$ is the one-sided power spectral-density of the detector. The *match* is defined as this inner product divided by the norm of the two waveforms and maximised over relative time and phase shifts between both of them,

$$\mathcal{M}(h_1, h_2) = \underset{t_0,\phi_0}{max} \frac{\langle h_1, h_2 \rangle}{\sqrt{\langle h_1, h_1 \rangle}\sqrt{\langle h_2, h_2 \rangle}}. \tag{3.52}$$

Accordingly, we define the mismatch between two waveforms as

$$\mathcal{MM}(h_1, h_2) = 1 - \mathcal{M}(h_1, h_2). \tag{3.53}$$

For our match calculations we use the Advanced-LIGO design sensitivity Zero-Detuned-High-Power PSD [66, 67] with a lower cutoff frequency for the integrations of 20 Hz.

In Fig. 3.13 we first show single-mode mismatches against a validation set consisting of 387 of our hybrid waveforms built from the latest SXS collaboration catalog, where we have discarded 152 hybrids, which show up as outliers in our calibration procedure for at least one of the modes, which we suspect to be due to quality problems with the waveforms. The list of SXS waveforms we have used is provided as supplementary material. The matches were computed for masses between $20M\odot$ and $300M\odot$, with a spacing of $10M\odot$ between subsequent bins.

We also show mismatches among IMRPhenomXHM, the previous IMRPhenomHM model and the independent NRHybSur3dq8 surrogate model. Total masses are log-uniformly distributed in the range $[3M_\odot, 150M_\odot]$ (with individual masses not smaller than $1M_\odot$). In Fig. 3.14 we show the mismatches for the calibration region of NRHybSur3dq8, for mass ratios below 9.09 and dimensionless spin magnitudes up to 0.8, and up to 0.5 in the neutron star sector of total masses up to $3M_\odot$. We carry out three sets of comparisons, in red we have the mismatches between IMRPhenomXHM and IMRPhenomHM, in blue IMRPhenomHM versus NRHybSur3dq8 and finally in green IMRPhenomXHM versus NRHybSur3dq8. The results show that IMRPhenomXHM

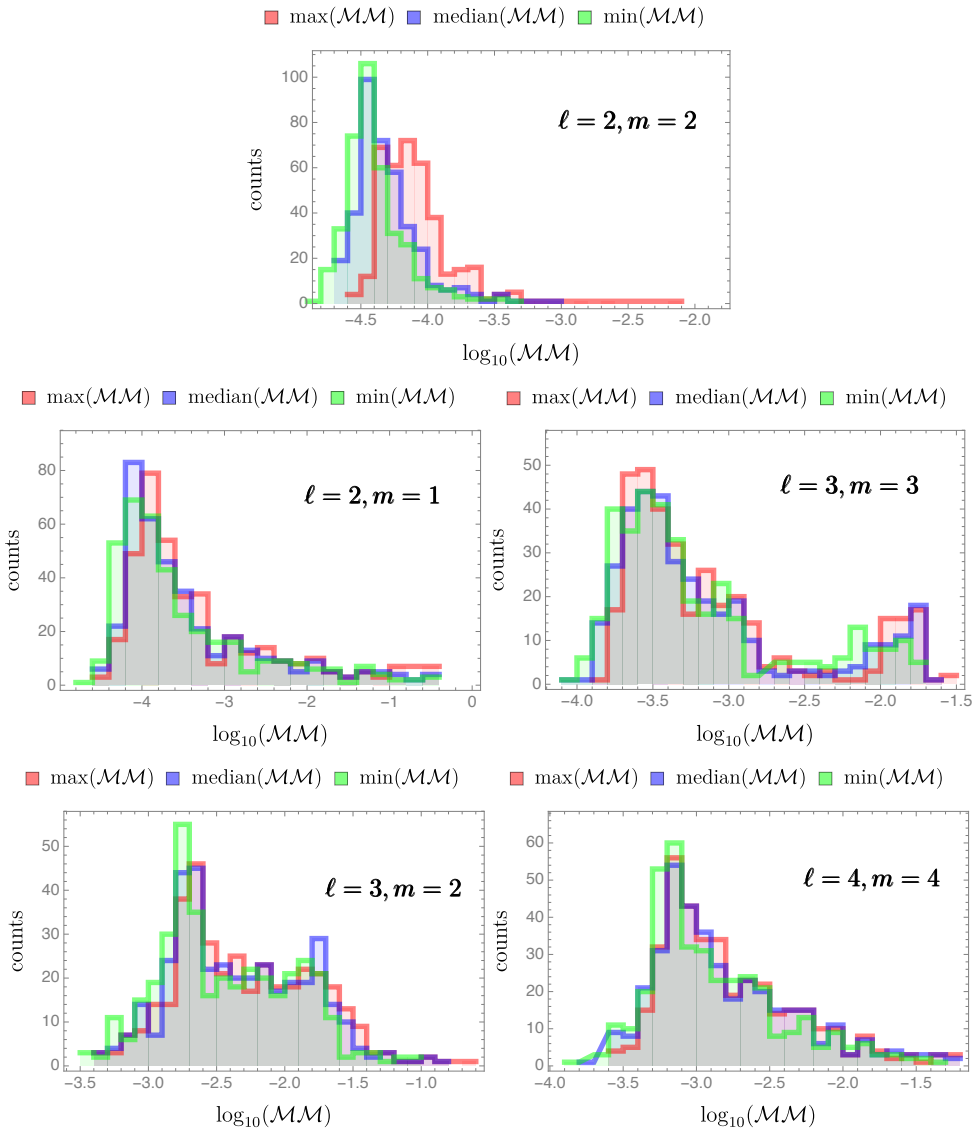

FIGURE 3.13: Mode-by-mode mismatches between IMRPHENOMXHM and a validation set of hybrids built using the latest release of the SXS collaboration catalog. Each plot shows the minimum (red), average (blue) and maximum (green) mismatch over a range of total masses between 20 and 300 solar masses.

is in a much better agreement with the surrogate model that the previous version IMRPHENOMHM, the improvement is particularly remarkable for the $(3, 2)$ mode due to the modelling of the mode-mixing. In Fig. 3.15 we show matches for cases outside of the spin region defined before to assess the effects of extrapolation beyond the calibration region.

3.7.2 Multi-Mode Matches

When having a multi-mode waveform, not only it is important to model accurately each individual mode but also the relative phases and time shifts between them. To test

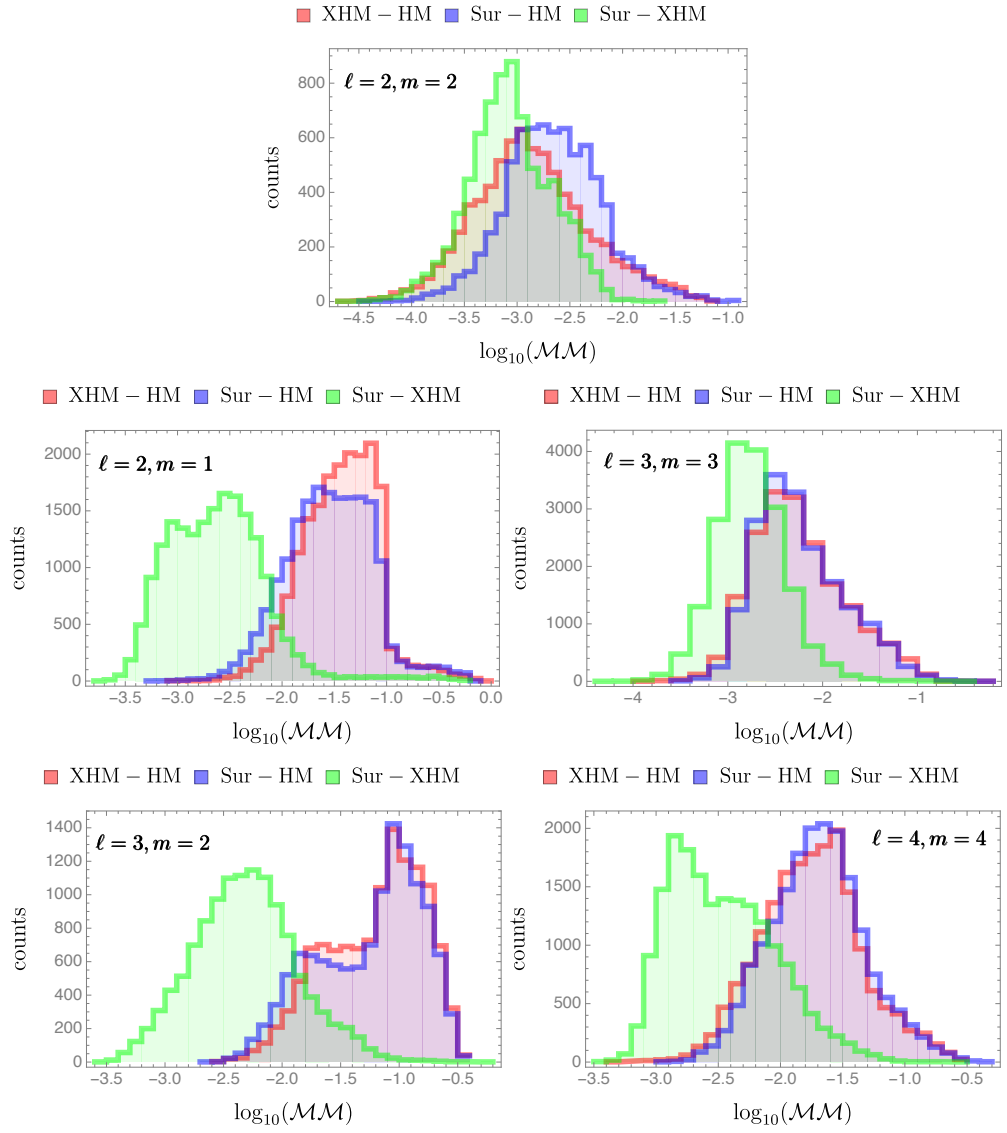

FIGURE 3.14: Mismatches between different models for all the modes modelled by IMRPHENOMXHM with the aLIGOZeroDetHighPower PSD (see the main text for further details). The parameter range is restricted to avoid extrapolation as detailed in the main text.

this we compute the mismatch for the h_+ and $h_\times$ polarizations between our hybrids and the model for three inclination values: 0, $\pi/3$ and $\pi/2$ (rad). The polarizations for the hybrids and the model are built with the same inclination, however the azimuthal angle entering the spherical harmonics can be different. We denote by ϕ_S and ϕ_T the azimuthal angle of the hybrids (source) and model (template) respectively. ϕ_S takes the values of an equally spaced grid of five points between 0 and 2π. Then for each value of ϕ_S we numerically optimize the value of ϕ_T that gives the best mismatch. For each configuration of inclination and ϕ_S the mismatch is computed for an array of 8 total masses from $20M_\odot$ to $300M_\odot$ logarithmically spaced and then we take the minimum, median and maximum values over all these configurations. Similarly to the single-mode

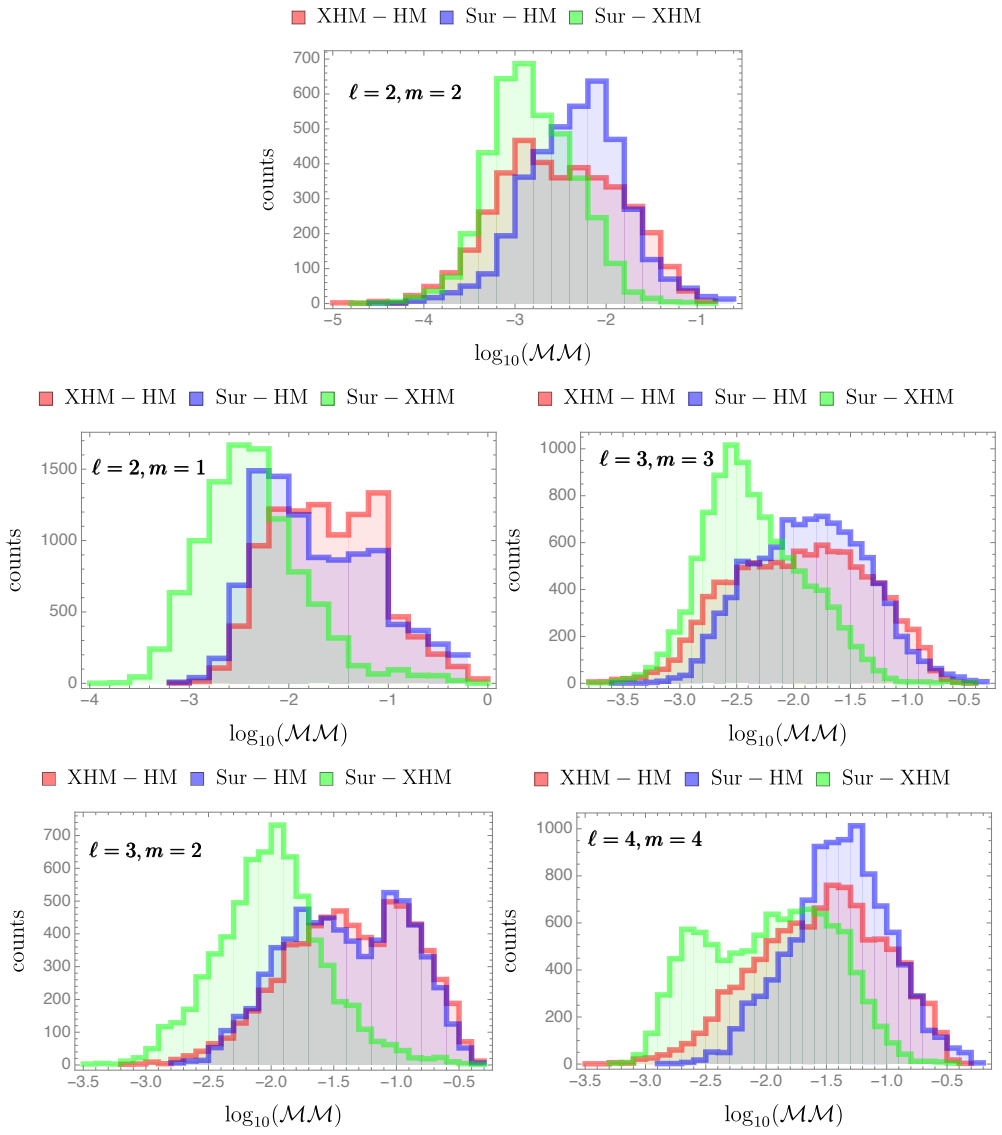

FIGURE 3.15: Mismatches between different models for all the modes modelled by IMRPHENOMXHM with the aLIGOZeroDetHighPower PSD (see the main text for further details). The parameter range is chosen to test the extrapolation region of parameter space detailed in the main text.

matches we used the Advanced-LIGO design sensitivity Zero-Detuned-High-Power noise curve and a lower cutoff of 20 Hz. The results are shown in Fig. 3.16. It can be observed that the mismatches degrade for higher inclinations due to the weaker contribution of the dominant $(2, 2)$ mode which is the best modelled mode, although events that are seen close to edge-on are much less likely to be detected due to the reduced signal-to-noise-ratio. For edge-on systems we only show results for the h_+ polarization, since the $h_\times$ vanishes. Alternative ways of quantifying multi-mode mismatches have been used in the literature, see e.g. [68] or [69], with different advantages and drawbacks. The quantities we show here are chosen for simplicity.

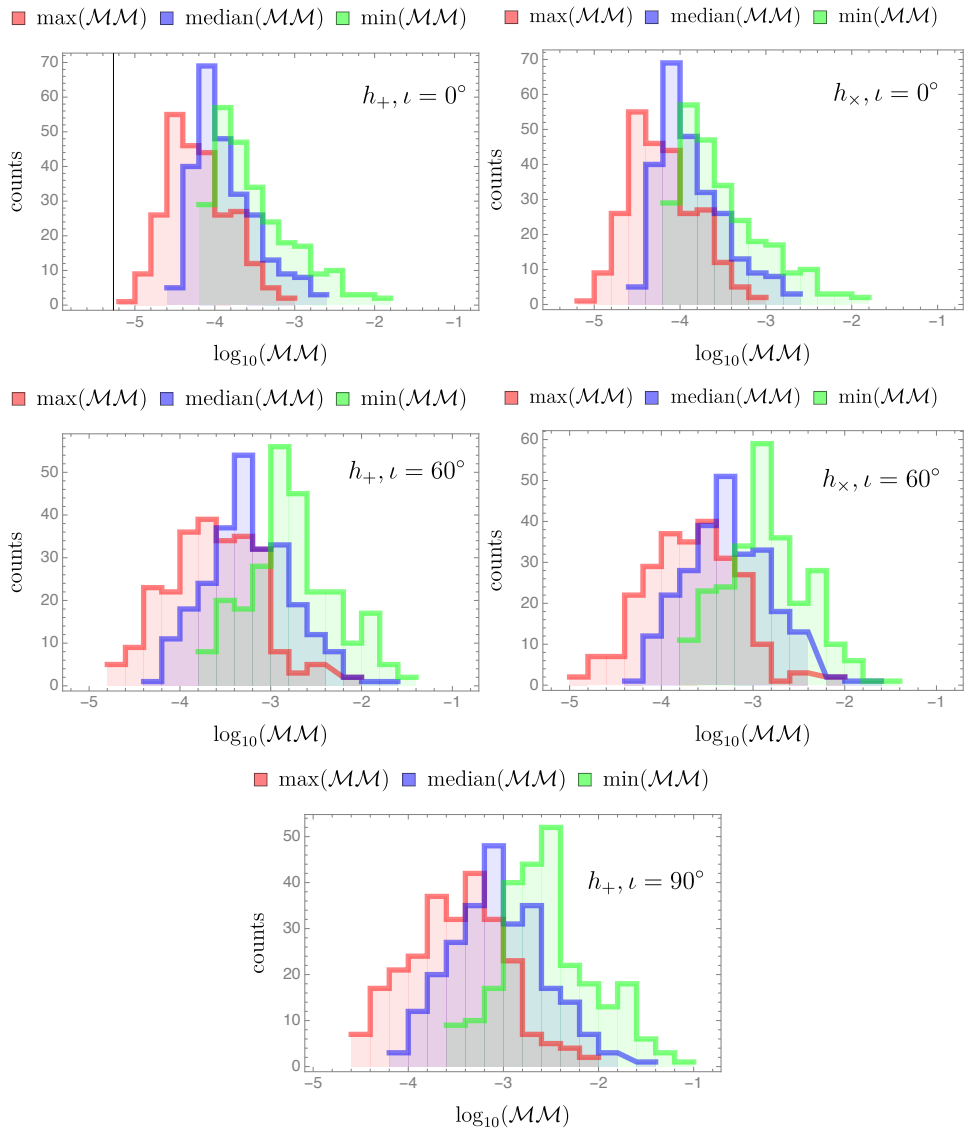

FIGURE 3.16: Mismatches for the h_+(left) and $h_\times$(right) polarizations between hybrids and IMRPHENOMXHM for three different inclinations. For edge-on systems we only show results for the h_+ polarization since $h_\times$ vanishes. The minimum, maximum and median legends are taken over the range of total masses and azimuthal angle ϕ_S for the hybrids. The mismatch is numerically optimized over the azimuthal angle ϕ_T of the model (see main text for the details).

3.7.3 Recoil

Asymmetric black-hole binaries will radiate gravitational waves anisotropically. This will result in a net emission of linear momentum, at a rate (in geometric units)

$$\frac{dP^k}{dt} = \frac{r^2}{16\pi} \int d\Omega \left(\dot{h}_+^2 + \dot{h}_\times^2\right) n^k, \tag{3.54}$$

where n^k is the radial unit-vector pointing away from the source, leading the final remnant to recoil in the opposite direction. The precise value of the final recoil velocity will depend

on the interactions among different GW multipoles. This quantity is extremely sensitive to the relative time and phase shifts among different modes and thus provides an excellent and physically meaningful test-bed for our model.

We computed the final recoil velocity predicted by IMRPhenomXHM for different binary configurations and compared the results with those obtained directly from our hybrid waveforms. As new numerical simulations became available, several works presented increasingly improved NR-based fits for the final recoil velocity (see for instance [70–73] and the latter reference for further works and comparisons). Below we compare our results to the fit of Ref. [71], for two test configurations: a black-hole binary where both bodies are non-spinning (Fig. 3.17), and one where both are spinning with Kerr parameters $\chi_1 = \chi_2 = 0.5$ (Fig. 3.18). For comparison, we also show the recoil velocities obtained with IMRPhenomHM.

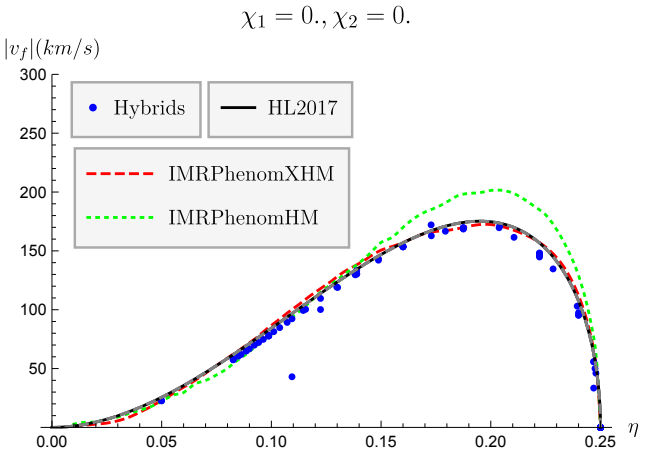

Figure 3.17: In this plot we show the absolute value of the final recoil velocity for a non-spinning black-hole binary, as computed with IMRPhenomXHM (in red) IMRPhenomHM (green), and with the fit of Ref. [71] (black). In blue we show the recoil velocity for all the non-spinning configurations in our calibration dataset. We can see that, when a good number of NR waveform is available, our calibrated model can reproduce with great accuracy the final velocity of the remnant.

3.7.4 Time-domain behaviour

We have checked that the model has a reasonable behaviour in regions of the parameter space where no simulations are available (e.g. $18 \leq q \leq 200$) and for extreme spins. We show here example-waveforms to test both these regimes. Figs. 3.19 and 3.20 show single-mode waveforms for binaries with parameters $(q, \chi_1, \chi_2) = (4, 1, 1)$ and $(q, \chi_1, \chi_2) = (100, 0.7, 0.7)$, respectively. We can see that in both cases the model returns well-behaved waveforms.

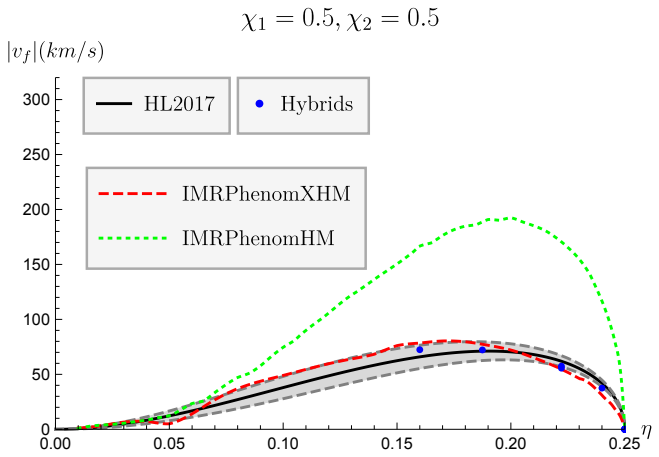

FIGURE 3.18: In this plot we show the absolute value of the final recoil velocity $|v_f|$ for an equally-spinning black-hole binary with adimensional spins $\chi_1 = \chi_2 = 0.5$, as computed with IMRPHENOMXHM (in red) IMRPHENOMHM (green), and with the fit of Ref. [71] (black, note that here we also shade in gray the fit's error margins, using the error estimates provided by the authors in Tab. IV of the aforementioned reference). In blue we show the recoil velocity for all the corresponding configurations in our calibration dataset. Note that, despite the loss of accuracy due to having fewer waveforms than in the non-spinning case, our model returns a value of $|v_f|$ much closer to NR than the uncalibrated version.

3.7.5 Parameter estimation: GW170729

In our companion paper to present IMRPHENOMXAS for the $(2, 2)$ mode we re-analyzed the data for the first gravitational wave event, GW150914, as an example for an application to PE. Here we present a re-analysis of GW170729, where the effect of models with subdominant higher harmonics has been discussed in the literature [16], and we will demonstrate broad agreement between IMRPHENOMXHM, IMRPHENOMHM and SEOBNRv4HM for this event. Again we use coherent Bayesian inference methods to determine the posterior distribution $p(\vec{\theta}|\vec{d})$ to derive expected values and error estimates for the parameters of the binary. Following [16], we use the public data for this event from the Gravitational Wave Open Science Center (GWOSC) [74–76] calibrated by a cubic spline and the PSDs used in [8]. We analyze four seconds of the strain data set with a lower cutoff frequency of 20Hz. For our analysis we use the `LALInference` [9] implementation of the nested sampling algorithm. We perform the runs using 2048 'live points' for five different seeds, then merge into a single posterior result. We choose the same priors used in [16], taking into account that IMRPHENOMXHM is a non-precessing model and we have to use aligned spin priors.

In Fig. 3.21 we compare our results with the higher mode models (IMRPHENOMHM and SEOBNRv4HM) and the (2,2) mode model results (IMRPHENOMD) published in [16]. We find that the posteriors derived from IMRPHENOMXHM are consistent with

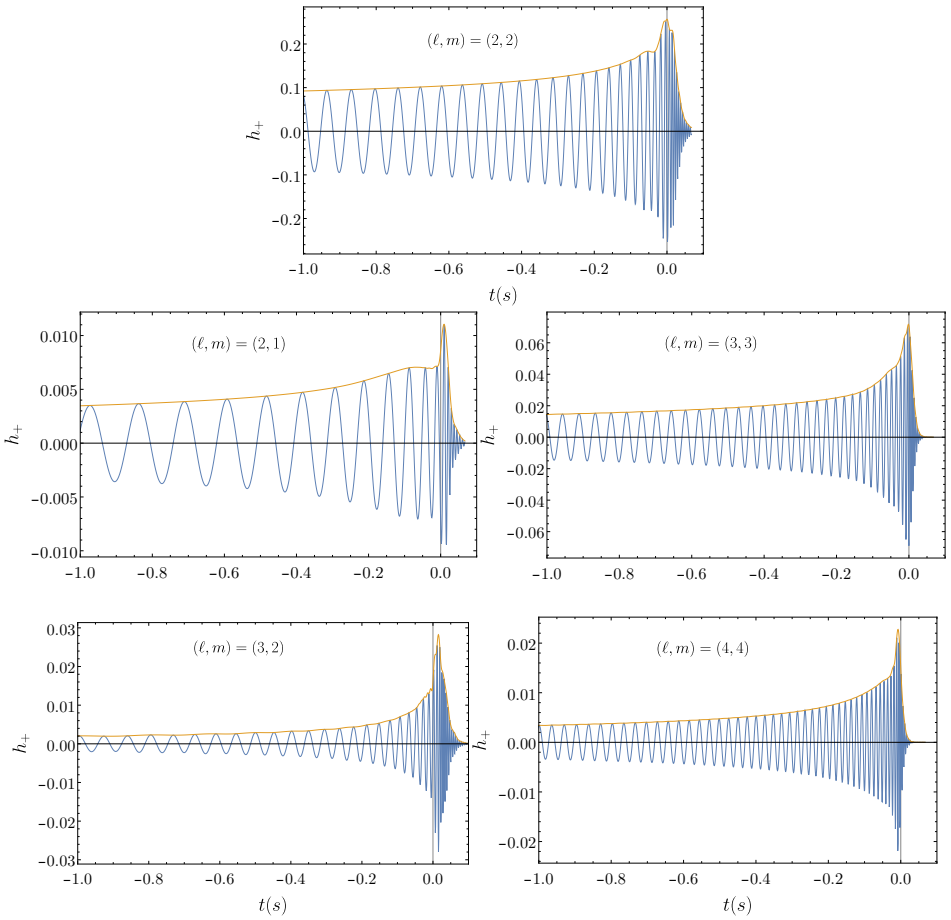

FIGURE 3.19: Single-mode waveforms for a binary with $q = 4$, with maximally spinning black holes. The model appears to extrapolate well beyond its calibration region ($|\chi_{1,2}| \leq 0.99$).

the two other models that include higher harmonics, which can be distinguished from the results obtained for models that only include the (2,2) mode.

3.7.6 NR injection study

As a further test of the improvements brought by IMRPHENOMXHM, we have performed PE of a synthetic signal generated using the public SXS waveform SXS:BBH:0110. This corresponds to a binary with strongly asymmetric masses ($q = 5$), and adimensional spin magnitudes $\chi_1 = 0.500, \chi_2 = 0.$ at a reference frequency of 20 Hz. We injected the signal into a Hanford-Ligo-Virgo detector network in zero-noise and used Advanced-LIGO design sensitivity PSDs. The mock signal had chirp mass $\mathcal{M} = 18.96 M_\odot$ and total mass $62 M_\odot$ in detector frame, right ascension ra $= 1.4$ rad, declination dec $= -0.6$ rad and geocentric time $t_c = 1126259600.0$ s. The source was placed at a luminosity distance $d_L = 600$ Mpc at an inclination $\iota = \pi/3$. The network SNR of this configuration was 17.9. For this analysis we used the gravitational-wave inference library PBILBY

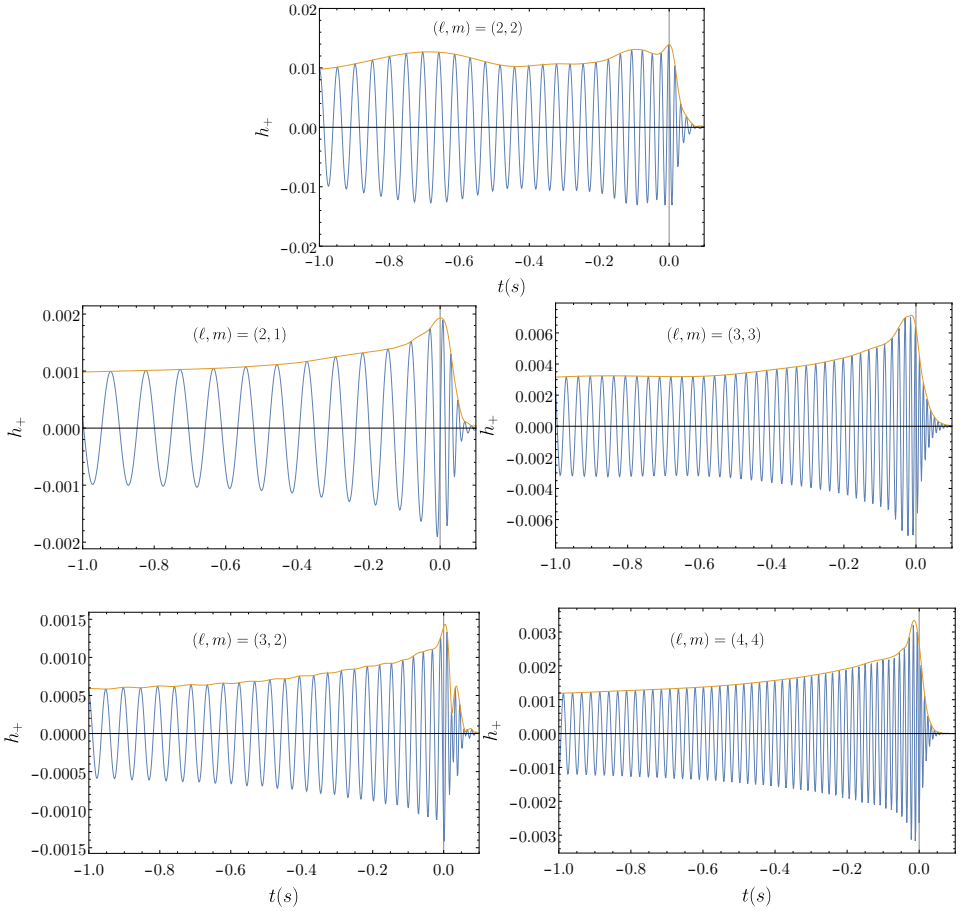

FIGURE 3.20: Single-mode waveforms for a binary with $q = 100, \chi_1 = \chi_2 = 0.7$. There are no NR simulations in our calibration dataset with $q > 18$, and the extrapolation to high mass-ratios is done by placing Teukolsky waveforms at the large-q boundary of the parameter space, as explained in Subsec. 3.3.2. Here we can see that the model achieves a smooth transition between NR and point-particle physics.

[10, 77] with dynamic nested sampling [78] and 2048 live points. We present our results in Fig. 3.22 and 3.23. IMRPHENOMXHM delivers a better recovery of the mass ratio (centre panel of Fig. 3.22) and, although the measurement of $\chi_{\rm eff}$ is very consistent with IMRPHENOMHM, the spin of the primary appears to be more tightly constrained by the upgraded model.

3.7.7 Computational cost

We will now compare the computational cost of the evaluation of different models available in `LALSimulation` compared to the IMRPhenomX family. Since the different models include a different number of modes we also show the evaluation time per mode. Using the `GenerateSimulation` executable within `LALSimulation` we compute the average evaluation time over 100 repetitions for a non-spinning case $(q, \chi_1, \chi_2) = (1.5, 0, 0)$ for a frequency range of 10 to 2048 Hz. We vary the total mass of the system from 3 to

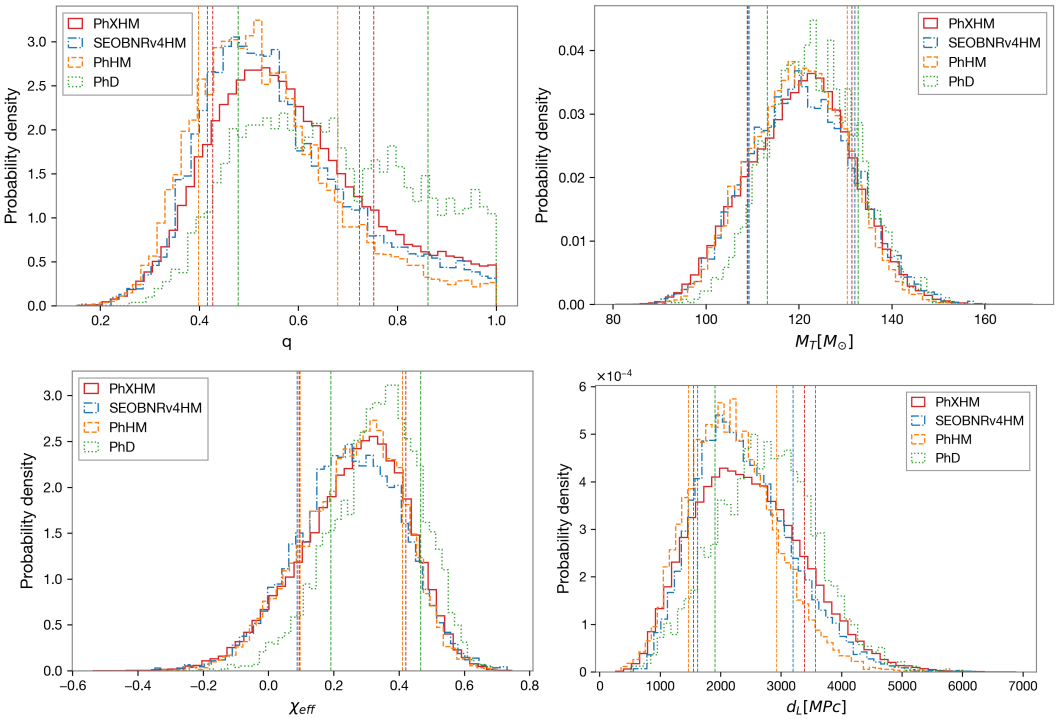

FIGURE 3.21: Comparison between IMRPHENOMXHM, IMRPHENOMHM, SEOBNRv4HM and IMRPHENOMD (results for the latter three models are taken from [16]) for the event GW170729 as discussed in Sec. 3.7.5. We show posterior distributions of mass ratio, total mass, effective aligned spin and luminosity distance. The dashed vertical lines mark the 90% confidence limits.

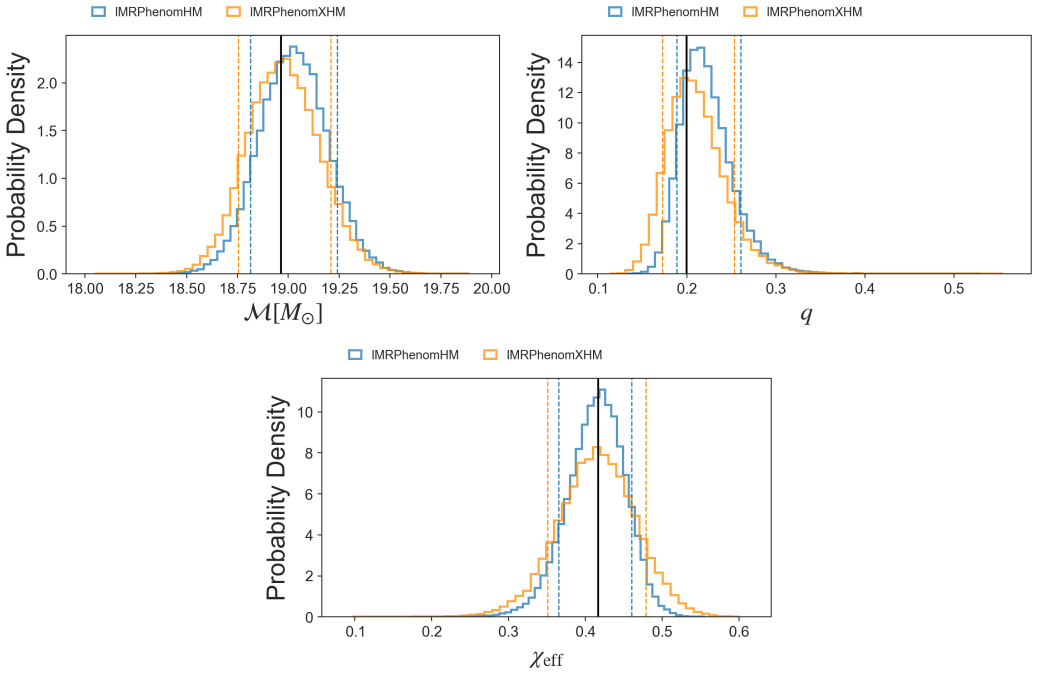

FIGURE 3.22: 1D posterior distributions for some of the mass and spin parameters characterizing the mock signal generated using the public SXS simulation SXS:BBH:0110. Results obtained with IMRPHENOMXHM and IMRPHENOMHM are plotted in orange and blue respectively. A vertical black line marks the injected value. Dashed lines indicate 90% credible intervals.

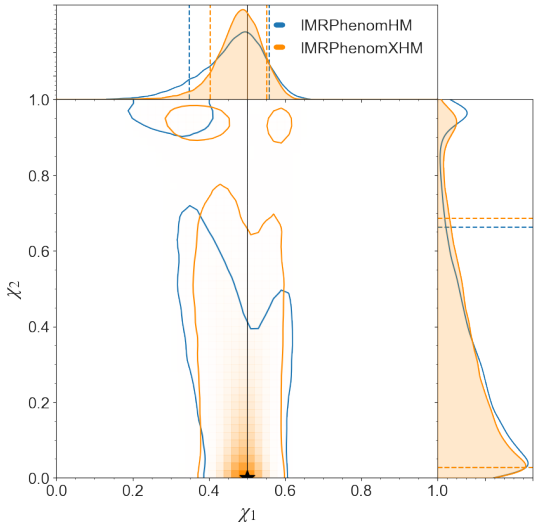

FIGURE 3.23: Joint posterior distributions for the individual spins χ_1, χ_2. Dashed lines indicate 90% credible intervals. Solid black lines mark the injected values for each parameter (note that the secondary has zero spin, and therefore the line in this case coincides with the x-axis).

300 solar masses and the frequency spacing *df* is automatically chosen by the function `SimInspiralFD` to take into account the length of the waveform in the time domain for the given parameters. All the timing calculations were carried out in the LIGO cluster CIT to allow comparison with the benchmarks we have shown in [30] to compare different accuracy thresholds of multibanding which is a technique that accelerate the evaluation of the model by evaluating it in a coarser non-uniform frequency grid and using interpolation to get the waveform in the final fine uniform grid, reducing considerably the computational cost.

In Fig. 3.24 the dashed lines represent models for only the $(2, 2)$ mode (IMRPHENOMD, SEOBNRV4_ROM and IMRPHENOMXAS). We see that the three models show very similar performance for low masses, while for higher masses the IMRPhenom models are faster. Models that include higher modes are shown with solid lines: NRHYBSUR3DQ8 (11 modes), IMRPHENOMHM (6 modes) and IMRPHENOMXHM (5 modes), the latter is shown with and without the acceleration technique of multibanding [30]. Since NRHYBSUR3DQ8 is a time domain model, for many applications the actual evaluation time would also include the time for the Fourier transformation to the frequency domain, which can also lead to requirements for a lower start frequency and windowing to avoid artefacts from the Fourier transforms, which again would increase evaluation time. We also see that the new model IMRPHENOMXHM without multibanding is already significantly faster than the previous IMRPHENOMHM model. Comparing the new model to the surrogate, IMRPHENOMXHM without multibanding is significantly faster when considering all the modes, but the evaluation cost per mode is only lower for high masses.

However, using the multibanding technique [30] with the threshold value of 10^{-3}, which is the default setting when calling the model in LALSuite (IMRPhenomXHM_MB3 in the plot), IMRPhenomXHM is significantly faster also for the evaluation time per mode. The threshold value can be adjusted to control the speed and accuracy of the algorithm as explained in appendix 3.C and in [30], where we have shown that for an example injection of a relatively high signal-to-noise ratio 28, even at a threshold of 10^{-1}, which evaluates significantly faster than the conservative default setting, differences in posteriors are hardly visible.

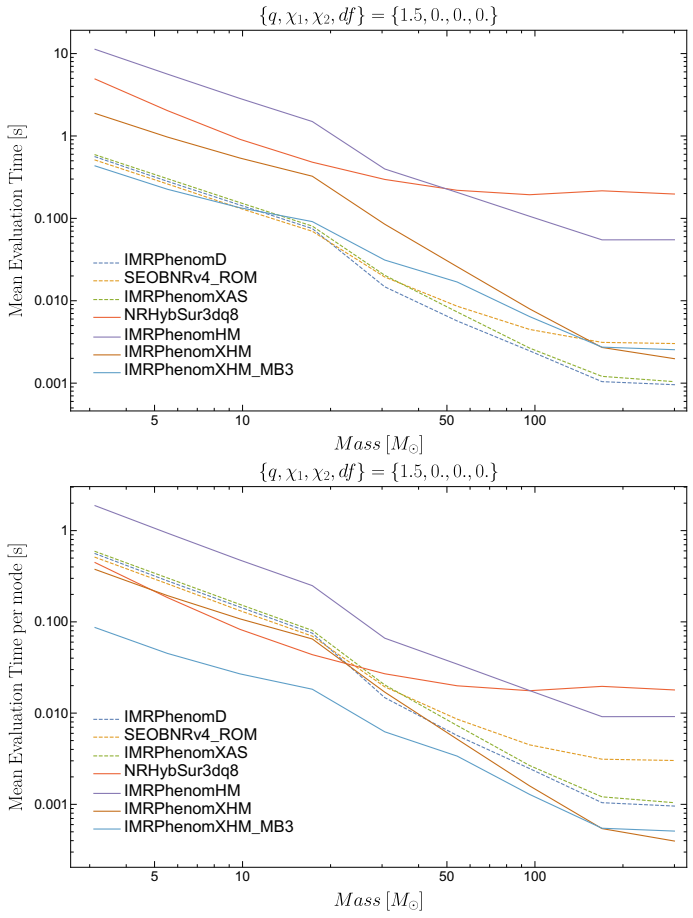

FIGURE 3.24: Evaluation time of different waveform models in `LALSimulation`. Top panel: we show the total contribution of the evaluation of the quadrupolar/multimode waveform. Bottom panel: evaluation time per mode, the models include different numbers of modes, so we average over this number for a fair comparison.

3.8 Conclusions

Phenomenological waveform models in the frequency domain have become a standard tool for gravitational wave PE [8] due to their computational efficiency, accuracy [79], and simplicity. The current generation of such models has been built on the IMRPhenomD

model for the (2,2) mode of the gravitational wave signal of non-precessing and non-eccentric coalescing black holes, which has been extended to precession by the IMRPhenomP [4, 80] and IMRPhenomPv3 [33] models, to sub-dominant harmonics by the IMRPhenomHM model, and to tidal deformations by the IMRPhenomPv2_NRTidal model [81, 82].

The present paper is the second in a series to provide a thorough update of the family of phenomenological frequency domain models: In a parallel paper [1] we have presented IMRPhenomXAS, which extends IMRPhenomD to a genuine double spin model, includes a calibration to extreme mass ratios, and improves the general accuracy of the model. In the present work we extend IMRPhenomXAS to subdominant modes. Contrary to IMRPhenomHM, the IMRPhenomXHM model we present here is calibrated to numerical hybrid waveforms, and we have tested in Sec. 3.7 that the new model is indeed significantly more accurate than IMRPhenomHM.

Calibration of the model to comparable mass numerical data has proceeded in two steps: we have started with a data set based on NR simulations we have performed with the BAM and Einstein Toolkit codes, and the data set corresponding to the 2013 edition of the SXS waveform catalog [52] (including updates up to 2018). The quality and number of waveforms available at the time has determined the number of modes we model in this paper, i.e. the $(2,1), (3,2), (3,3)$ and $(4,4)$ spherical harmonics. During the implementation of the model in LALSuite [2], the 2019 edition of the SXS waveform catalog [58] became available, and we have subsequently upgraded the calibration of IMRPhenomXAS and of the subdominant mode phases to the 2019 SXS catalog. We have not updated the amplitude calibrations, which are more involved but contribute less to the accuracy of the model. Instead, we plan to update the amplitude model in future work, where we will include further harmonics, in particular the $(4,3)$ and $(5,5)$ modes, which we can now calibrate to numerical date thanks to the increased number of waveforms and improved waveform quality of the latest SXS catalog.

The computational performance and a method to accelerate the waveform evaluation by means of evaluation on appropriately chosen unequally spaced grids and interpolation is presented in a companion paper [30].

While IMRPhenomXHM resolves various shortcomings of IMRPhenomHM, further improvements are called for by the continuous improvement of gravitational wave detectors: We will need to address the complex phenomenology of the (2,1) harmonic for close to equal masses, add further modes as indicated above, and include non-oscillatory $m = 0$ modes.

IMRPhenomXHM can be extended to precession following [4, 80, 33]. Regarding mode mixing in the context of precession one will however take into account that mixing then occurs between precessing modes [83], while current phenomenological precession extensions handle mode-mixing at the level of the co-precessing modes.

Acknowledgements

We thank Maria Haney for carefully reading the manuscript and valuable feedback, and the internal code reviewers of the LIGO and Virgo collaboration for their work on checking our LALSuite code implementation. We thank Alessandro Nagar, Sebastiano Bernuzzi and Enno Harms for giving us access to *Teukode* [60], which was used to generate our extreme-mass-ratio waveforms.

This work was supported by European Union FEDER funds, the Ministry of Science, Innovation and Universities and the Spanish Agencia Estatal de Investigación grants FPA2016-76821-P, RED2018-102661-T, RED2018-102573-E, FPA2017-90687-REDC, Vicepresid'encia i Conselleria d'Innovació, Recerca i Turisme, Conselleria d'Educació, i Universitats del Govern de les Illes Balears i Fons Social Europeu, Generalitat Valenciana (PROMETEO/2019/071), EU COST Actions CA18108, CA17137, CA16214, and CA16104, and the Spanish Ministry of Education, Culture and Sport grants FPU15/03344 and FPU15/01319. MC acknowledges funding from the European Union's Horizon 2020 research and innovation programme, under the Marie Skłodowska-Curie grant agreement No. 751492. The authors thankfully acknowledge the computer resources at MareNostrum and the technical support provided by Barcelona Supercomputing Center (BSC) through Grants No. AECT-2019-2-0010, AECT-2019-1-0022, AECT-2019-1-0014, AECT-2018-3-0017, AECT-2018-2-0022, AECT-2018-1-0009, AECT-2017-3-0013, AECT-2017-2-0017, AECT-2017-1-0017, AECT-2016-3-0014, AECT2016-2-0009, from the Red Española de Supercomputación (RES) and PRACE (Grant No. 2015133131). BAM and Einstein Toolkit simulations were carried out on the BSC MareNostrum computer under PRACE and RES (Red Española de Supercomputación) allocations and on the FONER computer at the University of the Balearic Islands. Benchmarks calculations were carried out on the cluster CIT provided by LIGO Laboratory and supported by National Science Foundation Grants PHY-0757058 and PHY-0823459. PE results used the public data obtained from the Gravitational Wave Open Science Center (https://www.gw-openscience.org), a service of LIGO Laboratory, the LIGO Scientific Collaboration and the Virgo Collaboration. LIGO is funded by the U.S. National Science Foundation. Virgo is funded by the French Centre National de Recherche Scientifique

(CNRS), the Italian Istituto Nazionale della Fisica Nucleare (INFN) and the Dutch Nikhef, with contributions by Polish and Hungarian institutes.

Appendices

3.A Conversion from spheroidal to spherical-harmonic modes

Spin-weighted spheroidal harmonics can be written as a linear combination of spherical ones:

$$ {}_sS(a,\theta,\phi)^m_l = \sum_{l'=2}^{\infty} \alpha_{l\,l'm}(a)\, {}_s\,Y(\theta,\phi)^m_{l'}. \tag{3.55} $$

In the sum above, each spherical harmonic is weighted by a mixing coefficient $\alpha_{l\,l'm}$ measuring its overlap with the corresponding spherical harmonic:

$$ \alpha_{l\,l'm} = \int d\Omega\, {}_sS(a,\theta,\phi)^m_l\, {}_s\,Y^*(\theta,\phi)^m_{l'}. \tag{3.56} $$

Note that the mixing coefficients are functions of the final spin only. Although in theory the $(3,2)$ couples to all the modes with $m = 2$, in practice we find that the strongest source of mode-mixing comes from the mixing with the $(2,2)$. Therefore, we choose to neglect the coupling to modes with $l > 3$.

Under this assumption the coefficients of the strain in the two bases of harmonics are related via the following simple linear transformation:

$$ \begin{pmatrix} h_{22} \\ h_{32} \end{pmatrix} = \begin{pmatrix} \alpha_{222} & \alpha_{232} \\ \alpha_{322} & \alpha_{332} \end{pmatrix} \begin{pmatrix} h^S_{22} \\ h^S_{32} \end{pmatrix}. \tag{3.57} $$

The mixing coefficients have been computed in [46] for black holes spinning up to $\chi_f = 0.9999$. To improve accuracy for extreme spins, we perform a quadratic-in-spin fit of all the data-points with $\chi_f \in [0.999, 0.9999]$ and use it to obtain the values of the mixing coefficients extrapolated at $|\chi_f| = 1$.

3.B Testing tetrad conventions

The relative phase-alignment of the different modes is established trough Eq. (3.34), which implies a specific choice of tetrad convention. One can check that, when calling the model in time-domain, IMRPhenomXHM returns modes that follow the same convention adopted for the LVCNR catalog [84]. One has that

$$\text{mod}\,(2\Phi_{\ell m} - m\Phi_{22}, 2\pi) = \begin{cases} \pi & \text{m odd} \\ 0 & \text{m even} \end{cases}$$

holds for both the LVCNR catalog and the IMRPhenomXHM higher-multipoles.

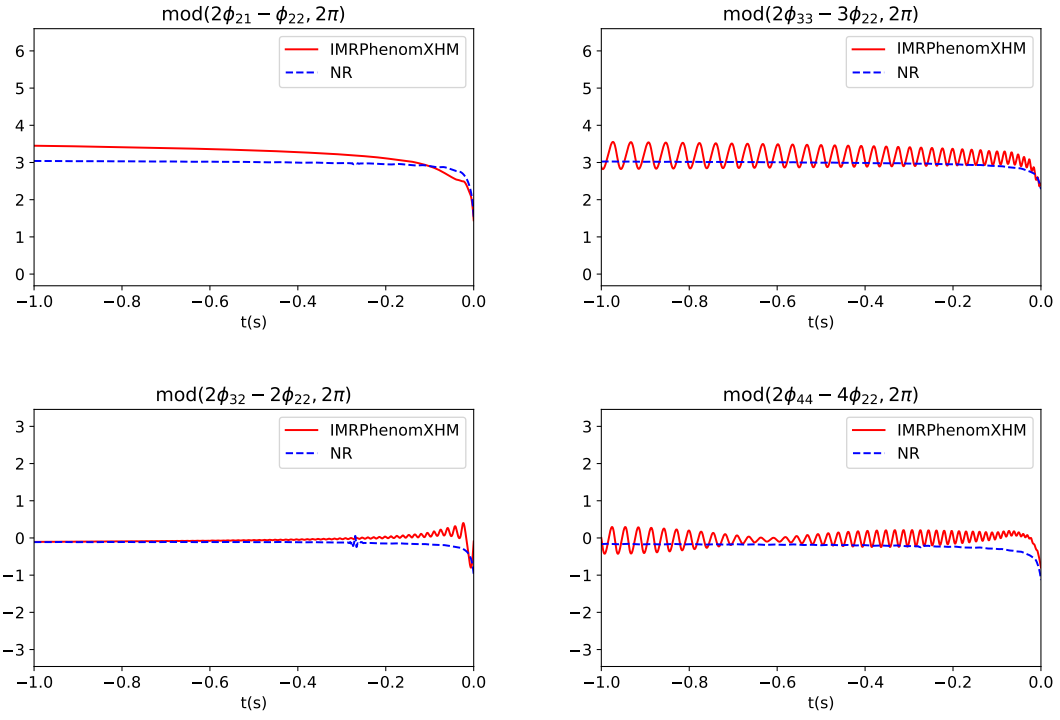

FIGURE 3.B.1: The quantity $\text{mod}\,(2\Phi_{\ell m} - m\Phi_{22}, 2\pi)$ can be used to discriminate between different tetrad conventions. Here we show that the time-domain conversion of IMRPhenomXHM follows the same tetrad choice implemented in the LVCNR catalog.

3.C Notes on the implementation of the IMRPhenomXHM model in the LIGO Algorithms Library

The IMRPhenomXHM model is implemented in the C language as part of the `LALSimIMR` package of inspiral-merger-ringdown waveform models, which is part of the `LALSimulation` collection of code for gravitational waveform and noise generation within LALSuite [2].

Online Doxygen documentation is available at `https://lscsoft.docs.ligo.org/lalsuite`, with top level information for the `LALSimIMR` package provided through the `LALSimIMR.h` header file. Externally callable functions of the IMRPhenomXHM model follow the `XLAL` coding standard of LALSuite.

Following our implementation of the IMRPhenomXAS model, our IMRPhenomXHM implementation is highly modularised, such that the inspiral, intermediate and ringdown parts can be updated independently, they are also tracked with independent version numbers, and are implemented in different files of the source code. Note that the `XLAL` standard implies that all the source code files are included via the C preprocessor into the main driver file, `LALSimIMRPhenomXHM.c`.

The model can be called both in the native Fourier domain, and in the time domain, where an inverse fast Fourier transformation is applied by the LALSuite code. The SWIG [85] software development tool is used to automatically create Python interfaces to all `XLAL` functions of our code, which can be used alternatively to the C interfaces.

Special attention is due for the time and phase alignment of our LALSuite implementation. As mentioned in Sec. 3.2.2, our hybrid waveforms are aligned in time such that the Newman-Penrose scalar for the $\ell = |m| = 2$ modes peaks $500M$ before the end of the waveform. In the LALSuite implementation, we first apply a global time-shift of $500M$ to our reconstructed waveforms, and then a parametric fit that accounts for the time-difference between the peak-time of ψ_4 and that of strain. An inverse Fourier transformation of the Fourier domain waveform, as produced by LALSuite, will then return a strain peaking around the end of the waveform.

When calling the model in the time domain through `LALSimulation`'s `ChooseTDWaveform` interface, the time coordinate is chosen such that $t = 0$ for the peak of the sum of the square of the polarizations:

$$A(t) = h_+^2(t) + h_\times^2(t), \tag{3.58}$$

$$A(t = 0) = A_{peak}. \tag{3.59}$$

These polarizations include all the modes used to generate the model and also depend on the line of sight from the detector to the source through the inclination and azimuthal angle. This choice is consistent with the choice made for the IMRPhenomHM model.

In `LALSimulation` the model is called through the function `ChooseFDWaveform`, whose input parameters `f_ref` and `phiRef` are used to define the phase of the $(2, 2)$ mode at some particular reference frequency. The rest of the modes are built with the correct relative phases with respect to the $(2, 2)$ mode. The argument `phiRef` is defined as the

orbital phase at the frequency `f_ref`. See our discussion in the context of IMRPhenomXAS [1] for further details. We relate this with the frequency domain $(2,2)$ phase by means of the SPA (see also our discussion in [1]).

$$\Psi_{2-2}(\texttt{f\_ref}) = 2\texttt{phiRef} - 2\pi\,\texttt{f\_ref}\,t_{\texttt{f\_ref}} + \frac{\pi}{4}. \tag{3.60}$$

Note that when talking about positive frequencies we have to refer to the negative mode, although we usually skip the minus sign for economy of the language.

Since our model is built in the Fourier domain we can not compute the quantity $t_{\texttt{f\_ref}}$ without a Fourier transformation to the time domain plus a numerical root finding, and we currently set it to $t_{\texttt{f\_ref}} = 0$. Furthermore, the expression (3.60) would not be valid if `f_ref` is situated in the merger-ringdown part of the waveform, because the SPA approximation is only reliable for the inspiral. This means that when comparing a time-domain model with our model with the exact same parameters we can only expect them to agree up to rotations, and would thus have to optimize over `phiRef` to achieve agreement.

In `LALSimulation` the azimuthal angle that enters in the spin-weighted spherical harmonics is defined as $\beta = \frac{\pi}{2} - \texttt{phiRef}$, this means that changing the parameter `phiRef` is equivalent to rotating the system: For example, by increasing the `phiRef` by a quantity $\delta\phi$, we would rotate the system an angle $-\delta\phi$. When the $(2,2)$ mode only is considered, `phiRef` acts just as a global phase factor for the waveform ($e^{i\,2\texttt{phiRef}}$) and the match is not affected since it maximizes over phase and time shifts. However, when higher modes are included this is not satisfied anymore since the term $e^{i\,m\texttt{phiRef}}$ is different for every mode and can not be factored out. Note that in our LALSuite code, this rotation is applied to every individual mode, such that individual modes and the mode sum are consistent with respect to rotations.

The user is free to specify the spherical harmonic modes that should be used to construct the waveform. The default behaviour is to use all the modes available: $((2\pm2)$, (2 ± 1), (3 ± 3), (3 ± 2), $(4\pm4))$, below we describe how the modes can be chosen through the different interfaces available for LALSuite waveforms.

Furthermore, the model implemented in LALSuite supports acceleration of waveform evaluation by interpolation of an unequispaced frequency grid broadly following the multibandin of [31]. Our version of the algorithm is described in [30] to do the evaluation faster and can also use a custom list of modes specified by the user. The multibanding algorithm is parameterized by a threshold, which describes the permitted local interpolation error for the phase in radians, lower values thus correspond to higher accuracy. The default value is set to a value of 10^{-3}.

Extensive debugging information can be enabled at compile time with the C preprocessor flag `-D PHENOMXHMDEBUG`.

`Python` Interface. To call the model with the default behaviour we use the function `SimInspiralChooseFDWaveform` from `lalsimulation` with the argument `lalparams` being an empty LALSuite dictionary `lalparams=lal.CreateDict()`. The threshold of the multibanding and the mode array can be changed by adding their values to the LALSuite dictionary in the following way:

```
lalsimulation.SimInspiralWaveformParamsInsertPhenomXHMThresholdMband(lalparams, threshold)
ModeArray = lalsimulation.SimInspiralCreateModeArray()
for mode in [[2,2],[2,-2],[2,1],[2,-1]]:
    lalsimulation.SimInspiralModeArrayActivateMode(ModeArray, mode[0], mode[1])
lalsimulation.SimInspiralWaveformParamsInsertModeArray(lalparams, ModeArray).
```

If `threshold`=0 then multibanding is switched off. By calling `ChooseFDWaveform` with this LALSuite dictionary we would get the hp and hc polarizations from the contribution of the $(2,2)$, $(2,-2)$, $(2,1)$, and $(2,-1)$ modes without using multibanding.

`GenerateSimulation` Interface. This is an executable in `LALSimulation` called through command line. The parameters to evaluate the model are passed by options like `-m1`, `-spin1z`, etc. The multibanding threshold and the mode array are specified as follows

```
./GenerateSimulation --approximant IMRPhenomXHM
...waveform params...
--phenomXHMMband 0.
--modesList "2,2, 2,-2, 2,1, 2,-1".
```

`LALInference` and `Bilby`. We also included the options in the two standard codes to perform Bayesian inference in gravitational wave data analysis: `LALInference`[86] and `Bilby` [10]. `LALInference` uses the same syntax than `GenerateSimulation` when called through the command line. You can also add these options to the config file and the example we have employed so far can be called as:

```
[engine]
...
approx = IMRPhenomXHMpseudoFourPN
modesList = "2,2, 2,-2, 2,1, 2,-1"
```

```
phenomXHMMband = 0
...
```

Note that in the current version of `LALInference` the string `pseudoFourPN` has to be added to the name of the approximant. For `Bilby` these options are specified in the `waveform_argument` dictionary defined in the configuration file. The equivalent example would be called as:

```
waveform_arguments =
dict(waveform_approximant="IMRPhenomXHM",
     reference_frequency=50.,
     minimum_frequency=20.,
     mode_array=[[2,2],[2,-2],[2,1],[2,-1]],
     phenomXHMMband=0.).
```

The released version of `Bilby` does not support the multibanding option yet, however a private branch that support this option can be downloaded with `git clone -b imrphenomx` https://git.ligo.org/cecilio.garcia-quiros/bilby.git. Equivalently we provide a branch for the `PyCBC` software [87] which can be obtained with the command `git clone -b imrphenomx` https://github.com/Ceciliogq/pycbc.git.

3.D Inspiral phase: higher-mode extension of IMRPhenomXAS

The inspiral orbital phase calibrated in IMRPhenomXAS can be written as a pseudo-PN expansion:

$$\phi_{22}(f) = \mathcal{N}(Mf)^{-5/3} \sum_{i=0}^{9} (Mf)^{i/3} \left(c_{22}^{i} + d_{22}^{i} \log f\right), \tag{3.61}$$

where $\mathcal{N}$ is a certain normalization constant. In the reconstruction of the higher-mode inspiral phase we need $\frac{m}{2}\phi_{22}(\frac{2}{m}f)$ (see Eq. (3.29)). To avoid recomputing the $(2,2)$-phase on a new frequency array for each mode, we wish to rewrite this quantity as

$$\frac{m}{2}\phi_{22}\left(\frac{2}{m}f\right) = \mathcal{N}(Mf)^{-5/3} \sum_{i=0}^{9} (Mf)^{i/3} \left(c_{m}^{i} + d_{m}^{i} \log f\right), \tag{3.62}$$

where all the rescaling factors have been reabsorbed in frequency-independent coefficients. It is straightforward to verify that the coefficients of the two expansions above

are related as follows:

$$c_m^i = \left(\frac{m}{2}\right)^{(8-i)/3} \left(c_{22}^i - d_{22}^i \log\frac{m}{2}\right),$$
$$d_m^i = \left(\frac{m}{2}\right)^{(8-i)/3} d_{22}^i. \tag{3.63}$$

3.E Fourier Domain Post-Newtonian amplitudes

When comparing the Fourier domain expressions for the spherical harmonic mode amplitudes given in equations (11-12) of [50] we found significant discrepancies with our numerical data. We have thus recomputed the mode amplitudes as outlined below, and include the explicit expressions we have used (which deviate from [50] at 2PN order), and which resolve the observed discrepancies with the numerical data, at the end of this appendix.

The time domain PN spherical harmonic modes are typically written in the form

$$h_{\ell m} = A_{\ell m} e^{-im\phi}, \quad A_{\ell m}(x) = 2\,\eta\, x \sqrt{\frac{16\pi}{5}} \hat{h}_{\ell m}. \tag{3.64}$$

Expressions for the $\hat{h}_{\ell m}$ can be found in [28], [88] and [89], including non-spinning terms up to 3PN order, and spinning terms up to 2PN order. The quantities $\hat{h}_{\ell m}$, and with them the time domain amplitudes $A_{\ell m}$ are complex functions. According to the SPA, the modes in the frequency domain can then be approximated as

$$\tilde{h}_{\ell m}(f) \approx A_{\ell m}(x) \sqrt{\frac{2\pi}{m\ddot{\phi}(x)}} e^{i\,\Psi_{\ell m}(f)}, \tag{3.65}$$

and we define $A_{\ell m}^{\rm SPA}(f) = A_{\ell m}(x)\sqrt{\frac{2\pi}{m\ddot{\phi}(x)}}$ (compare also with the expressions in [48]). The orbital phase ϕ is related to the freqency and the PN expansion parameter x by $\ddot{\phi} = \dot{\omega} = (3/2)\sqrt{x}\dot{x}$. The frequency f, which acts as the independent variable in the Fourier domain is related to x by $x = \left(\frac{2\pi\, f}{m}\right)^{2/3}$. We then obtain

$$A_{\ell m}^{\rm SPA}(f) = A_{\ell m}(x) \sqrt{\frac{2\pi}{m(3/2)\sqrt{x}\dot{x}}}. \tag{3.66}$$

We now need to compute $\dot{x}$. Using the TaylorT4 expression [90] we finally obtain:

$$
\begin{aligned}
\dot{x} =& \frac{-m_1 m_2}{32744250(m_1+m_2)^2}\Bigg[x^5\left(-419126400m_1^2 - 838252800m_1m_2 - 419126400m_2^2\right)\\
&+x^6\big(1152597600m_1^3m_2 + 1247400m_1^2\big(1848m_2^2+743\big)+\\
&\quad 2494800m_1m_2\big(462m_2^2+743\big) + 926818200m_2^2\big)\\
&+x^7\big(-1373803200m_1^4m_2^2 - 2747606400m_1^3m_2^3\\
&\quad + 207900m_1^3m_2\big(10206\chi_1^2 - 19908\chi_1\chi_2 + 10206\chi_2^2 - 13661\big)\\
&\quad - 23100m_1^2\big(59472m_2^4 + 91854\chi_1^2 + 34103\\
&\quad - 18m_2^2\big(10206\chi_1^2 - 19908\chi_1\chi_2 + 10206\chi_2^2 - 13661\big)\big)\\
&\quad + 23100m_1m_2\big(9m_2^2\big(10206\chi_1^2 - 19908\chi_1\chi_2 + 10206\chi_2^2 - 13661\big)\\
&\quad - 2\big(45927\chi_1^2 + 45927\chi_2^2 + 34103\big)\big) - 23100m_2^2\big(91854\chi_2^2 + 34103\big)\big)\\
&+x^{13/2}\big(6566313600m_1^4\chi_1 + 13132627200m_1^3m_2\chi_1 - 2619540000m_1^3\chi_1\\
&\quad - 34927200m_1^2(48\pi - m_2(188m_2(\chi_1+\chi_2)+75\chi_2))\\
&\quad - 34927200m_1m_2(96\pi - m_2(376m_2\chi_2+75\chi_1))\\
&\quad - 34927200m_2^2((75-188m_2)m_2\chi_2+48\pi)\big)\\
&+x^{15/2}\big(-34962127200m_1^5m_2\chi_1 - 69924254400m_1^4m_2^2\chi_1 + 14721814800m_1^4m_2\chi_1\\
&\quad + 17059026600m_1^4\chi_1 - 34962127200m_1^3m_2^3(\chi_1+\chi_2) - 14721814800m_1^3m_2^2\chi_2\\
&\quad + 5821200m_1^3m_2(5861\chi_1+1701\pi) - 4036586400m_1^3\chi_1\\
&\quad + 207900m_1^2\big(3\pi\big(31752m_2^2+4159\big) + 2m_2\big(-168168m_2^3\chi_2 - 35406m_2^2\chi_1\\
&\quad + 41027m_2(\chi_1+\chi_2) + 9708\chi_2\big)\big) + 415800m_1m_2\big(-84084m_2^4\chi_2 + 35406m_2^3\chi_2\\
&\quad + 82054m_2^2\chi_2 + 3\pi\big(7938m_2^2+4159\big) + 9708m_2\chi_1\big)\\
&\quad + 207900m_2^2(2m_2(41027m_2-9708)\chi_2 + 12477\pi)\big)\\
&+x^{17/2}\big(84184254000m_1^6m_2^2\chi_1 + 170726094000m_1^5m_2^3\chi_1 + 2357586000m_1^5m_2^3\chi_2\\
&\quad - 35665037100m_1^5m_2^2\chi_1 - 198816225300m_1^5m_2\chi_1 + 88899426000m_1^4m_2^4(\chi_1+\chi_2)\\
&\quad + 35665037100m_1^4m_2^3\chi_2 - 138600m_1^4m_2^2(3399633\chi_1 + 530712\chi_2 + 182990\pi)\\
&\quad + 33313480200m_1^4m_2\chi_1 + 87143248500m_1^4\chi_1 + 9702000m_1^3m_2^5(243\chi_1 + 17597\chi_2)\\
&\quad + 35665037100m_1^3m_2^4\chi_1 - 69300m_1^3m_2^3(4991769(\chi_1+\chi_2) + 731960\pi)\\
&\quad - 33313480200m_1^3m_2^2\chi_2 + 1925m_1^3m_2(97151928\chi_1 + 6613488\chi_2 - 12912300\pi)\\
&\quad - 14891068500m_1^3\chi_1 - 11550m_1^2\big(15\pi\big(146392m_2^4 + 286940m_2^2 - 2649\big)\\
&\quad + 2m_2\big(-3644340m_2^5\chi_2 + 1543941m_2^4\chi_2 + 54m_2^3(58968\chi_1 + 377737\chi_2)\\
&\quad + 1442142m_2^2\chi_1 - 4874683m_2(\chi_1+\chi_2) - 644635\chi_2\big)\big)\\
&\quad - 23100m_1m_2\big(m_2\big(m_2\big(8606763m_2^2 - 1442142m_2 - 8095994\big)\chi_2\\
&\quad + (-551124m_2 - 644635)\chi_1\big) + 15\pi\big(71735m_2^2 - 2649\big)\big)\\
&\quad + 57750m_2^2(2m_2(754487m_2 - 128927)\chi_2 + 7947\pi)\Bigg].
\end{aligned}
$$

We can now compute the complex non-polynomial Fourier domain PN amplitudes $A_{\ell m}$, that we re-expand up to 3PN order, as we have done for the $\ell = |m| = 2$ modes in IMRPhenomXAS. We list the resulting complex Fourier domain PN amplitudes following this method. We write them as a function of $v = \sqrt{x} = \left(\frac{2\pi f}{m}\right)^{1/3}$ and factor out a common term to simplify the comparison with [50] (note that there $\nu = \eta$, $V_m = v$ and $m\Psi_{\rm SPA} + \pi/4 = \Psi_{\ell m}$), finally obtaining

$$A^{\rm SPA}_{\ell m}(f) = \pi\sqrt{\frac{2\eta}{3}}v^{-7/2}\hat{H}_{\ell m} \tag{3.67}$$

The Post-Newtonian expressions that we use to calibrate the inspiral part of the amplitude are given by the expanded expressions below, as used in Eq. (3.66), except for the $(2,1)$ mode. We observed that for some cases with $q < 40$ the re-expansion of the $(2,1)$ mode breaks down before reaching the cutting frequency of the inspiral. For those cases the $(2,1)$ amplitude is very small (see Section 3.2.2) and the spinning contribution of higher PN terms is more important due to the different competing effects which can lead to cancellations in the waveform which are not captured by our 3PN accurate qusi-circular expressions. For the $(2,1)$ mode we therefore do not re-expand in a power series but keep the form of expression (3.66) when $q < 40$. The expression (3.66) is not used for $q > 40$ because it shows a divergence that appears before the inspiral cutting frequency for high spins.

$$\begin{aligned}
\hat{H}_{22} =& 1 + \left(\frac{451\eta}{168} - \frac{323}{224}\right)v^2 + v^3\left(\frac{27\delta\chi^z_a}{8} - \frac{11\eta\chi^z_s}{6} + \frac{27\chi^z_s}{8}\right) + \\
&+ v^4\left(-\frac{49\delta\chi^z_a\chi^z_s}{16} + \frac{105271\eta^2}{24192} + 6\eta(\chi^z_a)^2 + \frac{\eta\,(\chi^z_s)^2}{8} - \frac{1975055\eta}{338688} - \frac{49(\chi^z_a)^2}{32} - \frac{49\,(\chi^z_s)^2}{32}\right. \\
&\left. - \frac{27312085}{8128512}\right) \\
&+ v^6\left(\frac{107291\delta\eta\chi_a\chi_s}{2688} - \frac{875047\delta\chi_a\chi_s}{32256} + \frac{31\pi\delta\chi_a}{12} + \frac{34473079\eta^3}{6386688} + \frac{491\eta^2{\chi_a}^2}{84} - \frac{51329\eta^2\chi_s^2}{4032}\right. \\
&- \frac{3248849057\eta^2}{178827264} + \frac{129367\eta\chi_a^2}{2304} + \frac{8517\eta{\chi_s}^2}{224} - \frac{7\pi\eta\chi_s}{3} - \frac{205\pi^2\eta}{48} + \frac{545384828789\eta}{5007163392} \\
&\left. - \frac{875047}{64512}\left(\chi_a^2 + \chi_s^2\right) + \frac{31\pi\chi_s}{12} + \frac{428i\pi}{105} - \frac{177520268561}{8583708672}\right)
\end{aligned} \tag{3.68}$$

$$\begin{aligned}\hat{H}_{21} =&\frac{1}{3}i\sqrt{2}\Bigg[v\delta + v^2\left(-\frac{3\delta\chi_s^z}{2} - \frac{3\chi_a^z}{2}\right) + v^3\left(\frac{117\delta\eta}{56} + \frac{335\delta}{672}\right) + \\ &+v^4\left(-\frac{965}{336}\delta\eta\chi_s^z + \frac{3427\delta\chi_s^z}{1344} - \pi\delta - \frac{i\delta}{2} - \frac{1}{2}i\delta\log(16) - \frac{2101\eta\chi_a^z}{336} + \frac{3427\chi_a^z}{1344}\right) + \\ &+v^5\Bigg(\frac{21365\delta\eta^2}{8064} + 10\delta\eta\chi_a^2 + \frac{39}{8}\delta\eta\chi_s^2 - \frac{36529\delta\eta}{12544} - \frac{307\delta\chi_a^2}{32} - \frac{307\delta\chi_s^2}{32} + 3\pi\delta\chi_s - \\ &- \frac{964357\delta}{8128512} + \frac{213\eta\chi_a\chi_s}{4} - \frac{307\chi_a\chi_s}{16} + 3\pi\chi_a\Bigg) + \\ &+v^6\Bigg(-\frac{547}{768}\delta\eta^2\chi_s - 15\delta\eta\chi_a^2\chi_s - \frac{3}{16}\delta\eta\chi_s^3 - \frac{7049629\delta\eta\chi_s}{225792} + \frac{417\pi\delta\eta}{112} - \frac{1489i\delta\eta}{112} \\ &- \frac{89}{28}i\delta\eta\log(2) + \frac{729}{64}\delta\chi_a^2\chi_s + \frac{243\delta\chi_s^3}{64} + \frac{143063173\delta\chi_s}{5419008} - \frac{2455\pi\delta}{1344} - \frac{335i\delta}{1344} \\ &- \frac{335}{336}i\delta\log(2) + \frac{42617\eta^2\chi_a}{1792} - 15\eta\chi_a^3 - \frac{489}{16}\eta\chi_a{\chi_s}^2 - \frac{22758317\eta\chi_a}{225792} + \frac{243{\chi_a}^3}{64} \\ &+ \frac{729\chi_a\chi_s^2}{64} + \frac{143063173\chi_a}{5419008}\Bigg)\Bigg]\end{aligned} \tag{3.69}$$

$$\begin{aligned}\hat{H}_{33} =&-\frac{3}{4}i\sqrt{\frac{5}{7}}\Bigg[v\delta + v^3\delta\left(\frac{27}{8}\eta - \frac{1945}{672}\right) \\ &+v^4\left(-\frac{2}{3}\delta\eta\chi_s^z + \frac{65\delta\chi_s^z}{24} + \pi\delta - \frac{21i\delta}{5} + 6i\delta\log\left(\frac{3}{2}\right) - \frac{28\eta\chi_a^z}{3} + \frac{65\chi_a^z}{24}\right) + \\ &+v^5\Bigg(\frac{420389\delta\eta^2}{63360} + 10\delta\eta\chi_a^2 + \frac{1}{8}\delta\eta\chi_s^2 - \frac{11758073\delta\eta}{887040} - \frac{81\delta\chi_a^2}{32} - \frac{81\delta\chi_s^2}{32} - \frac{10776648667\delta}{447068160} \\ &+ \frac{81\eta\chi_a\chi_s}{4} - \frac{81\chi_a\chi_s}{16} + \Bigg) \\ &+v^6\Bigg(-\frac{67}{24}\delta\eta^2\chi_s - \frac{58745\delta\eta\chi_s}{4032} + \frac{131\pi\delta\eta}{16} - \frac{440957i\delta\eta}{9720} + \frac{69}{4}i\delta\eta\log\left(\frac{3}{2}\right) + \frac{163021\delta\chi_s}{16128} \\ &- \frac{5675\pi\delta}{1344} + \frac{389i\delta}{32} - \frac{1945}{112}i\delta\log\left(\frac{3}{2}\right) - \frac{137\eta^2\chi_a}{24} - \frac{148501\eta\chi_a}{4032} + \frac{163021\chi_a}{16128}\Bigg)\Bigg]\end{aligned} \tag{3.70}$$

$$\begin{aligned}\hat{H}_{32} =&\frac{1}{3}\sqrt{\frac{5}{7}}\Bigg[v^2(1-3\eta) + v^3 4\eta\chi_s^z + v^4\left(-\frac{589\eta^2}{72} + \frac{12325\eta}{2016} - \frac{10471}{10080}\right) + \\ &+v^5\left(\eta\left(\frac{113\delta\chi_a}{8} + \frac{1081\chi_s}{84} - \frac{66i}{5}\right) + \frac{1}{24}(-113\delta\chi_a - 113\chi_s + 72i) - 15\eta^2\chi_s\right) \\ &+v^6\Bigg(\eta\left(-\frac{1633\delta\chi_a\chi_s}{48} - \frac{563\chi_a^2}{32} - \frac{2549\chi_s^2}{96} + 8\pi\chi_s - \frac{8689883}{149022720}\right) + \frac{81\delta\chi_a\chi_s}{16} \\ &+ \frac{837223\eta^3}{63360} + \eta^2\left(30\chi_a^2 + \frac{313\chi_s^2}{24} - \frac{78584047}{2661120}\right) + \frac{81{\chi_a}^2}{32} + \frac{81\chi_s^2}{32} + \frac{824173699}{447068160}\Bigg)\Bigg]\end{aligned} \tag{3.71}$$

$$\hat{H}_{31} = \frac{i}{12\sqrt{7}}\Bigg[v\delta + v^3\left(\frac{17\delta\eta}{24} - \frac{1049\delta}{672}\right) + v^4\left(\frac{10\delta\eta\chi_s^z}{3} + \frac{65\delta\chi_s^z}{24} - \pi\delta - \frac{7i\delta}{5} - \frac{1}{5}i\delta\log(1024) - \frac{40\eta\chi_a^z}{3} + \frac{65\chi_a^z}{24}\right) + v^5\left(-\frac{4085\delta\eta^2}{4224} + 10\delta\eta\chi_a^2 + \frac{1}{8}\delta\eta\chi_s^2 - \frac{272311\delta\eta}{59136} - \frac{81\delta}{32}\left(\chi_a^2 + \chi_s^2\right) + \frac{904119161\delta}{89413632} - \frac{81\chi_a\chi_s}{16}(1-4\eta)\right) + v^6\left(\frac{803}{72}\delta\eta^2\chi_s - \frac{36187\delta\eta\chi_s}{1344} + \frac{245\pi\delta\eta}{48} - \frac{239i\delta\eta}{120} - \frac{5}{12}i\delta\eta\log(2) + \frac{264269\delta\chi_s}{16128} + \frac{313\pi\delta}{1344} + \frac{1049i\delta}{480} + \frac{1049}{336}i\delta\log(2) + \frac{2809\eta^2\chi_a}{72} - \frac{318205\eta\chi_a}{4032} + \frac{264269\chi_a}{16128}\right)\Bigg] \tag{3.72}$$

$$\hat{H}_{44} = \frac{4}{9}\sqrt{\frac{10}{7}}\Bigg[v^2(3\eta-1) + v^4\left(\frac{1063\eta^2}{88} - \frac{128221\eta}{7392} + \frac{158383}{36960}\right) + v^5\left(\pi(2-6\eta) + \frac{1}{120}\left(-\eta(1695\delta\chi_a + 2075\chi_s - 3579i + 2880i\log(2)) + 565\delta\chi_a + 1140\eta^2\chi_s + 565\chi_s - 1008i + 960i\log(2)\right)\right) + v^6\left(\eta\left(\frac{243\delta\chi_a\chi_s}{16} + \frac{563\chi_a^2}{32} + \frac{247{\chi_s}^2}{32} - \frac{22580029007}{880588800}\right) - \frac{81\delta\chi_a\chi_s}{16} - \frac{7606537\eta^3}{274560} + \eta^2\left(-30{\chi_a}^2 - \frac{3\chi_s^2}{8} + \frac{901461137}{11531520}\right) - \frac{81{\chi_a}^2}{32} - \frac{81\chi_s^2}{32} + \frac{7888301437}{29059430400}\right)\Bigg] \tag{3.73}$$

$$\hat{H}_{43} = \frac{3}{4}i\sqrt{\frac{3}{35}}\Bigg[v^3(2\delta\eta - \delta) + v^4\left(\frac{5\eta\chi_a}{2} - \frac{5\delta\eta\chi_s}{2}\right) + v^5\left(\frac{887\delta\eta^2}{132} - \frac{10795\delta\eta}{1232} + \frac{18035\delta}{7392}\right) + v^6\left(-\frac{469}{48}\delta\eta^2\chi_s + \frac{4399\delta\eta\chi_s}{448} + 2\pi\delta\eta - \frac{16301i\delta\eta}{810} + 12i\delta\eta\left(\frac{3}{2}\right) - \frac{113\delta\chi_s}{24} - \pi\delta + \frac{32i\delta}{5} - 6i\delta\log\left(\frac{3}{2}\right) - \frac{1643\eta^2\chi_a}{48} + \frac{41683\eta\chi_a}{1344} - \frac{113\chi_a}{24}\right)\Bigg] \tag{3.74}$$

Bibliography

[1] Geraint Pratten, Sascha Husa, Cecilio García-Quirós, Marta Colleoni, Antoni Ramos-Buades, Héctor Estellés, and Rafel Jaume. Setting the cornerstone for the IMRPhenomX family of models for gravitational waves from compact binaries: The dominant harmonic for non-precessing quasi-circular black holes. 2020.

[2] The LIGO Scientific Collaboration. LALSuite: LSC Algorithm Library Suite. https://www.lsc-group.phys.uwm.edu/daswg/projects/lalsuite.html, 2015.

[3] Sebastian Khan, Sascha Husa, Mark Hannam, Frank Ohme, Michael Pürrer, Xisco Jiménez Forteza, and Alejandro Bohé. Frequency-domain gravitational waves from nonprecessing black-hole binaries. II. A phenomenological model for the advanced detector era. *Phys. Rev.*, D93(4):044007, 2016. doi: 10.1103/PhysRevD.93.044007.

[4] Mark Hannam, Patricia Schmidt, Alejandro Bohé, Leïla Haegel, Sascha Husa, et al. Simple Model of Complete Precessing Black-Hole-Binary Gravitational Waveforms. *Phys.Rev.Lett.*, 113(15):151101, 2014. doi: 10.1103/PhysRevLett.113.151101.

[5] Alejandro Bohé, Mark Hannam, Sascha Husa, Frank Ohme, Michael Puerrer, and Patricia Schmidt. Phenompv2 - technical notes for lal implementation. Technical Report LIGO-T1500602, LIGO Project, 2016. URL https://dcc.ligo.org/LIGO-T1500602.

[6] Lionel London, Sebastian Khan, Edward Fauchon-Jones, Cecilio García, Mark Hannam, Sascha Husa, Xisco Jiménez-Forteza, Chinmay Kalaghatgi, Frank Ohme, and Francesco Pannarale. First higher-multipole model of gravitational waves from spinning and coalescing black-hole binaries. *Phys. Rev. Lett.*, 120(16):161102, 2018. doi: 10.1103/PhysRevLett.120.161102.

[7] B. P. Abbott et al. Properties of the Binary Black Hole Merger GW150914. *Phys. Rev. Lett.*, 116(24):241102, 2016. doi: 10.1103/PhysRevLett.116.241102.

[8] Abbott, B. P. and others. Gwtc-1: A gravitational-wave transient catalog of compact binary mergers observed by ligo and virgo during the first and second observing runs. *Phys. Rev. X*, 9:031040, Sep 2019. doi: 10.1103/PhysRevX.9.031040. URL https://link.aps.org/doi/10.1103/PhysRevX.9.031040.

[9] J. Veitch et al. Parameter estimation for compact binaries with ground-based gravitational-wave observations using the LALInference software library. *Phys. Rev.*, D91(4):042003, 2015. doi: 10.1103/PhysRevD.91.042003.

[10] Gregory Ashton et al. Bilby: A user-friendly Bayesian inference library for gravitational-wave astronomy. *Astrophys. J. Suppl.*, 241(2):27, 2019. doi: 10.3847/1538-4365/ab06fc.

[11] Vijay Varma, Parameswaran Ajith, Sascha Husa, Juan Calderon Bustillo, Mark Hannam, and Michael Pürrer. Gravitational-wave observations of binary black holes: Effect of nonquadrupole modes. *Phys. Rev. D*, 90:124004, Dec 2014. doi: 10.1103/PhysRevD.90.124004. URL https://link.aps.org/doi/10.1103/PhysRevD.90.124004.

[12] Vijay Varma and Parameswaran Ajith. Effects of nonquadrupole modes in the detection and parameter estimation of black hole binaries with nonprecessing spins. *Phys. Rev. D*, 96:124024, Dec 2017. doi: 10.1103/PhysRevD.96.124024. URL https://link.aps.org/doi/10.1103/PhysRevD.96.124024.

[13] Juan Calderón Bustillo, Sascha Husa, Alicia M. Sintes, and Michael Pürrer. Impact of gravitational radiation higher order modes on single aligned-spin gravitational wave searches for binary black holes. *Phys. Rev. D*, 93:084019, Apr 2016. doi: 10.1103/PhysRevD.93.084019. URL https://link.aps.org/doi/10.1103/PhysRevD.93.084019.

[14] Tyson B. Littenberg, John G. Baker, Alessandra Buonanno, and Bernard J. Kelly. Systematic biases in parameter estimation of binary black-hole mergers. *Phys. Rev.*, D87(10):104003, 2013. doi: 10.1103/PhysRevD.87.104003.

[15] Juan Calderón Bustillo, Sascha Husa, Alicia M. Sintes, and Michael Pürrer. Impact of gravitational radiation higher order modes on single aligned-spin gravitational wave searches for binary black holes. *Phys. Rev.*, D93(8):084019, 2016. doi: 10.1103/PhysRevD.93.084019.

[16] Katerina Chatziioannou et al. On the properties of the massive binary black hole merger GW170729. *Phys. Rev.*, D100(10):104015, 2019. doi: 10.1103/PhysRevD.100.104015.

[17] Chinmay Kalaghatgi, Mark Hannam, and Vivien Raymond. Parameter Estimation with a Spinning Multi-Mode Waveform Model: IMRPhenomHM. 2019.

[18] Feroz H. Shaik, Jacob Lange, Scott E. Field, Richard O'Shaughnessy, Vijay Varma, Lawrence E. Kidder, Harald P. Pfeiffer, and Daniel Wysocki. Impact of subdominant modes on the interpretation of gravitational-wave signals from heavy binary black hole systems. 2019.

[19] Roberto Cotesta, Alessandra Buonanno, Alejandro Bohé, Andrea Taracchini, Ian Hinder, and Serguei Ossokine. Enriching the Symphony of Gravitational Waves from Binary Black Holes by Tuning Higher Harmonics. *Phys. Rev.*, D98(8):084028, 2018. doi: 10.1103/PhysRevD.98.084028.

[20] Michael Pürrer. Frequency-domain reduced order models for gravitational waves from aligned-spin compact binaries. *Class. Quantum Grav.*, 31(19):195010, Sep 2014. ISSN 1361-6382. doi: 10.1088/0264-9381/31/19/195010. URL http://dx.doi.org/10.1088/0264-9381/31/19/195010.

[21] Michael Pürrer. Frequency domain reduced order model of aligned-spin effective-one-body waveforms with generic mass-ratios and spins. *Phys. Rev.*, D93(6):064041, 2016. doi: 10.1103/PhysRevD.93.064041.

[22] Alessandro Nagar and Piero Rettegno. Efficient effective one body time-domain gravitational waveforms. *Phys. Rev.*, D99(2):021501, 2019. doi: 10.1103/PhysRevD.99.021501.

[23] Vijay Varma, Scott E. Field, Mark A. Scheel, Jonathan Blackman, Lawrence E. Kidder, and Harald P. Pfeiffer. Surrogate model of hybridized numerical relativity binary black hole waveforms. *Phys. Rev.*, D99(6):064045, 2019. doi: 10.1103/PhysRevD.99.064045.

[24] Vijay Varma, Scott E. Field, Mark A. Scheel, Jonathan Blackman, Davide Gerosa, Leo C. Stein, Lawrence E. Kidder, and Harald P. Pfeiffer. Surrogate models for precessing binary black hole simulations with unequal masses. *Phys. Rev. Research.*, 1:033015, 2019. doi: 10.1103/PhysRevResearch.1.033015.

[25] Ajit Kumar Mehta, Chandra Kant Mishra, Vijay Varma, and Parameswaran Ajith. Accurate inspiral-merger-ringdown gravitational waveforms for nonspinning black-hole binaries including the effect of subdominant modes. *Phys. Rev.*, D96(12): 124010, 2017. doi: 10.1103/PhysRevD.96.124010.

[26] Ajit Kumar Mehta, Praveer Tiwari, Nathan K. Johnson-McDaniel, Chandra Kant Mishra, Vijay Varma, and Parameswaran Ajith. Including mode mixing in a higher-multipole model for gravitational waveforms from nonspinning black-hole binaries. *Phys. Rev.*, D100(2):024032, 2019. doi: 10.1103/PhysRevD.100.024032.

[27] Xisco Jiménez-Forteza, David Keitel, Sascha Husa, Mark Hannam, Sebastian Khan, and Michael Pürrer. Hierarchical data-driven approach to fitting numerical relativity data for nonprecessing binary black holes with an application to final spin and radiated energy. *Phys. Rev.*, D95(6):064024, 2017. doi: 10.1103/PhysRevD.95.064024.

[28] Luc Blanchet. Gravitational radiation from post-Newtonian sources and inspiralling compact binaries. *Living Reviews in Relativity*, 17, 2014. ISSN 1433-8351. doi: 10.12942/lrr-2014-2. URL http://dx.doi.org/10.12942/lrr-2014-2.

[29] K.D. Kokkotas and B.G. Schmidt. Quasi-normal modes of stars and black holes. *Living Reviews in Relativity*, 2, 1999. ISSN 1433-8351. URL https://doi.org/10.12942/lrr-1999-2.

[30] Cecilio García-Quirós, Sascha Husa, Maite Mateu-Lucena, and Angela Borchers. Accelerating the evaluation of inspiral-merger-ringdown waveforms with adapted grids. 2020.

[31] Serena Vinciguerra, John Veitch, and Ilya Mandel. Accelerating gravitational wave parameter estimation with multi-band template interpolation. *Class. Quant. Grav.*, 34(11):115006, 2017. doi: 10.1088/1361-6382/aa6d44.

[32] Patricia Schmidt, Mark Hannam, and Sascha Husa. Towards models of gravitational waveforms from generic binaries: A simple approximate mapping between precessing

and non-precessing inspiral signals. *Phys. Rev.*, D86:104063, 2012. doi: 10.1103/PhysRevD.86.104063.

[33] Sebastian Khan, Katerina Chatziioannou, Mark Hannam, and Frank Ohme. Phenomenological model for the gravitational-wave signal from precessing binary black holes with two-spin effects. *Phys. Rev. D*, 100:024059, Jul 2019. doi: 10.1103/PhysRevD.100.024059. URL https://link.aps.org/doi/10.1103/PhysRevD.100.024059.

[34] Sascha Husa, Marta Colleoni, Héctor Estellés, García Quirós Cecilio, Antoni Ramos-Buades, Geraint Pratten, Rafel Jaume, Xisco Jimenez-Forteza, and David Keitel. A catalogue of non-precessing multi-mode hybrid waveforms for quasi-circular black-hole binaries. in preparation, 2020.

[35] Yves Wiaux, L. Jacques, and P. Vandergheynst. Fast spin +-2 spherical harmonics transforms. *J. Comput. Phys.*, 226:2359–2371, 2007. doi: 10.1016/j.jcp.2007.07.005.

[36] Juan Calderón Bustillo, Alejandro Bohé, Sascha Husa, Alicia M. Sintes, Mark Hannam, and Michael Pürrer. Comparison of subdominant gravitational wave harmonics between post-Newtonian and numerical relativity calculations and construction of multi-mode hybrids. 1 2015.

[37] Luc Blanchet, Guillaume Faye, Bala R. Iyer, and Siddhartha Sinha. The Third post-Newtonian gravitational wave polarisations and associated spherical harmonic modes for inspiralling compact binaries in quasi-circular orbits. *Class. Quant. Grav.*, 25:165003, 2008. doi: 10.1088/0264-9381/25/16/165003,10.1088/0264-9381/29/23/239501. [Erratum: Class. Quant. Grav.29,239501(2012)].

[38] Thibault Damour, Bala R. Iyer, and B. S. Sathyaprakash. Frequency domain P approximant filters for time truncated inspiral gravitational wave signals from compact binaries. *Phys. Rev.*, D62:084036, 2000. doi: 10.1103/PhysRevD.62.084036.

[39] Sascha Husa, Sebastian Khan, Mark Hannam, Michael Pürrer, Frank Ohme, Xisco Jiménez Forteza, and Alejandro Bohé. Frequency-domain gravitational waves from nonprecessing black-hole binaries. I. New numerical waveforms and anatomy of the signal. *Phys. Rev.*, D93(4):044006, 2016. doi: 10.1103/PhysRevD.93.044006.

[40] Miriam Cabero, Alex B. Nielsen, Andrew P. Lundgren, and Collin D. Capano. Minimum energy and the end of the inspiral in the post-Newtonian approximation. *Phys. Rev.*, D95(6):064016, 2017. doi: 10.1103/PhysRevD.95.064016.

[41] Jeremy D. Schnittman, Alessandra Buonanno, James R. van Meter, John G. Baker, William D. Boggs, Joan Centrella, Bernard J. Kelly, and Sean T. McWilliams.

Anatomy of the binary black hole recoil: A multipolar analysis. *Phys. Rev.*, D77: 044031, 2008. doi: 10.1103/PhysRevD.77.044031.

[42] John G. Baker, William D. Boggs, Joan Centrella, Bernard J. Kelly, Sean T. McWilliams, and James R. van Meter. Mergers of non-spinning black-hole binaries: Gravitational radiation characteristics. *Phys. Rev.*, D78:044046, 2008. doi: 10.1103/PhysRevD.78.044046.

[43] Nils Andersson. Evolving test fields in a black hole geometry. *Phys. Rev.*, D55: 468–479, 1997. doi: 10.1103/PhysRevD.55.468.

[44] Saul A Teukolsky. Rotating black holes–separable wave equations for gravitational and electromagnetic perturbations. *Phys. Rev. Lett.*, 29:1114, 1972.

[45] Saul A Teukolsky. Perturbations of a rotating black hole. 1. Fundamental equations for gravitational electromagnetic and neutrino field perturbations. *Astrophys. J.*, 185:635, 1973.

[46] Emanuele Berti and Antoine Klein. Mixing of spherical and spheroidal modes in perturbed kerr black holes. *Phys. Rev. D*, 90:064012, Sep 2014. doi: 10.1103/PhysRevD.90.064012. URL https://link.aps.org/doi/10.1103/PhysRevD.90.064012.

[47] P. Ajith et al. Inspiral-merger-ringdown waveforms for black-hole binaries with non-precessing spins. *Phys. Rev. Lett.*, 106:241101, 2011. doi: 10.1103/PhysRevLett.106.241101.

[48] L. Santamaria et al. Matching post-Newtonian and numerical relativity waveforms: systematic errors and a new phenomenological model for non-precessing black hole binaries. *Phys. Rev.*, D82:064016, 2010. doi: 10.1103/PhysRevD.82.064016.

[49] P. Ajith. Addressing the spin question in gravitational-wave searches: Waveform templates for inspiralling compact binaries with nonprecessing spins. *Phys. Rev.*, D84:084037, 2011. doi: 10.1103/PhysRevD.84.084037.

[50] Chandra Kant Mishra, Aditya Kela, K. G. Arun, and Guillaume Faye. Ready-to-use post-newtonian gravitational waveforms for binary black holes with nonprecessing spins: An update. *Phys. Rev. D*, 93:084054, Apr 2016. doi: 10.1103/PhysRevD.93.084054. URL https://link.aps.org/doi/10.1103/PhysRevD.93.084054.

[51] Andrea Taracchini, Alessandra Buonanno, Gaurav Khanna, and Scott A. Hughes. Small mass plunging into a Kerr black hole: Anatomy of the inspiral-merger-ringdown waveforms. *Phys. Rev.*, D90(8):084025, 2014. doi: 10.1103/PhysRevD.90.084025.

[52] http://www.black-holes.org/waveforms, .

[53] https://www.black-holes.org/code/SpEC.html, .

[54] Harald P. Pfeiffer, Lawrence E. Kidder, Mark A. Scheel, and Saul A. Teukolsky. A multidomain spectral method for solving elliptic equations. *Computer Physics Communications*, 152(3):253 – 273, 2003. ISSN 0010-4655. doi: https://doi.org/10.1016/S0010-4655(02)00847-0. URL http://www.sciencedirect.com/science/article/pii/S0010465502008470.

[55] Bernd Brügmann, José A. González, Mark Hannam, Sascha Husa, Ulrich Sperhake, and Wolfgang Tichy. Calibration of moving puncture simulations. *Phys. Rev. D*, 77(2), Jan 2008. ISSN 1550-2368. doi: 10.1103/physrevd.77.024027. URL http://dx.doi.org/10.1103/PhysRevD.77.024027.

[56] Sascha Husa, Mark Hannam, Jose A. Gonzalez, Ulrich Sperhake, and Bernd Bruegmann. Reducing eccentricity in black-hole binary evolutions with initial parameters from post-Newtonian inspiral. *Phys. Rev.*, D77:044037, 2008. doi: 10.1103/PhysRevD.77.044037.

[57] Frank Löffler, Joshua Faber, Eloisa Bentivegna, Tanja Bode, Peter Diener, Roland Haas, Ian Hinder, Bruno C Mundim, Christian D Ott, Erik Schnetter, Gabrielle Allen, Manuela Campanelli, and Pablo Laguna. The einstein toolkit: a community computational infrastructure for relativistic astrophysics. *Classical and Quantum Gravity*, 29(11):115001, may 2012. doi: 10.1088/0264-9381/29/11/115001. URL https://doi.org/10.1088%2F0264-9381%2F29%2F11%2F115001.

[58] Michael Boyle et al. The SXS Collaboration catalog of binary black hole simulations. *Class. Quant. Grav.*, 36(19):195006, 2019. doi: 10.1088/1361-6382/ab34e2.

[59] David Keitel et al. The most powerful astrophysical events: Gravitational-wave peak luminosity of binary black holes as predicted by numerical relativity. *Phys. Rev.*, D96(2):024006, 2017. doi: 10.1103/PhysRevD.96.024006.

[60] Enno Harms, Sebastiano Bernuzzi, Alessandro Nagar, and Anıl Zenginoğlu. A new gravitational wave generation algorithm for particle perturbations of the kerr spacetime. *Classical and Quantum Gravity*, 31(24):245004, nov 2014. doi: 10.1088/0264-9381/31/24/245004. URL https://doi.org/10.1088%2F0264-9381%2F31%2F24%2F245004.

[61] Francesco Messina, Alberto Maldarella, and Alessandro Nagar. Factorization and resummation: A new paradigm to improve gravitational wave amplitudes. ii. the higher multipolar modes. *Phys. Rev. D*, 97:084016, Apr 2018. doi: 10.1103/

PhysRevD.97.084016. URL https://link.aps.org/doi/10.1103/PhysRevD.97.084016.

[62] Emanuele Berti. URL https://pages.jh.edu/~eberti2/ringdown/.

[63] Emanuele Berti, Vitor Cardoso, and Andrei O. Starinets. Quasinormal modes of black holes and black branes. *Class. Quant. Grav.*, 26:163001, 2009. doi: 10.1088/0264-9381/26/16/163001.

[64] Saul A. Teukolsky. Rotating black holes: Separable wave equations for gravitational and electromagnetic perturbations. *Phys. Rev. Lett.*, 29:1114–1118, Oct 1972. doi: 10.1103/PhysRevLett.29.1114. URL https://link.aps.org/doi/10.1103/PhysRevLett.29.1114.

[65] Curt Cutler and Eanna E. Flanagan. Gravitational waves from merging compact binaries: How accurately can one extract the binary's parameters from the inspiral wave form? *Phys. Rev.*, D49:2658–2697, 1994. doi: 10.1103/PhysRevD.49.2658.

[66] J. Aasi et al. Advanced LIGO. *Class. Quant. Grav.*, 32:074001, 2015. doi: 10.1088/0264-9381/32/7/074001.

[67] https://dcc.ligo.org/LIGO-T0900288/public. URL https://dcc.ligo.org/LIGO-T0900288/public.

[68] Roberto Cotesta, Alessandra Buonanno, Alejandro Bohé, Andrea Taracchini, Ian Hinder, and Serguei Ossokine. Enriching the symphony of gravitational waves from binary black holes by tuning higher harmonics. *Phys. Rev. D*, 98:084028, Oct 2018. doi: 10.1103/PhysRevD.98.084028. URL https://link.aps.org/doi/10.1103/PhysRevD.98.084028.

[69] Jonathan Blackman, Scott E. Field, Mark A. Scheel, Chad R. Galley, Daniel A. Hemberger, Patricia Schmidt, and Rory Smith. A surrogate model of gravitational waveforms from numerical relativity simulations of precessing binary black hole mergers. *Phys. Rev. D*, 95:104023, May 2017. doi: 10.1103/PhysRevD.95.104023. URL https://link.aps.org/doi/10.1103/PhysRevD.95.104023.

[70] James Healy, Carlos O. Lousto, and Yosef Zlochower. Remnant mass, spin, and recoil from spin aligned black-hole binaries. *Phys. Rev. D*, 90:104004, Nov 2014. doi: 10.1103/PhysRevD.90.104004. URL https://link.aps.org/doi/10.1103/PhysRevD.90.104004.

[71] James Healy and Carlos O. Lousto. Remnant of binary black-hole mergers: New simulations and peak luminosity studies. *Phys. Rev. D*, 95:024037, Jan 2017.

doi: 10.1103/PhysRevD.95.024037. URL https://link.aps.org/doi/10.1103/PhysRevD.95.024037.

[72] James Healy and Carlos O. Lousto. Hangup effect in unequal mass binary black hole mergers and further studies of their gravitational radiation and remnant properties. *Phys. Rev. D*, 97:084002, Apr 2018. doi: 10.1103/PhysRevD.97.084002. URL https://link.aps.org/doi/10.1103/PhysRevD.97.084002.

[73] Vijay Varma, Davide Gerosa, Leo C. Stein, François Hébert, and Hao Zhang. High-accuracy mass, spin, and recoil predictions of generic black-hole merger remnants. *Phys. Rev. Lett.*, 122(1):011101, 2019. doi: 10.1103/PhysRevLett.122.011101.

[74] Michele Vallisneri, Jonah Kanner, Roy Williams, Alan Weinstein, and Branson Stephens. The LIGO Open Science Center. *J. Phys. Conf. Ser.*, 610(1):012021, 2015. doi: 10.1088/1742-6596/610/1/012021.

[75] Gravitational Wave Open Science Center. URL https://www.gw-openscience.org.

[76] The GWOSC O2 Data Release. URL https://doi.org/10.7935/CA75-FM95.

[77] Rory Smith, Gregory Ashton, Avi Vajpeyi, and Colm Talbot. Massively parallel bayesian inference for transient gravitational-wave astronomy. *ArXiv:1909.11873*, 2019.

[78] Joshua S Speagle. dynesty: a dynamic nested sampling package for estimating Bayesian posteriors and evidences. *Monthly Notices of the Royal Astronomical Society*, 493(3):3132–3158, 02 2020. ISSN 0035-8711. doi: 10.1093/mnras/staa278. URL https://doi.org/10.1093/mnras/staa278.

[79] Prayush Kumar, Tony Chu, Heather Fong, Harald P. Pfeiffer, Michael Boyle, Daniel A. Hemberger, Lawrence E. Kidder, Mark A. Scheel, and Bela Szilagyi. Accuracy of binary black hole waveform models for aligned-spin binaries. *Phys. Rev.*, D93(10):104050, 2016. doi: 10.1103/PhysRevD.93.104050.

[80] Alejandro Bohe, Mark Hannam, Sascha Husa, Frank Ohme, Puerrer Michael, and Patricia Schmidt. Phenompv2 – technical notes for the lal implementation. 2016. URL https://dcc.ligo.org/LIGO-T1500602.

[81] Tim Dietrich et al. Matter imprints in waveform models for neutron star binaries: Tidal and self-spin effects. *Phys. Rev.*, D99(2):024029, 2019. doi: 10.1103/PhysRevD.99.024029.

[82] Tim Dietrich, Anuradha Samajdar, Sebastian Khan, Nathan K. Johnson-McDaniel, Reetika Dudi, and Wolfgang Tichy. Improving the NRTidal model for binary neutron star systems. *Phys. Rev.*, D100(4):044003, 2019. doi: 10.1103/PhysRevD.100.044003.

[83] Antoni Ramos-Buades, Patricia Schmidt, Geraint Pratten, and Sascha Husa. Validity of common modelling approximations for precessing binary black holes with higher-order modes. 2020. Submitted.

[84] Patricia Schmidt, Ian W. Harry, and Harald P. Pfeiffer. Numerical Relativity Injection Infrastructure. 2017.

[85] https://www.swig.org.

[86] J. Veitch, V. Raymond, B. Farr, W. Farr, P. Graff, S. Vitale, B. Aylott, K. Blackburn, N. Christensen, M. Coughlin, W. Del Pozzo, F. Feroz, J. Gair, C.-J. Haster, V. Kalogera, T. Littenberg, I. Mandel, R. O'Shaughnessy, M. Pitkin, C. Rodriguez, C. Röver, T. Sidery, R. Smith, M. Van Der Sluys, A. Vecchio, W. Vousden, and L. Wade. Parameter estimation for compact binaries with ground-based gravitational-wave observations using the lalinference software library. *Phys. Rev. D*, 91:042003, Feb 2015. doi: 10.1103/PhysRevD.91.042003. URL https://link.aps.org/doi/10.1103/PhysRevD.91.042003.

[87] Alex Nitz et al. gwastro/pycbc v1.15.3. URL https://zenodo.org/badge/31596861.svg.

[88] K. G. Arun, Alessandra Buonanno, Guillaume Faye, and Evan Ochsner. Higher-order spin effects in the amplitude and phase of gravitational waveforms emitted by inspiraling compact binaries: Ready-to-use gravitational waveforms. *Phys. Rev.*, D79:104023, 2009. doi: 10.1103/PhysRevD.79.104023,10.1103/PhysRevD.84.049901. [Erratum: Phys. Rev.D84,049901(2011)].

[89] Alessandra Buonanno, Guillaume Faye, and Tanja Hinderer. Spin effects on gravitational waves from inspiraling compact binaries at second post-newtonian order. *Phys. Rev. D*, 87:044009, Feb 2013. doi: 10.1103/PhysRevD.87.044009. URL https://link.aps.org/doi/10.1103/PhysRevD.87.044009.

[90] Alessandra Buonanno, Bala R. Iyer, Evan Ochsner, Yi Pan, and B. S. Sathyaprakash. Comparison of post-newtonian templates for compact binary inspiral signals in gravitational-wave detectors. *Phys. Rev. D*, 80:084043, Oct 2009. doi: 10.1103/PhysRevD.80.084043. URL https://link.aps.org/doi/10.1103/PhysRevD.80.084043.

Chapter 4

Accelerating waveform model evaluation with adapted grids: Multibanding

This chapter presents the article:

- *Accelerating the evaluation of inspiral-merger-ringdown waveforms with adapted grids.* Cecilio García-Quirós, Sascha Husa, Maite Mateu-Lucena, Angela Borchers. arXiv:2001.10897 [gr-qc] (2020),

which has been submitted for peer review to Classical Quantum Gravity.

Abstract

This paper presents an algorithm to accelerate the evaluation of inspiral-merger-ringdown waveform models for gravitational wave data analysis. While the idea can also be applied in the time domain, here we focus on the frequency domain, which is most typically used to reduce computational cost in gravitational wave data analysis. Our work extends the idea of multibanding [1], which has been developed to accelerate frequency domain waveforms, to include the merger and ringdown and spherical harmonics beyond the dominant quadrupole spherical harmonic. The original method of [1] is based on a heuristic algorithm based on the inspiral to redefine the equi-spaced frequency grid used for data analysis where a coarser grid is sufficient for accurate evaluation of a waveform model. Here we use a different criterion, based on the local interpolation error, which is more flexible and can easily be adapted to general waveforms, if their phenomenology is

understood. We discuss our implementation in the LIGO Algorithms Library [2] for the IMRPhenomXHM [3] frequency domain model, and report the acceleration in different parts of the parameter space of compact binary systems.

4.1 Introduction

The field of gravitational wave astronomy has been born through discoveries of coalescences of compact binary systems consisting of black holes and neutron stars [4–6]. For such systems, very successful programs are being carried out to model the gravitational waveforms expected according to general relativity (and possibly alternative theories) across the astrophysically plausible parameter space of observable binary systems (see e.g. [7–14]). These models are based on synthesising perturbative results, e.g. from PN theory [15], black hole perturbation theory [16] and more recently the self-force approach [17], with numerical solutions of the Einstein equations, with an important role played by the EOB approach [18, 19] to extend perturbative to non-perturbative descriptions.

Gravitational wave data analysis as applied to compact binary coalescence is typically split into two steps: searches and Bayesian PE. Searches can be performed independently from a waveform model [20], or use a fixed set of template waveforms and matched filter techniques [21, 22]. Bayesian PE [23, 24] is based on a likelihood function that compares the detector data with template waveforms. Several million template waveform evaluations may be required, and the computational cost of waveform evaluation makes Bayesian inference computationally expensive. In this paper we discuss the problem of accelerating the evaluation of the waveforms, intended in particular to reduce the computational cost of Bayesian PE.

A particularly computationally efficient approach to the construction of waveform models has been the phenomenological waveform approach (see e.g. [9–13]), where the waveform for each spherical harmonic is split into a small number (typically 2-4) regions based on physical intuition, and are written as closed-form expressions. In order to model simple non-oscillatory functions, it is further customary to split the waveform $h_{\ell m}(x, \Xi)$ for spherical harmonic (ℓ, m) into a real amplitude $A_{\ell,m}(x, \Xi)$ and a phase $\phi_{\ell,m}(x, \Xi)$. Here h would typically be the gravitational wave strain or its Fourier transform, and x the time or frequency, respectively. The quantity Ξ is a shorthand for all the intrinsic parameters of the waveform, such as masses and spins. We then compute the waveform of each spherical harmonic as

$$h_{\ell m} = A_{\ell m} e^{i\,\phi_{\ell m}}. \tag{4.1}$$

The evaluation of matched filters (e.g. due to optimization over time of arrival) typically requires the evaluation of fast Fourier transforms, which require equispaced grids. Typically, a computationally much cheaper interpolant could be constructed by only evaluating the model amplitude and phase on a much coarser grid without significant loss of accuracy, if the coarse grid points are chosen judiciously. Our goal is the same as that of [1]: to accelerate the evaluation of $A_{\ell m}$ and $\phi_{\ell m}$, but also the calculation of the complex exponential $e^{i\,\phi_{\ell m}}$, through an appropriate choice of coarse grid points and interpolation algorithm. For simplicity we will also us use the term "multibanding" to refer to this type of algorithm, and we also use the same two core ideas:

- We split the complete frequency or time range where we want to evaluate our model waveform into n sub-regions, where each region has a constant grid spacing Δx_n, chosen such that linear interpolation is sufficiently accurate for a given criterion of waveform accuracy. The final waveform can then be evaluated by simple linear interpolation to the fine grid with constant grid-spacing dx, which is determined by the requirements of gravitational wave data analysis. This step accelerates the evaluation of the amplitude and phase.

- For the phase, the computationally expensive evaluation of the complex exponential in Eq. (4.1) for each point of the fine grid is required. For coarse grids that are sufficiently dense for linear interpolation, a standard algorithm can be used to replace evaluation of the complex exponential at each point of the fine grid by evaluation only at the coarse grid points, and implementing linear interpolation as an iterative scheme.

The key difference between our work and [1] is that we change the criterion to compute the grid spacings Δx_n in the n coarse grids to use the standard estimate of the local interpolation error derived according to Taylor's theorem of basic calculus instead of a heuristic algorithm based on the relation between the duration of a data segment and the frequency spacing in the Fourier domain. Below we will analyze the required frequency spacing for the inspiral, merger and ringdown. We will first carry out the analysis separately for the amplitude and phase of different modes, and then define coarse grids that are appropriate for both phase and amplitude for each mode. For an overview of how the interpolation is incorporated in the context of the ROMs see [25].

This paper is organized as follows: In Sec. 4.2 we discuss the details of this algorithm, and how it is applied to quasi-circular non-precessing frequency domain waveforms for the inspiral, merger and ringdown. In Sec. 4.3 we present our results for computational efficiency and accuracy, and we conclude with a summary and comments on possible future work in Sec. 4.4.

4.2 Algorithms

4.2.1 Interpolation error

A real-valued differentiable function $g(x)$ can be approximated at a point x_0 by a linear approximation in the following sense: There exists a function $h(x)$ such that

$$g(x) = g(x_0) + g'(x_0)(x - x_0) + h(x)(x - x_0), \quad \lim_{x \to x_0} h(x) = 0. \tag{4.2}$$

The error $R(x)$ of the approximation is

$$R(x) = h(x)(x - x_0). \tag{4.3}$$

According to standard refinements of Taylor's theorem of basic calculus, the error term $R(x)$ can be estimated using the second derivative $g''(x)$ of the function g we want to approximate by the statement that there exists a ξ, $x_0 \leq \xi \leq x$, such that

$$R(x) = \frac{g''(\xi)}{2} (x - x_0)^2 . \tag{4.4}$$

If we apply this result to our problem of interpolating to a fine grid from a coarse grid with grid spacing Δx_n, then

$$R(x) \leq \max_{x_0 \leq \xi \leq x} \frac{g''(\xi)}{2} {\Delta x_n}^2. \tag{4.5}$$

Consequently we can choose our coarse grid spacing Δx_n to satisfy a given error threshold R as

$$\Delta x_n = \sqrt{\frac{2R}{\max_{x_0 \leq \xi \leq x} g''(\xi)}}. \tag{4.6}$$

Our application of interpolation will initially be guided by the requirements of phase accuracy, and we will then discuss in which sense these criteria also lead to a sufficiently small amplitude error. Below we will develop the details of constructing a hierarchy of grids as appropriate for linear interpolation of both the frequency domain phase and amplitude for different spherical or spheroidal harmonic modes, and describe how to efficiently evaluate complex exponentials of the phase on such a grid hierarchy.

The hierarchy of grids is determined by the behaviour of the second derivative of the phase as a function of the frequency according to Eq. (4.6). We distinguish between three main regions: inspiral, merger and ringdown. As shown in Fig. 4.1 the behaviour of the phase derivative is sharper and changes very drastically, then more points will be needed

in this region. However the merger and ringdown parts are "flatter" and less points will be necessary to describe these parts.

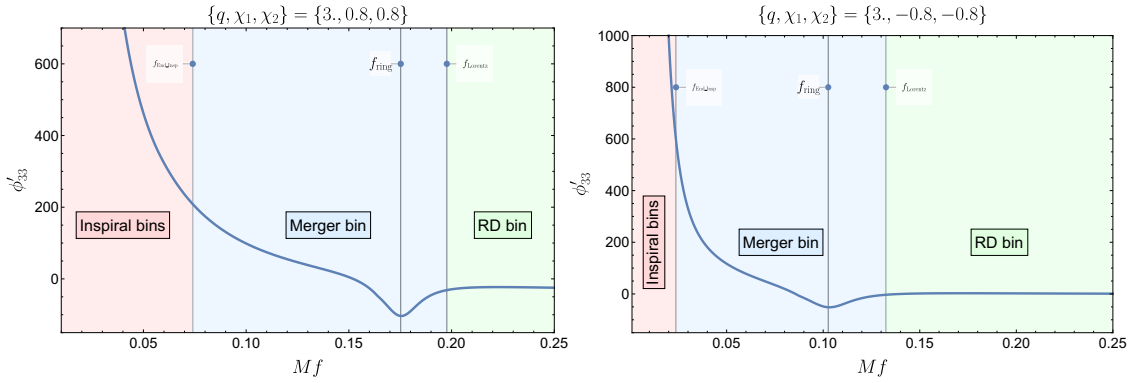

FIGURE 4.1: The phase derivative is shown for the $\ell = |m| = 3$ spherical harmonic mode for two different configurations with high spins. The phase derivative changes rapidly in the inspiral region, and thus many grid points are required for accurate interpolation, the ringdown part is however comparatively flat, thus only few points are needed to describe it. The merger bin is characterized by the shape of the Lorentzian and determines the resolution required in this region.

4.2.1.1 Inspiral in the frequency domain

In order to derive an appropriate frequency grid spacing Δf (f is the dimensionless frequency in geometric units $G = c = 1$) for the Fourier domain phase during inspiral, we will approximate the phase by the leading TaylorF2 phase expression [26],

$$\Phi_{\ell m} = c_0 + c_1 f + \frac{m}{2}\frac{3}{128\eta}\left(\frac{2\pi f}{m}\right)^{-5/3}, \tag{4.7}$$

where η is the symmetric mass ratio, which in terms of the component masses $m_{1,2}$ of the binary reads $\eta = m_1 m_2/(m_1+m_2)^2$, and c_0, c_1 are constants of integration that do not affect the second derivative, which reads

$$\Phi''_{\ell m} = \frac{m}{2}\frac{5}{48\eta}\left(\frac{2\pi}{m}\right)^{-5/3} f^{-11/3}. \tag{4.8}$$

The phase and phase derivatives becomes singular as the frequency f approaches zero, and the magnitude of the second derivative increases toward decreasing frequency. We can therefore estimate the maximal second phase derivative as the second derivative of the phase at the start of each frequency interval for which we want to use interpolation, assumed at frequency f, and obtain

$$\Delta f(f) \quad = \quad \sqrt{\frac{2R}{\Phi''(f)}} = \sqrt{\frac{2R}{c_{f,insp}}} f^{11/6}, \tag{4.9}$$

$$c_{f,insp} = \frac{m}{2}\frac{5}{48\eta}\left(\frac{2\pi}{m}\right)^{-5/3}. \tag{4.10}$$

In Sec. 4.2.3 we will use Eq. (4.9) to split the calculation of the phase into frequency bins, where in each bin the grid spacing Δf is kept constant, but it increases from bin to bin with increasing start frequency of the bin.

We now turn to the inspiral amplitude. For the modes we consider in this work we obtain the following leading order terms, see e.g. [3], where we use the definitions $v = (2\pi f/m)^{1/3}$ and $\delta = \sqrt{1-4\eta}$:

$$A_{\ell m} = \pi\sqrt{2\eta/3}\, v^{-7/2} a_{\ell m}, \tag{4.11}$$

$$a_{22} = 1 + O(v^2), \tag{4.12}$$

$$a_{21} = v\delta\frac{\sqrt{2}}{3} + O(v^2), \tag{4.13}$$

$$a_{33} = v\delta\frac{3}{4}\sqrt{\frac{5}{7}} + O(v^3), \tag{4.14}$$

$$a_{32} = v^2\frac{1}{3}\sqrt{\frac{5}{7}}(1-3\eta) + O(v^3), \tag{4.15}$$

$$a_{44} = v^2\frac{4}{9}\sqrt{\frac{10}{7}}(1-3\eta) + O(v^4). \tag{4.16}$$

For the amplitude it is natural to define a threshold for the relative error of the interpolation, which we denote by r. The frequency dependent coarse grid resolution $\Delta f(f)$ which results from specifying a relative error threshold r is then independent of η and depends linearly on the frequency,

$$\Delta f_{\ell m}(f) = \sqrt{\frac{2rA_{lm}}{A''_{lm}}} = c_{\ell m}\, f\sqrt{r}, \tag{4.17}$$

where

$$c_{22} = 6\sqrt{\frac{2}{91}}, \tag{4.18}$$

$$c_{21} = c_{33} = 6\sqrt{\frac{2}{55}}, \tag{4.19}$$

$$c_{44} = c_{32} = 2\sqrt{\frac{2}{3}}. \tag{4.20}$$

We can then write the ratio of coarse grid spacing required for the phase to stay below a phase error of R radians to the coarse grid spacing required for the amplitude to

guarantee a relative amplitude error below r as

$$\frac{\Delta f_{phase}}{\Delta f_{amp}} = \alpha_{\ell m} \left(f\pi\right)^{5/6} \sqrt{\eta} \sqrt{\frac{R}{r}}, \tag{4.21}$$

where

$$\alpha_{22} = 2\sqrt{\frac{91}{55}}, \quad \alpha_{21} = 2^{1/3}\sqrt{\frac{11}{3}}, \tag{4.22}$$

$$\alpha_{33} = \frac{2^{7/3}}{3^{11/6}}\sqrt{11}, \quad \alpha_{32} = \frac{6}{\sqrt{5}}, \quad \alpha_{44} = \frac{3}{2^{1/3}\sqrt{5}}. \tag{4.23}$$

Choosing e.g. $r = R$ the expression (4.21) is always smaller than unity up to the MECO frequency [27], the step size restriction for the phase is thus more restrictive than the one for the amplitude. For simplicity we will use the phase criteria to build just one coarse frequency array and use this for both the phase and amplitude. We discuss the merger and ringdown in the next section.

4.2.1.2 Merger and ringdown in the frequency domain

The merger-ringdown phase exhibits a morphology that is rather different from the inspiral. A detailed phenomenological description for the $\ell = |m| = 2$ is provided by the IMRPhenomD [12] and IMRPhenomXAS [28] waveform models, and for subdominant modes by IMRPhenomXHM [3]. This allows us to identify the crucial features of the merger-ringdown regime, and to adapt the estimate (4.6) for the step size as we have done for the inspiral.

The first ingredient will be to identify the end of the inspiral. In [29, 28, 3] we confirm that the minimum energy circular orbit (MECO) [27] provides a good approximation for the transition between inspiral and merger for comparable masses. In the merger-ringdown part the Fourier domain phase derivative is given by a superposition of a Lorentzian function and a background term [28, 3]. The Lorentzian dominates the phase derivative and is given by (see eq. (6.3) in [3]):

$$\Phi'(f) = \frac{a}{(f - f_0)^2 + b^2} \tag{4.24}$$

and the second derivative by

$$\Phi''(f) = -\frac{2a(f - f_0)}{((f - f_0)^2 + b^2)^2}, \tag{4.25}$$

where we have introduced the shorthands $a = a_\lambda f^{lm}_{\rm damp}$, $b = f^{lm}_{\rm damp}$, and $f_0 = f^{lm}_{\rm ring}$. Thus α_λ is a term that determines the overall amplitude of the Lorentzian, f_0 is the frequency at which the dip of the Lorentzian happens and b is a measure of the "width" of the dip. Inserting the expression for the Lorentzian into Eq. (4.6) we obtain

$$\Delta f(f) = \sqrt{\frac{2R}{\Phi''(f)}} = \sqrt{\frac{R}{a|f-f_0|}}\left((f-f_0)^2 + b^2\right), \tag{4.26}$$

which replaces Eq. (4.9) for computing the spacing of the coarse frequency grid in the merger and ringdown.

The spacing computed according to (4.6) depends on the absolute value of the second derivative, and we note that the second derivative of the Lorentzian phase function, Φ'', has two local maxima for $f_0 \pm b/\sqrt{3}$, with identical absolute value

$$\left|\Phi''\left(f_0 \pm \frac{b}{\sqrt{3}}\right)\right| = \frac{3\sqrt{3}a}{8b^3}. \tag{4.27}$$

While for the inspiral the number of frequency bins depends on the start frequency, as we will discuss in more detail below in Sec. 4.2.3, for the merger and ringdown we choose two bins which we call the *merger* and *ringdown* bins. The merger bin is defined by the frequency interval $(f_{\rm Insp}, f_{\rm Lorentzian})$, and captures the frequency regime where high resolution is required to capture the shape of the Lorentzian. The frequency $f_{\rm Insp}$ marks the end of the inspiral region of the IMRPhenomXAS model for the $\ell = |m| = 2$ mode and the IMRPhenomXHM model for the other harmonics, and is chosen approximately at the MECO frequency (see [28] and [3] for details). The frequency $f_{\rm Lorentzian}$ is defined as $f^{lm}_{\rm ring} + 2f^{lm}_{\rm damp}$ and is chosen to approximate the lowest frequency where the second phase derivative of the Lorentzian can be neglected, and the first phase derivative is approximately constant. The ringdown bin starts at this frequency, and is the highest frequency bin in our procedure. It is characterized by low resolution requirements for the phase due to neglecting Φ'' and ends at the end frequency of the waveform, the frequency range of this last bin is thus $(f_{\rm Lorentzian}, f_{\rm max})$.

We compute the grid spacing of both bins by evaluating the maximum value of $|\Phi''|$ in these two intervals according to Eqs. (4.9, 4.27) and inserting it into Eq. (4.6). For the merger bin this is the maximum of the inspiral value and the value for the Lorentzian, and thus

$$\Delta f^{phase}_{\rm merger} = \min\left(\sqrt{\frac{2R}{c_{f,insp}}} f_{insp}^{\frac{11}{6}}, \frac{4f^{lm}_{\rm damp}}{3^{3/4}}\sqrt{\frac{R}{|\alpha_\lambda|}}\right), \tag{4.28}$$

For the ringdown bin the second phase derivative $|\Phi''|$ decreases monotonically to zero, we thus take the value at the start of the region $f_{\text{Lorentzian}}$, which yields

$$\Delta f_{\text{RD}}^{phase} = 5\, f_{\text{damp}}^{lm} \sqrt{\frac{R}{2|\alpha_\lambda|}}. \tag{4.29}$$

Again we turn to the amplitude now. We approximate the amplitude falloff in the ringdown bin as

$$h \approx e^{-\Lambda f}, \tag{4.30}$$

with $\Lambda = \lambda/(f_{damp}^{lm}\sigma)$, where these coefficients correspond to those used in the ringdown ansatz for the IMRPhenomXHM model (see [3] for more details):

$$A_{RD}^{\ell m} \propto \frac{1}{\left(f - f_{ring}^{\ell m}\right)^2 + \left(f_{damp}^{\ell m}\,\sigma\right)^2} e^{-\frac{\left(f - f_{ring}^{\ell m}\right)\lambda}{f_{damp}^{\ell m}\sigma}}. \tag{4.31}$$

The grid spacing required to guarantee a relative error smaller than r is then given by

$$\Delta f_{RD}^{amp}(r) = \frac{\sqrt{2\,r}}{\Lambda}, \tag{4.32}$$

which is independent of the frequency f. For $r = R$ this condition is typically more restrictive than the condition (4.29) derived from the phase, the dependence across parameter space is however complicated. We therefore always compute the two frequency spacings, and then use the more restrictive one. We believe that this choice is quite conservative and that the choice could be relaxed in the future, since our ringdown bin only starts at frequencies where the amplitude is already quite small. Note that the start frequency of our ringdown region is either significantly higher than the ringdown frequency, or, for very high spins, the exponential falloff is significantly steeper than for moderate spins. In consequence we could use always the phase criterion (4.28) to set the grid spacing in the ringdown region without worrying too much about loss of accuracy. If greater amplitude accuracy for the ringdown would be required, it would be also possible to switch from linear interpolation to the fine grid to third order spline interpolation for the amplitude.

In the merger bin, the functional dependence of the mode amplitudes is more complex (see [3]). In this case we compute numerically the grid spacing Δf for the amplitude as

$$\Delta f_{merger}^{amp} = \sqrt{\frac{2\,r\,|h_{lm}(f)|}{|h_{lm}(f)|''}}.$$

We evaluate this quantity for the merger bin across our parameter space with the choice $r = R$ and compare with the grid spacing derived for the phase given by Eq. (4.28). We find that the ratio $\Delta f^{phase}_{merger}/\Delta f^{amp}_{merger}$ is typically lower than one so the criteria for the phase is more restrictive than the one for the amplitude. We find that for some cases with comparable masses and high positive spins the ratio is between a value of one and two, but for simplicity we will always choose the criterion for the phase and interpret this choice such that the actual relative amplitude and phase errors will be bounded by the thresholds within a factor of four. We leave refinements of the simple strategy to set $r = R$ to future work. Below we will study the mismatch between the original model and different levels of error threshold to arrive at a more practical evaluation of error than to check for local deviations between model and approximation, and in Sec. 4.3.3 we will perform a PE exercise and find that all choices of the value of $R = (0.1, 0.01, 0.001)$ lead to indistinguishable results for the case considered.

4.2.2 Efficient evaluation of complex exponentials

The evaluation of the complex exponential function when constructing the strain from amplitude and phase as in Eq. (4.1) is one of the most time consuming operations in the C-code of the LALSuite [2] implementation of our model. The number of required evaluations of the complex exponential (or, equivalently, of trigonometric functions), can however be reduced drastically by implementing the method described in [1] (adapted from [30]). Instead of interpolating the phase on the uniform fine grid and computing the complex exponential, we compute the complex exponential in the non-uniform coarse grid and then rewrite the interpolation of this quantity in terms of an iterative algorithm.

Let Φ_j be the phase at one coarse frequency point f_j and let $\hat{\Phi}_k$, f_k be the estimated phase and the frequency at one point of the final uniform frequency grid, the spacing of the uniform grid is therefore $df = f_{k+1} - f_k$. Then we use the recursive property

$$e^{i\hat{\Phi}_{k+1}} = e^{i\hat{\Phi}_k} e^{i\, df\, \frac{\Phi_{j+1}-\Phi_j}{f_{j+1}-f_j}}\,. \tag{4.33}$$

This property is used to compute the complex exponential in the fine frequency grid points that lay between two coarse frequency points j and $j+1$. The first of the fine points is given by $e^{i\hat{\Phi}_0} = e^{i\Phi_j}$.

4.2.3 Complete multibanding algorithm in the frequency domain

We will now describe our final algorithm for accelerated waveform evaluation, which is based on our previous results. Our final results will be the strain, evaluated on a uniform

frequency grid, with a resolution df that is adapted to the requirements of some given data analysis application. The motivation for uniform grid spacing stems for the typical context of matched filtering, where an inverse Fourier transform is used to optimize a match over the time shift between a signal and a template. We will refer to this uniform frequency grid as the fine grid. In order to accelerate the waveform evaluation we will however only evaluate our model waveform on a coarser non-uniform grid, and then use the iterative evaluation described above in Sec. 4.2.2 to evaluate the complex exponential of the phase.

By default we will use linear interpolation for the amplitude, with optional cubic spline interpolation. Both interpolation algorithms are currently using the open source `GSL` library [31], we do however expect a further speedup by replacing the `GSL` implementation by adding a standalone implementation of the required interpolations to our code.

We will now first discuss how to construct the non-uniform coarse frequency grid, and then the details of how to evaluate the waveform on the fine grid, first for spherical harmonics without mode mixing, and then for modes with mode mixing, which for the current IMRPhenomXHM models concerns only the $\ell = 3, |m| = 2$ mode.

4.2.3.1 Building the coarse frequency grid

We assume that we are given an input frequency range (f_{min}, f_{max}) where we need to evaluate the spherical harmonic modes of the waveform. We wish to construct a non-uniform frequency grid, such that for every two successive frequency points the grid spacing $\Delta f(f)$ between them is sufficiently small to guarantee that the local phase error resulting from using linear interpolation between the coarse frequency points is smaller than a given threshold value R. We can then use Eqs. (4.9, 4.26) to compute Δf as a function of the threshold R, the frequency f, the intrinsic parameters (q, χ_1, χ_2), and the spherical harmonic mode (ℓ, m) under consideration. The coarse grid will also depend on the desired grid spacing df for the final uniform grid, since we build the coarse frequency grid such that the coarse points also belong to the fine grid. This simplifies the interpolation procedure for the complex exponential.

Lower values for the threshold R result in smaller errors, but higher computational cost. In Sec. 4.3 we will compare different threshold settings and evaluate the computational cost and compare the actual errors with the chosen threshold R.

As mentioned above in Sec. 4.2.1 we split the frequency range into three regions corresponding to the inspiral, merger and ringdown. For the practical implementation, instead of using the continuously varying $\Delta f(f)$ of expressions (4.9, 4.26), we work with a series

of frequency bins where Δf is fixed in each bin. The merger and ringdown parts have a much smaller dynamic range for $\phi'(f)$ than the inspiral part (the phase "flattens out" from inspiral toward merger), and we just use one frequency bin for each region. Their spacings $\Delta f_{\rm merger}$ and $\Delta f_{\rm RD}$ are given by Eqs. (4.28) and (4.29-4.32) respectively.

However, the inspiral part has a large dynamic range, and Δf given by (4.9) changes with a power law of $f^{11/6}$ so it also changes fast. The spacing that would accurately describe the whole inspiral part would be $\Delta f(f_{\rm min})$, however if we used this spacing for the whole region, we would be using many more points than what are really needed since Δf increases so much for frequencies above $f_{\rm min}$. Therefore we use a varying number of frequency bins N, and we build each of them with a spacing Δf_i twice larger than the previous bin. For the first bin we set $\Delta f_0 = \Delta f(f_{\rm min})$, thus

$$\Delta f_0 = \sqrt{\frac{2R}{c_{insp}}} f_{min}^{11/6} \tag{4.34}$$

$$\Delta f_i = 2^i \, \Delta f_0, \qquad i = 1, 2, ..., N. \tag{4.35}$$

In practice we require that between two coarse points there is an integer number of fine frequency points, in consequence we modify Δf_0 such that

$$\Delta f_0' = \texttt{int}\left[\frac{\Delta f_0}{df}\right] df. \tag{4.36}$$

Now that we have computed the spacing of each frequency bin, we need to compute the final frequency of each bin $f_{i,\rm end}$, which is the frequency that doubles the spacing Δf of the current bin, i.e. we have to solve the equation $\Delta f(f_{i,\rm end}) = 2\,\Delta f_i$. Inserting this into Eq. (4.9) we obtain

$$f_{i,\rm end}^{\frac{11}{6}} = 2\, f_{i,\rm start}^{\frac{11}{6}}, \tag{4.37}$$

$$\frac{f_{i,\rm end}}{f_{i,\rm start}} = 2^{\frac{6}{11}}. \tag{4.38}$$

We require that in a frequency bin there must be an integer number of coarse frequency points, and so we modify the end frequencies of each bin to

$$f_{i,\rm end}' = \texttt{int}\left[\frac{f_{i,\rm end} - f_{i,\rm start}}{\Delta f_i}\right] \Delta f_i. \tag{4.39}$$

With the above frequency factor we can estimate the number N of bins that will be used in the inspiral. Since the inspiral regions ends at $f_{\rm insp}$, N has to satisfy the relation

$$\frac{f_{\rm insp}}{f_{\rm min}} = \left(2^{\frac{6}{11}}\right)^N, \tag{4.40}$$

and therefore we obtain

$$N = \log_{2^{\frac{11}{6}}} \left(\frac{f_{\rm insp}}{f_{\rm min}} \right) . \tag{4.41}$$

Since N is however the number of constant frequency bins for the inspiral, it has to be an integer, and we modify $f_{\rm insp}$ such that

$$N = \log_{2^{\frac{11}{6}}} \left(\frac{f'_{\rm insp}}{f_{\rm min}} \right) = \texttt{int} \left[\log_{2^{\frac{11}{6}}} \left(\frac{f_{\rm insp}}{f_{\rm min}} \right) \right] . \tag{4.42}$$

For the merger and ringdown regions, we proceed analogously to the inspiral region, and ensure that an integer number of fine grid points aligns with the coarse grid. Since this algorithm depends on the input values for f_{min}, f_{max} and df, we perform several sanity checks to ensure that there is not any overlapping between regions. For example, if $f_{\rm insp} > f_{\rm Lorentzian}$ we skip the merger bin or if $f_{\rm Lorentzian} > f_{max}$ we skip the ringdown bin.

In Fig. 4.2 we compare the final non-uniform coarse grid with the uniform grid. In the top panel we can see how the frequency spacing Δf increases for subsequent bins that constitute the inspiral part. In the case shown the merger bin has a slightly lower Δf than the last inspiral bin in order to resolve the Lorentzian feature of the phase derivative. For other cases where the Lorentzian is less pronounced the limiting factor will be the derivative at the end of the inspiral and then the merger will have exactly twice the spacing of the last inspiral bin. The ringdown bin is the one with a coarser Δf since there the phase derivative is practically flat. In the bottom panel we show the number of frequency points for the inspiral, merger and ringdown parts. The uniform grid has most of its frequency points in the merger-ringdown part, which leads to an excessive computational cost in these regions, where far fewer points are required to capute the flatter behaviour of the phase derivative (see Fig. 4.1). For the non-uniform grid most of the points are located in the inspiral part, where high resolution is needed to describe the phase derivative.

Now that we have described the non-uniform coarse frequency grid, the next step is to evaluate the model in this grid and carry out the interpolation to the fine grid. In this next step however, different procedures need to set up follow for the modes with and without mixing, as we discuss below.

4.2.3.2 Evaluate the modes on the fine grid, with and without mode-mixing

For the modes without mixing (at the moment all modes except $\ell = 3, |m| = 2$), the waveform modes are evaluated on the fine grid as follows:

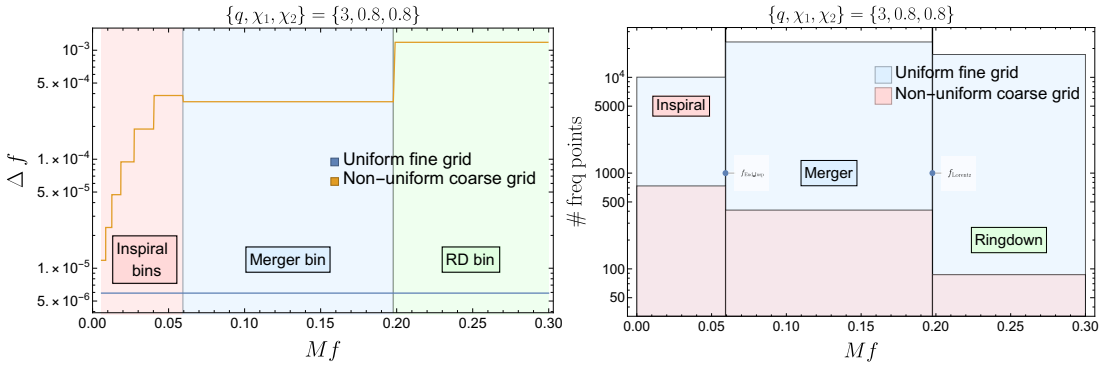

FIGURE 4.2: Comparison between uniform fine frequency grid and non-uniform coarse grid for the 33 mode for a high spin case. Left panel: The frequency spacing is shown for each frequency bin as a function of frequency. In the merger bin Δf is smaller than the last one of the inspiral due to the need of resolving the dip of the Lorentzian. Right panel: The number of frequency points is shown for each frequency region. In a uniform grid most of the points lie in the merger and ringdown part where they are not so necessary, however this is corrected in the non-uniform grid.

1. First the amplitude and phase are evaluated separately for the coarse frequency grid, which yields two 1D arrays, one for the amplitude and one for the phase.

2. The complex exponential $e^{i\phi}$ is computed on the coarse grid.

3. The fine uniform frequency grid is constructed with spacing df.

4. The complex exponential is interpolated to the final uniform frequency grid following the procedure described in Sec. 4.2.2.

5. The amplitude is interpolated to the fine grid by using linear (optionaly third) order interpolation (using the `GSL` library).

6. The complex waveform $\tilde{h}_{lm}$ is constructed by multiplying the arrays for the amplitude and the complex exponential on the fine grid.

For the modes with mixing (in our present implementation of IMRPHENOMXHM this is only the $\ell = 3, |m| = 2$ mode) our procedure is slightly different from the modes without mixing. To handle mode-mixing, in the ringdown region the model is built in terms of spheroidal harmonics instead of spherical harmonics, to simplify the waveform and avoid sharp features in the phase derivative and in the amplitude, as discussed in detail in [3]. After building the model waveform in terms of spheroidal harmonics, it is then rotated back to spherical harmonics and connected with the inspiral part, which is directly modelled in terms of spherical harmonics. Performing our interpolation in terms of the spherical harmonics as for the other modes would require significantly higher resolution and increase computational cost. We thus use the same strategy as we have employed to construct the original model, and apply our multibanding algorithm separately to the

inspiral region expressed in spherical harmonics, and to the ringdown part expressed in spheroidal harmonics, and then transform the latter to spherical harmonics once the fine grid values have been computed. Our detailed procedure is as follows:

1. We split the coarse frequency array into the spherical part, where we will perform the model evaluation and multibanding in terms of the spherical harmonics, and the spheroidal part, where we transform from the spheroidal to the spherical representation in the ringdown region.

   The start frequencies of the ringdown region for the phase and amplitude, $f_{RD}^{\rm phase}$, $f_{RD}^{\rm amp}$, are given in eq. (5.2) in [3]. Note that $f_{RD}^{\rm phase} < f_{RD}^{\rm amp}$. For our multibanding algorithm we split between the "spherical" and "spheroidal" coarse grids, where the spherical and spheroidal amplitude and phase are computed. There is some overlap between the frequency ranges of both in the interval ($f_{RD}^{\rm phase}$, $f_{RD}^{\rm amp}$), since the spherical array goes up to $f_{RD}^{\rm amp}$, but the spheroidal one starts at $f_{RD}^{\rm phase}$, see step (8) below.

2. Evaluate the spherical amplitude and phase in the spherical coarse array and evaluate the spheroidal amplitude and phase in the spheroidal coarse array, we get therefore four one-dimensional arrays.

3. Compute the complex exponential for the two coarse arrays of phases.

4. Build the uniform frequency grid with spacing df and split into spherical and spheroidal parts as above.

5. Interpolate the two arrays of complex exponential in their respective regions using the iterative procedure described in 4.2.2.

6. Interpolate the two arrays of amplitude in their respective regions using linear (optionally third) order splin interpolation using the `GSL` library [31].

7. We have thus obtained four arrays: spherical amplitude and complex exponential evaluated in the spherical fine grid, and spheroidal amplitude and complex exponential in the spheroidal fine grid.

8. Finally we combine amplitude and phase with different procedures in three frequency ranges:

   - $f_{min} \leq f < f_{RD}^{\rm phase}$: We directly multiply spherical harmonic amplitude and complex exponential.
   - $f_{RD}^{\rm phase} \leq f < f_{RD}^{\rm amp}$: We rotate to spherical the spheroidal complex exponential term (which requires the spheroidal amplitude), and then multiply the resulting spherical complex exponential with the spherical amplitude.

- $f_{RD}^{\mathrm{amp}} < f \leq f_{max}$: We first multiply the spheroidal amplitude and complex exponential and then transform to the spherical basis.

4.3 Results

4.3.1 Computational performance

In first place we test the gain in speed due to multibanding and compare the results for different threshold values and for different spacings of the fine frequency grid. Note that the frequency spacing df of the grid in the Fourier domain is related to the duration T of the time segment that is analyzed by

$$df = \frac{1}{T}, \tag{4.43}$$

and thus longer signals require a smaller grid spacing. To illustrate this dependency, in Fig. 4.1 we show the approximate duration of a binary black hole coalescence signal as a function of mass and mass ratio. To leading PN order the duration in dimensionless units is given by

$$T/M = \frac{5}{256\eta\,(\pi M f_0)^{8/3}}, \tag{4.44}$$

where f_0 is the frequency where the dominant spherical harmonic mode, $|\ell = |m| = 2$ enters the frequency band of the detector. Lower start frequencies thus imply much longer signals. In Fig. 4.1 we show results for two values of the lower frequency cutoff of the detector, $f_0 = 10$ Hz, 20 Hz, the latter is what is typical for current compact binary PE, see e.g. [32, 33]. The coalescence time is approximated with the TaylorT2 approximant at second PN order spins aligned with the orbital angular momentum, and extreme Kerr values, adding a time of $500M$ in geometric units to account for merger and ringdown, in order to obtain an approximate upper limit on the duration. The figures focus on short signals, where time duration of 4 seconds is appropriate, and show the range of signals and templates in mass and mass ratio that fit into this time window.

We will now discuss an example case of a non-spinning system of black holes with total mass of 50 solar masses and mass ratio $m_1/m_2 = 1.5$, and evaluate the computational cost as a function of frequency spacing df. In Fig. 4.2 we show the evaluation time of one waveform versus the spacing of the final uniform frequency grid. The frequency range spans from 10 to 4096 Hz and we fix the mass of the system to 50 $\mathrm{M}_\odot$. The dashed lines represent the waveforms generated without multibanding while the solid lines correspond to the multibanding version with different values of the threshold: 10^{-1}, 10^{-2}, 10^{-3} and 10^{-4}. First, we focus on the no-multibanding results, in principle we would expect

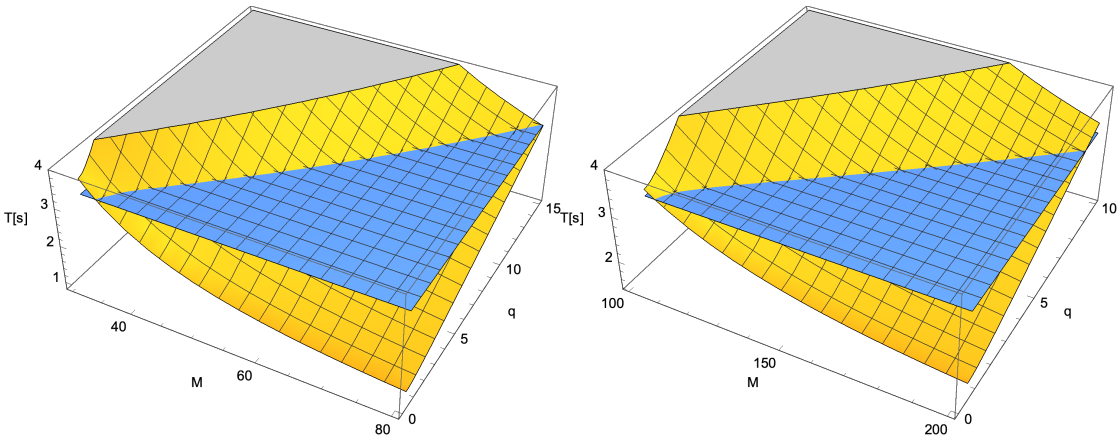

FIGURE 4.1: The approximate merger time observed by a detector with lower frequency cutoff at 20 Hz (left panel) and 10 Hz (right panel) is shown as a function of the total mass and the mass ratio of the system. The blue horizontal surface marks a duration of three seconds, which would allow for one second of buffer time between the signal duration and the length of the data segment. For a start frequency of 10 Hz only very high mass signals fit the time window.

that the higher-modes model is 5 times slower than the $(2, 2)$-mode-only model because IMRPHENOMXHM has 5 modes instead of just one. However it is a bit more expensive due to some particularities that are only present in the higher modes code, like the checks for the amplitude veto and mainly the extra steps needed to describe the mode-mixing of the $(3, 2)$ mode.

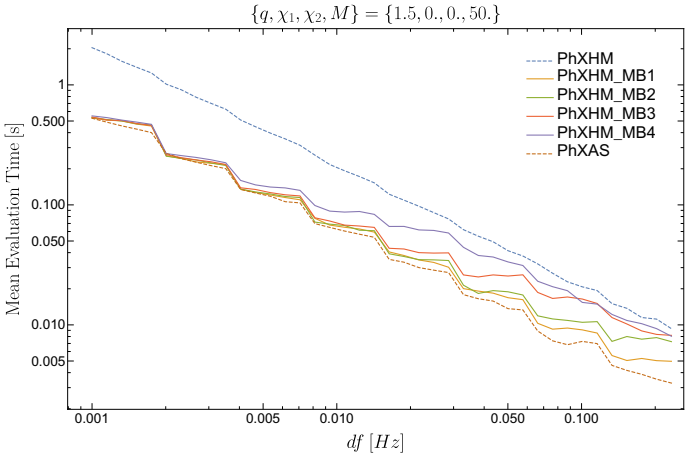

FIGURE 4.2: Evaluation time of the LALSuite code for waveforms with and without multibanding (solid and dashed lines respectively) for a total mass of 50 $M_\odot$. PhXAS denotes the quadrupole model, and the different "PhXHM_MB" items in the legend correspond to different values of the threshold R: 10^{-1}, 10^{-2}, 10^{-3} and 10^{-4}. The evaluation time is averaged over 100 repetitions. The results are shown as a function of the spacing of the fine uniform frequency grid df. They were obtained with the LIGO cluster CIT.

Focusing now on the results with multibanding, notice that when df is coarser the multibanding tends to equalize the no-multibanding. This is expected since for coarser df we have less frequency points and then the coarse and fine grid tends to be similar and there

is no gain by using the interpolation. Also it happens that the input *df* may be larger than the Δf of the coarse grid given by the multibanding criteria, in these cases we just evaluate in the frequency points of the fine grid and there is no gain in speed. In current LIGO-Virgo PE the highest *df* that is used is 0.25 Hz, since *df* is the inverse of the time duration of the signal as in Eq. (4.43), and in practice the smallest duration considered, e.g. for high mass events with very short duration, is four seconds. Note however that as low frequency noise is reduced in detectors, and the lower cutoff frequency for data analysis can be lowered, waveforms get longer and frequency spacings are reduced.

On the contrary, when *df* is very small we have a lot of points in the fine grid, then the interpolation is much more efficient and the multibanding has the highest gain in speed. The different values of the threshold behave as expected: larger values of the threshold are less accurate, but allow faster evaluation. For small *df* we observe however that the evaluation speed is almost independent of the threshold value. This is due to the fact that for small *df* the evaluation of the model at the coarse grid points is computationally much cheaper than the subsequent interpolation to the fine grid points. Future optimization of our code will be required to address this issue and intend to reduce the computational cost of the interpolation to the fine grid.

We now show the dependence of the evaluation time on the total mass of the system. In this case the spacing of the fine grid *df* is computed by the LALSuite function `XLALSimInspiralFD` which adapts the *df* accordingly to an internal estimation of the time duration of the signal which depend on the lower cutoff f_{min}, chosen here as $f_{min} = 10Hz$, and the mass of the system. This is similar in spirit to the estimate of the merger time that we have used in Fig. 4.1. In Fig. 4.3 we see qualitatively the same results than when simply scaling *df* as in Fig. 4.2. The multibanding is more efficient for lower masses where the duration of the signal is lower and therefore a smaller *df* is used.

4.3.2 Accuracy

In this section we discuss the accuracy of the multibanding algorithm as well as compare different choices of the threshold and motivate the choice of the default value for the model. In section 4.2.1 we explained that the non-uniform coarse grid is built such that the error in the phase (of a single mode) is below a threshold R. To check this we compute the waveform with and without multibanding for 150000 random configurations in the parameter range $M_{tot} \in [1, 500]M_{\odot}$, $q \in [1, 1000]$, $\chi_{1,2} \in [-1, 1]$, and *df* $\in [0.01, 0.25]$Hz. For the multibanding we compare again four different threshold values. In Fig. 4.4, we first show the maximum absolute error for the whole uniform frequency array for all

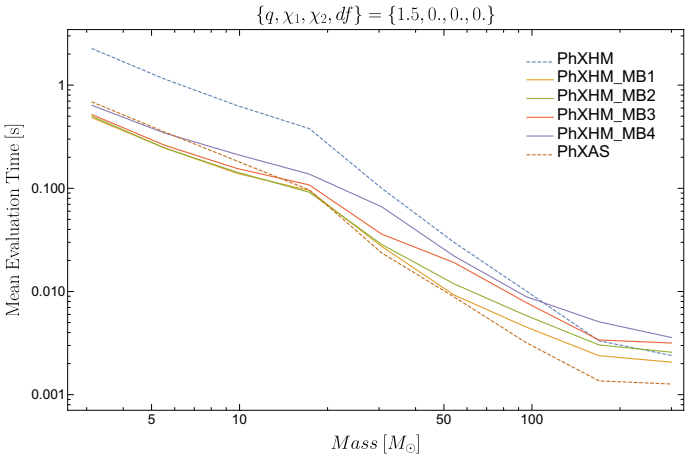

FIGURE 4.3: Evaluation time versus total mass of the system, choosing a fine grid spacing df that corresponds approximately to the inverse merger time at this mass ratio, as is common on data analysis applications (we denote this behaviour by writing $df = 0$). The evaluation time is averaged over 100 repetitions. Result were obtained with the LIGO cluster CIT.

the modes except $\ell = 3, m = 2$, where mode mixing needs to be taken into account for interpreting results as discussed below. We see that for most cases the maximum error is indeed below the threshold. However there can be special configurations where a few frequency points may give an error above the threshold. These few cases correspond typically to configurations where the approximations employed by the algorithm are less accurate, e.g. using the TaylorF2 phase to approximate the phase in the inspiral to compute Δf for extreme spins or for cases with high mass, where the inspiral starts at high frequencies where the TaylorF2 is again less accurate. In Fig. 4.5 we show the mean error, averaged over the frequency array, always remains below the thresholds. We will also compute mismatches between the original and the interpolated below, and find that we indeed achieve acceptably low values of the mismatch, see Fig. 4.8.

Now we consider the 32 mode, where mode mixing with the 22 mode is present. In Fig. 4.6 we show the results for the same test as shown in Fig. 4.4 for the other modes. The interpretation of the results is however different now, since the ringdown of the 32 mode, where mode mixing is present, is modelled and interpolated in terms of the spheroidal harmonics, see [3], where the waveform phenomenology is much simpler than in terms of spherical harmonics.

In Fig. 4.7 we show some typical behaviour for mode mixing in the ringdown: Here the complex waveform comes very close to or crosses zero, visible as a sharp feature in the logarithm of the amplitude. Near the zero-crossing splitting the waveform into a spherical harmonic amplitude and phase creates artefacts when computing phase differences or relative amplitude errors between two waveforms, even if they are very close. Comparing our theoretical thresholds with the phase only makes sense in the spheroidal basis, but

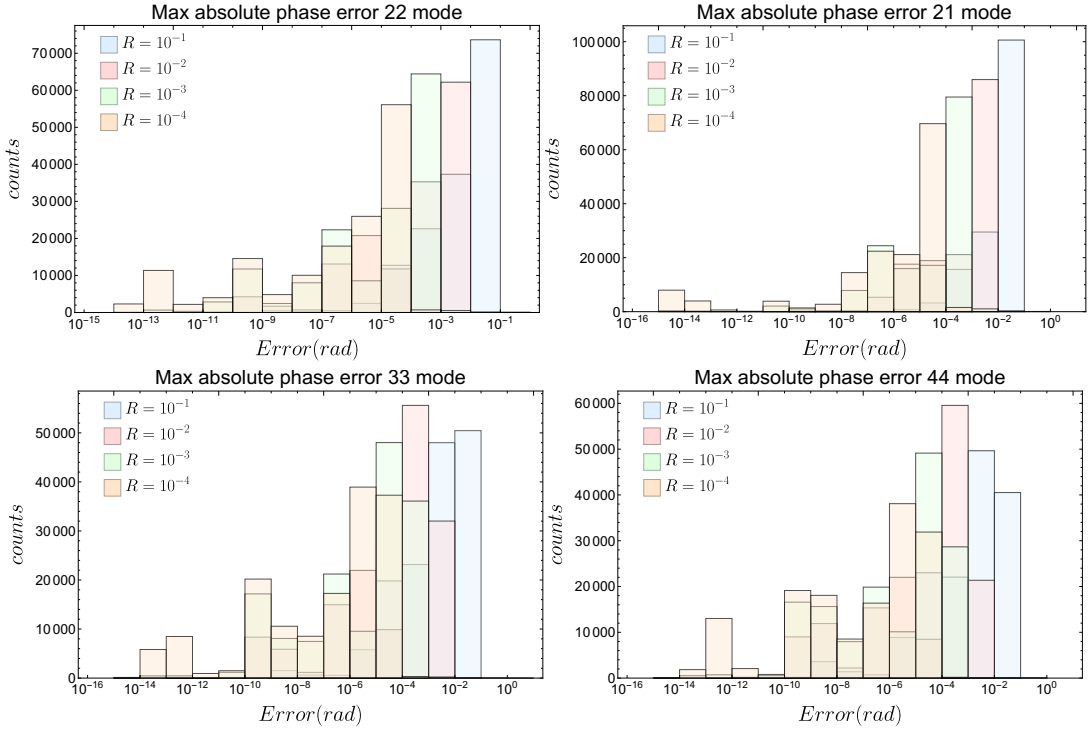

FIGURE 4.4: Maximum absolute error for the phase of the (l, m) mode between the multibanding and no-multibanding waveforms for four values of the threshold R. The threshold R can be interpreted as an approximate upper limit for the maximum absolute error introduced in the phase.

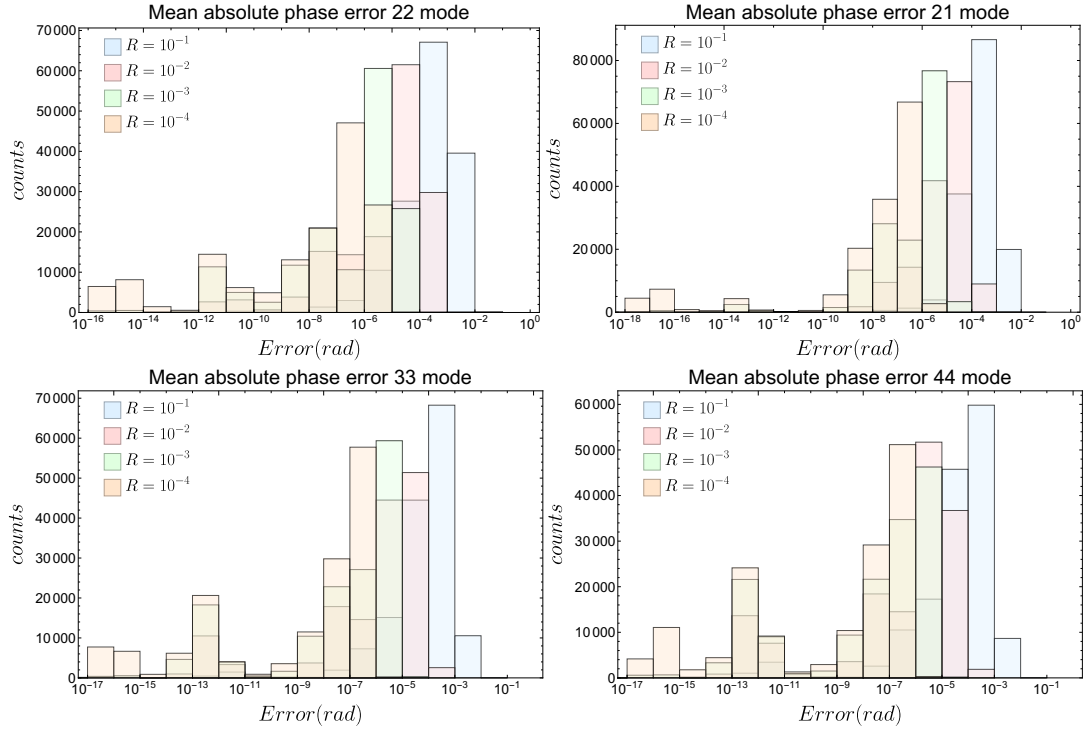

FIGURE 4.5: Absolute error for the phase averaged over the frequency array for the (l, m) modes between the multibanding and no-multibanding waveforms for four values of the threshold R. The threshold R can be interpreted as an approximate upper limit for the absolute error introduced in the phase.

not in the spherical one. We omit a comparison of the phase errors in the ringdown as computed in the spheroidal picture in order to avoid excess baggage in our LALSuite implementation. We thus arrive at the following interpretation of Fig. 4.6: while phase errors are typically small and below the threshold, a significant number of outliers arise due to the phenomenon shown in Fig. 4.7, they are however not due to problems of the multibanding algorithm, but due to keeping our test simple and uniformly comparing in the spherical harmonic picture for all modes and across the whole frequency range.

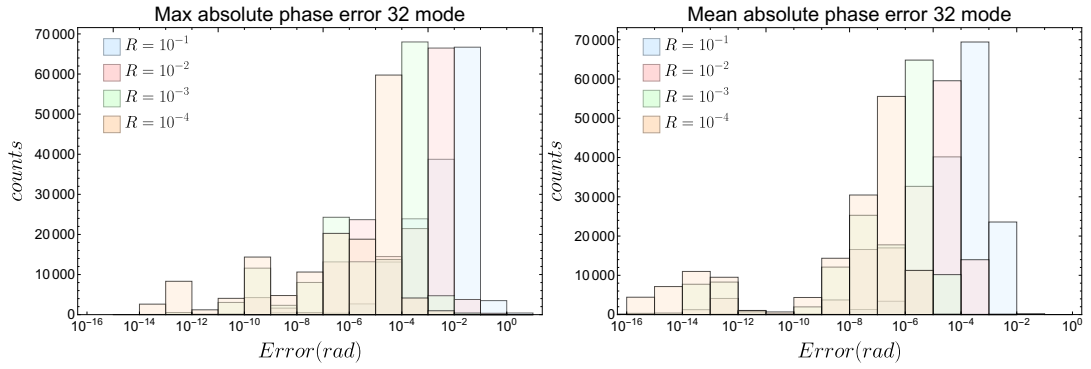

FIGURE 4.6: Maximum absolute error (left) and averaged over the frequency array (right) for the phase of the $(3, 2)$ mode between the multibanding and no-multibanding waveforms for four values of the threshold R.

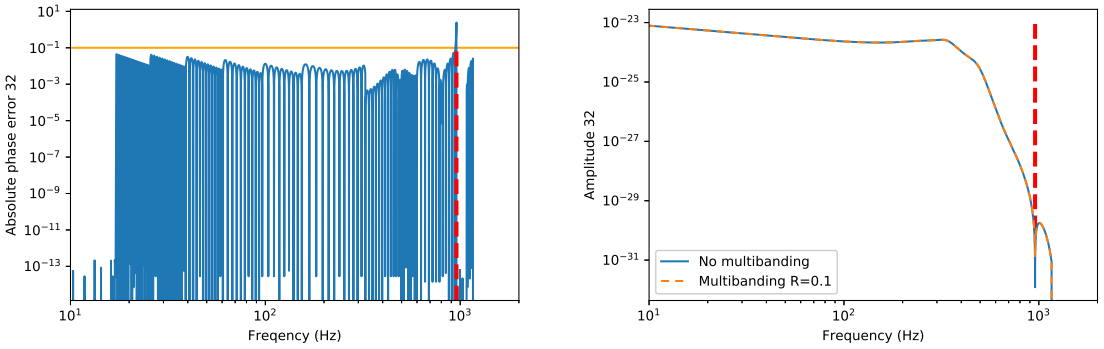

FIGURE 4.7: Example case that produces a maximum phase error above the threshold for the 32 mode. The parameters for this case are $m_1 = 35.7M_\odot$, $m_2 = 16.6M_\odot$, $\chi_1 = 0.33$, $\chi_2 = -0.54$. Lefth panel: Absolute phase error between the no-multibanding and multibanding waveform with $R = 0.1$ versus the frequency. Right panel: amplitude of the $(3, 2)$ mode for the no-multibanding and multibanding. Notice the correspondence of the maximum phase error with the deep in the amplitude of the $(3, 2)$ mode.

To truly understand the accuracy of the algorithm we have to compute the mismatch between the two waveforms. In the following we evaluate the multimode waveform and compute the mismatch for the h_+ polarization. We carry out an extensive study across the whole parameter space also to test the robustness of the algorithm and evaluate one million of random configurations in the parameter space. The results are shown in Fig. 4.8. As expected the threshold 10^{-4} has the lowest mismatches since it is the most accurate and the threshold 0.1 has the worst mismatches because it is the less

accurate. The reader may be wondering why there are a significant number of cases with mismatch 10^{-16} since we would expect that the number of cases decreases with the higher accuracy. The explanation is that in this bin the randomly chosen *df* is coarser than the Δf that the multibanding criteria provides, and in this case we replace Δf with *df* and in consequence there is no difference between the multibanding and no-multibanding and we reach matching precision.

Fig. 4.8 is also very useful to decide which threshold we want to use as default value in the LALSuite code. We consider that $R = 10^{-3}$ performs well in accuracy and given that is faster than the 10^{-4} we set this as the default value.

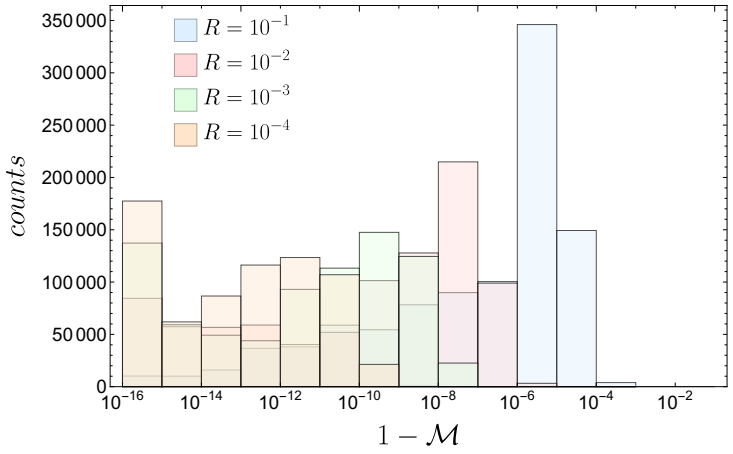

FIGURE 4.8: Mismatches between the no-multibanding and multibanding waveforms for one million random configurations across parameter space. We show the results for four different values of threshold. The configurations are choosen randomly with $q \in [1, 1000]$, $\chi_{1,2} \in [-1, 1]$, $\mathrm{M_t} \in [1, 500] M_\odot$, $df \in [0.01, 0.3]$ Hz, $\iota \in [0, \pi]$, $f_{min} = 10Hz$, $f_{max} = 1024Hz$. The mismatch is computed for the h_+ polarization.

4.3.3 Parameter estimation

In order to illustrate our algorithm in a PE application, we compare the performance of the original model and different choices for the threshold parameter R.

We select a publicly available NR data set from the SXS waveform catalogue [34], `SXS:BBH:0264`, which corresponds to a binary black hole merger at mass ratio 3, with individual spins of -0.6 anti-aligned with the orbital momentum. Then we inject this NR simulation into zero noise as a way to get a non-precessing and non-eccentric strain of 4 seconds of duration, with 100 $M_\odot$ total mass, near edge on with $\pi/3$ rad of inclination. We use a relatively close source at 430 Mpc, which implies a signal-to-noise ratio of 28. Recovery of the signal uses the advanced LIGO zero detuning high power noise curve [35]. We choose the parameters in order to challenge our approximations in the regime where higher modes are particularly relevant, not in order to demonstrate significant

computational gains, which by Fig. 4.1 when the lower cutoff frequency of the detector sensitivity would be lower than the 20 Hz we have chosen here to compute the likelihood function in our Bayesian inference algorithm (see e.g. [23, 24] for details of Bayesian inference for compact binary coalescence signals). Note that the start frequency of the NR waveform we choose here is approximately 9 Hz at $M = 100M_\odot$.

For our analysis we use a sampling method called "Nested Sampling" [36], in particular the CPNest sampler [37] as implemented in the Python-based Bayesian inference framework Bilby [24]. For each waveform model used, we carry out runs with five different seeds and 2048 "live points" in the language of nested sampling, and we merge the results from the five seeds to a single posterior result.

We define prior distributions as follows: The mass ratio is assumed to be uniform between 0.125 and 1, and the chirp mass prior is assumed uniform between 15 and 60 $M_\odot$. The luminosity distance is uniform in volume with a maximal allowed distance at 1500 MPc. Finally, the magnitudes of the dimensionless black hole spins are uniform with an upper limit at 0.99.

Our main results concern the comparison of the IMRPhenomXHM model, evaluated with different values of the threshold parameter, $R = (10^{-1},\ 10^{-2},\ 10^{-3})$ as well as without multibanding, which corresponds to $R = 0$. The IMRPhenomXHM model includes the spherical harmonic modes $(l, |m|) = ((2,2), (2,1), (3,2), (3,3), (4,4))$. Differences between the recovered value of parameters and the injected parameters may arise due to the approximations in our multibanding algorithm, errors in the IMRPhenomXHM model, errors in the NR waveform, and the absence of modes in the model, which are present in the NR data set (which contains all modes up to $l = 8$). We also compare with the IMRPhenomXAS model, which corresponds to IMRPhenomXHM with only the $(l, |m|) = (2, 2)$ modes and no multibanding. The latter serves as a comparison in terms of the errors in recovering the injection parameters.

Our results are presented in Fig. 4.9. In the case of the higher modes model, the injected values are recovered by the most probable regions of the posterior distributions. However, for the dominant mode model, a significant bias in the recovered parameters can be observed. This confirms the importance of the higher mode contributions for the case we have chosen. All the results for IMRPhenomXHM are consistent within the statistical errors implied by our finite sampling. As expected, in the case presented here the sampling time only decreases weakly when increasing the threshold value. We attribute the observed parameter bias for IMRPhenomXHM to the incomplete set of modes described by the model, as well as modelling errors. Future work will investigate the effect of dropping modes in the model in more detail.

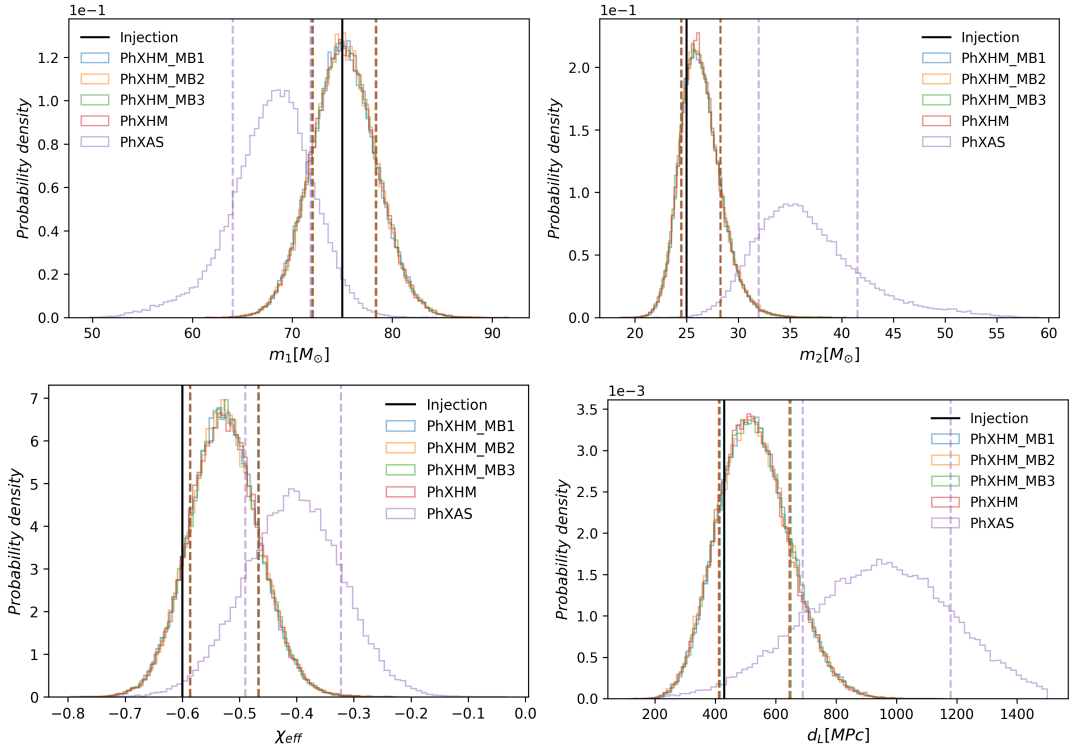

FIGURE 4.9: Posterior distributions of component masses, effective aligned spin and inclination respectively using waveforms with multibanding (PhXHM_MB) for different values of threshold (10^{-1}, 10^{-2}, 10^{-3}) and without it (PhXHM and PhXAS). The dashed vertical lines mark the 90% confidence limits.

4.4 Conclusions

We have presented a simple way to accelerate the evaluation of frequency domain waveforms by first evaluating on a coarse grid, and then interpolating to a fine grid with an iterative scheme to evaluate complex exponential functions (or equivalently trigonometric functions). This works builds upon the method presented in [1], but represents the heuristic criterion used there to determine the spacing of the coarse grid by the standard estimate for first order interpolation error, and then extends the criterion for the coarse frequency spacing to the merger and ringdown. Several extensions of our algorithm are possible: First, similar techniques can also be developed for the time domain. The simple estimates to determine the appropriate coarse grid spacing given a threshold parameter could be improved, e.g. by adding low order spin terms. The amplitude could be treated in a similarly careful way as the phase. Second, we have already applied a simple version of multibanding acceleration to the Euler angle descriptions used in the modelling of precessing waveforms [38]. Further work is required to refine this technique to properly account for the precessing phenomenology at merger and ringdown, and other details due to precession dynamics, such as oscillations in different quantities. A better understanding of how to best apply multibanding acceleration to precession is also expected

to inform how to treat eccentric waveforms.

Acceleration is more significant for smaller spacings of the fine grid, as is appropriate for smaller masses, and for detectors with broader sensitivity in frequency, e.g. future detectors such as the upgrades of the current generation of the advanced detector network, the Einstein Telescope [39] or LISA [40]. For total masses around three solar masses, as is appropriate for binary neutron star masses, the current speed of the multi-mode IMRPhenomXHM roughly equals the speed of IMRPhenomXAS for the $\ell = |m|$ modes. Detailed profiling of the code reveals this rough equality as a coincidence, and performance is limited by a small number of bottlenecks, e.g. evaluating the spline interpolation for the amplitude, for which we use the `GSL` library [31]. Future optimization work will focus on these bottlenecks. Another possible avenue for further speedup would be an implementation on GPUs or similar highly parallel hardware.

The availability of a threshold parameter that regulates accuracy and speed also allows future applications to tune codes for PE, where the threshold parameter could be set depending on the information associated with the detection in a search (such as the signals rough parameter estimate from the search and its signal-to-noise ratio), or the threshold could be changed dynamically, and could be relaxed in the burn-in-phase of a PE simulation, or in the early stages of a nested sampling run. The coupling of strategies to accelerate the evaluation of individual waveforms evaluation and Bayesian PE simulations as a whole may also have implications on the development of future waveform models, which could introduce further parameters to tune accuracy and evaluation speed.

Acknowledgements

We thank G. Pratten, M. Colleoni for discussions on the development of the IMRPhenomXAS and IMRPhenomXHM [28, 3] models, and the internal reviewers of the LIGO-Virgo collaboration for their careful checking of our LALSuite code implementation and their valuable feedback. This work was supported by European Union FEDER funds, the Ministry of Science, Innovation and Universities and the Spanish Agencia Estatal de Investigación grants FPA2016-76821-P, RED2018-102661-T, RED2018-102573-E, FPA2017-90687-REDC, Vicepresid'encia i Conselleria d'Innovació, Recerca i Turisme, Conselleria d'Educació, i Universitats del Govern de les Illes Balears i Fons Social Europeu, Generalitat Valenciana (PROMETEO/2019/071), EU COST Actions CA18108, CA17137, CA16214, and CA16104, and the Spanish Ministry of Education, Culture

and Sport grants FPU15/01319. The authors thankfully acknowledge the computer resources at MareNostrum and the technical support provided by Barcelona Supercomputing Center (BSC) through Grants No. AECT-2019-2-0010, AECT-2019-1-0022, AECT-2018-3-0017, AECT-2018-2-0022, AECT-2018-1-0009, AECT-2017-3-0013, AECT-2017-2-0017, AECT-2017-1-0017, AECT-2016-3-0014, AECT2016-2-0009, from the Red Española de Supercomputación (RES) and PRACE (Grant No. 2015133131). `Bilby` and `LALInference` simulations were carried out on the BSC MareNostrum computer under RES (Red Española de Supercomputación) allocations and on the FONER computer at the University of the Balearic Islands. The authors are also grateful for computational resources provided by the LIGO Laboratory and supported by National Science Foundation Grants PHY-0757058 and PHY-0823459.

Bibliography

[1] Serena Vinciguerra, John Veitch, and Ilya Mandel. Accelerating gravitational wave parameter estimation with multi-band template interpolation. *Class. Quant. Grav.*, 34(11):115006, 2017. doi: 10.1088/1361-6382/aa6d44.

[2] The LIGO Scientific Collaboration. LALSuite: LSC Algorithm Library Suite. https://www.lsc-group.phys.uwm.edu/daswg/projects/lalsuite.html, 2015.

[3] Cecilio García Quirós, Marta Colleoni, Héctor Estellés, Geraint Pratten, Antoni Ramos-Buades, Maite Mateu-Lucena, and Rafel Jaume. IMRPhenomXHM: A multi-mode frequency-domain model for the gravitational wave signal from non-precessing black-hole binaries. 2020.

[4] B. P. Abbott et al. Observation of gravitational waves from a binary black hole merger. *Phys. Rev. Lett.*, 116:061102, Feb 2016. doi: 10.1103/PhysRevLett.116.061102. URL https://link.aps.org/doi/10.1103/PhysRevLett.116.061102.

[5] B. P. Abbott et al. Gw170817: Observation of gravitational waves from a binary neutron star inspiral. *Phys. Rev. Lett.*, 119:161101, Oct 2017. doi: 10.1103/PhysRevLett.119.161101. URL https://link.aps.org/doi/10.1103/PhysRevLett.119.161101.

[6] B. P. Abbott et al. GWTC-1: A Gravitational-Wave Transient Catalog of Compact Binary Mergers Observed by LIGO and Virgo during the First and Second Observing Runs. 2018.

[7] Andrea Taracchini, Alessandra Buonanno, Gaurav Khanna, and Scott A. Hughes. Small mass plunging into a Kerr black hole: Anatomy of the inspiral-merger-ringdown waveforms. *Phys. Rev.*, D90(8):084025, 2014. doi: 10.1103/PhysRevD.90.084025.

[8] Alejandro Bohé et al. Improved effective-one-body model of spinning, nonprecessing binary black holes for the era of gravitational-wave astrophysics with advanced detectors. *Phys. Rev.*, D95(4):044028, 2017. doi: 10.1103/PhysRevD.95.044028.

[9] P Ajith, S Babak, Y Chen, M Hewitson, B Krishnan, J T Whelan, B Brügmann, P Diener, J Gonzalez, M Hannam, and et al. A phenomenological template family for black-hole coalescence waveforms. *Class. Quantum Grav.*, 24(19):S689–S699, Sep 2007. ISSN 1361-6382. doi: 10.1088/0264-9381/24/19/s31. URL http://dx.doi.org/10.1088/0264-9381/24/19/S31.

[10] P. Ajith, M. Hannam, S. Husa, Y. Chen, B. Brügmann, N. Dorband, D. Müller, F. Ohme, D. Pollney, C. Reisswig, and et al. Inspiral-merger-ringdown waveforms for black-hole binaries with nonprecessing spins. *Physical Review Letters*, 106(24), Jun 2011. ISSN 1079-7114. doi: 10.1103/physrevlett.106.241101. URL http://dx.doi.org/10.1103/PhysRevLett.106.241101.

[11] Mark Hannam, Patricia Schmidt, Alejandro Bohé, Leïla Haegel, Sascha Husa, et al. Simple Model of Complete Precessing Black-Hole-Binary Gravitational Waveforms. *Phys.Rev.Lett.*, 113(15):151101, 2014. doi: 10.1103/PhysRevLett.113.151101.

[12] Sascha Husa, Sebastian Khan, Mark Hannam, Michael Pürrer, Frank Ohme, Xisco Jiménez Forteza, and Alejandro Bohé. Frequency-domain gravitational waves from nonprecessing black-hole binaries. I. New numerical waveforms and anatomy of the signal. *Phys. Rev.*, D93(4):044006, 2016. doi: 10.1103/PhysRevD.93.044006.

[13] Sebastian Khan, Sascha Husa, Mark Hannam, Frank Ohme, Michael Pürrer, Xisco Jiménez Forteza, and Alejandro Bohé. Frequency-domain gravitational waves from nonprecessing black-hole binaries. II. A phenomenological model for the advanced detector era. *Phys. Rev.*, D93(4):044007, 2016. doi: 10.1103/PhysRevD.93.044007.

[14] Jonathan Blackman, Scott E. Field, Chad R. Galley, Bela Szilagyi, Mark A. Scheel, et al. Fast and accurate prediction of numerical relativity waveforms from binary black hole mergers using surrogate models. 2015.

[15] Luc Blanchet. Gravitational radiation from post-Newtonian sources and inspiralling compact binaries. *Living Reviews in Relativity*, 17, 2014. ISSN 1433-8351. doi: 10.12942/lrr-2014-2. URL http://dx.doi.org/10.12942/lrr-2014-2.

[16] K.D. Kokkotas and B.G. Schmidt. Quasi-normal modes of stars and black holes. *Living Reviews in Relativity*, 2, 1999. ISSN 1433-8351. URL https://doi.org/10.12942/lrr-1999-2.

[17] Leor Barack and Adam Pound. Self-force and radiation reaction in general relativity. *Rept. Prog. Phys.*, 82(1):016904, 2019. doi: 10.1088/1361-6633/aae552.

[18] A. Buonanno and T. Damour. Effective one-body approach to general relativistic two-body dynamics. *Phys. Rev.*, D59:084006, 1999. doi: 10.1103/PhysRevD.59.084006.

[19] A. Buonanno and T. Damour. Effective one-body approach to general relativistic two-body dynamics. *Phys. Rev. D*, 59(8), Mar 1999. ISSN 1089-4918. doi: 10.1103/physrevd.59.084006. URL http://dx.doi.org/10.1103/PhysRevD.59.084006.

[20] S. Klimenko et al. Method for detection and reconstruction of gravitational wave transients with networks of advanced detectors. *Phys. Rev.*, D93(4):042004, 2016. doi: 10.1103/PhysRevD.93.042004.

[21] Samantha A. Usman et al. The PyCBC search for gravitational waves from compact binary coalescence. *Class. Quant. Grav.*, 33(21):215004, 2016. doi: 10.1088/0264-9381/33/21/215004.

[22] Surabhi Sachdev et al. The GstLAL Search Analysis Methods for Compact Binary Mergers in Advanced LIGO's Second and Advanced Virgo's First Observing Runs. 2019.

[23] J. Veitch et al. Parameter estimation for compact binaries with ground-based gravitational-wave observations using the LALInference software library. *Phys. Rev.*, D91(4):042003, 2015. doi: 10.1103/PhysRevD.91.042003.

[24] Gregory Ashton et al. Bilby: A user-friendly Bayesian inference library for gravitational-wave astronomy. *Astrophys. J. Suppl.*, 241(2):27, 2019. doi: 10.3847/1538-4365/ab06fc.

[25] Michael Pürrer. Frequency-domain reduced order models for gravitational waves from aligned-spin compact binaries. *Classical and Quantum Gravity*, 31(19):195010, sep 2014. doi: 10.1088/0264-9381/31/19/195010. URL https://doi.org/10.1088%2F0264-9381%2F31%2F19%2F195010.

[26] Alessandra Buonanno, Bala Iyer, Evan Ochsner, Yi Pan, and B. S. Sathyaprakash. Comparison of post-Newtonian templates for compact binary inspiral signals in gravitational-wave detectors. *Phys. Rev.*, D80:084043, 2009. doi: 10.1103/PhysRevD.80.084043.

[27] Miriam Cabero, Alex B. Nielsen, Andrew P. Lundgren, and Collin D. Capano. Minimum energy and the end of the inspiral in the post-Newtonian approximation. *Phys. Rev.*, D95(6):064016, 2017. doi: 10.1103/PhysRevD.95.064016.

[28] Geraint Pratten, Sascha Husa, Cecilio García-Quirós, Marta Colleoni, Antoni Ramos-Buades, Héctor Estellés, and Rafel Jaume. Setting the cornerstone for the IMRPhenomX family of models for gravitational waves from compact binaries: The dominant harmonic for non-precessing quasi-circular black holes. 2020.

[29] Sascha Husa, Marta Colleoni, Héctor Estellés, García Quirós Cecilio, Antoni Ramos-Buades, Geraint Pratten, Rafel Jaume, Xisco Jimenez-Forteza, and David Keitel. A catalogue of non-precessing multi-mode hybrid waveforms for quasi-circular black-hole binaries. 2020.

[30] W. H. Press, S. A. Teukolsky, W. T. Vetterling, and B. P. Flannery. *Numerical recipes: the art of scientific computing*. 2007.

[31] Galassi, Mark and Davies, Jim and Theiler, James and Gough, Brian and Jungman, Gerard and Alken, Patrick and Booth, Michael and Rossi, Fabrice and Ulerich, Rhys . The gnu scientific library version 2.6. https://www.gnu.org/software/gsl, 2019.

[32] B. P. Abbott et al. Properties of the Binary Black Hole Merger GW150914. *Phys. Rev. Lett.*, 116(24):241102, 2016. doi: 10.1103/PhysRevLett.116.241102.

[33] Katerina Chatziioannou et al. On the properties of the massive binary black hole merger GW170729. *Phys. Rev.*, D100(10):104015, 2019. doi: 10.1103/PhysRevD.100.104015.

[34] http://www.black-holes.org/waveforms.

[35] https://dcc.ligo.org/LIGO-T0900288/public. URL https://dcc.ligo.org/LIGO-T0900288/public.

[36] John Skilling. Nested sampling for general Bayesian computation. *Bayesian Analysis*, 1(4):833–859, 2006. doi: 10.1214/06-BA127.

[37] John Veitch and Walter Del Pozzo. CPNEST. 10.5281/zenodo.322819, 2017. URL https://github.com/johnveitch/cpnest/.

[38] Geraint Pratten et al. Let's twist again: computationally efficient models for the dominant and sub-dominant harmonic modes of precessing binary black holes. 4 2020.

[39] M Punturo, M Abernathy, F Acernese, B Allen, N Andersson, K Arun, F Barone, B Barr, M Barsuglia, and et al. The third generation of gravitational wave observatories and their science reach. *Classical and Quantum Gravity*, 27(8):084007, apr 2010. doi: 10.1088/0264-9381/27/8/084007. URL https://doi.org/10.1088%2F0264-9381%2F27%2F8%2F084007.

[40] Pau Amaro-Seoane, Heather Audley, Stanislav Babak, John Baker, Enrico Barausse, Peter Bender, Emanuele Berti, and et al. Laser Interferometer Space Antenna. *arXiv e-prints*, art. arXiv:1702.00786, Feb 2017.

Chapter 5

Modelling precessing binary black holes for the subdominant harmonics: IMRPhenomXPHM

This chapter presents the article:

- *Let's twist again: computationally efficient models for the dominant and sub-dominant harmonic modes of precessing binary black holes.* Geraint Pratten, Cecilio García-Quirós, Marta Colleoni, Antoni Ramos-Buades, Héctor Estellés, Maite Mateu-Lucena, Rafel Jaume, Maria Haney, David Keitel, Jonathan E. Thompson, Sascha Husa. arXiv:2004.06503 [gr-qc] (2020),

which has been submitted for peer review to Physical Review D.

Abstract

We present IMRPhenomXPHM, a phenomenological frequency-domain model for the gravitational-wave signal emitted by quasi-circular precessing binary black holes, which incorporates multipoles beyond the dominant quadrupole in the precessing frame. The model is a precessing extension of IMRPhenomXHM, based on approximate maps between aligned-spin waveform modes in the co-precessing frame and precessing waveform modes in the inertial frame, which is commonly referred to as "twisting up" the non-precessing waveforms. IMRPhenomXPHM includes IMRPhenomXP as a special case, the restriction to the dominant quadrupole contribution in the co-precessing frame. We implement two alternative mappings, one based on a single-spin PN approximation,

as used in IMRPhenomPv2 [1], and one based on the double-spin MSA approach of [2]. We include a detailed discussion of conventions used in the description of precessing binaries and of all choices made in constructing the model. The computational cost of IMRPhenomXPHM is further reduced by extending the interpolation technique of [3] to the Euler angles. The accuracy, speed, robustness and modularity of the IMRPhenomX family will make these models productive tools for gravitational wave astronomy in the current era of greatly increased number and diversity of detected events.

5.1 Introduction

We have recently presented IMRPhenomXAS [4], a phenomenological model for the $\ell = |m| = 2$ dominant quadrupole spherical harmonic modes of the gravitational wave signal emitted by coalescing black holes in quasi-circular orbits, and with spin vectors orthogonal to the orbital plane. This model improves over the IMRPhenomD model [5, 6] that is routinely used in gravitational wave data analysis. The improvements include modifications of the phenomenological ansatz, a systematic approach to modelling the dependence of phenomenological parameters on the three-dimensional parameter space of non-precessing quasi-circular binaries of black holes [7, 8], extending the set of NR waveforms our model is calibrated to from 19 to 461, incorporating additional numerical perturbative waveforms for mass ratios up to 1000 into the calibration data set, and calibrating to a more accurate description of the inspiral [9].

Building on IMRPhenomXAS, we have also presented IMRPhenomXHM [10], which extends the model to the leading subdominant harmonics, in particular the $(\ell, |m|) = (2,2), (2,1), (3,3), (3,2), (4,4)$ modes, and includes mode mixing effects in the $\ell = 3$, $|m| = 2$ harmonics as described in [10]. This extension is aimed to supersede the IMRPhenomHM model [11], where the subdominant harmonics are not calibrated to NR waveforms, and instead an approximate map from the $(2,2)$ to the sub-dominant harmonics is employed.

These models are formulated in the frequency domain, which is typically employed in matched filter calculations, in order to reduce the computational cost of gravitational wave data analysis. In order to accelerate the evaluation of the waveform model, which is particularly important for computationally expensive applications such as Bayesian inference [12, 13], we have further developed the multibanding interpolation method of [14] as described in [3].

Phenomenological waveform models for non-precessing systems have been extended to precessing systems [1, 15, 16] by a construction that is based on an approximate map

between precessing and non-precessing systems, and is commonly referred to as "twisting up" [17, 18, 1]. The aim of the present paper is to revisit the twisting-up procedure, first by documenting it in detail and deriving the equations that define the model in the frequency domain, and then to extend IMRPhenomXAS and IMRPhenomXHM to precession, resulting in the IMRPhenomXP and IMRPhenomXPHM models, which are publicly available as implemented in the LALSuite [19] library for gravitational wave data analysis.

Approximate maps between the gravitational wave signals of precessing and non-precessing systems can be constructed based on the fact that the orbital timescale is much smaller than the precession timescale, and correspondingly the amount of gravitational waves emitted due to the precessing motion is relatively small and contributes little to the phasing of the gravitational wave signal when observed in a non-inertial co-precessing frame. Rather, the dominant effect of precession is an amplitude and phase modulation that can be approximated in terms of a time-dependent rotation of a non-precessing system [17, 18].

We will describe this rotation in terms of three time-dependent Euler angles, and our non-precessing gravitational wave signal will be described by the IMRPhenomXHM model (or IMRPhenomXAS for the dominant quadrupole modes). The waveform for precessing binaries can thus be approximated by interpreting a non-precessing waveform as an approximation to the precessing waveform observed in a non-inertial frame that tracks the precession of the orbital plane [17]. This map is greatly simplified by the approximate decoupling between the spin components parallel and perpendicular to the orbital angular momentum $\mathbf{L}$ [18]. See however [20] for an instability for approximately opposite spins that can result in breaking this assumption in a small part of the parameter space.

In addition to the time-dependent rotation, the approximate map also requires a second element, which is to modify the final spin of the merger remnant, which is in general different from the non-precessing case, essentially due to the vector addition of the individual spins and angular momentum. The final mass of the remnant is much less affected by precession, since the scalar quantity of radiated energy is not significantly affected by the precessing motion due to its slower time scale compared to the orbital motion.

An important shortcoming of this construction as presented here is that it does not include the asymmetries in the $(\ell, |m|) = (2, 2)$ modes that are responsible for large recoils, see e.g. [21]. For brevity we will refer to the approximations that are used in the "twisting up" procedure as the "twisting approximation". For a recent detailed discussion of the effect of these approximations, with special consideration of the effect on subdominant harmonics, see [22].

Our model currently uses two alternative descriptions for the Euler angles that characterize the approximate map: the one used previously in [1, 23] assumes that the spin of the smaller black hole vanishes, while the one developed in [2] and previously used in [15, 16] describes double-spin systems. The code we have developed as part of LALSuite [19] is modular, and allows to independently update different components, such as the calibrations of particular regions (inspiral, merger, or ringdown) for particular spherical harmonics, or the precession Euler angles, and supports calling particular versions of these components.

In a previous study of waveform systematics [24] it was found that while models such as IMRPhenomD and IMRPhenomPv2 were sufficiently accurate for the first detection of gravitational waves [25], further improvements in accuracy were called for. The IMRPhenomX family of waveform models addresses this, and the present work completes the IMRPhenomX family of waveform models to serve as a tool for gravitational wave data analysis that models quasi-circular systems, and to serve as a basis for extensions: e.g. to address eccentricity and model fully generic mergers of black holes in general relativity, to address remaining shortcomings in describing quasi-circular systems, and as a basis for tests of general relativity.

The paper is organized as follows: We first discuss our notation and conventions in Sec. 5.2 and the basic concepts of the modelling of precessing binaries in Sec. 5.3. We then present the construction of the model in Sec. 5.4 and our tests of quality and computational efficiency in Sec. 5.5. This also includes Bayesian inference results with the new model on real gravitational wave data. We conclude the paper in Sec. 5.6.

Several appendices provide further technical details: In appendix 5.A we list the Wigner-d matrices we use to express rotations. In appendix 5.B we summarize conventions regarding non-precessing waveforms. In appendix 5.C we discuss frame transformations and the effect in the gravitational wave polarizations. In appendix 5.D we discuss how our choice of polarization relates to other choices in the literature. In appendix 5.E we spell out the derivation of the frequency domain gravitational waveform. Appendix 5.F contains details of the LALSuite implementation. In appendix 5.G.1 we write out the explicit PN expressions for the next-to-next-to-leading order (NNLO) Euler-angle descriptions that we use here. Finally in appendix 5.G.2 we write out the coefficients of the PN approximation we use for the orbital angular momentum.

We define the mass ratio $q = m_1/m_2 \geq 1$, total mass $M = m_1 + m_2$, and symmetric mass ratio $\eta = m_1 m_2/M^2$. We use geometric units $G = c = 1$ unless explicitly stated (in particular when using seconds, Hz or solar masses as units).

5.2 Notation and Conventions

For non-precessing systems we have recently provided a detailed discussion of our conventions in [4, 10]. Our work here is consistent with these conventions, but we drop the restriction to spins orthogonal to the orbital plane. As the twisting construction is based on mapping non-precessing waveforms to precessing ones, the properties of non-precessing waveforms, in particular the consequences of equatorial symmetry with respect to the orbital plane, are still relevant for the map, and we summarize these conventions in appendix 5.B.

As our primary coordinate system we use a standard inertial spherical coordinate system (t, r, θ, φ), where t is the inertial time coordinate of distant observers, r is the luminosity distance to the source, and θ and φ are polar angles in the sky of the source. Associated with this spherical coordinate system will be a Cartesian coordinate system with axes $(\hat{\mathbf{x}}_J, \hat{\mathbf{y}}_J, \hat{\mathbf{z}}_J)$. We will take the $\hat{\mathbf{z}}_J$ axis to be the direction of the total angular momentum $\mathbf{J}$, and we will refer to this inertial coordinate system as the J-frame. In most binaries, the orbital and spin angular momenta will precess around the $\mathbf{J}$ [26, 27]. Here we will take the direction of $\mathbf{J}$ to be fixed, i.e. $\hat{\mathbf{J}}(t) \simeq \hat{\mathbf{J}}_{t\to-\infty}$. This is a limitation of the model and excludes special cases, such as transitional precession, where there is no fixed precession axis and the direction of $\mathbf{J}$ will evolve.

Our final result will be the calculation of the observed gravitational wave polarizations in a frame where the z-axis corresponds to the direction $\hat{\mathbf{N}}$ of the line of sight toward the observer, which we will refer to as the N-frame. The observer of the gravitational wave signal will be located at the sky position $\theta = \theta_{JN}$ and $\varphi = \phi_{JN}$ in the J-frame.

We will use a third coordinate system to describe precession in terms of a rotating orbital plane, which is orthogonal to the Newtownian orbital angular momentum $\mathbf{L_N} = \mu\, \mathbf{n} \times \mathbf{v}$, where μ is the Newtonian reduced mass, $\mathbf{n}$ the vector from the position of the secondary black hole to the primary, and $\mathbf{v}$ the relative velocity. In the presence of spin precession, the direction of the actual orbital angular momentum $\mathbf{L}$ will in general differ from the direction of $\mathbf{L_N}$ due to the presence of spin components in the orbital plane, orthogonal to $\mathbf{L_N}$, see e.g. the discussions in [17] related to Eq. (4.6) of that paper. These corrections enter $\mathbf{L}$ at the first PN order and modulate the rotation of the orbital axis. In our present implementation of the twisting-up approximation, we will neglect the influence of this effect on the final waveform, as has been done in previous implementations [1, 23, 15, 16]. We will refer to a coordinate system where the z-axis is chosen as $\mathbf{L}$ or $\mathbf{L_N}$ as the L-frame, and will discuss different choices for approximating $\mathbf{L}$ in Sec. 5.4.3.

When setting up initial data for NR simulations, it is common to choose spin components for the initial data set in the L-frame, where approximations for $\mathbf{L}$ may or may not be

applied. We will refer to the inertial coordinate frame, which corresponds to the L-frame at some initial reference time as the L_0-frame.

Our setup in this paper is constructed to be consistent with [28], which discusses conventions for relating the N-frame (referred to as the wave frame) and the L_0-frame (referred to as the source frame), which have been adopted by the LALSuite [19] framework for gravitational wave data analysis, where we have implemented our model as open source code. Appendix 5.C discusses how we use the remaining freedom to fix the J, N, and L (or equivalently L_0) frames, which corresponds to fixing the freedom of rotating around the z-axes of each frame, and to the three Euler angles that rotate a given coordinate frame into another.

We will perform the "twisting up" construction of the gravitational-wave signal in terms of its decomposition into spin-weighted spherical harmonics in the J-frame, [29]

$$h^J = h^J_+ - i h^J_\times = \sum_{\ell \geq 2} \sum_{m=-\ell}^{\ell} h^J_{\ell m} \, {}_{-2}Y_{\ell m}(\theta, \varphi), \tag{5.1}$$

where

$${}_{-2}Y_{\ell m}(\theta, \varphi) = \mathcal{Y}_{\ell m}(\theta) e^{im\varphi} \tag{5.2}$$

are the spin-weighted spherical harmonics of spin-weight -2 [30], defined as in [31].

We adopt the LALSuite conventions for the Fourier transform of a signal $h(t)$ and its inverse

$$\tilde{h}(f) = \mathrm{FT}\left[h\right](f) = \int h(t)\, e^{-2\pi i f t} dt, \tag{5.3}$$

$$h(t) = \mathrm{IFT}\left[\tilde{h}\right](t) = \int \tilde{h}(f)\, e^{2\pi i f t} df. \tag{5.4}$$

With this definition of the Fourier transform we can convert Eq. (5.1) that defines the two gravitational wave polarizations in terms of the real and imaginary part of the time domain gravitational wave strain to expressions in the frequency domain,

$$\tilde{h}_+(f) = \mathrm{FT}[\,\mathrm{Re}(h(t))\,] = \frac{1}{2}\left[\tilde{h}(f) + \tilde{h}^*(-f)\right], \tag{5.5}$$

$$\tilde{h}_\times(f) = -\mathrm{FT}[\,\mathrm{Im}(h(t))\,] = \frac{i}{2}\left[\tilde{h}(f) - \tilde{h}^*(-f)\right]. \tag{5.6}$$

5.3 Modelling Precessing Binaries

5.3.1 The twisting construction in terms of Euler angles

One of the key breakthroughs in the modelling of precessing binaries was the insight that such models can be simplified by formulating them in a non-inertial frame that tracks the approximate motion of the orbital plane, and that the resulting waveform approximately resembles some corresponding aligned-spin waveform [17]. In particular, one finds that a mode hierarchy consistent with non-precessing binaries is restored, allowing to define an approximate mapping between the seven-dimensional space of generic precessing binaries and the three-dimensional space of non-precessing binaries [18]. This identification immediately implies that the inverse procedure can be used to approximate the waveform modes of a precessing binary in the inertial frame [18, 1], namely to apply a time-dependent rotation to the aligned-spin waveform modes.

In the conventions adopted in this paper, we define (α, β, γ) as the Euler angles that describe an active rotation from the inertial J-frame to the precessing L-frame in the (z, y, z) convention. The angles α and β are spherical angles that approximately track the direction of the Newtonian angular momentum. The third angle can be gauge-fixed by enforcing the minimal rotation condition [32], demanding the absence of rotation in the precessing frame about the orbital angular momentum[1]

$$\dot{\gamma} = -\dot{\alpha}\,\cos\beta. \tag{5.7}$$

In the conventions adopted here, α will typically increase during the inspiral, while γ will typically decrease. The gravitational-wave modes between these two frames can be related via the transformation of a Weyl scalar under a rotation $\mathbf{R} \in \mathrm{SO}(3)$ [30, 17]

$$h^J_{\ell m} = \sum_{m'=-\ell}^{\ell} \mathcal{D}^{\ell *}_{mm'}(\alpha, \beta, \gamma)\, h^L_{\ell m'}, \tag{5.8}$$

$$h^L_{\ell m'} = \sum_{m=-\ell}^{\ell} \mathcal{D}^{\ell}_{mm'}(\alpha, \beta, \gamma)\, h^J_{\ell m}, \tag{5.9}$$

where $\mathcal{D}^{\ell}_{mm'}$ are the Wigner D-matrices[2]

$$\mathcal{D}^{\ell}_{mm'}(\alpha, \beta, \gamma) = e^{im\alpha} e^{im'\gamma} d^{\ell}_{mm'}(\beta), \tag{5.10}$$

[1] Note that $\epsilon = -\gamma$ is sometimes used in the literature, e.g. [23].

[2] Note that the convention for the Wigner d-matrices adopted here implies [33, 34]

$$\mathcal{D}^{\ell}_{mm'}(\alpha, \beta, \gamma) = \mathcal{D}^{\ell,\mathrm{ABFO}}_{m'm}(\alpha, \beta, \gamma).$$

and $d^{\ell}_{mm'}$ are the real-valued Wigner-d matrices and are polynomial functions in $\cos(\beta/2)$ and $\sin(\beta/2)$, as detailed in appendix 5.A. Note that Eq. (5.9) follows from inverting Eq. (5.8). We provide a Mathematica [35] notebook as supplementary material, which allows to conveniently check key conventions, such as those related to the Wigner-d matrices.

Schematically, we construct precessing waveform models using the following "twisting" algorithm:

- Model waveform modes in the precessing non-inertial L-frame, in our case these models are IMRPhenomXAS and IMRPhenomXHM.
- Perform an active rotation from the precessing L-frame to the inertial J-frame using a given model for the precession dynamics, as encoded in (α, β, γ). The inertial frame is defined such that $z_J = \mathbf{J}$, where $\mathbf{J}$ is approximately constant, and a full discussion of the relation between different frames and the conventions chosen to represent precessing motion is given in appendix 5.C. In order to achieve closed-form expressions in the Fourier domain, the SPA approximation is used, with the result stated in the next section (5.3.2), and a full derivation deferred to appendix 5.E.
- Project gravitational-wave polarizations into the N-frame as discussed in appendix 5.C.

5.3.2 Gravitational-Wave Polarizations in the Frequency Domain

The frequency-domain expressions for the gravitational-wave polarizations in the inertial J-frame $\tilde{h}^J_{+,\times}(f)$ in terms of spherical harmonic modes $\tilde{h}^L_{\ell m}(f)$ in the co-precessing L-frame are derived in appendix 5.E, starting from Eq. (5.8), and performing Fourier transformations with the stationary phase transformation (SPA) [36–38]. The result for the gravitational-wave polarizations in terms of modes in the precessing L-frame reads

$$\tilde{h}^J_+(f>0) = \frac{1}{2}\sum_{\ell\geq 2}\sum_{m'>0}^{l} \tilde{h}^L_{\ell -m'}(f) e^{i m' \gamma} \sum_{m=-\ell}^{\ell} \left[A^{\ell}_{m\,-m'} + (-1)^{\ell} A^{\ell *}_{m\,m'}\right], \tag{5.11}$$

$$\tilde{h}^J_\times(f>0) = \frac{i}{2}\sum_{\ell\geq 2}\sum_{m'>0}^{\ell} \tilde{h}^L_{\ell -m'}(f) e^{i\, m' \gamma} \sum_{m=-\ell}^{\ell} \left[A^{\ell}_{m -m'} - (-1)^{\ell} A^{\ell *}_{m m'}\right], \tag{5.12}$$

where we have introduced mode-by-mode transfer functions

$$A^{\ell}_{m\,m'} = e^{-i\, m\, \alpha} d^{\ell}_{mm'}(\beta)\ {}_{-2}Y_{\ell m}. \tag{5.13}$$

The modes in the precessing L-frame can be approximated with non-precessing waveform modes [17, 18, 1]. Here we use IMRPhenomXHM [4, 10], which contains the $(\ell, |m|) = (2,2), (2,1), (3,3), (3,2), (4,4)$ modes. Note that, as discussed in [22], our treatment of mode-mixing in the non-precessing case does not strictly carry over to precession, as one would need to consider mode mixing in the inertial frame, and not in the co-precessing frame corresponding to the aligned-spin waveform. An analysis of the shortcomings of our treatment of mode-mixing and further improvements of the model will be the subject of future work.

5.4 Constructing the Model

A core ingredient in modelling precessing binaries is a description for the precession dynamics in terms of the three Euler angles $\{\alpha, \beta, \gamma\}$ describing the active transformation from the precessing to the inertial frame. For IMRPhenomXPHM, we have implemented two different prescriptions for the precession angles. The first model, described below in Sec. 5.4.1, is based on the NNLO single-spin PN expressions used in IMRPhenomPv2 [1, 23]. The second model, described in Sec. 5.4.2, is based on the 2PN expressions from [2], derived using a multiple scale analysis (MSA). Such modularity will help us to gauge systematics in modelling precession and its implications for gravitational-wave data analysis.

5.4.1 Post-Newtonian NNLO Euler Angles

The single-spin description of the Euler angles is based on a PN re-expansion setting $\boldsymbol{S}_2 = 0$, and restricting to spin-orbit interactions [23]. This framework was implemented in IMRPhenomPv2 [1, 23] and has been actively used in the analysis of gravitational-wave data [39].

In the PN framework, we first solve for the evolution equations of the moving triad $\{\boldsymbol{n}, \boldsymbol{\lambda}, \boldsymbol{\ell}\}$ at a given PN order in the conservative dynamics before re-introducing radiation-reaction effects. The angular momentum $\boldsymbol{J}$, neglecting radiation reaction effects, is approximately conserved and can be used to define a fixed direction $\mathbf{z}$. Completed with two constant unit vectors $\mathbf{x}$ and $\mathbf{y}$, this forms an orthonormal triad. We can define a separation vector $\boldsymbol{n}$ between the two black holes such that $\mathbf{r} = r\boldsymbol{n}$ with $\mathbf{r} = \mathbf{r}_1 - \mathbf{r}_2$. The unit normal to the instantaneous orbital plane, $\boldsymbol{\ell}$, is defined by $\boldsymbol{\ell} = \boldsymbol{n} \times \boldsymbol{v}/|\boldsymbol{n} \times \boldsymbol{v}|$, where $\boldsymbol{v} = \boldsymbol{v}_1 - \boldsymbol{v}_2$ is the relative velocity. Finally, the orthonormal triad is completed

by $\boldsymbol{\lambda} = \boldsymbol{\ell} \times \boldsymbol{n}$. The evolution of the triad is given by [40, 41]

$$\frac{d\boldsymbol{n}}{dt} = \omega \boldsymbol{\lambda}, \tag{5.14a}$$
$$\frac{d\boldsymbol{\lambda}}{dt} = -\omega \boldsymbol{n} + \bar{\omega} \boldsymbol{\ell}, \tag{5.14b}$$
$$\frac{d\boldsymbol{\ell}}{dt} = -\bar{\omega} \boldsymbol{\lambda}, \tag{5.14c}$$

where $\bar{\omega}$ is the precession angular frequency. Introducing an orthonormal basis such that the z-axis points along $\boldsymbol{J}$, as we do in appendix 5.C, we can introduce the Euler angles $\{\alpha, \beta, \gamma\}$ to track the position of $\boldsymbol{L}$ with respect to this fixed basis. The evolution of the Euler angles follows from Eqs. (5.14):

$$\frac{d\alpha}{dt} = -\frac{\bar{\omega}}{\sin\beta} \frac{J_n}{\sqrt{J_n^2 + J_\lambda^2}}, \tag{5.15a}$$
$$\frac{d\beta}{dt} = \bar{\omega} \frac{J_\lambda}{\sqrt{J_n^2 + J_\lambda^2}}, \tag{5.15b}$$
$$\frac{d\gamma}{dt} = -\dot{\alpha} \cos\beta. \tag{5.15c}$$

The only assumption made in deriving these equations is that the direction of the total angular momentum is approximately constant and that we may neglect radiation reaction effects [40].

In the regime of simple precession, in which the total angular momentum is not small compared to the orbital and spin angular momenta, the opening angle β of the precession cone is approximately constant and is constrained by the minimal rotation condition [32], as in Eq. (5.7). Under the approximation that the direction of the total angular momentum, $\hat{\boldsymbol{J}}$, is constant throughout the evolution, the angle β can be determined using the closure relation $\boldsymbol{J} = \boldsymbol{L} + \boldsymbol{S}_1$, yielding

$$\cos\beta = \boldsymbol{\ell} \cdot \frac{\boldsymbol{J}}{|\boldsymbol{J}|} = \frac{J_\ell}{\sqrt{J_\ell^2 + J_n^2 + J_\lambda^2}}. \tag{5.16}$$

With a PN re-expansion of the right hand side and decomposing the spin into contributions parallel and perpendicular to the orbital angular momentum, $\boldsymbol{S} = \boldsymbol{S}_\parallel + \boldsymbol{S}_\perp$, the expression for β reduces to [23]

$$\cos\beta = \frac{L + S_\parallel}{\sqrt{(L + S_\parallel)^2 + S_\perp^2}} = \pm(1 + s^2)^{-1/2}, \tag{5.17}$$

where $s = S_\perp/(L + S_\parallel)$ and the overall sign is dependent on the sign of $L + S_\parallel$. This approximation was used in IMRPhenomPv2, coupled with a 2PN non-spinning approximation of the orbital angular momentum L [27]. In [42] we discuss the use of a numerical fit to the orbital angular momentum in a non-precessing merger, and here we use different alternative PN approximations as discussed in Sec. 5.4.3.

The dynamics for $\dot{\alpha}$ are determined using the results obtained in [40] together with the NNLO spin-orbit contributions derived in [41]:

$$\frac{d\alpha}{dt} = -\frac{\bar{\omega}}{\sin\beta}\frac{J_n}{\sqrt{J_n^2 + J_\lambda^2}}, \tag{5.18}$$

where $\bar{\omega}$ is defined by Eq. (5.14). The right-hand side of Eq. (5.18) is PN re-expanded and orbit-averaged in order to re-express the spin components $S_{1,\lambda}$ and $S_{1,n}$ in terms of an effective spin parameter χ_p [43]. Radiation reaction effects can be incorporated by using the evolution of the frequency, $\dot{\omega}/\omega^2$, to re-express Eq. (5.18) as

$$\frac{d\alpha}{d\omega} = \frac{1}{\dot{\omega}}\frac{d\alpha}{dt}. \tag{5.19}$$

In IMRPhenomPv2, corrections up to 3.5PN in both the orbital and spin-orbit sectors were used for the evolution of ω. Equation (5.19) is re-expanded as a PN series in ω and is integrated term-by-term to yield a closed-form expression for $\alpha(\omega)$, up to an overall constant of integration. A similar strategy is employed for deriving $\gamma(\omega)$ using the relation in Eq. (5.7). The constants of integration arising when solving Eqs. (5.14) are fixed by the orientation of the spins at a given reference frequency $f_{\rm ref}$ as discussed in appendix 5.C.

The effective spin precession parameter χ_p [43] provides a mapping from the four in-plane spin degrees of freedom to a single parameter that captures the dominant effect of precession. As discussed in [43], the magnitudes of the in-plane spins $S_{i,\perp}$ will oscillate about a mean value, with the relative angle between the spin vectors changing continuously. Averaging over many precession cycles, the average magnitude of the spins can be written as [43]

$$S_p = \frac{1}{2}\left(A_1 S_{1,\perp} + A_2 S_{2,\perp} + |A_1 S_{1,\perp} - A_2 S_{2,\perp}|\right), \tag{5.20}$$

$$= \max\left(A_1 S_{1,\perp}, A_2 S_{2,\perp}\right), \tag{5.21}$$

where $A_1 = 2 + 3/(2q)$. For most binaries, the spin of the larger black hole will dominate and S_p reduces to $A_1 S_{1,\perp}$. As the in-plane spin of the smaller black hole will become

increasingly negligible at higher mass ratios, the dimensionless effective precession parameter is defined by assigning the precession spin to the larger black hole [43]

$$\chi_p = \frac{S_p}{A_1 m_1^2}. \tag{5.22}$$

In IMRPhenomPv2, a choice was made to calculate the PN Euler angles by placing all of the spin on the larger black hole, i.e. $\chi_2 = 0$. IMRPhenomXPHM inherits this choice in this first prescription for the Euler angles.

5.4.2 MSA Euler Angles

The second formulation of the precession angles that we implement is based on the application of *multiple scale analysis* (MSA) [44] to the PN equations of motion [45–47, 20, 48, 2]. This approach employs a perturbative expansion in terms of the ratios of distinct characteristic scales in the system. For precessing binaries, a natural hierarchy of timescales can be identified with the orbital time scale being shorter than the precessing time scale, which is again shorter than the radiation reaction timescale. In [2], the time-domain PN precession equations are solved by incorporating radiation reaction effects through the multiple scale analysis. The resulting time domain waveforms are then transformed to the frequency domain using *shifted uniform asymptotics* [49], helping to overcome a number of limitations and failures in the more conventional SPA approach.By decomposing the waveform into Bessel functions, the resulting Fourier integral can be evaluated term-by-term using SPA and resummed using the exponential shift theorem. The concomitant frequency domain inspiral waveforms contain spin-orbit and spin-spin effects at leading order in the conservative dynamics and up to 3.5PN order in the dissipative dynamics, neglecting spin-spin terms. The MSA formulation of the PN Euler angles enables double-spin effects, as recently first incorporated into the phenomenological framework in [15, 16]. The SPA treatment used here corresponds to the leading order, local-in-frequency correction and is equivalent to the zeroth order of the SUA [49, 33].

The precession angles are given in terms of a PN series plus an additional MSA correction. The full solution for α in the MSA approach is [2][3]

$$\alpha = \alpha_{-1} + \alpha_0 + \mathcal{O}(\epsilon), \tag{5.23}$$

[3]Note that [2] adopts the notation $\phi_z \to \alpha, \zeta \to -\gamma$ and $\cos\theta_L \to \cos\beta$.

where

$$\alpha_{-1} = \sum_{n=0}^{5} \langle \Omega_\alpha \rangle^{(n)} \alpha^{(n)} + \alpha^0_{-1} \tag{5.24}$$

is the leading order MSA correction given in Eq. (66) of [2] and α_0 is the first-order correction to the MSA given by Eq. (67) of [2]. A similar approach is taken for γ, with the leading order MSA correction given by Eq. (F5) of [2] and the first-order MSA correction given in Eq. (F19) of appendix F of [2].

Again, the Euler angles are fixed by the orientation of the spins at a given reference frequency $f_{\rm ref}$ as discussed in appendix 5.C. Similarly to the PN re-expanded results used in IMRPhenomPv2, the identification of $\hat{\boldsymbol{J}}$ as an approximately conserved quantity leads to the preferred coordinate frame in which $\hat{z} = \hat{\boldsymbol{J}}$ with the angle β defining the precession cone, as in Eq. (8) of [2]:

$$\cos\beta = \hat{\boldsymbol{J}} \cdot \hat{\boldsymbol{L}} = \frac{J^2 + L^2 - S^2}{2JL}. \tag{5.25}$$

Together with the expressions for α and γ, this defines the complete set of equations describing the Euler angles in the MSA framework.

The MSA expressions are series expansions in terms of the orbital velocity or, equivalently, the GW frequency $f^{-4/3+n/3}$, where $n \in [1, 6]$ denotes the order of the series. As discussed in [2, 15], γ is fully PN re-expanded whereas α involves both PN re-expanded and un-expanded terms. This choice was motivated by solutions to the exact precession-averaged equations $\langle \dot{\alpha} \rangle_{\rm pr}$ leading to α_{-1} being ill-behaved in the equal mass ratio limit and divergences when the total spin angular momentum is (anti)aligned with the orbital angular momentum [2]. A more detailed discussion can be found in Sec IV D 1 and appendix E of [2]. The order to which we retain terms in the MSA series can be controlled and, as in [15], we drop the highest-order terms in the expansion. The impact of the expansion order on the Euler angles is highlighted in Fig. 5.1 where the NNLO angles from Sec. 5.4.1 are shown for comparison.

The subset of equal-mass binaries present a number of qualitative features that distinguish them from the generic unequal mass ratio cases. In particular, by setting $q = 1$ in the MSA framework we find that the expressions lead to singular behaviour in various aspects of the model [47, 20, 2]. Of particular note is the singular behaviour of the precession-averaged spin couplings [2], which are used in the construction of the final spin estimate detailed in Sec. 5.4.4. These terms must be regularized in the equal-mass limit to avoid singular behaviour.

As discussed above, the MSA system of equations is known to result in numerical instabilities when $\boldsymbol{S}$ and $\boldsymbol{L}$ are nearly mis-aligned. Such instabilities result in a failure at the waveform generation level. In order to help alleviate these situations, we have opted to use the NNLO angles described in Sec. 5.4.1 as a fallback in the default LALSuite implementation, though the end-user can still demand a terminal error for these cases.

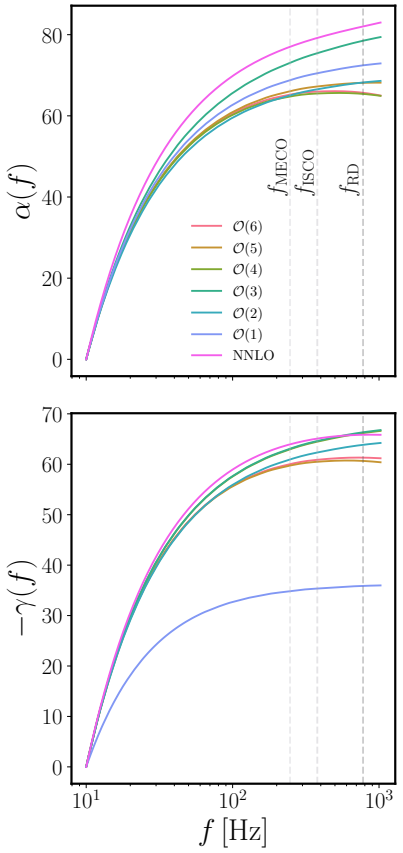

FIGURE 5.1: The Euler angles α and γ obtained by solving the MSA system of [2] and the NNLO PN equations for a binary of mass $M = 20M_\odot$, $q = 10$, $\chi_1 = (0.4, 0, 0.4)$ and $\chi_2 = (0.3, 0, -0.3)$, with a starting frequency of 10Hz. The vertical dashed lines correspond to the MECO [50], ISCO and ringdown frequency in increasing order. The multiple shaded lines denote the Euler angles evaluated using different orders for the MSA correction used in the MSA system and the NNLO angles.

5.4.3 Post-Newtonian Orbital Angular Momentum

In order to calculate the orbital angular momentum, we use an aligned-spin 4PN approximation [51–56]

$$L = \frac{\eta}{\sqrt{x}}\left[L_0 + L_1 x + L_2 x^2 + L_3 x^3 + L_4 x^4 + \right. \tag{5.26}$$

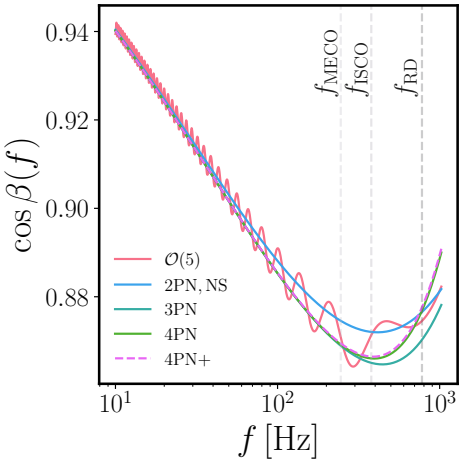

FIGURE 5.2: Comparison of the NNLO Euler angle $\cos\beta$ against the MSA versions for the same binary as shown in Fig. 5.1. We show the impact of different PN orders for the orbital angular momentum $\boldsymbol{L}$ on the determination of the opening angle.

$$+ L^{\rm SO}_{1.5} x^{3/2} + L^{\rm SO}_{2.5} x^{5/2} + L^{\rm SO}_{3.5} x^{7/2} \Big],$$

where L_a are the orbital coefficients at a-PN order, $L^{\rm SO}$ are the spin-orbit contributions and we neglect spin-spin terms. The coefficients are given in appendix 5.G.2. This is in contrast to IMRPHENOMPV2, which used a non-spinning 2PN approximation to the orbital angular momentum

$$L_{\rm 2PN} = \frac{\eta}{\sqrt{x}} \left[1 + \left(\frac{3}{2} + \frac{\eta}{6} \right) x + \left(\frac{27}{8} - \frac{19\eta}{8} + \frac{\eta^2}{24} \right) x^2 \right]. \tag{5.27}$$

Our implementation in the LALSuite code also supports dropping various terms in the 4PN expression of Eq. (5.26), including reducing the approximation to Eq. (5.27). In addition, we have also implemented the option to incorporate spin effects at leading PN order at all orders in spin [57–59], as given in appendix 5.G.2. Note that, consistent with our approximation of the co-precessing dynamics and waveform with the corresponding aligned-spin quantities we neglect contributions to the angular momentum of the spin components in the orbital plane. Modelling of the orbital angular momentum is most relevant for calculating the opening angle β. The impact of different orders for $L_{\rm PN}$ is shown in Fig. 5.2, where we observe significant differences between the non-spinning 2PN approximation used in [23] and higher-order PN approximants that incorporate aligned-spin contributions.

5.4.4 Modelling the Final State

In our twisting construction, approximating a precessing waveform with a non-precessing one implies that the radiated energy and the radiated angular momentum orthogonal to the orbital plane are identical to the non-precessing values. Indeed, comparisons of the final mass from precessing NR simulations with fits for the final mass resulting from non-precessing mergers, see e.g. [60, 61], show only a weak dependence of the final mass on precession.

We do however need to take into account the dependence of the final spin on precession, which is essentially due to the vector addition of the individual spins and angular momentum, as will be discussed below. A surrogate model for the final spin of precessing mergers for a limited range in mass ratio and spins has been produced recently [61]. Here, however, we will proceed differently in order not to compromise the simplicity and domain of validity of our model and employ a simple estimate for the final spin magnitude based on accurate fits for the final spin of non-precessing mergers, simple geometric arguments, and our assumptions related to those underlying the twisting approximation.

In order to incorporate precession into the final spin prediction, we can argue as follows (compare also to [62]): we first write the total angular momentum $\mathbf{J}$ as the sum of individual spins $\mathbf{S}_i$ and orbital angular momentum $\mathbf{L}$:

$$\mathbf{J} = \mathbf{S_1} + \mathbf{S_2} + \mathbf{L}.$$

We can now apply this equation to compute the final angular momentum $\mathbf{S_{fin}}$ of the remnant black hole, interpreting the quantities $(\mathbf{S_1}, \mathbf{S_2}, \mathbf{L})$ as the values at merger, where the further emission of angular momentum effectively shuts off. We split the spin vectors of the individual black holes into their orthogonal components parallel (or anti-parallel) and orthogonal to the unit vector in the direction of the orbital angular momentum $\hat{\mathbf{L}}$, and introduce the quantities (for $i = 1, 2$):

$$S_{i,||} = \mathbf{S_i} \cdot \hat{\mathbf{L}}, \quad S_{||} = S_{1,||} + S_{2,||}, \tag{5.28}$$

$$\mathbf{S_{i,\perp}} = \mathbf{S_i} - S_{i,||}\hat{\mathbf{L}}, \quad \mathbf{S}_\perp = \mathbf{S_{1,\perp}} + \mathbf{S_{2,\perp}}. \tag{5.29}$$

We can now compute the final angular momentum as the vector-sum of 2 orthogonal components, and then the magnitudes of the final spin $S_{\rm fin}$ and final Kerr parameter $a_{\rm fin}$ are given as

$$|S_{\rm fin}| \equiv M_{\rm fin}^2 |a_{\rm fin}| = \sqrt{\mathbf{S}_\perp{}^2 + (S_{||} + L_{\rm fin})^2}. \tag{5.30}$$

Here, $M_{\rm fin}$ is the final mass, and $L_{\rm fin}$ is defined in terms of the final mass and spin as

$$S_{||} + L_{\rm fin} = M_{\rm fin}^2 a_{\rm fin}^{||}, \tag{5.31}$$

where $a_{\rm fin}^{||}$ is the final Kerr parameter in the corresponding non-precessing configuration. We compute $a_{\rm fin}$ and $M_{\rm fin}$ as functions of the symmetric mass ratio and the spin projections in the direction of $\mathbf{L}$, using the same fit to NR data [7] that was used in the non-precessing IMRPhenomXAS and IMRPhenomXHM models. Note that the fit for $a_{\rm fin}$ is in fact constructed as a fit for $L_{\rm fin}$, and $a_{\rm fin}$ is then computed using Eq. (5.31).

In the twisting approximation we assume that in a co-moving frame the waveform is well approximated by a twisted-up non-precessing waveform. In addition, one usually assumes for simplicity that the total spin magnitudes, as well as the magnitudes of the projections of $\mathbf{S_1} + \mathbf{S_2}$ onto $\mathbf{L}$ ($S_{||}$) and orthogonal to it ($S_{\perp}$) are preserved as well.

The spin components $S_{\perp}$ and $S_{||}$ that enter the final spin estimate in Eq. (5.30) can now be computed in different ways. The simplest choice is to use the non-precessing value for $S_{||}$, and the appropriately averaged value of $S_{\perp}$, which enters our inspiral descriptions. For the NNLO angle description summarised in Sec. 5.4.1, which is an effective single spin description, the quantity χ_p (5.20-5.22) acts as an average in-plane spin, and can be used to estimate $S_{\perp}$ at merger. This is the choice that has been made for the IMRPhenomP [1] and IMRPhenomPv2 [23] models, and it will be the default choice we have implemented when using one of the NNLO angle descriptions. For the double spin MSA description outlined in Sec. 5.4.2, one can rely on the precession-averaged spin couplings of Eqs. (A9-A11) in [2]. This can be best seen by rewriting Eq. (5.30) more explicitly as

$$\begin{aligned} S_{\rm fin}^2 &= S_1^2 + S_2^2 + 2S_1 \cdot S_2 + L_{\rm fin}^2 + \\ &+ 2L_{\rm fin}\left(\mathbf{S_1} \cdot \hat{\mathbf{L}} + \mathbf{S_2} \cdot \hat{\mathbf{L}}\right). \end{aligned} \tag{5.32}$$

Averaging over one precession cycle, the above equation can be rewritten as:

$$\langle S_{\rm fin}^2 \rangle_{\rm pr} = S_{\rm av}^2 + L_{\rm fin}^2 + 2L_{\rm fin}(\langle \mathbf{S_1} \cdot \hat{\mathbf{L}} \rangle_{\rm pr} + \langle \mathbf{S_2} \cdot \hat{\mathbf{L}} \rangle_{\rm pr}). \tag{5.33}$$

This will serve as our default choice when using the MSA formulation to compute the Euler angles.

Assuming that the spin components at merger are equal to the average quantities during the inspiral has the advantage of providing unambiguous values. However, this neglects the two facts that the averaged quantities do not predict the value of the spin components at any particular time, and that they do not accurately describe the spin dynamics shortly

before and at merger. We therefore also discuss alternative descriptions, which contain additional freedom to approximately account for the unmodeled information about the spin components at merger.

We will first discuss the simpler single-spin case, assuming that only the larger black hole, labelled with index $i = 1$, carries spin, and the spin of the smaller black hole vanishes. We first rewrite Eq. (5.30) in the form

$$|S_{\rm fin}| = \sqrt{S_1^2 + L_{\rm fin}^2 + 2S_{1,||}L_{\rm fin}}\,. \tag{5.34}$$

We assume that the total spin $\mathbf{S_1}$ does not change during the coalescence process, and that $L_{\rm fin}$ is given by the non-precessing value as in Eq. (5.31), where for $S_{||}$ we take its initial value, i.e. the value we have used during the inspiral. In previous work [1, 23] this initial value of $S_{||}$ has also been used in the final spin estimate of Eq. (5.34), consistent with the approximation that $S_\perp$ and $S_{||}$ are approximately preserved during the inspiral. Due to the strong spin interaction close to merger, this approximation may however not be accurate, and alternatively we may only assume that the spin magnitude is preserved and treat the value of $S_{1,||}$ as unknown. We can then determine the value of $S_{1,||}$ that best fits a given precessing waveform subject to the condition $0 \leq |S_{1,||}| \leq S$. We currently do not provide this option in our LALSuite code, in order to avoid book-keeping of extra parameters that are not typically used in PE.

Instead we provide a toy model solution for the single-spin case, where χ_p is replaced by χ_{1x}, i.e. the x-component of the spin of the larger black hole. This particular choice of toy model has been implemented to facilitate comparisons with an earlier version of the IMRPhenomPv3HM model [16].[4] The rotational freedom in the in-plane spin then allows to vary the in-plane spin component that enters the final spin estimate between zero and the magnitude of the in-plane spin.

Note that in [1, 23] a free parameter λ was introduced as

$$|a_{\rm fin}| = \sqrt{\left(S_\perp^2 \frac{\lambda}{M_{\rm fin}^2}\right)^2 + {a_{\rm fin}^{||}}^2}, \tag{5.35}$$

and was set to the ad-hoc value $\lambda = M_{\rm fin}^2$, consistent with [62], in order to reduce the residuals of the final spin estimate when comparing with NR data sets.

We now consider the double-spin case, where we also have to take into account the time-dependent angle between the in-plane components of the spins. We can write Eq. (5.30)

[4] This earlier version of IMRPhenomPv3HM with χ_{1x} passed to the final spin function was introduced in version 2f1596262c3af9832dfe2a52944472cb3be81e0a of the https://git.ligo.org/lscsoft/lalsuite/ repository and changed to χ_p in b60bec3aef3be3c346fd349ddd738e55a2af4b6d.

in a form similar to Eq. (5.34) as

$$S_{\rm fin}^2 = (\mathbf{S_1}_{,\perp} + \mathbf{S_2}_{,\perp})^2 + (S_{1,||} + S_{2,||} + L_{\rm fin})^2 \tag{5.36a}$$

$$= S_1^2 + S_2^2 + L_{\rm fin}^2 + 2S_{1,\perp}S_{2,\perp}\cos\phi_{12} \tag{5.36b}$$

$$+ 2S_{1,||}S_{2,||} + 2L_{\rm fin}(S_{1,||} + S_{2,||}). \tag{5.36c}$$

One could now choose the unmodeled parameters in this equation and fit them to the best values in a given data set: e.g. one could leave the parallel components free analogous to Eq. (5.34), or simply neglect the tilt of the spins at merger and use $\cos\phi_{12}$ as a free parameter. We reserve these options for future work, as they would require to perform Bayesian PE with a different parameterization than usual within LALSuite. Instead, we provide the option to model $S_\perp$ as

$$S_\perp^2 = (\mathbf{S_1}_{,\perp} + \mathbf{S_2}_{,\perp})^2, \tag{5.37}$$

which provides the freedom for cancellations between the two spin components.

In our LALSuite code we currently provide four options to set the magnitude of the final spin, see also appendix 5.F. We either proceed in analogy with Eq. (5.35) and set

$$|a_{\rm fin}| = \sqrt{\left(\bar{\chi}_p^2 \frac{m_1^2}{(m_1+m_2)^2}\right)^2 + {a_{\rm fin}^{||}}^2}, \tag{5.38}$$

where $\bar{\chi}_p$ can be chosen as one of three alternatives,

$$\bar{\chi}_p = \chi_p, \tag{5.39}$$

$$\bar{\chi}_p = \chi_{1x}, \tag{5.40}$$

$$\bar{\chi}_p = \frac{S_\perp (m_1+m_2)^2}{m_1^2}, \tag{5.41}$$

or by setting

$$|a_{\rm fin}| = \frac{\sqrt{\langle S_{\rm fin}^2 \rangle_{\rm pr}}}{M^2}, \tag{5.42}$$

where $S_\perp$ in Eq. (5.41) is defined as in Eq. (5.37) and for Eq. (5.42) we have used Eq. (5.33). Here Eq. (5.39) corresponds to the choice of IMRPhenomP [1] and IMRPhenomPv2 [23] and is the default choice when using the NNLO description of the Euler angles, Eq. (5.40) has been implemented to compare with a previous version of IMRPhenomPv3HM, and Eq. (5.42) is the default choice when using the MSA description of the Euler angles.

In Sec. 5.5 we will provide results for different final spin choices. A detailed investigation of the differences between final spin estimates is beyond the scope of the present paper

and will be investigated in future work, along with further improvements.

Due to the change of the directions of $\mathbf{S}_i$ and $\mathbf{L}$ from precession, the estimates we have discussed only concern the final spin magnitude and not its direction. If we restrict to simple precession, including the case that the waveform starts after a flip of the direction of $\mathbf{J}$ in a case of transitional precession, we can assume that the direction of $\mathbf{J}$ is approximately preserved and agrees with the final spin direction.

5.5 Model Performance and Validation

In this section, we perform various tests of our model, ranging from comparisons against NR to real-world PE applications.

5.5.1 Comparison of Euler angles with Numerical Relativity

Both descriptions for the precession angles implemented in our model, and described in Sec. 5.4.1 and Sec. 5.4.2, are based on PN analytical approximations to the solution of the angular momenta evolution equations and therefore are expected to lose accuracy when the assumptions of the PN formalism start to fail as the frequency becomes too high. A full systematic understanding of the limitations of both descriptions is out of the scope of this work, but to illustrate the differences between both descriptions, in Fig. 5.1 we compare them with two precessing simulations from the SXS catalog [63, 64]: a single-spin simulation [SXS:BBH:0094 with mass ratio $q = 1.5$ and initial dimensionless spin vectors $\boldsymbol{\chi}_1 = (0.5, 0, 0)$ and $\boldsymbol{\chi}_2 = (0, 0, 0)$] and a double-spin simulation [SXS:BBH:0053 with $q = 3$, $\boldsymbol{\chi}_1 = (0.5, 0, 0)$ and $\boldsymbol{\chi}_2 = (-0.5, 0, 0)$].

Here the Euler angles of the NR simulations are computed with the "quadrupole alignment" procedure, see [17, 32] and [22] for a recent discussion in the context of waveform modelling. For the NNLO description outlined in Sec. 5.4.1, the in-plane spin is described by the single constant quantity χ_p defined in Eq. (5.22). In contrast, the MSA description (summarized in Sec. 5.4.2) contains information about both individual spins and is able to predict the evolution of the norm of the total spin $\mathbf{S} = \mathbf{S}_1 + \mathbf{S}_2$, which allows it to capture the time/frequency dependent oscillations of the Euler angles on the precession timescale caused by the evolution of the norm of the total spin.

For the single-spin simulation shown in the left panel of Fig. 5.1, both descriptions present a very similar behaviour for the opening angle β and for the inspiral cycles in the precessing angle α, though the MSA description seems to remain closer to NR as the end of the inspiral is approached. For the double-spin case in the right panel of Fig. 5.1,

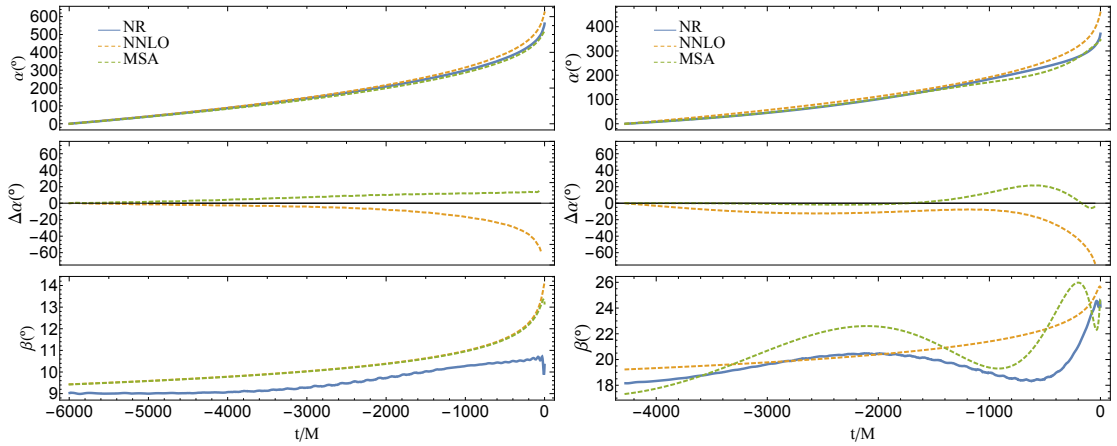

FIGURE 5.1: Comparison of Euler angles with Numerical Relativity. Left: SXS:BBH:0094 ($q = 1.5$, $\boldsymbol{\chi}_1 = (0.5, 0, 0)$, $\boldsymbol{\chi}_2 = (0, 0, 0)$). Right: SXS:BBH:0053 ($q = 3$, $\boldsymbol{\chi}_1 = (0.5, 0, 0)$, $\boldsymbol{\chi}_2 = (-0.5, 0, 0)$). Solid blue: Quadrupole-aligned Euler angles extracted from NR simulation. Dashed orange: NNLO implementation (version 102). Dashed green: MSA implementation (version 223).

one can see that the behaviour of the precessing angle α during the inspiral is better reproduced by the MSA description and the MSA opening angle β can also reproduce the oscillatory structure observed in the NR simulation. The oscillations due to double-spin effects dephase however relative to NR as the end of the inspiral is approached, which can even lead to a worse description of the late inspiral than the one provided by the NNLO single-spin description, as seen in the example for the precessing angle α. Strategies to improve the behaviour of the PN precessing angles descriptions in the high-frequency regime will be addressed in future work.

5.5.2 Time Domain Waveforms

To best appreciate the differences between precessing waveforms constructed using NNLO and MSA Euler angle prescriptions, we have generated time-domain waveforms with IMRPhenomXPHM for both versions of the "twisting-up" angles, and compared with the precessing surrogate model NRSur7dq4 [65]. In Fig. 5.2 we plot the cross polarization for a double-spin configuration with high in-plane spins, varying the mass ratio. For increasing q, the MSA description tends to stay closer to NRSur7dq4. The differences between the two descriptions become particularly strong for high mass-ratio systems, as shown in Fig. 5.3, with the MSA description appearing to be more stable in this regime. This is particularly evident in the lower panels, where we show a $q = 12$ and a $q = 16$ configuration. Notice that the non-smoothness of the NNLO angles in some regions of the parameter space led us to impose a more stringent threshold on the multibanding of the Euler angles for this precession version (see Sec.5.5.4 for a detailed discussion).

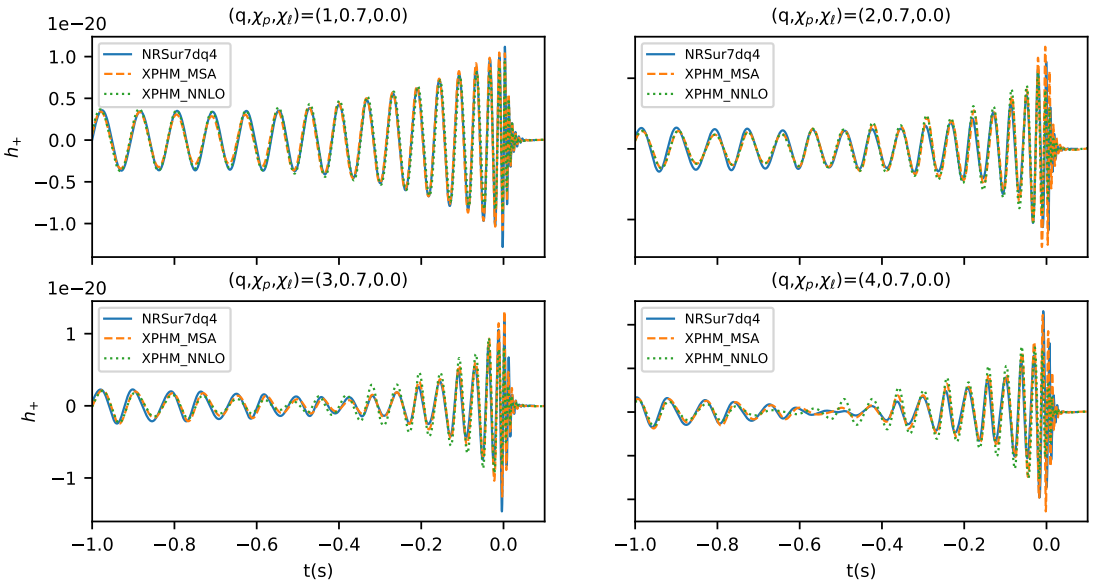

FIGURE 5.2: We compare the relative performance of NNLO and MSA angles against NRSUR7DQ4, by plotting the plus polarization returned by the different models for a double-spin configuration with high in-plane spins. Each panel refers to the same spin configuration, but we allow the mass ratio to vary from 1 to 4, which is the upper limit of the calibration region of NRSUR7DQ4. Overall NNLO angles perform well, although we do observe some disagreement with respect to NRSUR7DQ4 as we increase the mass ratio (lower panels).

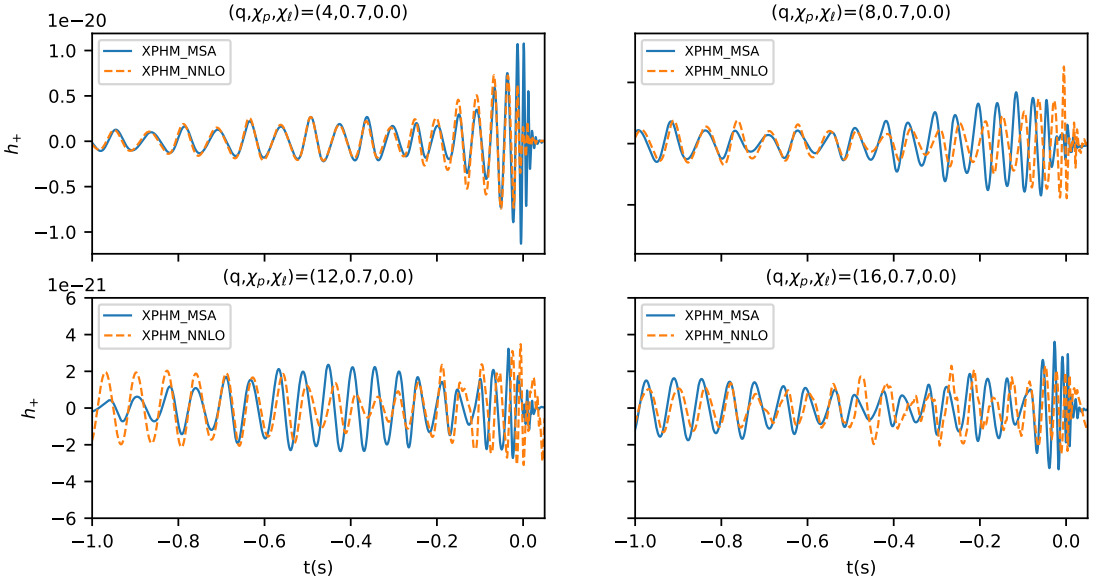

FIGURE 5.3: We compare the behaviour of the two twisting-up methods implemented in IMRPHENOMXPHM for the same spin configuration chosen in Fig. 5.2, varying the mass ratio between 4 and 16. For $q = 4$ we observe good agreement between the two angle descriptions, especially during the inspiral. However, as the mass ratio increases the agreement degrades and NNLO angles tend to produce non-smooth features in the waveform.

5.5.3 Match Calculations for Precessing Waveforms

In order to check the agreement between our waveform model and other descriptions we follow standard practice and compute matches between waveforms across a portion of the parameter space. In Sec. 5.5.3.1 we present matches between our model and NR waveforms, and in Sec. 5.5.3.2 we compare with other waveform models. As in our previous work [4, 10] we use the standard definition of the inner product (see e.g. [37]),

$$\langle h_1, h_2 \rangle = 4\Re \int_{f_{\rm min}}^{f_{\rm max}} \frac{\tilde{h_1}(f)\, \tilde{h_2^*}(f)}{S_{\rm n}(f)}, \tag{5.43}$$

where $S_{\rm n}(f)$ is the one-sided power spectral-density of the detector noise. The *match* is defined as this inner product divided by the norm of the two waveforms and maximized over relative time and phase shifts between both of them,

$$\mathcal{M}(h_1, h_2) = \max_{t_0, \phi_0} \frac{\langle h_1, h_2 \rangle}{\sqrt{\langle h_1, h_1 \rangle}\sqrt{\langle h_2, h_2 \rangle}}. \tag{5.44}$$

It is advantageous to visualize deviations between waveforms in terms of the mismatch rather than the match, where the mismatch is defined as

$$\mathcal{MM}(h_1, h_2) = 1 - \mathcal{M}(h_1, h_2). \tag{5.45}$$

We use the Advanced-LIGO [66] design sensitivity Zero-Detuned-High-Power PSD [67] with a lower cutoff frequency for the integrations of 20 Hz and an upper cutoff at 2048 Hz. We analytically optimize over the template polarization angle, following [68], and numerically optimize over reference phase and rigid rotations of the in-plane spins at the reference frequency. We do this rather than optimizing over the reference frequency as suggested in [16], as this allows to set unambiguous bounds for the parameters involved in the optimization. In order to perform the numerical optimization we use the dual annealing algorithm as implemented in the `SciPy Python` package [69].

5.5.3.1 Matches Against SXS Numerical Relativity Simulations

We have computed mismatches for IMRPhenomXPHM against 99 precessing SXS waveforms [63, 64], picking for each binary configuration the highest resolution available in the `lvcnr` catalogue [28]. As a lower cutoff for the match integration, we took the minimum between 20 Hz and the starting frequency of each NR waveform. We repeated the calculation for three representative inclinations between the orbital angular momentum and the line of sight $(0, \pi/3, \pi/2)$ and total masses ranging from 64 $M_\odot$ to 250 $M_\odot$. As low matches tend to be correlated with low signal-to-noise ratio (SNR) and,

therefore, with a lower probability for the signal to be observed, we compute here the SNR-weighted match $\mathcal{M}_{\rm w}$ [70]

$$\mathcal{M}_{\rm w} = \left(\frac{\sum_i \mathcal{M}_i^3 \langle h_{i,\rm NR}, h_{i,\rm NR} \rangle^{3/2}}{\sum_i \langle h_{i,\rm NR}, h_{i,\rm NR} \rangle^{3/2}} \right)^{1/3}, \tag{5.46}$$

where the subscript i refers to different choices of polarization and reference phase of the source i.e. in our case of the NR waveform. The results are shown in Fig. 5.4. The large majority of the cases considered here resulted in mismatches between 10^{-3} and 10^{-2}, with a consistent number of cases below 10^{-3} for face-on sources.

We observed, however, three cases for which matches are below 95% for at least one value of the inclination (`SXS:0057, SXS:0058, SXS:0062`) and one case where this happens for all the inclinations (`SXS:0165`). These all correspond to high mass-ratio, strongly precessing binaries: `SXS:0057, SXS:0058, SXS:0062` are $q = 5$ simulations with $\chi_p \geq 0.4$ and `SXS:0165` is a $q = 6$ simulation with $\chi_p = 0.78$. For this type of systems, the complex interaction between different waveform multipoles can result in a non-trivial dependence of the SNR on the orientation of the source, with face-on configurations not being necessarily favoured (see, for instance, [71] for a related discussion). We observe this in `SXS:0057, SXS:0062, SXS:0165`, for which the highest values of SNR do not necessarily concentrate around zero inclination. This explains why for these simulations the match increases, rather than decreases, with the inclination of the source.

5.5.3.2 Matches Against other Models

We now turn to computing the mismatch with other waveform models. In contrast to the comparison with NR waveforms shown in Sec. 5.5.3.1, where SNR-weighted mismatches are presented, we show "raw" mismatches between models, without weighting them. We compute matches in the calibration regime of the NRSur7dq4 model, $1 \leq m_1/m_2 \leq 4$ and dimensionless spin magnitudes up to 0.8.

We compare against a number of other waveform models, which are routinely used for gravitational wave data analysis:

- Previous models from the phenomenological waveform family including IMRPhenomD [5, 6], IMRPhenomHM [11], IMRPhenomPv3HM [16] and IMRPhenomPv3 [15], and the spin-aligned basis waveforms of the new IMRPhenomX family: IMRPhenomXAS [4] and IMRPhenomXHM [10].

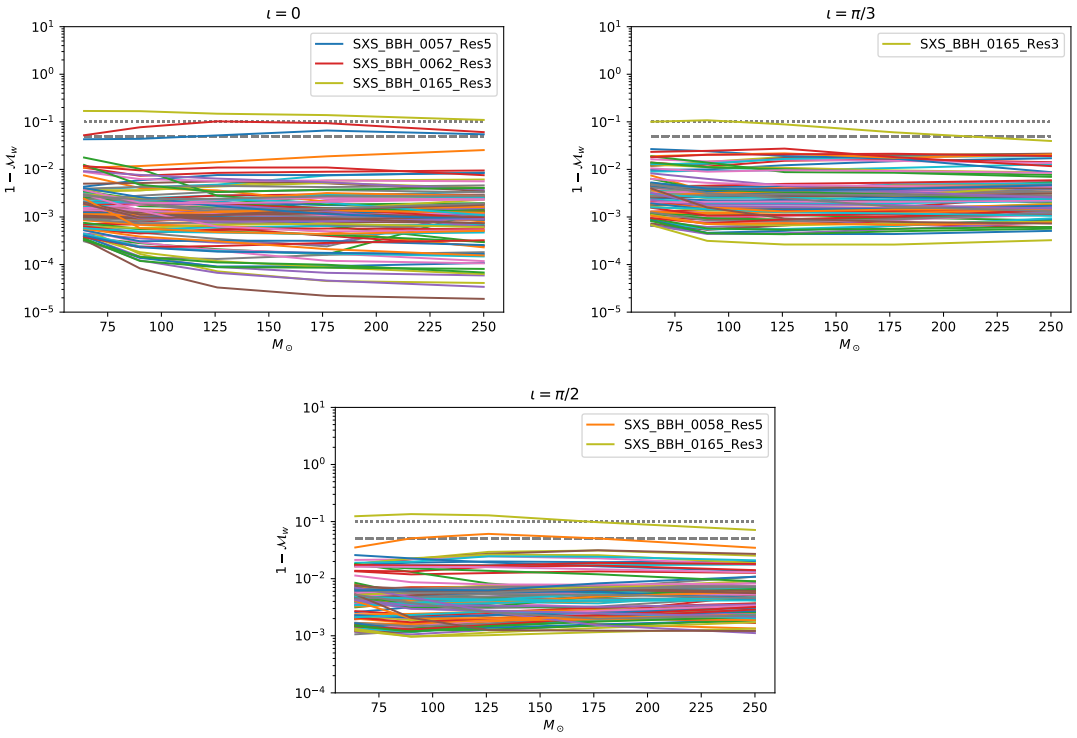

FIGURE 5.4: In the plots above, we show the SNR-weighted mismatch $1 - \mathcal{M}_w$ of IMRPHENOMXPHM against 99 SXS precessing waveforms of the `lvcnr` catalog, in order of ascending inclination. A dashed and a dotted line mark the 5% and 10% mismatch thresholds respectively.

- A NR surrogate model NRSUR7DQ4 [65] that interpolates between NR waveforms, calibrated for precessing simulations up to mass ratios of $q = 4$ and spin magnitudes up to 0.8.
- A similar non-precessing surrogate model NRHYBSUR3DQ8 [72], calibrated to aligned-spin hybrid waveforms up to mass ratios of $q = 8$ and spin magnitudes up to 0.8.
- A non-precessing, higher-modes model SEOBNRV4HM_ROM [73] which is a reduced order model of SEOBNRV4HM [9, 74], an EOB model calibrated to NR waveforms.

We choose NRSUR7DQ4 as the reference model for high mass precessing waveforms, where higher mode contributions are significant, since this is still the only precessing model calibrated to precessing NR waveforms. Due to the limited length of the NR waveforms used to calibrate the model (4000 total mass units), we restrict to large masses above 90 solar masses and compute the mismatch for a fixed list of masses, $(90, 126, 177, 249, 350)M_\odot$. Note that for large masses, the impact of higher mode effects and precession effects in the strong field regime on the waveform is more pronounced.

In Fig. 5.5 we show mismatches both with the precessing NRSur7dq4 [65] and the non-precessing NRHybSur3dq8 [72]. The comparisons with the latter allow to put the mismatches we see for precessing higher-modes models into the context of mismatches in the non-precessing case, where waveform models are significantly more mature.

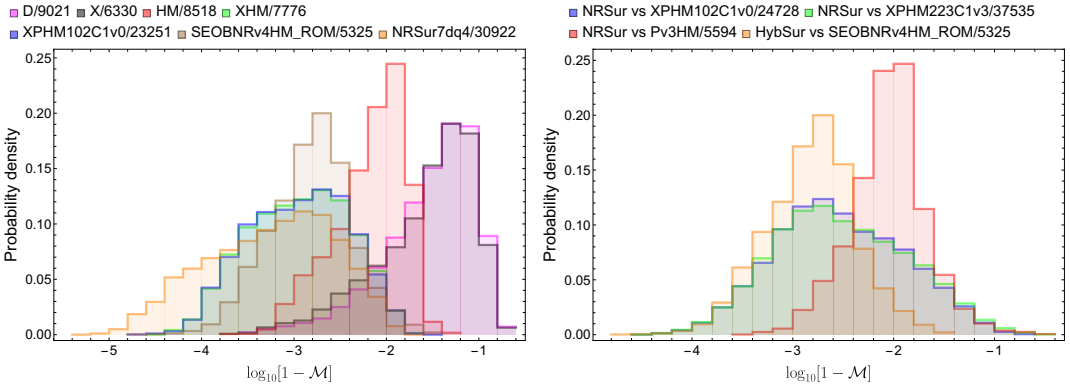

Figure 5.5: In the left panel we compare the non-precessing models IMRPhenomD, IMRPhenomXAS, IMRPhenomHM, IMRPhenomXHM, SEOBNRv4HM_ROM and the precessing IMRPhenomXPHM and NRSur7dq4 models with the non-precessing NRHybSur3dq8 model as discussed in the main text. In the right panel we compare two versions of our IMRPhenomXPHM model (NNLO-based version 102 with final spin version 0 and MSA-based version 223 with final spin version 3, see Table 5.F.1), and IMRPhenomPv3HM with NRSur7dq4, as discussed in the main text. For comparison we show also the mismatch between NRHybSur3dq8 and SEOBNRv4HM_ROM as displayed in the upper panel. The number of samples for each comparison is indicated in the legend.

In the upper panel of Fig. 5.5 we also show the comparison of models that only contain the $\ell = |m| = 2$ modes with NRHybSur3dq8. One can see that while IMRPhenomXAS is significantly more accurate than IMRPhenomD as discussed in [4], this only yields a small advantage when comparing raw mismatches with a higher-modes model. A model that does include higher modes, even when those are not calibrated to NR, such as IMRPhenomHM, gains significant accuracy. The relative gain from calibrating higher modes is however comparable. The difference between the IMRPhenomXHM and SEOBNRv4HM_ROM [73] models is small, in particular considering that they do not describe the same set of sub-dominant harmonics, with IMRPhenomXHM having a larger fraction of very accurate waveforms. We have also included a variant of our precessing IMRPhenomXPHM model (variant 102 based on NNLO angles and final spin version 0, see Table 5.F.1). One can see that results are consistent with the manifestly non-precessing model IMRPhenomXHM (up to sampling errors), which provides an end-to-end test of consistent behaviour of our new model in the aligned-spin limit. A number of more stringent tests of the appropriate aligned-spin limit have been carried out as part of the LALSuite code review. Finally, NRSur7dq4 is most consistent with NRHybSur3dq8, but the advantage is not very pronounced, and is likely to be significantly reduced by adding further harmonics to IMRPhenomXPHM, in particular the

$\ell = |m| = 5$ modes already present in SEOBNRv4HM_ROM and the $\ell = 4, |m| = 3$ modes present in IMRPhenomHM.

In the lower panel of Fig. 5.5 we finally show mismatches against the precessing NRSur7dq4 model. One can see that the distributions of mismatches are roughly similar to the non-precessing case, but with a tail of high mismatches, which is similar to IMRPhenomPv3HM. The tail of small mismatches is similar to that when comparing the two non-precessing models SEOBNRv4HM_ROM and NRHybSur3dq8, while in the bulk IMRPhenomXPHM clearly outperforms IMRPhenomPv3HM, which is not calibrated to numerical data for subdominant harmonics.

5.5.4 Multibanding and Euler Angles

In [3] we have discussed our implementation of an algorithm to accelerate waveform evaluation by first evaluating the waveform on a coarse unequispaced grid, before linear interpolation to an equispaced fine grid, following [14]. The grid spacing on the coarse grid is chosen to satisfy a given error threshold for linear interpolation (a different criterion to set the grid spacing has previously been used in [14]). An iterative expression can then be used to accelerate the evaluation of computationally expensive trigonometric expressions, such as those required to compute the strain from the phase (and amplitude).

In [3] we derived simple estimates to set the grid spacing in terms of the phase errors and relative amplitude errors as a function of the grid spacing, and we have implemented a conservative default threshold of 10^{-3} radians of local phase error and of relative amplitude error 10^{-3}.

Here we apply the same idea to the Euler angles. For the inspiral, in [3] we have derived the required grid spacing for accurate linear interpolation from the leading singular term of the TaylorF2 phase expression for the gravitational wave phase of spherical harmonic mode $h_{\ell m}$, which reads [75],

$$\Phi_{\ell m} = \frac{m}{2}\frac{3}{128\eta}\left(\frac{2\pi f}{m}\right)^{-5/3}, \tag{5.47}$$

where η is the symmetric mass ratio and constants of integration that do not affect the second derivative, and thus the error estimate, have been dropped. The leading term for the NNLO angles α and ϵ is the same

$$\alpha = \left(-\frac{5\delta}{64 m_1} - \frac{35}{192}\right)(\pi f)^{-1} + \text{higher order terms}, \tag{5.48}$$

see appendix 5.G.1. Similar to the evaluation of the inspiral gravitational wave phase, we need to evaluate expressions of the type

$$e^{im\alpha(2\pi f/m)}, \tag{5.49}$$

for spherical harmonic modes $h_{\ell m}$, see appendix 5.E, and we thus have to apply multi-banding interpolation to the arguments of the complex exponentials of the type in Eq. (5.49). The ratio of the maximal allowed step sizes for achieving the same interpolation error for the gravitational wave phase and Euler angles is thus given by the (inverse) ratio of second derivatives with respect to the frequency f, which evaluates to

$$\frac{df_\Phi}{df_\alpha} = \left|\frac{m\alpha''(2\pi f/m)}{\Phi''_{\ell m}}\right| = \frac{(\pi f)^{2/3}\left(13\sqrt{1-4\eta}+7\right)\eta}{\sqrt{1-4\eta}+1}, \tag{5.50}$$

which is smaller than unity during the inspiral ($f \leq 0.1$) and vanishes both in the low-frequency and extreme-mass-ratio limits. The third Euler angle β is a regular function during the inspiral, and thus does not require high resolution for accurate interpolation.

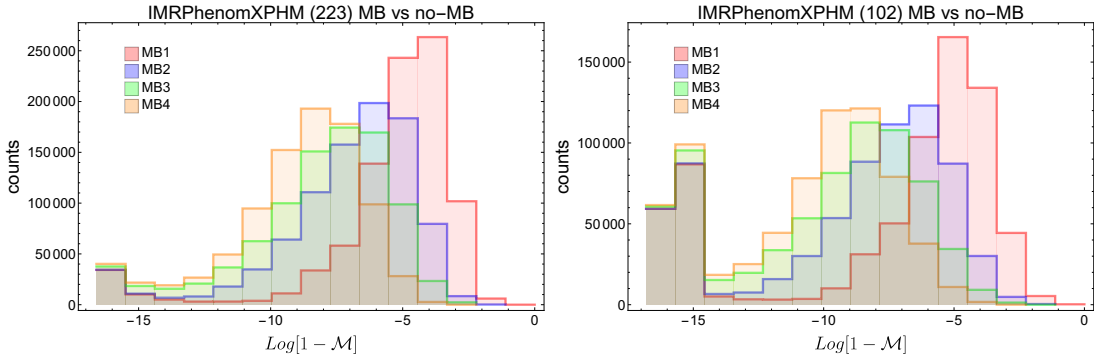

FIGURE 5.6: Histograms of a mismatch calculation for h_+ between versions of IMRPHENOMXPHM without using multibanding for the Euler angles, and with four different levels of multibanding threshold: 10^{-1}, 10^{-2}, 10^{-3}, 10^{-4}. The top panel show the results for the MSA prescription (version 223) and the bottom panel shows the result for NNLO angles (version 102). 10^6 waveforms were generated across a parameter space as described in the main text. The threshold 10^{-3} (MB3 in the plot) has been chosen as the default value in the LALSuite implementation.

During the merger and ringdown the angles have a simpler functional form than the gravitational wave phase, which is characterized by a Lorentzian. The exponential falloff of the mode amplitudes in the ringdown phase also requires significant resolution. The Euler angles in turn carry significant systematic errors, e.g. due to applying the SPA approximation for the whole waveform. Note that the MSA prescription for the angles causes oscillations in the angle β, however the angle prescriptions still broadly agree with the NNLO description.

Future work will attempt to calibrate the angle descriptions to NR and better understand the phenomenology during the merger and ringdown, which in turn will require improved

estimates for the required grid spacing in order to not loose accuracy due to multibanding.

At the current level of accuracy produced from the precession angle models, it does not seem necessary to attempt more precise prescriptions to apply multibanding to the Euler angles. For simplicity we thus use the same coarse grid for each spherical harmonic mode that we have utilized in [3]. To quantitatively assess the impact that multibanding of the Euler angles has on the precessing waveforms, we compute matches between the original waveform, generated without angle multibanding, and waveforms produced with the identical parameters except with multibanding, varying the multibanding threshold between 0.1 and 0.0001.

The results of this comparison are shown in Fig. 5.6 for waveforms twisted up using the MSA angles (top panel) and the NNLO angles (bottom panel). They are generated over a broad parameter space range with $1 \leq m_{1,2} \leq 500$ and dimensionless spin magnitudes up to unity, corresponding to the extreme Kerr limit. The frequencies span from 10 to 1024 Hz and the grid spacing df ranges from 0.01 to 0.3 Hz. In typical Bayesian inference applications, the value of df is not chosen randomly but adjusted to the segment length of the data to be analyzed, which is itself adjusted to the time a signal is observable in the sensitive band of the detector. Here we have chosen to use a random df which could lead to downsampled waveforms and hence worse matches, however the random df allows us to stress-test the robustness of the multibanding algorithm and check that any kind of uniform frequency grid is supported.

The results in Fig. 5.6 show that indeed the lower the threshold the better is the match (at the expense of loosing speed). There is a tail of very low mismatches which is much more pronounced for version 102 than for 223; this tail corresponds to cases where the multibanding was switched off automatically by the code and hence the match is close to machine precision. The multibanding is automatically switched off in the following cases:

- For total mass $M_{\rm tot}$ higher than 500 $M_\odot$. This cutoff is already present in the non-precessing model IMRPhenomXHM and is motivated by the short length of the waveform in the frequency band of the detector for these massive systems, which renders multibanding less efficient but also unnecessary.
- When using MSA angles: for $q > 50$ and $M_{\rm tot} > 100\, M_\odot$. This corner of the parameter space corresponds to cases where the MSA angles do not have a mild behaviour and lead to 'noisy' waveforms. Applying multibanding to these cases would amplify errors, and is thus switched off.
- When using NNLO angles: for $q > 8$. It is well known that the NNLO angles can behave badly for high mass ratios and can even be pathological, see e.g. our

discussion in Sec. 5.5.2. Once again the multibanding would not properly work for theses case and is switched off.

The veto for the multibanding in the NNLO angles is much broader than for MSA, leading to the more pronounced tail of lower mismatches.

We also perform a PE study with different multibanding thresholds, to test the effect on recovered posterior distributions. We perform the same NR injections as described in Sec. 5.5.6.3 with version 223 for the MSA angles and compare the results between thresholds of $0, 10^{-1}, 10^{-2}, 10^{-3}, 10^{-4}$. As seen in Fig. 5.7 the results are highly consistent. Considering these results together with the benchmarking results shown in Fig. 5.8 and discussed in the next section, we however make a conservative choice for the default multibanding threshold for the Euler angles and set the value to 10^{-3}. This can be changed as described in appendix 5.F.

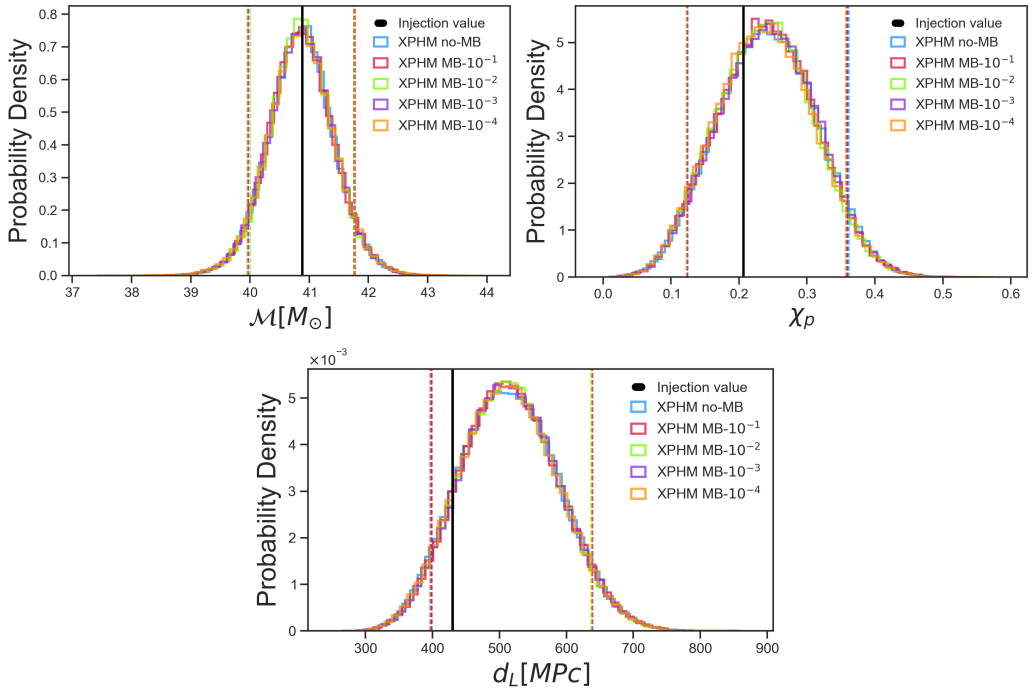

FIGURE 5.7: Injection recovery results for `SXS:BBH:0143` for IMRPhenomXPHM without multibanding in the Euler angles and with four different thresholds $(10^{-1}, 10^{-2}, 10^{-3}, 10^{-4})$ for multibanding in the angles. No appreciable differences arise in the posteriors, meaning that a more relaxed threshold than the default of 10^{-3} could be used in PE studies, reducing even more the computational cost of the runs.

5.5.5 Benchmarking

In Fig. 5.8 we show benchmarking results for one precessing case in a frequency range from 10 to 2048 Hz comparing the previous precessing PHENOM models with different

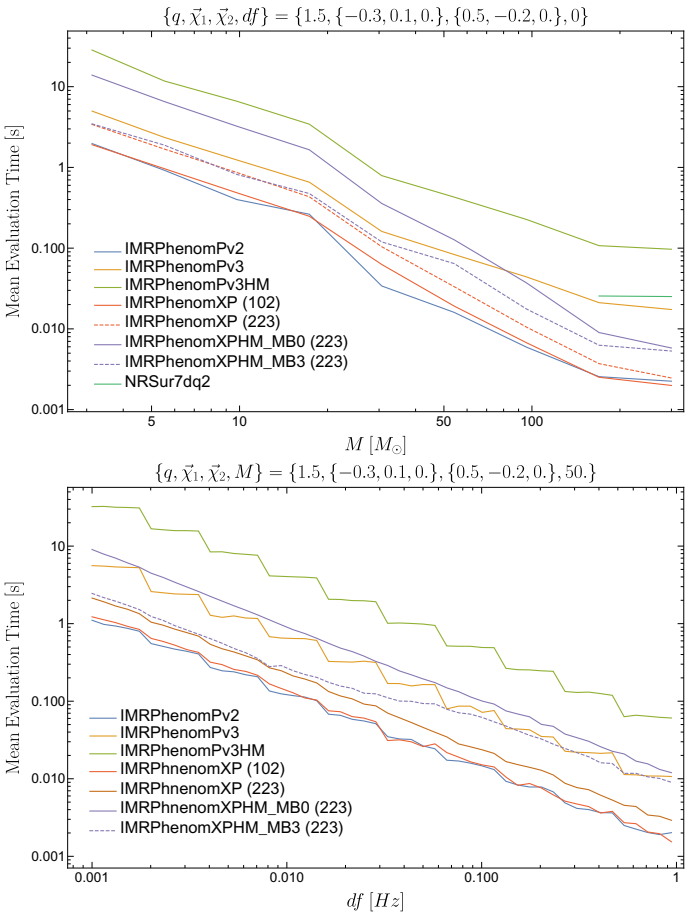

FIGURE 5.8: Mean evaluation time for different precessing models as a function of the total mass (left panel) and as a function of the spacing of the frequency grid (right panel). The NRSUR7DQ4 model can not be evaluated for such low frequencies as the PHENOM models; hence it only appears in the left panel for high masses, but not in the right panel, where we are using a total mass of $50M_\odot$.

$M_{\rm min}[M_\odot]$	ΔT	IMRPhenomXP	IMRPhenomPv2	IMRPhenomPv3	SEOBNRv4P	IMRPhenomXPHM	IMRPhenomPv3HM	SEOBNRv4PHM	NRSurd7q4
20	4 s	8.6	5.7	29.1	2691.4	31.8	160.3	4259.9	-
	8 s	16.8	11.2	56.4	2976.6	52.8	311.7	4540.9	-
60	4 s	5.8	4.1	29.4	1492.1	21.4	161.7	3016.2	60.5
	8 s	11.4	8.0	56.6	1483.9	36.3	312.8	2951.5	59.9

TABLE 5.1: Mean likelihood evaluation time in milliseconds for several precessing models for equal masses. The numbers represent averages over a mass range of $[M_{min}, 100]\,M_\odot$ with $M_{min} = 20, 60M_\odot$ and random spin orientations and magnitudes. The first column indicates the data analysis segment length in seconds.

settings of IMRPhenomXP and IMRPhenomXPHM. The timing is carried out with the executable `GenerateSimulation` (included in LALSuite/`LALSimulation`), averaging over 100 repetitions. In the top panel we show the dependeny on total mass. The frequency grid spacing *df* is computed automatically by the `SimInspiralFD` interface to take into account the length of the waveform in the time domain for the given parameters. In the bottom panel instead we show the dependency on the frequency grid spacings a function of the total mass, where the frequency spacing is computed as $df = 1/T$, where T is a simple estimate of the duration of the signal, see the discussion of Fig. 5 in [3]. In the labels for IMRPhenomXP and IMRPhenomXPHM, the numbers between brackets refer to the version of Euler angles: 102 uses the NNLO description, while 223 uses the MSA description (for a complete list of options see Table 5.F.1). For IMRPhenomXPHM we also show the result without applying multibanding in the Euler angles (MB0) and when using multibanding with threshold 10^{-3} (MB3).

For both plots the conclusion is the same, IMRPhenomXPHM without multibanding in the Euler angles is already faster than its counterpart IMRPhenomPv3HM, and when multibanding is included it is even faster than the "$(2, 2)$-mode only" version IMRPhenomPv3. The threshold of the multibanding used here is the default 10^{-3}, however the user can modify this parameter at will. Higher values of the threshold will accelerate the evaluation further at the price of decreased accuracy, which may be found acceptable based on the signal-to-noise ratio of a given event that is analyzed.

We have also estimated the efficiency of our models IMRPhenomXP and IMRPhenomXPHM compared to other precessing models by computing their mean likelihood evaluation time in the `LALInference` Bayesian PE code [12]. To perform this test, we have chosen an equal-mass configuration, 100 different total masses in the range $[M_{min}, 100]\, M_\odot$ with $M_{\rm min} = 20$, except for the precessing surrogate model NRSur7dq4, where we have set a higher minimum total mass of $M_{\rm min} = 60 M_\odot$, due to its limitations in start frequency. Dimensionless spin magnitudes are distributed randomly between $[0, 0.99]$ with a random isotropic distribution of spin vectors, and a reference frequency of 20 Hz. Two different segment lengths of $\Delta T = 4\,\mathrm{s}$, $8\,\mathrm{s}$ are studied as they are typical for the currently detected BBH GW signals [39]. As for our match calculations in Secs. 5.5.3.1 and 5.5.3.2 and NR injection studies in Sec. 5.5.6 the Advanced-LIGO design sensitivity Zero-Detuned-High-Power PSD [67] is used here for likelihood evaluations. For each total mass we perform 100 likelihood evaluations with randomly chosen spin configurations. The average of these 10^4 likelihood evaluations for each model is shown in Table 5.1.

The results confirm that the IMRPhenomXPHM model is the most efficient precessing waveform model with higher harmonics: ~ 5.4 times faster than IMRPhenomPv3HM

[16] for $\Delta T = 4\,\mathrm{s}$ and ~ 495 times faster than SEOBNRv4PHM for $\Delta T = 4\,\mathrm{s}$. SEOBNRv4PHM [76] is a precessing extension to the SEOBNRv4HM model [74] and is predicated on the numerical integration of computationally expensive ordinary differential equations, making the waveform slow to evaluate. Though we note that there has been significant work on improving waveform generation costs of EOB models, such as the post-adiabatic scheme introduced in [77] or reduced order models [78]. Regarding precessing models including only the $(2, \pm 2)$ mode in the co-precessing frame, IMRPhenomXP is slightly slower than IMRPhenomPv2 as a trade-off of the inclusion of the double-spin effects in the Euler angles, although it is much faster than the other phenomenological and SEOB models: ~ 3.4 times faster than IMRPhenomPv3 for $\Delta T = 4\,\mathrm{s}$ and ~ 312 times faster than SEOBNRv4P for $\Delta T = 4\,\mathrm{s}$. While an increase of the segment length increases the mean evaluation time for all models, the relative differences in evaluation costs at $\Delta T = 8\,\mathrm{s}$ are still similar to those at 4 s. The numbers reported in Table 5.1 illustrate the huge impact in efficiency that our new precessing models may have on data analysis studies like PE, where millions of likelihood evaluations are performed per run.

Finally, we note that computational cost of Bayesian inference can be significantly reduced through the use of reduced order quadratures (ROQ) [79–81]. This framework has been applied to a number of waveform models, including IMRPhenomPv2 [82]. We note that our model is amenable to such an approach following the methodology detailed in [82].

5.5.6 Parameter estimation

We use coherent Bayesian inference methods to determine the posterior distribution $p(\theta|d)$ for the parameters θ that characterize a binary, given some data d. From Bayes' theorem, we have

$$p(\theta|d) = \frac{\mathcal{L}(d|\theta)\,\pi(\theta)}{\mathcal{Z}}, \tag{5.51}$$

where $\mathcal{L}(d|\theta)$ is the Gaussian noise likelihood [83, 84, 12], $\pi(\theta)$ the prior distribution for θ and $\mathcal{Z}$ the evidence

$$\mathcal{Z} = \int d\theta\, \mathcal{L}(d|\theta)\,\pi(\theta). \tag{5.52}$$

For the analysis here, we use both the nested sampling [85] algorithm implemented in `LALInference` [12] and the nested sampling algorithm `Dynesty` [86] implemented in

`Bilby` [13] and `Parallel Bilby` [87]. We use the public strain data from the GWOSC [88–91]. Following [39], we marginalize over the frequency-dependent spline calibration envelopes that characterize the uncertainty in the detector amplitude and strain [92–94].

5.5.6.1 GW150914

As a prototypical example of the application of IMRPhenomXPHM to GW data analysis we re-analyze GW150914, the first direct observation of GWs from the merger of two black holes [25]. For GW150914 we use the nested sampling algorithm implemented in `LALInference` [12]. Our PE uses 2048 live points and coherently analyzes 8s of data. We use priors as detailed in appendix C of [39] and use the PSDs [91] and detector calibration envelopes [90] as available on GWOSC [88].

Using the inherent modularity of IMRPhenomXPHM, we can try to gauge the impact of systematics arising from the modelling of spin-precession effects by performing coherent Bayesian PE using the different prescriptions for the Euler angles discussed in Sec. 5.4. The final spin descriptions used here are the ones based on averaged in-plane spin for the NNLO and MSA Euler angle formulations, i.e. final spin version 0 for model version 102 (NNLO) and final spin version 3 for model version 223 (MSA), see appendix 5.F for details.

As can be seen in Figures 5.9 and 5.10, constraints on parameters such as the effective aligned-spin parameter $\chi_{\rm eff}$ and mass ratio q are consistent between the different waveform models whereas the effective precessing spin χ_p is not meaningfully constrained. This is in agreement with studies detailing the impact of waveform systematics on the analysis of GW150914 [24], which conclude that systematic errors and biases are small compared to statistical errors.

5.5.6.2 GW170729

We now turn our attention to the analysis of GW170729, the BBH GW signal with the highest mass detected during the O1 and O2 LIGO-Virgo observing runs [39]. Both the high mass and the significant posterior support for a mass ratio different from unity makes it a good candidate to test the impact of higher-order modes on the estimation of its parameters.

This fact has motivated several studies of this event in the literature with non-precessing higher-order modes models [95, 96] like the phenomenological IMRPhenomHM [11], the EOB SEOBNRv4HM [74], and the NR surrogate NRHybSur3dq8 [72]. We also reanalyzed this event with the upgraded version of the phenomenological non-precessing

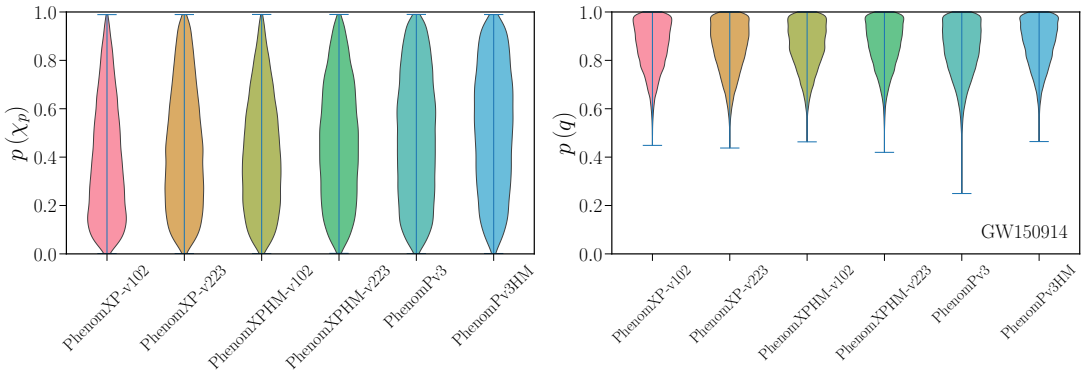

FIGURE 5.9: Bayesian inference results for GW150914: one-dimensional posterior probability distributions for the effective precessing spin parameter χ_p and the mass ratio q. (Here q is the inverse of our definition in Sec. 5.1, following the `LALInference` convention.) We show results for IMRPHENOMXPHM with and without higher modes, using NNLO and MSA angles respectively, as discussed in Sec. 5.4. For comparison, we also show results for IMRPHENOMPV3 and IMRPHENOMPV3HM. The labels of the different versions of IMRPhenomXPHM are explained in appendix 5.F.

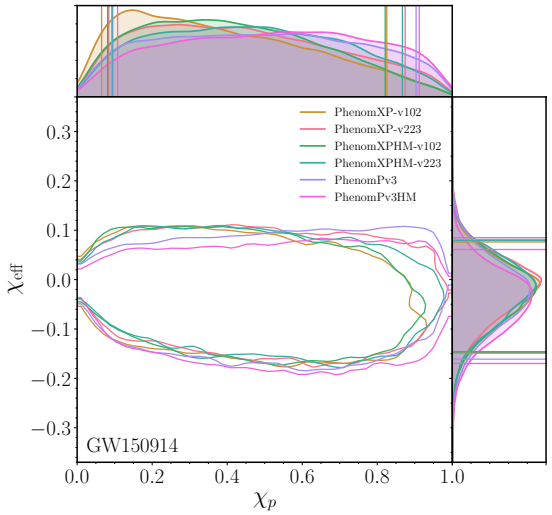

FIGURE 5.10: Bayesian inference results for GW150914: posterior probability distributions for the effective spin parameters $\chi_{\rm eff}$ and χ_p with two-dimensional 90% credible intervals. Here we show results for IMRPHENOMXPHM with and without higher modes, using NNLO and MSA angles respectively, as discussed in Sec. 5.4. For comparison, we also show results for IMRPHENOMPV3 and IMRPHENOMPV3HM.

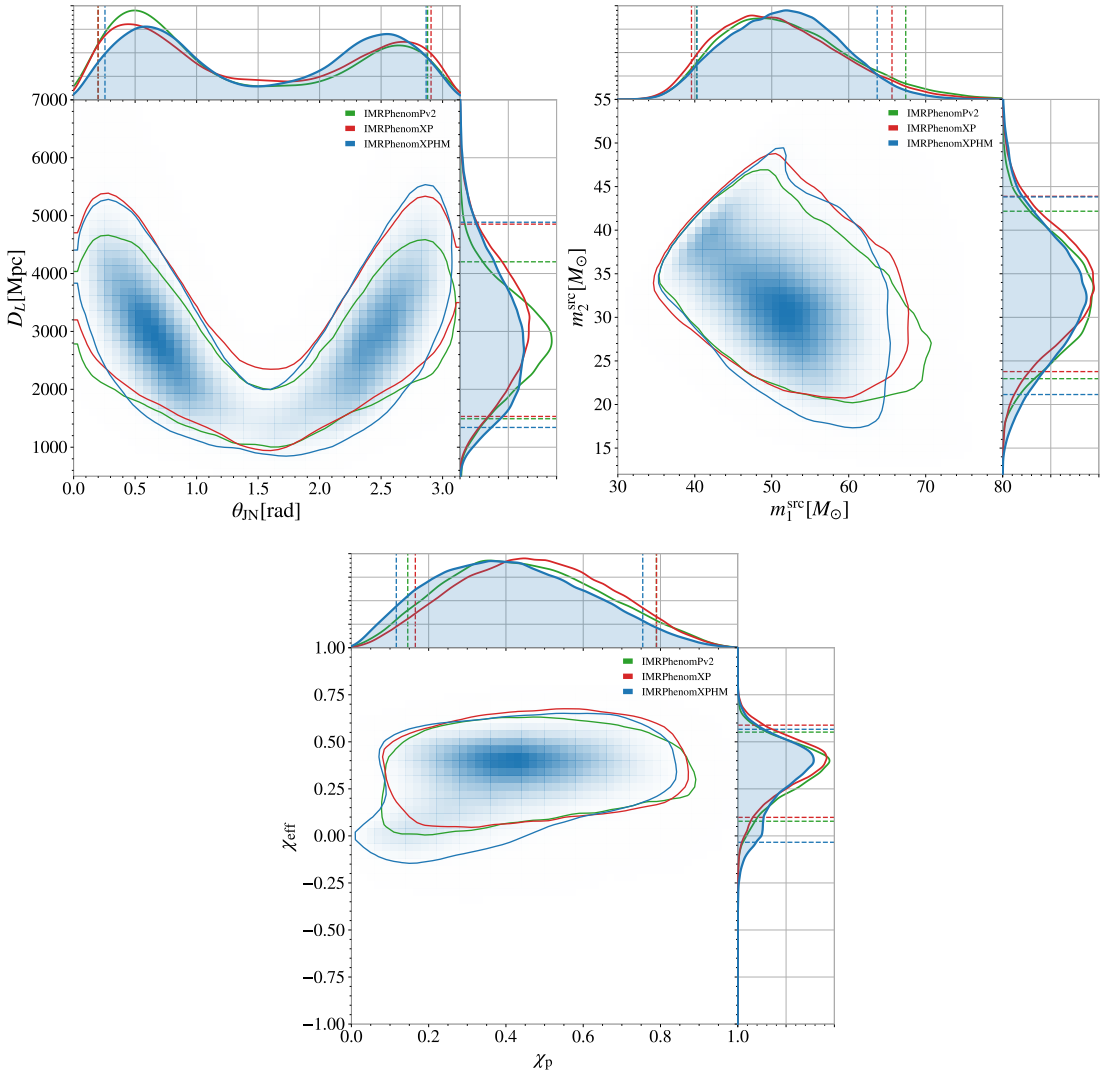

FIGURE 5.11: Bayesian inference results for GW170729: Posterior probability distributions for the effective spin parameters $\chi_{\rm eff}$ and χ_p, the component masses m_1 and m_2, distance D_L and the angle θ_{JN} between angular momentum and line of sight. The 90 % credible intervals are represented by vertical (contour) lines in the 1D (2D) plots.

models IMRPHENOMXHM in [3] and found consistency with the results in [95]. Furthermore, there have been investigations of this event with precessing waveform models, in [39] with IMRPHENOMPV2 and in [15, 16] with IMRPHENOMPV3 and IMRPHENOMPV3HM.

Here we report on the analysis of GW170729 with our new precessing IMRPHENOMXPHM model, which upgrades IMRPHENOMPV3HM. For our analysis we use 4 s of the publicly available strain data from the GWOSC [88, 89] with a lower cutoff frequency of 20 Hz. This data is calibrated by a cubic spline and we use the same PSDs utilized in [39]. We analyze the strain with the Python-based Bayesian inference framework `Parallel Bilby` [87], which uses a parallel version of the nested sampling code `Dynesty` [86]. We carry out the PE runs using 4096 live points, choose the maximum number of

MCMC steps to take as 10^4, and require 10 auto-correlation times (ACT) before accepting a point. We merge results from four different seeds in order to get a single posterior distribution. The simulations are performed for the default options of the LALSuite implementation of IMRPhenomXPHM (the precessing version 223, final spin version 3 and convention 1, see appendix 5.F). The priors are the same as used in [95] but adapted to precessing models.

NR Simulation	Version	$m_1/M_\odot$	$m_2/M_\odot$	$\mathcal{M}_c/M_\odot$	q	D_L/Mpc	$\chi_{\rm eff}$	$\chi_{\rm p}$	$\theta_{\rm JN}$ (rad)
SXS:BBH:0143	v102 FS0	$65.78^{+2.24}_{-2.40}$	$34.27^{+1.54}_{-1.54}$	$40.89^{+0.67}_{-0.69}$	$0.52^{+0.04}_{-0.04}$	504^{+87}_{-91}	$0.26^{+0.04}_{-0.04}$	$0.24^{+0.06}_{-0.06}$	$1.04^{+0.10}_{-0.10}$
	v102 FS1	$65.86^{+2.21}_{-2.36}$	$34.18^{+1.53}_{-1.52}$	$40.86^{+0.67}_{-0.68}$	$0.52^{+0.04}_{-0.04}$	515^{+92}_{-92}	$0.26^{+0.05}_{-0.04}$	$0.25^{+0.06}_{-0.08}$	$1.03^{+0.12}_{-0.11}$
	v102 FS2	$65.71^{+2.24}_{-2.43}$	$34.30^{+1.57}_{-1.59}$	$40.90^{+0.69}_{-0.69}$	$0.52^{+0.04}_{-0.04}$	506^{+89}_{-92}	$0.26^{+0.04}_{-0.04}$	$0.24^{+0.06}_{-0.07}$	$1.04^{+0.11}_{-0.11}$
	v223 FS2	$65.46^{+2.22}_{-2.39}$	$34.34^{+1.59}_{-1.59}$	$40.85^{+0.70}_{-0.70}$	$0.52^{+0.03}_{-0.04}$	516^{+93}_{-97}	$0.26^{+0.04}_{-0.04}$	$0.24^{+0.09}_{-0.10}$	$1.01^{+0.12}_{-0.11}$
	v223 FS3	$65.39^{+2.21}_{-2.39}$	$34.37^{+1.55}_{-1.58}$	$40.85^{+0.67}_{-0.69}$	$0.53^{+0.04}_{-0.04}$	513^{+92}_{-98}	$0.26^{+0.04}_{-0.04}$	$0.24^{+0.09}_{-0.09}$	$1.01^{+0.12}_{-0.11}$
	Injected	65.77	34.26	40.88	0.52	430	0.26	0.21	1.12
SXS:BBH:0165	v102 FS0	$85.85^{+2.31}_{-2.86}$	$14.26^{+0.56}_{-0.47}$	$28.35^{+0.29}_{-0.27}$	$0.17^{+0.02}_{-0.01}$	433^{+23}_{-26}	$-0.44^{+0.02}_{-0.03}$	$0.78^{+0.05}_{-0.04}$	$0.35^{+0.03}_{-0.03}$
	v102 FS1	$85.88^{+2.81}_{-3.83}$	$14.27^{+0.69}_{-0.54}$	$28.36^{+0.33}_{-0.28}$	$0.17^{+0.02}_{-0.01}$	444^{+34}_{-40}	$-0.43^{+0.04}_{-0.03}$	$0.78^{+0.06}_{-0.05}$	$0.35^{+0.03}_{-0.04}$
	v102 FS2	$85.54^{+2.23}_{-2.87}$	$14.30^{+0.56}_{-0.47}$	$28.35^{+0.29}_{-0.27}$	$0.17^{+0.01}_{-0.01}$	433^{+24}_{-26}	$-0.44^{+0.02}_{-0.03}$	$0.78^{+0.05}_{-0.04}$	$0.35^{+0.03}_{-0.03}$
	v223 FS2	$84.79^{+2.96}_{-3.23}$	$14.42^{+0.61}_{-0.61}$	$28.39^{+0.37}_{-0.34}$	$0.17^{+0.01}_{-0.01}$	442^{+29}_{-32}	$-0.44^{+0.04}_{-0.04}$	$0.77^{+0.03}_{-0.04}$	$0.36^{+0.08}_{-0.09}$
	v223 FS3	$84.72^{+2.94}_{-3.22}$	$14.44^{+0.62}_{-0.59}$	$28.40^{+0.37}_{-0.34}$	$0.17^{+0.01}_{-0.01}$	442^{+29}_{-32}	$-0.44^{+0.04}_{-0.04}$	$0.77^{+0.03}_{-0.04}$	$0.36^{+0.08}_{-0.09}$
	Injected	85.73	14.28	28.36	0.17	430	-0.44	0.78	0.35

TABLE 5.2: Black hole binary recovered parameters for two injected NR waveforms from Figs. 5.12 and 5.13. The first column shows the identifier of the injected NR waveform, then we specify the version of the IMRPhenomXPHM model, the component masses (m_1, m_2), chirp mass $\mathcal{M}_c$, mass ratio $q(=m_2/m_1)$, luminosity distance D_L, effective spin parameter $\chi_{\rm eff}$, effective precessing spin parameter $\chi_{\rm p}$, and the angle between the total angular momentum and the line of sight, $\theta_{\rm JN}$. For each NR waveform the injected values are also displayed.

We have analyzed this event with the non-precessing IMRPhenomXAS and IMRPhenomXHM models in [10], where we have also compared with results available in the literature and obtained with other non-precessing models. Our results based on the MSA versions of IMRPhenomXP and IMRPhenomXPHM are shown in Fig. 5.11, and compared with the IMRPhenomPv2 model that is routinely used for PE, but lacks higher modes. We show posteriors for the effective spin parameters $\chi_{\rm eff}$ and χ_p, the component masses, distance D_L and the angle θ_{JN} between total angular momentum and line of sight.

The results show agreement between the new IMRPhenomXP model and the old IMRPhenomPv2 model, although small differences in the shape of the posterior distributions are due to the inclusion of double-spin effects in IMRPhenomXP. The inclusion of higher-order modes produces a shift in the posterior distributions of some quantities like the primary component mass. These changes in some parameters due to the inclusion of precessing higher-order modes are consistent with those observed in [16] for this particular event.

5.5.6.3 Numerical relativity injections

We test for possible PE bias with our model by applying Bayesian inference to recover zero-noise injections of two public binary black hole NR simulations from the first SXS waveform catalogue [64]. We choose `SXS:BBH:0143` corresponding to a mass ratio 2 simulation with positive $\chi_{\rm eff}$ and small χ_p, and `SXS:BBH:0165`, a mass ratio 6 simulation with negative $\chi_{\rm eff}$ and high χ_p. We set a total mass for both injected waveforms of 100 $M_\odot$ and a luminosity distance of 430 Mpc, which results in signal-to-noise ratios of 52 and 26 for `SXS:BBH:0143` and `SXS:BBH:0165`, respectively. We analyze a 4 s segment of data with a lower cutoff frequency of 20 Hz. The parameters of the injected waveforms are listed in Table 5.2, together with the recovery results as discussed below.

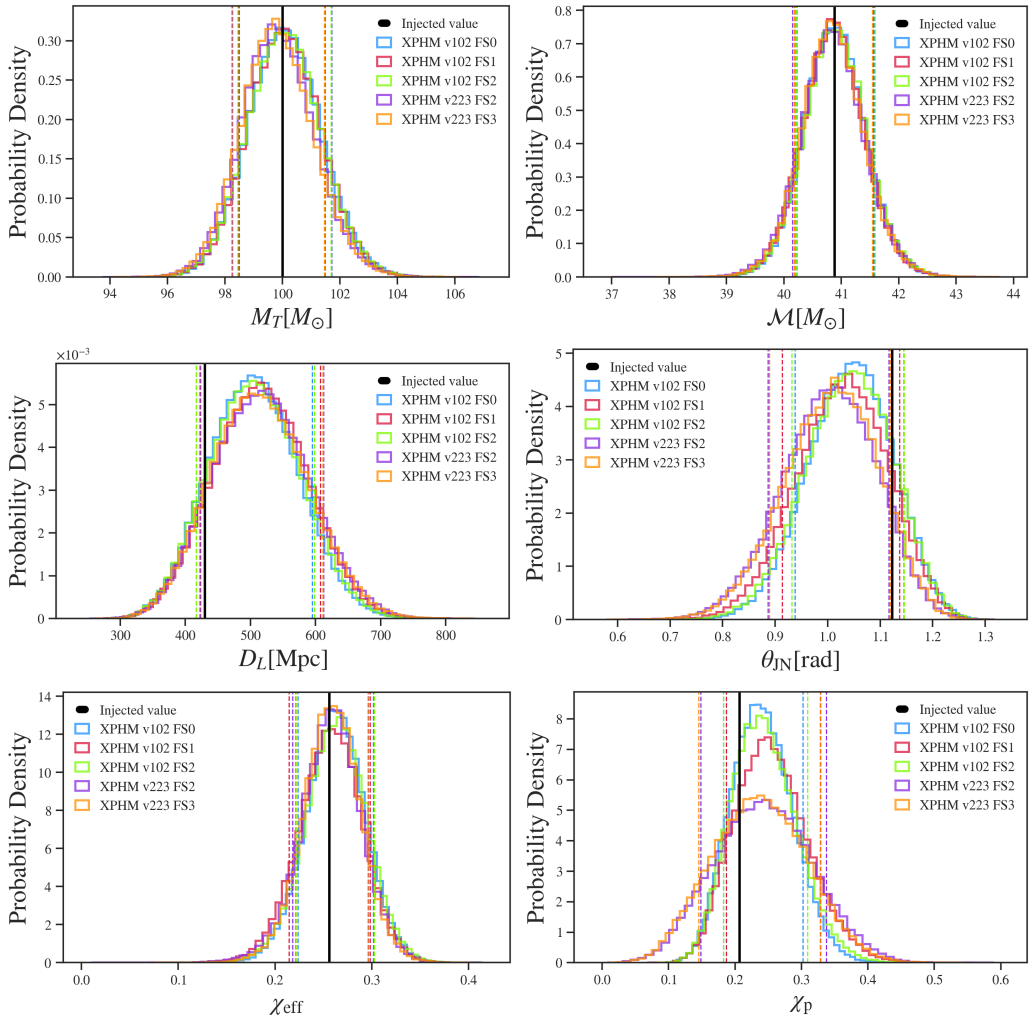

FIGURE 5.12: Injection recovery results for `SXS:BBH:0143`. Top row: posterior probability distributions for the total mass in the detector frame and the chirp mass. Middle row: posterior probability distributions for the luminosity distance and the angle $\theta_{\rm JN}$ between the total angular momentum and line of sight. Bottom row: posterior probability distributions for χ_p and $\chi_{\rm eff}$. The dashed vertical lines represent 90 % credible intervals, while the thick black lines represent the injected value. The notation for the different versions of IMRPHENOMXPHM is described in appendix 5.F.

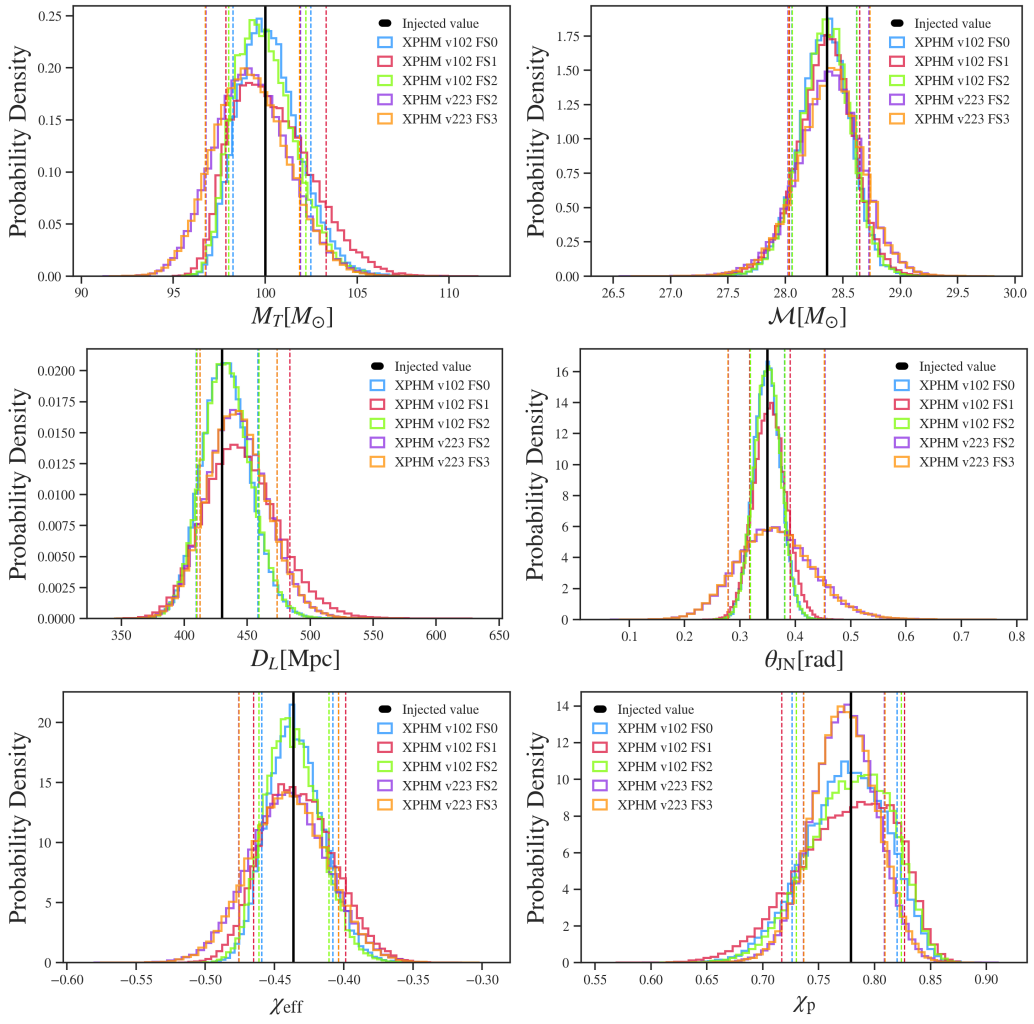

FIGURE 5.13: Injection recovery results for `SXS:BBH:0165`. All panels are the same as in Fig. 5.12.

As for our analysis of GW170729 above, we use the `Parallel Bilby` code [87] with the `Dynesty` [86] nested sampler. We perform these runs using 2048 live points, 5 ACTs and marginalization over time and distance.

We set the prior distributions for the source parameters as follows: For the first injection of `SXS:BBH:0143`, we restrict to mass ratios up to $q = 8$, and the chirp mass prior is assumed uniform between 30 and 55 $M_\odot$. The component masses are constrained to be between 10 and 80 $M_\odot$. The luminosity distance is uniform in volume with maximal distance at 2000 Mpc. For the `SXS:BBH:0165` injection, we allow mass ratios up to $q = 1000$ and set a chirp mass prior uniform between 20 and 40 $M_\odot$. The component masses are constrained to be between 50 and 100 $M_\odot$ and between 1 and 30 $M_\odot$ respectively. The luminosity distance prior is again chosen as uniform in volume with a maximal allowed distance at 2000 Mpc. For both injection recoveries dimensionless spin magnitudes are allowed up to the extreme Kerr limit.

In Figs. 5.12 and 5.13 we show 1D probability distributions for the main parameters for the injected `SXS:BBH:0143` and `SXS:BBH:0165` waveforms using different versions of the IMRPhenomXPHM model as the model waveform. The mean values of the recovered parameters for the different versions of the IMRPhenomXPHM model for both injected NR waveforms are reported in Table 5.2. In both figures one observes that the model is able to successfully recover all the source parameters.

Particularly in Fig 5.12, corresponding to the injection of `SXS:BBH:0143`, we observe that the differences between the several versions of the models are very small except for χ_p and the angle $\theta_{\rm JN}$ between the total angular momentum and the line of sight. This is expected as the injected waveform has small mass ratio and χ_p values and, hence, precession effects are not so relevant, although one can already appreciate that the χ_p and $\theta_{\rm JN}$ parameters are sensitive to the different modelling strategies.

For a higher mass ratio and χ_p case like `SXS:BBH:0165`, the posterior distributions between different versions of IMRPhenomXPHM show increased differences for more parameters, as shown in Fig. 5.13. Still, all versions are able to recover the injected values within the estimated statistical error bars. Variants of option 223 with different final spin modifications (see appendix 5.F for a description of the notation) provide very similar posteriors with slight differences in the mass parameters. This indicates that the double-spin effects in the Euler angles provide a good recovery of the parameters, and that here the different final spin prescriptions correspond to a subdominant effect. However, we find that for version 102 the different final spin modifications do have a larger impact on the shape of the posterior distributions in this case. A systematic study of the effects of final spin prescription goes beyond the scope of this work, and will be pursued in the future, along with further improvements of the model.

We also note that `SXS:BBH:0165` corresponds to the NR waveform that is responsible for the highest mismatch in Fig. 5.4. The results obtained in Fig. 5.13 show that even for a case with a high mismatch our models can accurately recover the injected source parameters. This observation illustrates that results for mismatches only give an indication of waveform quality, but do not provide a reliable prediction of performance for PE. As a result, we observe that our models have the freedom to adapt for the missing information at merger, due to the non-calibration to precessing NR simulations, to accurately reproduce the injected parameters for a challenging precessing configuration.

5.6 Conclusions

With this paper we conclude the construction of a first version of the IMRPhenomX waveform family for coalescences of non-eccentric binary black holes. We have shown that including subdominant harmonics and precession in a waveform model does not have to come at the expense of evaluation speed. This opens up the possibility to routinely perform PE for the larger numbers of events observed as gravitational wave detector sensitivity increases without neglecting subdominant harmonics and precession.

Our model and its LALSuite implementation have been designed with flexibility and modularity as key design elements, not only in order to incorporate future improvements, but also to allow a wide range of computational experiments – as a first application we have shown PE studies that compare different prescriptions for the final spin.

A number of further improvements are foreseen: first, the increasing number and quality of NR waveforms will allow to calibrate further non-precessing subdominant harmonics to NR, e.g. the $(5, 5)$ and $(4, 3)$ modes, and to further increase the quality of the model for non-precessing waveforms.

Regarding precession, several challenges need to be addressed (see also [22]): First, it will be desirable to develop a computationally inexpensive numerical fit for the final spin of precessing coalescences. Another natural extension will be to develop a phenomenological ansatz for the Euler angle description, and calibrate it to NR. Other challenges are the development and calibration of a phenomenological description for the complete precessing waveform for the merger and ringdown, where the SPA approximation is invalid, and which should also include the asymmetries responsible for large recoils [21]. Finally, we note that precession is currently measured in PE in terms of the parameter χ_p, which is motivated by the NNLO inspiral description, and it is likely to be fruitful to also consider other parameters in the future.

Some of these challenges will be difficult to address in the frequency domain, and we foresee synergies between the development of time domain and frequency domain approaches. As a first step we have constructed IMRPhenomTP, a time domain version of the ideas underlying the IMRPhenomXP model, which is aimed to serve as a tool to better understand and remedy current shortcomings of our construction, and is presented in [42]. We expect our code to be sufficiently flexible to serve as a basis for a future implementation of the IMRPhenomTP model.

Planned extensions regard the incorporation of eccentricity, and of matter effects along the lines of [97–99]. We note that the accelaration technique of multibanding is particularly important for lower-mass systems like binary neutron star and black hole–neutron

star systems. Finally we note that our code implementation leaves much room for increasing computational efficiency, e.g. by utilizing GPUs.

Acknowledgements

This work was supported by European Union FEDER funds, the Ministry of Science, Innovation and Universities and the Spanish Agencia Estatal de Investigación grants FPA2016-76821-P, RED2018-102661-T, RED2018-102573-E, FPA2017-90687-REDC, Vicepresid'encia i Conselleria d'Innovació, Recerca i Turisme, Conselleria d'Educació, i Universitats del Govern de les Illes Balears i Fons Social Europeu, Generalitat Valenciana (PROMETEO/2019/071), EU COST Actions CA18108, CA17137, CA16214, and CA16104, and the Spanish Ministry of Education, Culture and Sport grants FPU15/03344 and FPU15/01319. M.C. acknowledges funding from the European Union's Horizon 2020 research and innovation programme, under the Marie Skłodowska-Curie grant agreement No. 751492. M.H. acknowledges support from Swiss National Science Foundation (SNSF) grant IZCOZ0-177057. D.K. is supported by the Spanish Ministerio de Ciencia, Innovación y Universidades (ref. BEAGAL 18/00148) and cofinanced by the Universitat de les Illes Balears. J.T. was supported by the Science and Technology Facilities Council (STFC) grant ST/L000962/1 and by the European Research Council Consolidator Grant 647839. The authors thankfully acknowledge the computer resources at MareNostrum and the technical support provided by Barcelona Supercomputing Center (BSC) through Grants No. AECT-2019-2-0010, AECT-2019-1-0022, AECT-2019-1-0014, AECT-2018-3-0017, AECT-2018-2-0022, AECT-2018-1-0009, AECT-2017-3-0013, AECT-2017-2-0017, AECT-2017-1-0017, AECT-2016-3-0014, AECT2016-2-0009, from the Red Española de Supercomputación (RES) and PRACE (Grant No. 2015133131). BAM and Einstein Toolkit simulations were carried out on the BSC MareNostrum computer under PRACE and RES (Red Española de Supercomputación) allocations and on the FONER computer at the University of the Balearic Islands. Authors also acknowledge the computational resources at the cluster CIT provided by LIGO Laboratory and supported by National Science Foundation Grants PHY-0757058 and PHY-0823459, as well as the cluster HAWK provided by Cardiff University and supported by STFC grant ST/I006285/1. This research has made use of data obtained from the Gravitational Wave Open Science Center [88], a service of LIGO Laboratory, the LIGO Scientific Collaboration and the Virgo Collaboration. LIGO is funded by the U.S. National Science Foundation. Virgo is funded by the French Centre National de Recherche Scientifique (CNRS), the Italian Istituto Nazionale della Fisica Nucleare (INFN) and the Dutch Nikhef, with contributions by Polish and Hungarian institutes.

Appendices

5.A Wigner-d Matrices

The real-valued Wigner-d matrices are defined by [30, 100]

$$d^{\ell}_{mm'}(\beta) = \sum_{k=k_{\min}}^{k_{\max}} \frac{(-1)^k}{k!} \frac{\sqrt{(l+m)!(l-m)!\,(l+m')!\,(l-m')!}}{(l+m-k)!\,(l-m'-k)!\,(k-m+m')!} \tag{5.53}$$

$$\cdot \left(\cos\frac{\beta}{2}\right)^{2\ell+m-m'-2k} \left(\sin\frac{\beta}{2}\right)^{2k-m+m'}, \tag{5.54}$$

with $k_{\min} = \max(0, m-m')$ and $k_{\max} = \min(\ell+m, \ell-m')$, where analogous expressions for $d^{\ell}_{m-m'}$ can be constructed using the symmetry of the Wigner d-matrices

$$d^{\ell}_{-m-m'} = (-1)^{(m-m')} d^{\ell}_{mm'}, \tag{5.55}$$

$$d^{\ell}_{mm'}(\beta) = (-1)^{m+m'}\, d^{\ell}_{m'm}(\beta), \tag{5.56}$$

$$d^{\ell}_{mm'}(\beta) = d^{\ell}_{m'm}(-\beta). \tag{5.57}$$

Here we provide explicit expressions for the Wigner $d^{\ell}_{mm'}(\beta)$ matrices for all modes involved in the underlaying non-precessing model. We also include the 43 mode since it is used by the option that twists IMRPhenomHM.

$\ell = 2,\ m' = 2$

$$\begin{aligned}
d^{2}_{22}(\beta) &= \cos^4\frac{\beta}{2}, \\
d^{2}_{12}(\beta) &= 2\,\cos^3\frac{\beta}{2}\,\sin\frac{\beta}{2}, \\
d^{2}_{02}(\beta) &= \sqrt{6}\,\cos^2\frac{\beta}{2}\,\sin^2\frac{\beta}{2}, \\
d^{2}_{-12}(\beta) &= 2\,\cos\frac{\beta}{2}\,\sin^3\frac{\beta}{2}, \\
d^{2}_{-22}(\beta) &= \sin^4\frac{\beta}{2}.
\end{aligned}$$

$\ell = 2,\ m' = 1$

$$
\begin{aligned}
d^2_{21}(\beta) &= -2\ \cos^3\frac{\beta}{2}\ \sin\frac{\beta}{2},\\
d^2_{11}(\beta) &= \cos^2\frac{\beta}{2}\left(\cos^2\frac{\beta}{2} - 3\sin^2\frac{\beta}{2}\right),\\
d^2_{01}(\beta) &= \sqrt{6}\ \left(\cos^3\frac{\beta}{2}\sin\frac{\beta}{2} - \cos\frac{\beta}{2}\sin^3\frac{\beta}{2}\right),\\
d^2_{-11}(\beta) &= \sin^2\frac{\beta}{2}\left(3\cos^2\frac{\beta}{2} - \sin^2\frac{\beta}{2}\right),\\
d^2_{-21}(\beta) &= 2\ \cos\frac{\beta}{2}\ \sin^3\frac{\beta}{2}.
\end{aligned}
$$

$\ell = 3,\ m' = 3$

$$
\begin{aligned}
d^3_{33}(\beta) &= \cos^6\frac{\beta}{2},\\
d^3_{23}(\beta) &= \sqrt{6}\ \cos^5\frac{\beta}{2}\ \sin\frac{\beta}{2},\\
d^3_{13}(\beta) &= \sqrt{15}\ \cos^4\frac{\beta}{2}\ \sin^2\frac{\beta}{2},\\
d^3_{03}(\beta) &= 2\sqrt{5}\ \cos^3\frac{\beta}{2}\ \sin^3\frac{\beta}{2},\\
d^3_{-13}(\beta) &= \sqrt{15}\ \cos^2\frac{\beta}{2}\ \sin^4\frac{\beta}{2},\\
d^3_{-23}(\beta) &= \sqrt{6}\ \cos\frac{\beta}{2}\ \sin^5\frac{\beta}{2},\\
d^3_{-33}(\beta) &= \sin^6\frac{\beta}{2}.
\end{aligned}
$$

$\ell = 3,\ m' = 2$

$$
\begin{aligned}
d^3_{32}(\beta) &= -\sqrt{6}\ \cos^5\frac{\beta}{2}\ \sin\frac{\beta}{2},\\
d^3_{22}(\beta) &= \cos^4\frac{\beta}{2}\left(\cos^2\frac{\beta}{2} - 5\sin^2\frac{\beta}{2}\right),\\
d^3_{12}(\beta) &= \sqrt{10}\cos^3\frac{\beta}{2}\left(\cos^2\frac{\beta}{2}\sin\frac{\beta}{2} - 2\sin^3\frac{\beta}{2}\right)\\
d^3_{02}(\beta) &= \sqrt{30}\cos^2\frac{\beta}{2}\sin^2\frac{\beta}{2}\left(\cos^2\frac{\beta}{2} - \sin^2\frac{\beta}{2}\right),\\
d^3_{-12}(\beta) &= \sqrt{10}\sin^3\frac{\beta}{2}\left(2\cos^3\frac{\beta}{2} - \cos\frac{\beta}{2}\sin^2\frac{\beta}{2}\right),\\
d^3_{-22}(\beta) &= \sin^4\frac{\beta}{2}\left(5\cos^2\frac{\beta}{2} - \sin^2\frac{\beta}{2}\right),
\end{aligned}
$$

$$d^3_{-32}(\beta) = \sqrt{6}\cos\frac{\beta}{2}\,\sin^5\frac{\beta}{2}.$$

$\ell = 4,\ m' = 4$

$$\begin{aligned}
d^4_{44}(\beta) &= \cos^8\frac{\beta}{2},\\
d^4_{34}(\beta) &= 2\sqrt{2}\,\cos^7\frac{\beta}{2}\,\sin\frac{\beta}{2},\\
d^4_{24}(\beta) &= 2\sqrt{7}\,\cos^6\frac{\beta}{2}\,\sin^2\frac{\beta}{2},\\
d^4_{14}(\beta) &= 2\sqrt{14}\,\cos^5\frac{\beta}{2}\,\sin^3\frac{\beta}{2},\\
d^4_{04}(\beta) &= \sqrt{70}\,\cos^4\frac{\beta}{2}\,\sin^4\frac{\beta}{2},\\
d^4_{-14}(\beta) &= 2\sqrt{14}\,\cos^3\frac{\beta}{2}\,\sin^5\frac{\beta}{2},\\
d^4_{-24}(\beta) &= 2\sqrt{7}\,\cos^2\frac{\beta}{2}\,\sin^6\frac{\beta}{2},\\
d^4_{-34}(\beta) &= 2\sqrt{2}\,\cos\frac{\beta}{2}\,\sin^7\frac{\beta}{2},\\
d^4_{-44}(\beta) &= \sin^8\frac{\beta}{2}.
\end{aligned}$$

$\ell = 4,\ m' = 3$

$$\begin{aligned}
d^4_{43}(\beta) &= -2\sqrt{2}\sin\left(\frac{\beta}{2}\right)\cos^{\,7}\left(\frac{\beta}{2}\right),\\
d^4_{33}(\beta) &= \cos^8\left(\frac{\beta}{2}\right) - 7\sin^2\left(\frac{\beta}{2}\right)\cos^6\left(\frac{\beta}{2}\right),\\
d^4_{23}(\beta) &= \sqrt{14}\sin\left(\frac{\beta}{2}\right)\cos^7\left(\frac{\beta}{2}\right) - 3\sqrt{14}\sin^3\left(\frac{\beta}{2}\right)\cos^{\,5}\left(\frac{\beta}{2}\right),\\
d^4_{13}(\beta) &= 3\sqrt{7}\sin^2\left(\frac{\beta}{2}\right)\cos^{\,6}\left(\frac{\beta}{2}\right) - 5\sqrt{7}\sin^4\left(\frac{\beta}{2}\right)\cos^4\left(\frac{\beta}{2}\right),\\
d^4_{03}(\beta) &= 2\sqrt{35}\sin^3\left(\frac{\beta}{2}\right)\cos^{\,5}\left(\frac{\beta}{2}\right) - 2\sqrt{35}\sin^5\left(\frac{\beta}{2}\right)\cos^3\left(\frac{\beta}{2}\right),\\
d^4_{-13}(\beta) &= 5\sqrt{7}\sin^4\left(\frac{\beta}{2}\right)\cos^{\,4}\left(\frac{\beta}{2}\right) - 3\sqrt{7}\sin^6\left(\frac{\beta}{2}\right)\cos^2\left(\frac{\beta}{2}\right),\\
d^4_{-23}(\beta) &= 3\sqrt{14}\sin^5\left(\frac{\beta}{2}\right)\cos^{\,3}\left(\frac{\beta}{2}\right) - \sqrt{14}\sin^7\left(\frac{\beta}{2}\right)\cos\left(\frac{\beta}{2}\right),\\
d^4_{-33}(\beta) &= 7\sin^6\left(\frac{\beta}{2}\right)\cos^2\left(\frac{\beta}{2}\right) - \sin^8\left(\frac{\beta}{2}\right),\\
d^4_{-43}(\beta) &= 2\sqrt{2}\sin^7\left(\frac{\beta}{2}\right)\cos\left(\frac{\beta}{2}\right).
\end{aligned}$$

5.B Conventions for non-Precessing Modes

In the precessing L-frame we can decompose the gravitational wave strain into spherical harmonic modes $h_{\ell m}$ as

$$h^L = \sum_{\ell=2,\, m=-\ell}^{4,\ell} h^L_{\ell m}(t)\ {}_{-2}Y^L_{\ell m}, \tag{5.58}$$

where the ${}_{-2}Y^L_{\ell m}$ are spherical harmonics in the precessing L-frame defined in Sec. 5.C. In our twisting approximation we identify the modes $h^L_{\ell m}$ in the non-inertial precessing frame with the spherical harmonic modes described by the non-precessing IMRPhenomXAS and IMRPhenomXHM models, which are however modified by changing the complex ringdown frequencies in the waveform to be consistent with the estimate for the precessing final spin, which we have described in Sec. 5.4.4.

The time domain modes can be written in terms of positive amplitudes $a_{\ell m}(t)$ and phases $\phi_{\ell m}(t)$ such that

$$h^L_{\ell m}(t) = a_{\ell m}(t) e^{-i\phi_{\ell m}(t)}, \tag{5.59}$$

where we assume that the phase of the aligned-spin modes is a monotonically increasing function of t

$$\dot{\phi}_{\ell m}(t) > 0. \tag{5.60}$$

As discussed in detail in [10] there are only two inequivalent choices of tetrad convention that are consistent with equatorial symmetry, and for simplicity we adopt the convention that for low frequencies the time domain phases satisfy

$$\Phi_{\ell m} \approx \frac{m}{2}\Phi_{22}. \tag{5.61}$$

This differs from the convention of Blanchet et al. [101] by overall factors of $(-1)(-\iota)^m$ in front of the $h^L_{\ell m}$ modes.

The equatorial symmetry of non-precessing binaries implies

$$h^L_{\ell m}(t) = (-1)^\ell h^{*L}_{\ell -m}(t). \tag{5.62}$$

With our conventions for the Fourier transform (5.3), the time domain relations between modes (5.62) that express equatorial symmetry can be converted to the Fourier domain, where they read

$$\tilde{h}^L_{\ell m}(f) = (-1)^\ell \tilde{h}^{*L}_{\ell -m}(-f). \tag{5.63}$$

The definitions above then also imply that $\tilde{h}^L_{\ell m}(f)$ (with $m > 0$) is concentrated in the negative frequency domain and $\tilde{h}^L_{\ell -m}(f)$ in the positive frequency domain.

The Fourier amplitudes $A_{\ell m}(f > 0)$ are then non-negative functions for positive frequencies, and zero otherwise, and the Fourier domain phases $\Phi_{\ell m}(f > 0)$, defined by

$$\tilde{h}^L_{\ell -m}(f) = A_{\ell m}(f)\, e^{-i\Phi_{\ell m}(f)}. \tag{5.64}$$

5.C Frames Transformations and Polarization Basis

We construct our waveform model in terms of a transformation from spherical harmonics $h^L_{\ell m}$ in the precessing L-frame to spherical harmonics $h^J_{\ell m}$ in the inertial J-frame. The input to our model consists of intrinsic parameters that specify the masses and spin vectors of the binary system, and extrinsic parameters which describe the location of the source and its spatial orientation relative to the frame of the observer, which we have chosen to refer to as the N-frame, where $\hat{\mathbf{N}}$ is the direction from the source to the observer.

We need to guarantee that our model returns an unambiguous waveform for given values of the intrinsic and extrinsic parameters, in particular we carefully need to specify in which coordinate system we specify the spin vectors, and how to specify the spatial orientation of the source as needed to define all extrinsic parameters. To this end, in this section we will discuss the relation between the different coordinate frames we are using, and identify a complete set of input parameters.

We will work with three inertial frames, which we have introduced in Sec. 5.2: the L_0-frame, the J-frame and N-frame or wave frame. These three frames will have their z-axis aligned with $\mathbf{L_0}$, $\mathbf{J}$ and $\hat{\mathbf{N}}$ respectively, and they do not evolve in time. The L_0-frame will also be referred to as the source frame, since in accordance with the LALSuite software infrastructure the IMRPhenomXP and IMRPhenomXPHM models parameterize the two spin vectors of the black holes by Cartesian components in this frame.

In addition to the three inertial frames we will consider the non-inertial L-frame that tracks the precession of the orbital plane, and coincides with the L_0-frame at a chosen reference frequency f_{ref}. Choosing a different value for f_{ref} while fixing the initial spin components, which we have chosen to specify with respect to the L_0-frame, will thus in general corresponds to a different waveform.

We will denote the triads of our frames by $\{\hat{\mathbf{x}}_{\mathbf{L_0}}, \hat{\mathbf{y}}_{\mathbf{L_0}}, \hat{\mathbf{z}}_{\mathbf{L_0}}\}$, $\{\hat{\mathbf{x}}_{\mathbf{L}}, \hat{\mathbf{y}}_{\mathbf{L}}, \hat{\mathbf{z}}_{\mathbf{L}}\}$, $\{\hat{\mathbf{x}}_{\mathbf{J}}, \hat{\mathbf{y}}_{\mathbf{J}}, \hat{\mathbf{z}}_{\mathbf{J}}\}$ and $\{\hat{\mathbf{x}}_{\hat{\mathbf{N}}}, \hat{\mathbf{y}}_{\hat{\mathbf{N}}}, \hat{\mathbf{z}}_{\hat{\mathbf{N}}}\}$ and choose the z-axes as

$$\hat{\mathbf{z}}_{\mathbf{L_0}} = \hat{\mathbf{L}}_0, \quad \hat{\mathbf{z}}_{\mathbf{L}} = \hat{\mathbf{L}}, \quad \hat{\mathbf{z}}_{\mathbf{J}} = \hat{\mathbf{J}}, \quad \hat{\mathbf{z}}_{\hat{\mathbf{N}}} = \hat{\mathbf{N}}. \tag{5.65}$$

Note that the $\hat{\mathbf{x}}_{\mathbf{L_0}} - \hat{\mathbf{y}}_{\mathbf{L_0}}$ plane correspond to initial orbital plane.

For clarity, in what follows we will provide explicit expressions for the vectors $\hat{\mathbf{L}}_0, \hat{\mathbf{N}}, \mathbf{J}$ in the L_0 and J-frames. We will write the components of a generic vector $\mathbf{u}$ in a particular frame as

$$\mathbf{u} \doteq \begin{pmatrix} u_{x,frame} \\ u_{y,frame} \\ u_{z,frame} \end{pmatrix}_{frame}, \tag{5.66}$$

e.g. the vector $\mathbf{J}$ will have the following components in the L_0 frame

$$\mathbf{J} \doteq \begin{pmatrix} J_{x,L_0} \\ J_{y,L_0} \\ J_{z,L_0} \end{pmatrix}_{L_0}. \tag{5.67}$$

So far we have characterized our three inertial coordinate frames by the choice of z-axis, and we have defined the precessing L-frame as the time evolution of the L_0-frame. We now need to complete our definitions of the three inertial frames by fixing the freedom of rotations around the axes, which precisely corresponds to the freedom of specifying three Euler angles to fix a spatial rotation. In the L_0 frame, which we have chosen as the frame where we parametrize our input spin components, we choose the line of sight $\hat{\mathbf{N}}$ to have spherical angles $\left(\iota, \frac{\pi}{2} - \phi_{ref}\right)$, which is chosen to adopt to the conventions of [17], where this choice corresponds to Eq. (31c) and setting the angle Φ in this equation to $\Phi = \phi_{ref}$. We call ι the inclination of the system, and interpret ϕ_{ref} as fixing the freedom of rotations in the orbital plane. We treat ι and ϕ_{ref} as input parameters that the user specifies when calling the waveform model.

In the L_0 frame the components of $\hat{\mathbf{N}}$ are thus

$$\hat{\mathbf{N}} \doteq \begin{pmatrix} \sin\iota \cos\left(\frac{\pi}{2} - \phi_{ref}\right) \\ \sin\iota \sin\left(\frac{\pi}{2} - \phi_{ref}\right) \\ \cos\iota \end{pmatrix}_{L_0}, \tag{5.68}$$

while the vector $\mathbf{J}$ reads

$$\mathbf{J} \doteq \begin{pmatrix} m_1^2\chi_{1x} + m_2^2\chi_{2x} \\ m_1^2\chi_{1y} + m_2^2\chi_{2y} \\ L_0 + m_1^2\chi_{1z} + m_2^2\chi_{2z} \end{pmatrix}_{L_0} . \tag{5.69}$$

From the above equation it follows that the spherical angles $(\theta_{JL_0}, \phi_{JL_0})$ of $\mathbf{J}$ in this frame are given by:

$$\theta_{JL_0} = \arccos \frac{J_{z,L_0}}{|\mathbf{J}|} = \arccos \frac{L_0 + m_1^2\chi_{1z} + m_2^2\chi_{2z}}{|\mathbf{J}|}, \tag{5.70}$$

$$\phi_{JL_0} = \arctan \frac{J_{y,L_0}}{J_{x,L_0}} = \arctan \frac{m_1^2\chi_{1y} + m_2^2\chi_{2y}}{m_1^2\chi_{1x} + m_2^2\chi_{2x}}. \tag{5.71}$$

We will now turn to describing the J-frame. We will fix the orientation of the axes in this frame by requiring that the line of sight $\hat{\mathbf{N}}$ lies in the $\hat{\mathbf{x}}_\mathbf{J} - \mathbf{J}$ plane and has positive projection on the $\hat{\mathbf{x}}_\mathbf{J}$-axis. If we denote by θ_{JN} the angle between $\hat{\mathbf{N}}$ and the $\hat{\mathbf{z}}_\mathbf{J}$ axis, this choice implies

$$\hat{\mathbf{N}} \doteq \begin{pmatrix} \sin\theta_{JN} \\ 0 \\ \cos\theta_{JN} \end{pmatrix}_J . \tag{5.72}$$

With the above definition of θ_{JN}, and using Eqs. (5.68, 5.69) one has

$$\theta_{\mathrm{JN}} = \arccos\left(\frac{\mathbf{J}\cdot\hat{\mathbf{N}}}{|\mathbf{J}|}\right) \tag{5.73}$$

$$= \frac{J_{x,L_0}\sin\iota\sin\phi_{\mathrm{ref}} + J_{y,L_0}\sin\iota\cos\phi_{\mathrm{ref}} + J_{z,L_0}\cos\iota}{\sqrt{J_{x,L_0}^2 + J_{y,L_0}^2 + J_{z,L_0}^2}}. \tag{5.74}$$

Consequently, in the twisting-up formula (5.1), the spherical harmonics ${}_{-2}Y_{\ell m}(\theta,\phi)$ will have arguments $(\theta,\phi) = (\theta_{\mathrm{JN}}, 0)$. Having specified our convention regarding the J-frame, we can determine unambiguously the Euler angles relating it to the L_0-frame. We can identify two of these angles with θ_{JL_0} and ϕ_{JL_0}, as two successive rotations $\mathbf{R}_y(-\theta_{JL_0})\cdot\mathbf{R}_z(-\phi_{JL_0})$ will align $\hat{\mathbf{J}}$ with the $\hat{\mathbf{z}}_{\mathbf{L_0}}$ axis, we call this intermediate frame as J'-frame. In order to bring $\hat{\mathbf{N}}$ in the $\hat{\mathbf{x}}_\mathbf{J} - \hat{\mathbf{z}}_\mathbf{J}$ plane, we need to apply a further rotation around the $\hat{\mathbf{z}}_{\mathbf{L_0}}$-axis by an angle $-\kappa$, so that Eq. (5.72) is satisfied. To this end, we first compute

$$\begin{pmatrix} \hat{N}_{x,J'} \\ \hat{N}_{y,J'} \\ \hat{N}_{z,J'} \end{pmatrix}_{J'} = \mathbf{R}_y(-\theta_{JL_0})\cdot\mathbf{R}_z(-\phi_{JL_0})\cdot\begin{pmatrix} \hat{N}_{x,L_0} \\ \hat{N}_{y,L_0} \\ \hat{N}_{z,L_0} \end{pmatrix}_{L_0} , \tag{5.75}$$

and then take

$$\kappa = \arctan \frac{\hat{N}_{y,J'}}{\hat{N}_{x,J'}}. \tag{5.76}$$

The three Euler angles relating the L_0 and J frames are therefore $\kappa, \theta_{JL_0}, \phi_{JL_0}$. The components of any vector $\mathbf{u}$ in the two frames are related via:

$$\begin{pmatrix} u_{x,J} \\ u_{y,J} \\ u_{z,J} \end{pmatrix}_J = \mathbf{R}_z(-\kappa) \cdot \mathbf{R}_y(-\theta_{JL_0}) \cdot \mathbf{R}_z(-\phi_{JL_0}) \cdot \begin{pmatrix} u_{x,L_0} \\ u_{y,L_0} \\ u_{z,L_0} \end{pmatrix}_{L_0}. \tag{5.77}$$

Equivalently, a generic vector in the J-frame can be rotated to the L_0-frame by applying the inverse transformation

$$\begin{pmatrix} u_{x,L_0} \\ u_{y,L_0} \\ u_{z,L_0} \end{pmatrix}_{L_0} = \mathbf{R}_z(\phi_{JL_0}) \cdot \mathbf{R}_y(\theta_{JL_0}) \cdot \mathbf{R}_z(\kappa) \cdot \begin{pmatrix} u_{x,J} \\ u_{y,J} \\ u_{z,J} \end{pmatrix}_J. \tag{5.78}$$

Notice that, in the J-frame, the initial angular momentum has components:

$$\hat{\mathbf{L}}_0 \doteq \begin{pmatrix} \sin\beta_0 \cos\alpha_0 \\ \sin\beta_0 \sin\alpha_0 \\ \cos\beta_0 \end{pmatrix}_J. \tag{5.79}$$

We can compute the initial value of the Euler angles (α, β, γ) introduced in Sec. 5.3, by identifying the product of rotations in Eq. (5.77) with $\mathbf{R}_z(\alpha_0) \cdot \mathbf{R}_y(\beta_0) \cdot \mathbf{R}_z(\gamma_0)$, whence it follows that

$$\alpha_0 = \pi - \kappa, \tag{5.80a}$$

$$\beta_0 = \theta_{JL_0}, \tag{5.80b}$$

$$\gamma_0 = -\epsilon_0 = \pi - \phi_{JL_0} \tag{5.80c}$$

It can be checked that, with the choice of offsets above, the initial angular momentum in the J-frame is indeed rotated to the $\hat{\mathbf{z}}_{\mathbf{L_0}}$-axis by the transformation of Eq. (5.78).

The NNLO and MSA angle prescriptions provide expressions described in Secs. 5.4.1 and 5.4.2 for the Euler angles as functions of frequency. In order to initialize the angles to prescribed values α_0, β_0, ϵ_0 according to Eqs. (5.80) at a given reference frequency f_{ref}, we have to add an offset to the functional dependence of the NNLO/MSA angles in the following way

$$\alpha(f) = \alpha_{\text{NNLO/MSA}}(f) - \alpha_{\text{offset}} \tag{5.81a}$$

$$\epsilon(f) = \epsilon_{\mathrm{NNLO/MSA}}(f) - \epsilon_{\mathrm{offset}} \tag{5.81b}$$

Here the offsets are constant values that correspond to frequency-independent rotations of the system into the desired state at the reference frequency, and a typical example would be to choose the α offset as $-(\alpha(f_{ref}) - \alpha_0)$. Our code offers different options to compute these offsets, which we discuss in appendix 5.F and list in Table 5.F.2.

Finally we fix the remaining freedom in the N-frame. We have previously aligned the $\hat{\mathbf{z}}_{\hat{\mathbf{N}}}$ axis with $\hat{\mathbf{N}}$, so we just have to fix a rotation around $\hat{\mathbf{N}}$. Following the LALSuite convention [102, 28] we choose the $\hat{\mathbf{x}}_{\hat{\mathbf{N}}}$-axis such that the vector $\mathbf{L_0}$ lies in the $\hat{\mathbf{x}}_{\hat{\mathbf{N}}} - \hat{\mathbf{z}}_{\hat{\mathbf{N}}}$ plane with positive projection over $\hat{\mathbf{x}}_{\hat{\mathbf{N}}}$, and $\hat{\mathbf{y}}_{\hat{\mathbf{N}}}$ so that it completes the triad. Equivalently:

$$\hat{\mathbf{L}}_0 \cdot \hat{\mathbf{x}}_{\hat{\mathbf{N}}} = \sin\iota, \;\; \hat{\mathbf{y}}_{\hat{\mathbf{N}}} = \frac{\hat{\mathbf{N}} \times \hat{\mathbf{x}}_{\hat{\mathbf{N}}}}{|\hat{\mathbf{N}} \times \hat{\mathbf{x}}_{\hat{\mathbf{N}}}|}. \tag{5.82}$$

In the N-frame the components of $\hat{\mathbf{L}}_0$ are then given by

$$\hat{\mathbf{L}}_0 \doteq (\sin\iota, 0, \cos\iota)_N. \tag{5.83}$$

The $\hat{\mathbf{x}}_{\hat{\mathbf{N}}}$, $\hat{\mathbf{y}}_{\hat{\mathbf{N}}}$ axes we have just introduced do not coincide with the spherical basis vectors orthogonal to $\hat{\mathbf{N}}$ that determine the arguments of the weighted spherical harmonics in our J-frame. Therefore, we have to compute the angle ζ that rotates one basis into the other. We will call the original polarization axes $\hat{\mathbf{x}}'_{\hat{\mathbf{N}}}$ and $\hat{\mathbf{y}}'_{\hat{\mathbf{N}}}$. Note that, geometrically, these vectors can be defined as

$$\hat{\mathbf{x}}'_{\hat{\mathbf{N}}} = \frac{\hat{\mathbf{y}}'_{\hat{\mathbf{N}}} \times \hat{\mathbf{N}}}{|\hat{\mathbf{y}}'_{\hat{\mathbf{N}}} \times \hat{\mathbf{N}}|}, \quad \hat{\mathbf{y}}'_{\hat{\mathbf{N}}} = \frac{\mathbf{J} \times \hat{\mathbf{N}}}{|\mathbf{J} \times \hat{\mathbf{N}}|}, \tag{5.84}$$

and are therefore equivalent to the choice made in [27], as we explain in App. 5.D below. Under a rotation by an angle ζ, the polarization basis-vectors transform as:

$$\hat{\mathbf{x}}'_{\hat{\mathbf{N}}} = \cos(\zeta)\hat{\mathbf{x}}_{\hat{\mathbf{N}}} - \sin(\zeta)\hat{\mathbf{y}}_{\hat{\mathbf{N}}} \tag{5.85a}$$

$$\hat{\mathbf{y}}'_{\hat{\mathbf{N}}} = \sin(\zeta)\hat{\mathbf{x}}_{\hat{\mathbf{N}}} + \cos(\zeta)\hat{\mathbf{y}}_{\hat{\mathbf{N}}}. \tag{5.85b}$$

Since ζ can vary from 0 to 2π, we will use the C function `atan2` to track the correct quadrant and set

$$\zeta = \texttt{atan2}\left(\hat{\mathbf{x}}_{\hat{\mathbf{N}}} \cdot \hat{\mathbf{y}}'_{\hat{\mathbf{N}}}, \hat{\mathbf{x}}_{\hat{\mathbf{N}}} \cdot \hat{\mathbf{x}}'_{\hat{\mathbf{N}}}\right). \tag{5.86}$$

In the code implementation the scalar products above are computed in the J-frame, where the vectors $\hat{\mathbf{x}}'_{\hat{\mathbf{N}}}$ and $\hat{\mathbf{y}}'_{\hat{\mathbf{N}}}$ have components

$$\hat{\mathbf{x}}'_{\hat{\mathbf{N}}} \doteq \begin{pmatrix} \cos\theta_{JN} \\ 0 \\ -\sin\theta_{JN} \end{pmatrix}_J , \quad \hat{\mathbf{y}}'_{\hat{\mathbf{N}}} \doteq \begin{pmatrix} 0 \\ 0 \\ 1 \end{pmatrix}_J . \tag{5.87}$$

The components of $\hat{\mathbf{x}}_{\hat{\mathbf{N}}}$ in the J-frame can be computed by applying the transformation (5.77) to $\hat{\mathbf{x}}_{\hat{\mathbf{N}}}$ expressed in the L_0-frame, giving

$$\hat{\mathbf{x}}_{\hat{\mathbf{N}}} \doteq \begin{pmatrix} -\cos\iota\ \sin\phi_{ref} \\ -\cos\iota\ \cos\phi_{ref} \\ \sin\iota \end{pmatrix}_{L_0} . \tag{5.88}$$

5.D Choices of polarization vectors P and Q

In the literature it is common to introduce a polarization basis $(\hat{P}^i, \hat{Q}^i)$ such that the strain tensor is constructed in the usual way as [34, 28]

$$h_+ = \frac{1}{2}\left(\hat{P}^i\hat{P}^j - \hat{Q}^i\hat{Q}^j\right) h_{ij}, \tag{5.89}$$

$$h_\times = \frac{1}{2}\left(\hat{P}^i\hat{Q}^j + \hat{Q}^i\hat{P}^j\right) h_{ij}. \tag{5.90}$$

Different choices of polarization basis can be achieved through a rotation around the $\hat{\mathbf{z}}_{\hat{\mathbf{N}}}$-axis, i.e. the line of sight. In the convention followed by Arun et al. [34], the polarization basis is given by

$$\hat{\mathbf{P}}_{\text{ABFO}} = \frac{\hat{\mathbf{N}}\times\mathbf{J}}{|\hat{\mathbf{N}}\times\mathbf{J}|}, \quad \hat{\mathbf{Q}}_{\text{ABFO}} = \frac{\hat{\mathbf{N}}\times\hat{\mathbf{P}}_{\text{ABFO}}}{|\hat{\mathbf{N}}\times\hat{\mathbf{P}}_{\text{ABFO}}|}, \tag{5.91}$$

whereas the basis chosen by Kidder [27] is

$$\hat{\mathbf{P}}_{\text{Kidder}} = \frac{\hat{\mathbf{Q}}_{\text{Kidder}}\times\hat{\mathbf{N}}}{|\hat{\mathbf{Q}}_{\text{Kidder}}\times\hat{\mathbf{N}}|}, \quad \hat{\mathbf{Q}}_{\text{Kidder}} = \frac{\mathbf{J}\times\hat{\mathbf{N}}}{|\mathbf{J}\times\hat{\mathbf{N}}|}. \tag{5.92}$$

Note that, from the above definitions, it follows that

$$\hat{\mathbf{P}}_{\text{ABFO}} = -\hat{\mathbf{Q}}_{\text{Kidder}}, \quad \hat{\mathbf{Q}}_{\text{ABFO}} = \hat{\mathbf{P}}_{\text{Kidder}}, \tag{5.93}$$

and, using Eqs. (5.85), one can equivalently say that the two polarization bases are related by a rotation of $\zeta = \pi/2$. This translates into an overall sign difference in the gravitational-wave polarizations h_+ and $h_\times$, since these transform under a rotation by ζ

around the line of sight according to

$$h'_+ = \cos(2\zeta)\, h_+ - \sin(2\zeta)\, h_\times, \tag{5.94}$$

$$h'_\times = \sin(2\zeta)\, h_+ + \cos(2\zeta)\, h_\times. \tag{5.95}$$

5.E Derivation of the frequency domain waveform

The waveform modes in the inertial J-frame and the precessing L-frame can be related via a time-domain transformation

$$h^J_{\ell m}(t) = e^{-i\, m\alpha(t)} \sum_{m'=-\ell}^{\ell} e^{i\, m'\epsilon(t)} d^\ell_{mm'}(\beta(t)) h^L_{\ell m'}(t) \tag{5.96}$$

Performing a Fourier transform, and making use of the SPA, as done in [23], we obtain

$$\tilde{h}^J_{\ell m}(f) = \sum_{m'=-\ell}^{\ell} e^{i\, m'\epsilon\left(\frac{2\pi f}{m'}\right)} e^{-i\, m\alpha\left(\frac{2\pi f}{m'}\right)} d^\ell_{mm'}\left(\beta\left(\frac{2\pi f}{m'}\right)\right) \tilde{h}^L_{\ell m'}(f). \tag{5.97}$$

We now follow the standard paradigm and approximate the precessing frame modes with some equivalent non-precessing modes [17, 18, 1]. In our conventions, the positive m-modes are defined with support only for negative frequencies while the negative m-modes are defined with support for positive frequencies, i.e. $\tilde{h}^J_{\ell m'>0}(f > 0) = 0$ and $\tilde{h}^J_{\ell m'<0}(f < 0) = 0$. We can therefore re-write the above expression as

$$\tilde{h}^J_{\ell m}(f > 0) = \sum_{m'>0}^{\ell} e^{-i\, m'\epsilon\left(\frac{2\pi f}{m'}\right)} e^{-i\, m\alpha\left(\frac{2\pi f}{m'}\right)} d^\ell_{m-m'}\left(\beta\left(\frac{2\pi f}{m'}\right)\right) \tilde{h}^L_{\ell -m'}(f) \tag{5.98}$$

$$\tilde{h}^J_{\ell m}(f < 0) = \sum_{m'>0}^{\ell} e^{i\, m'\epsilon\left(\frac{-2\pi f}{m'}\right)} e^{-i\, m\alpha\left(\frac{-2\pi f}{m'}\right)} d^\ell_{mm'}\left(\beta\left(\frac{-2\pi f}{m'}\right)\right) (-1)^l \tilde{h}^{L*}_{\ell -m'}(-f) \tag{5.99}$$

We now wish to construct expressions for the gravitational-wave polarizations h_+ and $h_\times$. First we start with the gravitational-wave strain

$$h^J(t) = h^J_+(t) - i\, h^J_\times(t) = \sum_{\ell\geq 2} \sum_{m=-\ell}^{m=\ell} h^J_{\ell m}(t)\, {}_{-2}Y_{\ell m}. \tag{5.100}$$

The individual polarizations can therefore be written as

$$h^J_+(t) = \frac{1}{2} \sum_{\ell\geq 2} \sum_{m=-\ell}^{m=\ell} \left(h^J_{\ell m}(t)\, {}_{-2}Y_{\ell m} + h^{J*}_{\ell m}(t)\, {}_{-2}Y^*_{\ell m}\right), \tag{5.101}$$

$$h^J_\times(t) = \frac{i}{2}\sum_{\ell\geq 2}\sum_{m=-\ell}^{m=\ell}\left(h^J_{\ell m}(t)\,{}_{-2}Y_{\ell m} - h^{J*}_{\ell m}(t)\,{}_{-2}Y^*_{\ell m}\right), \tag{5.102}$$

which, after performing a Fourier transformation, can be written as frequency-domain functions

$$\tilde{h}^J_+(f) = \frac{1}{2}\sum_{\ell\geq 2}\sum_{m=-\ell}^{m=\ell}\left(\tilde{h}^J_{\ell m}(f)\,{}_{-2}Y_{\ell m} + \tilde{h}^{J*}_{\ell m}(-f)\,{}_{-2}Y^*_{\ell m}\right), \tag{5.103}$$

$$\tilde{h}^J_\times(f) = \frac{i}{2}\sum_{\ell\geq 2}\sum_{m=-\ell}^{m=\ell}\left(\tilde{h}^J_{\ell m}(f)\,{}_{-2}Y_{\ell m} - \tilde{h}^{J*}_{\ell m}(-f)\,{}_{-2}Y^*_{\ell m}\right). \tag{5.104}$$

Now we insert Eq. (5.97) into the above expressions to expand the polarizations in terms of the non-precessing modes $h^L_{\ell m}(f)$

$$\begin{aligned}\tilde{h}^J_+(f) = \frac{1}{2}\sum_{\ell\geq 2}\sum_{m=-\ell}^{m=\ell}\Bigg(&\sum_{m'=-\ell}^{\ell} e^{i\,m'\epsilon}e^{-i\,m\alpha}d^\ell_{mm'}(\beta)\,\tilde{h}^L_{\ell m'}(f)\,{}_{-2}Y_{\ell m} \\ &+ \sum_{m'=-\ell}^{\ell} e^{-i\,m'\epsilon}e^{i\,m\alpha}d^\ell_{mm'}(\beta)\,\tilde{h}^{L*}_{\ell m'}(-f)\,{}_{-2}Y^*_{\ell m}\Bigg),\end{aligned} \tag{5.105}$$

$$\begin{aligned}\tilde{h}^J_\times(f) = \frac{i}{2}\sum_{\ell\geq 2}\sum_{m=-\ell}^{m=\ell}\Bigg(&\sum_{m'=-\ell}^{\ell} e^{i\,m'\epsilon}e^{-i\,m\alpha}d^\ell_{mm'}(\beta)\,\tilde{h}^L_{\ell m'}(f)\,{}_{-2}Y_{\ell m} \\ &- \sum_{m'=-\ell}^{\ell} e^{-i\,m'\epsilon}e^{i\,m\alpha}d^\ell_{mm'}(\beta)\,\tilde{h}^{L*}_{\ell m'}(-f)\,{}_{-2}Y^*_{\ell m}\Bigg).\end{aligned} \tag{5.106}$$

We can now use the equatorial symmetry of the non-precessing modes to relate the positive m and negative m modes via $\tilde{h}^L_{\ell m}(f) = (-1)^\ell \tilde{h}^{L*}_{\ell -m}(-f)$. Inserting this into the above equations, we find

$$\begin{aligned}\tilde{h}^J_+(f) = \frac{1}{2}\sum_{\ell\geq 2}\sum_{m=-\ell}^{\ell}\Bigg(&\sum_{m'=-\ell}^{\ell} e^{i\,m'\epsilon}e^{-i\,m\alpha}d^\ell_{mm'}(\beta)\,\tilde{h}^L_{\ell m'}(f)\,{}_{-2}Y_{\ell m} \\ &+ \sum_{m'=-\ell}^{\ell} e^{-i\,m'\epsilon}e^{i\,m\alpha}d^\ell_{mm'}(\beta)\,(-1)^\ell\tilde{h}^L_{\ell -m'}(f)\,{}_{-2}Y^*_{\ell m}\Bigg),\end{aligned} \tag{5.107}$$

$$\begin{aligned}\tilde{h}^J_\times(f) = \frac{i}{2}\sum_{\ell\geq 2}\sum_{m=-\ell}^{\ell}\Bigg(&\sum_{m'=-\ell}^{\ell} e^{i\,m'\epsilon}e^{-i\,m\alpha}d^\ell_{mm'}(\beta)\,\tilde{h}^L_{\ell m'}(f)\,{}_{-2}Y_{\ell m} \\ &- \sum_{m'=-\ell}^{\ell} e^{-i\,m'\epsilon}e^{i\,m\alpha}d^\ell_{mm'}(\beta)\,(-1)^\ell\tilde{h}^L_{\ell -m'}(f)\,{}_{-2}Y^*_{\ell m}\Bigg).\end{aligned} \tag{5.108}$$

Since the polarizations $\tilde{h}^J_{+,\times}(f)$ are Fourier transforms of real functions $h^J_{+,\times}(t)$, they satisfy the property $\tilde{h}^J_{+,\times}(f) = \tilde{h}^{J,*}_{+,\times}(-f)$. This means that we can work with just one

of the frequency regimes, i.e. positive or negative. We opt to work with the positive frequencies, following the standard convention in LALSuite. Restricting the expressions to positive frequencies, and remembering that only the negative non-precessing modes are non-zero, we find that Eqs. (5.107, 5.108) reduce to

$$\tilde{h}^J_+(f>0) = \frac{1}{2}\sum_{\ell\geq 2}\sum_{m=-\ell}^{\ell}\Bigg(\sum_{m'>0}^{\ell} e^{-i\,m'\epsilon}e^{-i\,m\alpha}d^{\ell}_{m-m'}(\beta)\,\tilde{h}^L_{\ell-m'}(f)\,{}_{-2}Y_{\ell m} + \sum_{m'>0}^{\ell} e^{-i\,m'\epsilon}e^{i\,m\alpha}d^{\ell}_{mm'}(\beta)\,(-1)^{\ell}\tilde{h}^L_{\ell-m'}(f)\,{}_{-2}Y^*_{\ell m}\Bigg), \tag{5.109}$$

$$\tilde{h}^J_\times(f>0) = \frac{i}{2}\sum_{\ell\geq 2}\sum_{m=-\ell}^{\ell}\Bigg(\sum_{m'>0}^{\ell} e^{-i\,m'\epsilon}e^{-i\,m\alpha}d^{\ell}_{m-m'}(\beta)\,\tilde{h}^L_{\ell-m'}(f)\,{}_{-2}Y_{\ell m} - \sum_{m'>0}^{\ell} e^{-i\,m'\epsilon}e^{i\,m\alpha}d^{\ell}_{mm'}(\beta)\,(-1)^{\ell}\tilde{h}^L_{\ell-m'}(f)\,{}_{-2}Y^*_{\ell m}\Bigg). \tag{5.110}$$

Rearranging terms and swapping the sums in m and m' we get

$$\tilde{h}^J_+(f>0) = \frac{1}{2}\sum_{\ell\geq 2}\sum_{m'>0}^{\ell} e^{-i\,m'\epsilon}\tilde{h}^L_{\ell-m'}(f)\sum_{m=-\ell}^{m=\ell}\big(e^{-i\,m\alpha}d^{\ell}_{m-m'}(\beta)\,{}_{-2}Y_{\ell m} + e^{i\,m\alpha}d^{\ell}_{mm'}(\beta)\,(-1)^{\ell}{}_{-2}Y^*_{\ell m}\big), \tag{5.111}$$

$$\tilde{h}^J_\times(f>0) = \frac{i}{2}\sum_{\ell\geq 2}\sum_{m'>0}^{\ell} e^{-i\,m'\epsilon}\tilde{h}^L_{\ell-m'}(f)\sum_{m=-\ell}^{m=\ell}\big(e^{-i\,m\alpha}d^{\ell}_{m-m'}(\beta)\,{}_{-2}Y_{\ell m} - e^{i\,m\alpha}d^{\ell}_{mm'}(\beta)\,(-1)^{\ell}\,{}_{-2}Y^*_{\ell m}\big). \tag{5.112}$$

We define now the transfer function $A^{\ell}_{mm'}(f) = e^{-im\alpha}d^{\ell}_{mm'}(\beta){}_{-2}Y_{\ell m}$ and rewrite the above expressions in a more compact form,

$$\tilde{h}^J_+(f>0) = \frac{1}{2}\sum_{\ell\geq 2}\sum_{m'>0}^{\ell} e^{-i\,m'\epsilon}\tilde{h}^L_{\ell-m'}(f)\sum_{m=-\ell}^{m=\ell}\left(A^{\ell}_{m-m'} + (-1)^{\ell}\,A^{\ell *}_{mm'}\right), \tag{5.113}$$

$$\tilde{h}^J_\times(f>0) = \frac{i}{2}\sum_{\ell\geq 2}\sum_{m'>0}^{\ell} e^{-i\,m'\epsilon}\tilde{h}^L_{\ell-m'}(f)\sum_{m=-\ell}^{m=\ell}\left(A^{\ell}_{m-m'} - (-1)^{\ell}\,A^{\ell *}_{mm'}\right), \tag{5.114}$$

which are equivalent to the expressions in Eqs. (5.11, 5.12). Note that the Euler angles are evaluated at the SPA frequencies $2\pi f/m'$.

5.F LALSuite Implementation

TheIMRPhenomXP and IMRPhenomXPHM models are implemented as part of the `LALSimIMR` package of inspiral-merger-ringdown waveform models as extensions of the

non-precessing models IMRPhenomXAS [4] and IMRPhenomXHM [10]. The code is implemented in the C language, and `LALSimIMR` is part of the `LALSimulation` collection of code for gravitational waveform and noise generation within LALSuite [19]. Online Doxygen documentation is available at `https://lscsoft.docs.ligo.org/lalsuite`, with top level information for the `LALSimIMR` package provided through the `LALSimIMR.h` header file. Externally callable functions follow the `XLAL` coding standard of LALSuite.

Notes about the implementation of the IMRPhenomXHM model, and on calling the code through different interfaces, in particular through `Python`, `GenerateSimulation`, `LALInference` [12] and `Bilby` [13] can be found in appendix C of [10]. Here we extend this documentation to the specific properties of IMRPhenomXP and IMRPhenomXPHM. The LALSuite code provides the option to call the model in the time domain, where an inverse fast Fourier transformation is applied, in addition to the native Fourier domain. The SWIG [103, 104] software development tool is used to automatically create Python interfaces to all `XLAL` functions [105] of our code, which can be used alternatively to the C interfaces.

In `LALSimulation` the model is called through the function `ChooseFDWaveform`, whose input parameters `f_ref` and `phiRef` are used to define the phase of the 22 mode at some particular reference frequency.

The user is free to specify the spherical harmonic modes in the co-precessing L-frame, $h^L_{\ell m}$, that should be used to construct the waveform. The default behaviour is to use all the modes available: $((2\pm2), (2\pm1), (3\pm3), (3\pm2), (4\pm4))$, but subsets can be selected with the *ModeArray* option available in `LALSimulation`. The negative modes are always included in the twisting-up procedure, even if not specified in the mode array, thus the list $((2,2),(2,1),(3,3),(3,2),(4,4))$ would return the same result as the default setting. Specifying only negative modes is however not supported, e.g. when only specifying the array $((2,2),(2,-1))$ only the $((2,2),(2-2))$ modes would be twisted up.

Furthermore, the model implemented in LALSuite supports acceleration of waveform evaluation by interpolation of an unequispaced frequency grid broadly following the "multibanding" approach of [14]. Our version of the algorithm is described in [3] to do the evaluation faster and can also use a custom list of modes specified by the user. The multibanding algorithm is parameterized by a threshold, which describes the permitted local interpolation error for the phase in radians. Lower values thus correspond to higher accuracy. The default multibanding threshold for computing the non-precessing modes is set to a value of 10^{-3} and, as for IMRPhenomXHM, is modified through the *ThresholdMband* option. For multibanding in the Euler angles, the default threshold is 10^{-3} for the MSA versions and 10^{-4} for all NNLO versions; this can be changed

through the *PrecThresholdMband* option. The multibanding is only supported in the IMRPhenomXPHM model not so in IMRPhenomXP.

PrecVersion	Explanation
101	NNLO PN Euler angles and a 2PN non-spinning approximation to L
102	NNLO PN Euler angles and a 3PN spinning approximation to L
103	NNLO PN Euler angles and a 4PN spinning approximation to L
104	NNLO PN Euler angles and a 4PN spinning approximation to L augmented with leading PN order at all order in spin terms.
220	MSA Euler angles and a 3PN spinning approximation to L. Fall back to NNLO angles with 3PN approximation to L if MSA system fails to initialize.
221	MSA Euler angles and a 3PN spinning approximation to L. Throw error message if MSA system fails to initialize.
222	MSA Euler angles close to Pv3HM implemenation. Throw error message if MSA system fails to initialize.
223 (default)	MSA Euler angles closer to Pv3HM implemenation. Fall back to NNLO with 3PN approximation to L if MSA system fails to initialize.
224	As version 220 but using the $\phi_{z,0}$ and $\zeta_{z,0}$ prescription from 223.

Table 5.F.1: Options in the LALSuite implementation to change between different descriptions of the Euler angles.

Convention	$\alpha_{\rm offset}$	$\epsilon_{\rm offset}$	`phiRef` argument passed to non-precessing modes
0	$\alpha_{\rm NNLO/MSA}(f_{\rm ref}) - \alpha_0^{\rm XP}$	$\epsilon_{\rm NNLO/MSA}(f_{\rm ref})$	ϕ_{JL_0}
1 (default)	$\alpha_{\rm NNLO/MSA}(f_{\rm ref}) - \alpha_0^{\rm Pv2}$	$\epsilon_{\rm NNLO/MSA}(f_{\rm ref}) - \epsilon_0^{\rm XP}$	0
5	$-\alpha_0^{\rm Pv2}$	0	`phiRef`
6	$\alpha_{\rm NNLO/MSA}(f_{\rm ref}) - \alpha_0^{\rm XP}$	$\epsilon_{\rm NNLO/MSA}(f_{\rm ref}) - \epsilon_0^{\rm XP}$	`phiRef`
7	$-\alpha_0^{\rm XP}$	0	`phiRef`

Table 5.F.2: The superscript XP means that the initial angle was computed as described in Eqs. (5.80) and the superscript Pv2 following the conventions detailed in [1, 23].

The IMRPhenomXP and IMRPhenomXPHM models add further precession-specific options to those already documented in appendix C of [10]. The default values of these options are set up in the file `LALSimInspiralWaveformParams.c`. Available choices for the Euler angles are listed in Table 5.F.1 and set by a parameter *PrecVersion*. The principal choice is between the NNLO and MSA angle descriptions discussed in sections 5.4.1 and 5.4.2. In addition for the NNLO angles different PN orders for the angular momentum can be chosen, as discussed in Sec. 5.4.3. Different implementation choices are also available for the MSA angles.

FinalSpinMod	Explanation
0	Final spin formula based on χ_p. Default value for NNLO angles.
1	Final spin formula based on χ_{1x}. Not recommended, introduced to compare to IMRPhenomPv3 before bug fix.
2	Final spin formula based on the norm for the total in-plane spin vector
3	Final spin formula based on precession-averaged couplings from MSA analysis. Default value for MSA angles.

TABLE 5.F.3: Options for changing the final spin prescription in the LALSuite implementation of IMRPhenomXP and IMRPhenomXPHM.

Option	Values	Default	Explanation
TwistPhenomHM	0, 1	0 (False)	Twist-up IMRPhenomHM instead of IMRPhenomXHM. With *Convention* = 5 this produces a faster implementation of IMRPhenomPv3HM.
PrecModes	0, 1	0 (False)	When calling the individual modes functions return the modified non-precessing modes before the twist-up.
UseModes	0, 1	0 (False)	When computing the polarizations first call all the individual modes in the J-frame and sum them all.
PrecThresholdMband	Float	10^{-3}	Threshold value for the multibanding algorithm applied to the Euler angles. If 0 then multibanding for angles is switched off.
MBandPrecVersion	0	0	Control the version for the coarse grid used for the multibanding of Euler angles. Currently there is only one implementation and the grid is the same than for the non-precessing model.

TABLE 5.F.4: Extra options in the LALSuite implementation of IMRPhenomXPHM.

Option	`LALInference`	`Bilby`	`PyCBC`	`GenerateSimulation`
ModesList	`modeList`	`mode_array`	`mode_array`	`modesList`
PrecVersion	`phenomXPrecVersion`	`phenomXPrecVersion`	`phenomXPrecVersion`	`phenomXPrecVersion`
FinalSpinMod	`phenomXPFinalSpinMod`	`phenomXPFinalSpinMod`	-	-
PrecThresholdMband	`phenomXPHMMband`	`phenomXPHMMband`	`phenomXPHMMband`	`phenomXPHMMband`
UseModes	-	-	-	`phenomXPHMUseModes`

TABLE 5.F.5: Labels used to pass IMRPhenomXPHM options to different external codes.

The NNLO and MSA angle prescriptions provide expressions for frequency-dependent Euler angles. In order to initialize the angles to prescribed values α_0, β_0, ϵ_0 at a given reference frequency $f_{\rm ref}$ according to Eqs. (5.80), appropriate offsets need to be added as in Eqs. (5.81). Our code offers different options to compute these offsets, which we list in Table 5.F.2. These conventions are changed with the option *Convention*, which also controls how the argument `phiRef` enters in the model. The default choice is set to option 1. Note that option 7 does not set offsets for a given reference frequency. This option is implemented for its correspondence to the implementation of the IMRPhenomPv3HM [16] model, which sets the offset of α equal to $-\alpha_0$ and the offset of ϵ equal to 0; the

argument `phiRef` is passed when calling the non-precessing model.

Several variants are available to compute the final spin, which are selected with the option *FinalSpinMod*. By default, the final spin is computed by using orbit-averaged quantities for the in-plane spin components: When choosing NNLO angles, the default spin version is set to 0, corresponding to Eq. (5.39), while for MSA angles, the default spin version is set to 3, corresponding to Eq. (5.42). In addition, two non-averaged options are provided, which allow for cancellations between spin components as discussed in Sec. 5.4.4: setting the spin version to 1 corresponds to Eq. (5.40), while version 2 selects Eq. (5.41).

Finally, in Table 5.F.4 we summarize further options available. We make some of these options also callable from other codes that may use the model like `LALInference`, `Bilby`, `PyCBC` or `GenerateSimulation`. In Table 5.F.5 we summarize the options that can be called through the different codes and the label that is used to specify their value. Since the released versions of some of these codes do not support these features yet, we provide dedicated branches for that:

- `Bilby`: https://git.ligo.org/cecilio.garcia-quiros/bilby/-/tree/imrphenomx
- `Bilby_pipe`: https://git.ligo.org/maite.mateu-lucena/bilby_pipe
- `PyCBC`: https://github.com/Ceciliogq/pycbc/tree/imrphenomx/pycbc

Extensive debugging information can be enabled at compile time with the C preprocessor flag `-D PHENOMXHMDEBUG`.

5.G Post-Newtonian Results

We consider a compact binary with masses $m_{1,2}$ and spin angular momenta $S_{1,2}$. The PN results presented in this section can be expressed in terms of the following variables:

$$\delta = \sqrt{1-4\eta}, \tag{5.115}$$

$$m_1 = \frac{1+\delta}{2}, \quad m_2 = \frac{1-\delta}{2}, \tag{5.116}$$

$$\chi_i = \frac{S_i}{m_1^2}, \tag{5.117}$$

$$\chi_\ell = m_1\chi_{1\ell} + m_2\chi_{2\ell}, \tag{5.118}$$

$$S_\ell = m_1^2\chi_{1\ell} + m_2^2\chi_{2\ell}, \tag{5.119}$$

$$\Sigma_\ell = \chi_{2\ell}m_2 - \chi_{1\ell}m_1. \tag{5.120}$$

5.G.1 NNLO PN Euler Angles

For completeness we write out the explicit expressions for the Euler angles α and ϵ, computed to NNLO accuracy for single spin systems as used in the single spin version of our model, see 5.4.1. Both α and ϵ have the same functional form as functions of the frequency f,

$$\alpha_{\rm NNLO}(\omega) = \sum_{i=-3}^{1} \alpha_i \, (\pi f M)^{i/3} + \alpha_{\log} \log(\pi f M), \tag{5.121}$$

$$\epsilon_{\rm NNLO}(\omega) = \sum_{i=-3}^{1} \epsilon_i \, (\pi f M)^{i/3} + \alpha_{\log} \log(\pi f M). \tag{5.122}$$

The coefficients α_0 and ϵ_0 are determined by Eqs. (5.80). The coefficients for α are listed below as functions of the intrinsic parameters (η, χ_l, χ_p).

$$\alpha_{-3} = -\frac{5\delta}{64 m_1} - \frac{35}{192} \tag{5.123a}$$

$$\alpha_{-2} = -\frac{5 m_1 \chi_\ell \, (3\delta + 7 m_1)}{128\eta} \tag{5.123b}$$

$$\alpha_{-1} = -\frac{5(824\eta + 1103)}{3072} - \frac{15\delta^2\eta}{256 m_1^2} - \frac{15\delta m_1^3 \chi_p^2}{128\eta^2} - \frac{5\delta(980\eta + 911)}{7168 m_1} - \frac{35 m_1^4 \chi_p^2}{128\eta^2} \tag{5.123c}$$

$$\begin{aligned}\alpha_1 = {} & \frac{5(36\eta(85568\eta + 23817) + 8024297)}{9289728} + \frac{5 m_1^2 \left(3\delta^2\chi_p^2 + 75\delta^2\chi_\ell^2 - 112\pi\chi_\ell\right)}{256\eta} \\ & - \frac{15\delta m_1^7 \left(\chi_p^4 - 4\chi_p^2\chi_\ell^2\right)}{512\eta^4} + \frac{5\delta m_1^3 \left((812\eta - 97)\chi_p^2 + 20328\eta\chi_\ell^2\right)}{14336\eta^2} - \frac{15\pi\delta m_1\chi_\ell}{16\eta} \\ & - \frac{35 m_1^8 \left(\chi_p^4 - 4\chi_p^2\chi_\ell^2\right)}{512\eta^4} + \frac{m_1^4 \left(25(92\eta + 19)\chi_p^2 + 52640\eta\chi_l^2\right)}{6144\eta^2} + \frac{15\delta^3\eta^2}{1024 m_1^3} \\ & + \frac{5\delta^2\eta(784\eta + 323)}{28672 m_1^2} + \frac{5\delta(504\eta(7630\eta - 159) + 5579177)}{21676032 m_1}\end{aligned} \tag{5.123d}$$

$$\begin{aligned}\alpha_{\log} = {} & -\frac{5}{48}\left(7\pi - 3\delta^2\chi_\ell\right) - \frac{5\delta m_1^5\chi_p^2\chi_\ell}{128\eta^3} + \frac{5\delta(7168\eta + 407) m_1\chi_\ell}{21504\eta} - \frac{35 m_1^6\chi_p^2\chi_\ell}{384\eta^3} \\ & + \frac{5(4072\eta + 599) m_1^2\chi_\ell}{9216\eta} - \frac{5\pi\delta}{16 m_1}.\end{aligned} \tag{5.123e}$$

$$\epsilon_{-3} = \alpha_{-3} \tag{5.123f}$$

$$\epsilon_{-2} = \alpha_{-2} \tag{5.123g}$$

$$\epsilon_{-1} = -\frac{5(824\eta + 1103)}{3072} - \frac{15\delta^2\eta}{256 m_1^2} - \frac{5\delta(980\eta + 911)}{7168 m_1} \tag{5.123h}$$

$$\begin{aligned}\epsilon_1 = {} & \frac{5(36\eta(85568\eta + 23817) + 8024297)}{9289728} + \frac{5 m_1^2\chi_\ell \left(75\delta^2\chi_l - 112\pi\right)}{256\eta} + \frac{1815\delta m_1^3\chi_\ell^2}{256\eta} \\ & - \frac{15\pi\delta m_1\chi_\ell}{16\eta} + \frac{1645 m_1^4\chi_l^2}{192\eta} + \frac{15\delta^3\eta^2}{1024 m_1^3} + \frac{5\delta^2\eta(784\eta + 323)}{28672 m_1^2} \\ & + \frac{5\delta(504\eta(7630\eta - 159) + 5579177)}{21676032 m_1}\end{aligned} \tag{5.123i}$$

$$\epsilon_{\log} = -\frac{5}{48}\left(7\pi - 3\delta^2\chi_\ell\right) + \frac{5\delta(7168\eta+407)m_1\chi_\ell}{21504\eta} + \frac{5(4072\eta+599)m_1^2\chi_\ell}{9216\eta} - \frac{5\pi\delta}{16m_1}. \tag{5.123j}$$

5.G.2 Orbital Angular Momentum

The orbital angular momentum is estimated using an aligned-spin approximation with orbital terms up to 4PN and spin-orbit terms up to 3.5PN. We neglect spin-spin couplings.

$$L_0 = 1, \tag{5.124a}$$

$$L_1 = \frac{\eta}{6} + \frac{3}{2}, \tag{5.124b}$$

$$L_2 = \frac{\eta^2}{24} - \frac{19\eta}{8} + \frac{27}{8}, \tag{5.124c}$$

$$L_3 = \frac{7\eta^3}{1296} + \frac{31\eta^2}{24} + \left(\frac{41\pi^2}{24} - \frac{6889}{144}\right)\eta + \frac{135}{16}, \tag{5.124d}$$

$$\begin{aligned} L_4 = &-\frac{55\eta^4}{31104} - \frac{215\eta^3}{1728} + \left(\frac{356035}{3456} - \frac{2255\pi^2}{576}\right)\eta^2 \\ &+ \eta\left(-\frac{64}{3}\log(16x) - \frac{6455\pi^2}{1536} - \frac{128\gamma}{3} + \frac{98869}{5760}\right) + \frac{2835}{128}, \end{aligned} \tag{5.124e}$$

$$L_{1.5}^{\mathrm{SO}} = -\frac{35}{6}S_\ell - \frac{5}{2}\frac{\delta m}{m}\Sigma_\ell, \tag{5.124f}$$

$$L_{2.5}^{\mathrm{SO}} = \left(-\frac{77}{8} + \frac{427}{72}\eta\right)S_\ell + \frac{\delta m}{m}\left(-\frac{21}{8} + \frac{35}{12}\eta\right)\Sigma_\ell, \tag{5.124g}$$

$$L_{3.5}^{\mathrm{SO}} = \left(-\frac{405}{16} + \frac{1101}{16}\eta - \frac{29}{16}\eta^2\right)S_\ell + \frac{\delta m}{m}\left(-\frac{81}{6} + \frac{117}{4}\eta - \frac{15}{16}\eta^2\right)\Sigma_\ell, \tag{5.124h}$$

$$L_2^{\mathrm{LO-S}^\infty} = \left(\frac{1}{2} + \frac{\delta}{2} - \eta\right)\chi_1^2 + 2\eta\chi_{1\ell}\chi_{2\ell} + \left(\frac{1}{2} - \frac{\delta}{2} - \eta\right)\chi_{2\ell}^2, \tag{5.124i}$$

$$\begin{aligned} L_{3.5}^{\mathrm{LO-S}^\infty} = &\ \chi_{1\ell}^3\left(\frac{3\delta\eta}{4} - \frac{3\eta^2}{2} + \frac{3\eta}{4}\right) + \chi_{1\ell}^2\,\chi_{2\ell}\left(\frac{3\delta\eta}{4} + \frac{3\eta^2}{2} + \frac{3\eta}{4}\right) \\ &+\chi_{1\ell}\,\chi_{2\ell}^2\left(-\frac{3\delta\eta}{4} + \frac{3\eta^2}{2} + \frac{3\eta}{4}\right) + \chi_{2\ell}^3\left(-\frac{3\delta\eta}{4} - \frac{3\eta^2}{2} + \frac{3\eta}{4}\right). \end{aligned} \tag{5.124j}$$

Bibliography

[1] Mark Hannam, Patricia Schmidt, Alejandro Bohé, Leïla Haegel, Sascha Husa, et al. Simple Model of Complete Precessing Black-Hole-Binary Gravitational Waveforms. *Phys.Rev.Lett.*, 113(15):151101, 2014. doi: 10.1103/PhysRevLett.113.151101.

[2] Katerina Chatziioannou, Antoine Klein, Nicolás Yunes, and Neil Cornish. Constructing Gravitational Waves from Generic Spin-Precessing Compact Binary Inspirals. *Phys. Rev.*, D95(10):104004, 2017. doi: 10.1103/PhysRevD.95.104004.

[3] Cecilio García-Quirós, Sascha Husa, Maite Mateu-Lucena, and Angela Borchers. Accelerating the evaluation of inspiral-merger-ringdown waveforms with adapted grids. *ArXiv e-prints*, 2020.

[4] Geraint Pratten, Sascha Husa, Cecilio Garcia-Quiros, Marta Colleoni, Antoni Ramos-Buades, Hector Estelles, and Rafel Jaume. Setting the cornerstone for the IMRPhenomX family of models for gravitational waves from compact binaries: The dominant harmonic for non-precessing quasi-circular black holes. *ArXiv e-prints*, 2020.

[5] Sascha Husa, Sebastian Khan, Mark Hannam, Michael Pürrer, Frank Ohme, Xisco Jiménez Forteza, and Alejandro Bohé. Frequency-domain gravitational waves from nonprecessing black-hole binaries. I. New numerical waveforms and anatomy of the signal. *Phys. Rev.*, D93(4):044006, 2016. doi: 10.1103/PhysRevD.93.044006.

[6] Sebastian Khan, Sascha Husa, Mark Hannam, Frank Ohme, Michael Pürrer, Xisco Jiménez Forteza, and Alejandro Bohé. Frequency-domain gravitational waves from nonprecessing black-hole binaries. II. A phenomenological model for the advanced detector era. *Phys. Rev.*, D93(4):044007, 2016. doi: 10.1103/PhysRevD.93.044007.

[7] Xisco Jiménez-Forteza, David Keitel, Sascha Husa, Mark Hannam, Sebastian Khan, and Michael Pürrer. Hierarchical data-driven approach to fitting numerical relativity data for nonprecessing binary black holes with an application to final spin and radiated energy. *Phys. Rev.*, D95(6):064024, 2017. doi: 10.1103/PhysRevD.95.064024.

[8] David Keitel, Xisco Jiménez Forteza, Sascha Husa, Lionel London, Sebastiano Bernuzzi, Enno Harms, Alessandro Nagar, Mark Hannam, Sebastian Khan, Michael Pürrer, Geraint Pratten, and Vivek Chaurasia. The most powerful astrophysical events: Gravitational-wave peak luminosity of binary black holes as predicted by numerical relativity. *Phys. Rev.*, D96(2):024006, 2017. doi: 10.1103/PhysRevD.96.024006.

[9] Alejandro Bohé et al. Improved effective-one-body model of spinning, nonprecessing binary black holes for the era of gravitational-wave astrophysics with advanced detectors. *Phys. Rev.*, D95(4):044028, 2017. doi: 10.1103/PhysRevD.95.044028.

[10] Cecilio García-Quirós, Marta Colleoni, Sascha Husa, Héctor Estellés, Geraint Pratten, Antoni Ramos-Buades, Maite Mateu-Lucena, and Rafel Jaume. IMRPhenomXHM: A multi-mode frequency-domain model for the gravitational wave signal from non-precessing black-hole binaries. *ArXiv e-prints*, 2020.

[11] Lionel London, Sebastian Khan, Edward Fauchon-Jones, Cecilio García, Mark Hannam, Sascha Husa, Xisco Jiménez-Forteza, Chinmay Kalaghatgi, Frank Ohme, and Francesco Pannarale. First higher-multipole model of gravitational waves from spinning and coalescing black-hole binaries. *Phys. Rev. Lett.*, 120(16):161102, 2018. doi: 10.1103/PhysRevLett.120.161102.

[12] J. Veitch et al. Parameter estimation for compact binaries with ground-based gravitational-wave observations using the LALInference software library. *Phys. Rev.*, D91(4):042003, 2015. doi: 10.1103/PhysRevD.91.042003.

[13] Gregory Ashton et al. BILBY: A user-friendly Bayesian inference library for gravitational-wave astronomy. *Astrophys. J. Suppl.*, 241(2):27, 2019. doi: 10.3847/1538-4365/ab06fc.

[14] Serena Vinciguerra, John Veitch, and Ilya Mandel. Accelerating gravitational wave parameter estimation with multi-band template interpolation. *Class. Quant. Grav.*, 34(11):115006, 2017. doi: 10.1088/1361-6382/aa6d44.

[15] Sebastian Khan, Katerina Chatziioannou, Mark Hannam, and Frank Ohme. Phenomenological model for the gravitational-wave signal from precessing binary black holes with two-spin effects. *Phys. Rev.*, D100(2):024059, 2019. doi: 10.1103/PhysRevD.100.024059.

[16] Sebastian Khan, Frank Ohme, Katerina Chatziioannou, and Mark Hannam. Including higher order multipoles in gravitational-wave models for precessing binary black holes. *Phys. Rev.*, D101(2):024056, 2020. doi: 10.1103/PhysRevD.101.024056.

[17] Patricia Schmidt, Mark Hannam, Sascha Husa, and P. Ajith. Tracking the precession of compact binaries from their gravitational-wave signal. *Phys. Rev.*, D84:024046, 2011. doi: 10.1103/PhysRevD.84.024046.

[18] Patricia Schmidt, Mark Hannam, and Sascha Husa. Towards models of gravitational waveforms from generic binaries: A simple approximate mapping between precessing and non-precessing inspiral signals. *Phys. Rev.*, D86:104063, 2012. doi: 10.1103/PhysRevD.86.104063.

[19] LIGO Scientific Collaboration. LIGO Algorithm Library - LALSuite. free software (GPL), https://doi.org/10.7935/GT1W-FZ16, 2020.

[20] Davide Gerosa, Michael Kesden, Richard O'Shaughnessy, Antoine Klein, Emanuele Berti, Ulrich Sperhake, and Daniele Trifirò. Precessional instability in binary black holes with aligned spins. *Phys. Rev. Lett.*, 115:141102, 2015. doi: 10.1103/PhysRevLett.115.141102.

[21] Bernd Bruegmann, Jose A. Gonzalez, Mark Hannam, Sascha Husa, and Ulrich Sperhake. Exploring black hole superkicks. *Phys. Rev.*, D77:124047, 2008. doi: 10.1103/PhysRevD.77.124047.

[22] Antoni Ramos-Buades, Patricia Schmidt, Geraint Pratten, and Sascha Husa. Validity of common modelling approximations for precessing binary black holes with higher-order modes. *ArXiv e-prints*, 2020.

[23] Alejandro Bohé, Mark Hannam, Sascha Husa, Frank Ohme, Michael Puerrer, and Patricia Schmidt. Phenompv2 - technical notes for lal implementation. Technical Report LIGO-T1500602, LIGO Project, 2016. URL https://dcc.ligo.org/LIGO-T1500602.

[24] Benjamin P. Abbott et al. Effects of waveform model systematics on the interpretation of GW150914. *Class. Quant. Grav.*, 34(10):104002, 2017. doi: 10.1088/1361-6382/aa6854.

[25] B. P. Abbott et al. Observation of Gravitational Waves from a Binary Black Hole Merger. *Phys. Rev. Lett.*, 116(6):061102, 2016. doi: 10.1103/PhysRevLett.116.061102.

[26] Theocharis A. Apostolatos, Curt Cutler, Gerald J. Sussman, and Kip S. Thorne. Spin induced orbital precession and its modulation of the gravitational wave forms from merging binaries. *Phys. Rev.*, D49:6274–6297, 1994. doi: 10.1103/PhysRevD.49.6274.

[27] Lawrence E. Kidder. Coalescing binary systems of compact objects to post-Newtonian 5/2 order. 5. Spin effects. *Phys. Rev.*, D52:821–847, 1995. doi: 10.1103/PhysRevD.52.821.

[28] Patricia Schmidt, Ian W. Harry, and Harald P. Pfeiffer. Numerical Relativity Injection Infrastructure. *ArXiv e-prints*, 2017.

[29] K. S. Thorne. Multipole Expansions of Gravitational Radiation. *Rev. Mod. Phys.*, 52:299–339, 1980. doi: 10.1103/RevModPhys.52.299.

[30] J. N. Goldberg, A. J. MacFarlane, E. T. Newman, F. Rohrlich, and E. C. G. Sudarshan. Spin s spherical harmonics and edth. *J. Math. Phys.*, 8:2155, 1967. doi: 10.1063/1.1705135.

[31] Yves Wiaux, L. Jacques, and P. Vandergheynst. Fast spin +-2 spherical harmonics transforms. *J. Comput. Phys.*, 226:2359–2371, 2007. doi: 10.1016/j.jcp.2007.07.005.

[32] Michael Boyle, Robert Owen, and Harald P. Pfeiffer. A geometric approach to the precession of compact binaries. *Phys. Rev. D*, 84:124011, 2011. doi: 10.1103/PhysRevD.84.124011.

[33] Sylvain Marsat and John G. Baker. Fourier-domain modulations and delays of gravitational-wave signals. *ArXiv e-prints*, 2018.

[34] K. G. Arun, Alessandra Buonanno, Guillaume Faye, and Evan Ochsner. Higher-order spin effects in the amplitude and phase of gravitational waveforms emitted by inspiraling compact binaries: Ready-to-use gravitational waveforms. *Phys. Rev.*, D79:104023, 2009. doi: 10.1103/PhysRevD.79.104023,10.1103/PhysRevD.84.049901. [Erratum: Phys. Rev.D84,049901(2011)].

[35] Wolfram Research, Inc. Mathematica, Version 12.0, 2019. URL https://www.wolfram.com/mathematica. Champaign, IL.

[36] Lee Samuel Finn and David F. Chernoff. Observing binary inspiral in gravitational radiation: One interferometer. *Phys. Rev.*, D47:2198–2219, 1993. doi: 10.1103/PhysRevD.47.2198.

[37] Curt Cutler and Eanna E. Flanagan. Gravitational waves from merging compact binaries: How accurately can one extract the binary's parameters from the inspiral wave form? *Phys. Rev.*, D49:2658–2697, 1994. doi: 10.1103/PhysRevD.49.2658.

[38] Serge Droz, Daniel J. Knapp, Eric Poisson, and Benjamin J. Owen. Gravitational waves from inspiraling compact binaries: Validity of the stationary phase approximation to the Fourier transform. *Phys. Rev.*, D59:124016, 1999. doi: 10.1103/PhysRevD.59.124016.

[39] B. P. Abbott et al. GWTC-1: A Gravitational-Wave Transient Catalog of Compact Binary Mergers Observed by LIGO and Virgo during the First and Second Observing Runs. *Phys. Rev.*, X9(3):031040, 2019. doi: 10.1103/PhysRevX.9.031040.

[40] Luc Blanchet, Alessandra Buonanno, and Guillaume Faye. Tail-induced spin-orbit effect in the gravitational radiation of compact binaries. *Phys. Rev.*, D84:064041, 2011. doi: 10.1103/PhysRevD.84.064041.

[41] Sylvain Marsat, Luc Blanchet, Alejandro Bohe, and Guillaume Faye. Gravitational waves from spinning compact object binaries: New post-Newtonian results. 2013.

[42] Héctor Estellés, Antoni Antoni Ramos, Sascha Husa, Cecilio García Quirós, and Leila Haegel. IMRPhenomTP: A phenomenological time domain model for dominant quadrupole gravitational wave signal of coalescing binary black holes. *in preparation*, 2020.

[43] Patricia Schmidt, Frank Ohme, and Mark Hannam. Towards models of gravitational waveforms from generic binaries II: Modelling precession effects with a single effective precession parameter. *Phys. Rev.*, D91(2):024043, 2015. doi: 10.1103/PhysRevD.91.024043.

[44] C. M. Bender and Orszag S. A. *Advanced Mathematical Methods of Scientists and Engineers I, Asymptotic Methods and Perturbation Theory.* Springer, New York, 1999.

[45] Etienne Racine. Analysis of spin precession in binary black hole systems including quadrupole-monopole interaction. *Phys. Rev.*, D78:044021, 2008. doi: 10.1103/PhysRevD.78.044021.

[46] Antoine Klein, Neil Cornish, and Nicolás Yunes. Gravitational waveforms for precessing, quasicircular binaries via multiple scale analysis and uniform asymptotics: The near spin alignment case. *Phys. Rev.*, D88(12):124015, 2013. doi: 10.1103/PhysRevD.88.124015.

[47] Michael Kesden, Davide Gerosa, Richard O'Shaughnessy, Emanuele Berti, and Ulrich Sperhake. Effective potentials and morphological transitions for binary black-hole spin precession. *Phys. Rev. Lett.*, 114(8):081103, 2015. doi: 10.1103/PhysRevLett.114.081103.

[48] Katerina Chatziioannou, Antoine Klein, Nicolás Yunes, and Neil Cornish. Gravitational Waveforms for Precessing, Quasicircular Compact Binaries with Multiple Scale Analysis: Small Spin Expansion. *Phys. Rev.*, D88(6):063011, 2013. doi: 10.1103/PhysRevD.88.063011.

[49] Antoine Klein, Neil Cornish, and Nicolás Yunes. Fast Frequency-domain Waveforms for Spin-Precessing Binary Inspirals. *Phys. Rev.*, D90:124029, 2014. doi: 10.1103/PhysRevD.90.124029.

[50] Miriam Cabero, Alex B. Nielsen, Andrew P. Lundgren, and Collin D. Capano. Minimum energy and the end of the inspiral in the post-Newtonian approximation. *Phys. Rev.*, D95(6):064016, 2017. doi: 10.1103/PhysRevD.95.064016.

[51] Luc Blanchet. Gravitational radiation from post-Newtonian sources and inspiralling compact binaries. *Living Rev. Rel.*, 9:4, 2006.

[52] Alexandre Le Tiec, Luc Blanchet, and Bernard F. Whiting. The First Law of Binary Black Hole Mechanics in General Relativity and Post-Newtonian Theory. *Phys. Rev.*, D85:064039, 2012. doi: 10.1103/PhysRevD.85.064039.

[53] Alejandro Bohe, Sylvain Marsat, Guillaume Faye, and Luc Blanchet. Next-to-next-to-leading order spin-orbit effects in the near-zone metric and precession equations of compact binaries. *Class. Quant. Grav.*, 30:075017, 2013. doi: 10.1088/0264-9381/30/7/075017.

[54] Thibault Damour, Piotr Jaranowski, and Gerhard Schäfer. Nonlocal-in-time action for the fourth post-Newtonian conservative dynamics of two-body systems. *Phys. Rev.*, D89(6):064058, 2014. doi: 10.1103/PhysRevD.89.064058.

[55] Laura Bernard, Luc Blanchet, Guillaume Faye, and Tanguy Marchand. Center-of-Mass Equations of Motion and Conserved Integrals of Compact Binary Systems at the Fourth Post-Newtonian Order. *Phys. Rev.*, D97(4):044037, 2018. doi: 10.1103/PhysRevD.97.044037.

[56] Luc Blanchet and Alexandre Le Tiec. First Law of Compact Binary Mechanics with Gravitational-Wave Tails. *Class. Quant. Grav.*, 34(16):164001, 2017. doi: 10.1088/1361-6382/aa79d7.

[57] Sylvain Marsat. Cubic order spin effects in the dynamics and gravitational wave energy flux of compact object binaries. *Class. Quant. Grav.*, 32(8):085008, 2015. doi: 10.1088/0264-9381/32/8/085008.

[58] Justin Vines and Jan Steinhoff. Spin-multipole effects in binary black holes and the test-body limit. *Phys. Rev.*, D97(6):064010, 2018. doi: 10.1103/PhysRevD.97.064010.

[59] Nils Siemonsen, Jan Steinhoff, and Justin Vines. Gravitational waves from spinning binary black holes at the leading post-Newtonian orders at all orders in spin. *Phys. Rev.*, D97(12):124046, 2018. doi: 10.1103/PhysRevD.97.124046.

[60] Nathan K. Johnson-McDaniel, Anuradha Gupta, P. Ajith, David Keitel, Ofek Birnholtz, Frank Ohme, and Sascha Husa. Determining the final spin of a binary black hole system including in-plane spins: Method and checks of accuracy. Technical Report LIGO-T1600168, LIGO, 2016. URL https://dcc.ligo.org/T1600168/public. https://dcc.ligo.org/LIGO-T1600168/public/main.

[61] Vijay Varma, Davide Gerosa, Leo C. Stein, François Hébert, and Hao Zhang. High-accuracy mass, spin, and recoil predictions of generic black-hole merger remnants. *Phys. Rev. Lett.*, 122(1):011101, 2019. doi: 10.1103/PhysRevLett.122.011101.

[62] Luciano Rezzolla, Enrico Barausse, Ernst Nils Dorband, Denis Pollney, Christian Reisswig, Jennifer Seiler, and Sascha Husa. On the final spin from the coalescence of two black holes. *Phys. Rev.*, D78:044002, 2008. doi: 10.1103/PhysRevD.78.044002.

[63] Michael Boyle et al. The SXS Collaboration catalog of binary black hole simulations. *Class. Quant. Grav.*, 36(19):195006, 2019. doi: 10.1088/1361-6382/ab34e2.

[64] SXS Collaboration. SXS Gravitational Waveform Database. https://www.black-holes.org/waveforms, 2019.

[65] Vijay Varma, Scott E. Field, Mark A. Scheel, Jonathan Blackman, Davide Gerosa, Leo C. Stein, Lawrence E. Kidder, and Harald P. Pfeiffer. Surrogate models for precessing binary black hole simulations with unequal masses. *Phys. Rev. Research.*, 1:033015, 2019. doi: 10.1103/PhysRevResearch.1.033015.

[66] J. Aasi et al. Advanced LIGO. *Class. Quant. Grav.*, 32:074001, 2015. doi: 10.1088/0264-9381/32/7/074001.

[67] L. Barsotti, P. Fritschel, M. Evans, and S. Gras. The updated Advanced LIGO design curve. Technical Report LIGO-T1800044, LIGO Project, 2018. URL https://dcc.ligo.org/T1800044/public.

[68] Ian Harry, Stephen Privitera, Alejandro Bohé, and Alessandra Buonanno. Searching for gravitational waves from compact binaries with precessing spins. *Phys. Rev. D*, 94:024012, Jul 2016. doi: 10.1103/PhysRevD.94.024012. URL https://link.aps.org/doi/10.1103/PhysRevD.94.024012.

[69] Pauli Virtanen, Ralf Gommers, Travis E. Oliphant, Matt Haberland, Tyler Reddy, David Cournapeau, and et al.cec. SciPy 1.0: Fundamental Algorithms for Scientific Computing in Python. *Nature Methods*, 17:261–272, 2020. doi: https://doi.org/10.1038/s41592-019-0686-2.

[70] Ian Harry, Stephen Privitera, Alejandro Bohé, and Alessandra Buonanno. Searching for gravitational waves from compact binaries with precessing spins. *Phys. Rev. D*, 94:024012, Jul 2016. doi: 10.1103/PhysRevD.94.024012. URL https://link.aps.org/doi/10.1103/PhysRevD.94.024012.

[71] Juan Calderón Bustillo, Pablo Laguna, and Deirdre Shoemaker. Detectability of gravitational waves from binary black holes: Impact of precession and higher modes. *Phys. Rev. D*, 95:104038, May 2017. doi: 10.1103/PhysRevD.95.104038. URL https://link.aps.org/doi/10.1103/PhysRevD.95.104038.

[72] Vijay Varma, Scott E. Field, Mark A. Scheel, Jonathan Blackman, Lawrence E. Kidder, and Harald P. Pfeiffer. Surrogate model of hybridized numerical relativity

binary black hole waveforms. *Phys. Rev.*, D99(6):064045, 2019. doi: 10.1103/PhysRevD.99.064045.

[73] Roberto Cotesta, Sylvain Marsat, and Michael Pürrer. Frequency domain reduced order model of aligned-spin effective-one-body waveforms with higher-order modes. *ArXiv e-prints*, 2020.

[74] Roberto Cotesta, Alessandra Buonanno, Alejandro Bohé, Andrea Taracchini, Ian Hinder, and Serguei Ossokine. Enriching the Symphony of Gravitational Waves from Binary Black Holes by Tuning Higher Harmonics. *Phys. Rev.*, D98(8):084028, 2018. doi: 10.1103/PhysRevD.98.084028.

[75] Alessandra Buonanno, Bala Iyer, Evan Ochsner, Yi Pan, and B. S. Sathyaprakash. Comparison of post-Newtonian templates for compact binary inspiral signals in gravitational-wave detectors. *Phys. Rev.*, D80:084043, 2009. doi: 10.1103/PhysRevD.80.084043.

[76] Serguei Ossokine et al. Multipolar Effective-One-Body Waveforms for Precessing Binary Black Holes: Construction and Validation. 4 2020.

[77] Alessandro Nagar and Piero Rettegno. Efficient effective one body time-domain gravitational waveforms. *Phys. Rev.*, D99(2):021501, 2019. doi: 10.1103/PhysRevD.99.021501.

[78] Michael Pürrer. Frequency domain reduced order model of aligned-spin effective-one-body waveforms with generic mass-ratios and spins. *Phys. Rev.*, D93(6):064041, 2016. doi: 10.1103/PhysRevD.93.064041.

[79] Harbir Antil, Scott E. Field, Frank Herrmann, Ricardo H. Nochetto, and Manuel Tiglio. Two-step greedy algorithm for reduced order quadratures. *J. Sci. Comput.*, 57:604–637, 2013. doi: 10.1007/s10915-013-9722-z.

[80] Priscilla Canizares, Scott E. Field, Jonathan R. Gair, and Manuel Tiglio. Gravitational wave parameter estimation with compressed likelihood evaluations. *Phys. Rev.*, D87(12):124005, 2013. doi: 10.1103/PhysRevD.87.124005.

[81] Priscilla Canizares, Scott E. Field, Jonathan Gair, Vivien Raymond, Rory Smith, and Manuel Tiglio. Accelerated gravitational-wave parameter estimation with reduced order modeling. *Phys. Rev. Lett.*, 114(7):071104, 2015. doi: 10.1103/PhysRevLett.114.071104.

[82] Rory Smith, Scott E. Field, Kent Blackburn, Carl-Johan Haster, Michael Pürrer, Vivien Raymond, and Patricia Schmidt. Fast and accurate inference on gravitational waves from precessing compact binaries. *Phys. Rev. D*, 94:044031, Aug 2016.

doi: 10.1103/PhysRevD.94.044031. URL https://link.aps.org/doi/10.1103/PhysRevD.94.044031.

[83] John Veitch and Alberto Vecchio. Assigning confidence to inspiral gravitational wave candidates with Bayesian model selection. *Class. Quant. Grav.*, 25:184010, 2008. doi: 10.1088/0264-9381/25/18/184010.

[84] J. Veitch and A. Vecchio. Bayesian coherent analysis of in-spiral gravitational wave signals with a detector network. *Phys. Rev.*, D81:062003, 2010. doi: 10.1103/PhysRevD.81.062003.

[85] J. Skilling. Nested Sampling. In R. Fischer, R. Preuss, and U. V. Toussaint, editors, *24th International Workshop on Bayesian Inference and Maximum Entropy Methods in Science and Engineering*, volume 735 of *AIP Conf. Proc.*, pages 395–405, November 2004. doi: 10.1063/1.1835238.

[86] Joshua S Speagle. dynesty: a dynamic nested sampling package for estimating bayesian posteriors and evidences. *Monthly Notices of the Royal Astronomical Society*, 493(3):3132–3158, Feb 2020. ISSN 1365-2966. doi: 10.1093/mnras/staa278. URL http://dx.doi.org/10.1093/mnras/staa278.

[87] Rory Smith and Gregory Ashton. Expediting Astrophysical Discovery with Gravitational-Wave Transients Through Massively Parallel Nested Sampling. *ArXiv e-prints*, 2019.

[88] LIGO Scientific Collaboration, Virgo Collaboration. Gravitational Wave Open Science Center. https://www.gw-openscience.org, 2019.

[89] Rich Abbott et al. Open data from the first and second observing runs of Advanced LIGO and Advanced Virgo. *ArXiv e-prints*, 2019.

[90] LIGO Scientific Collaboration, Virgo Collaboration. Calibration uncertainty envelope release for GWTC-1, 2019. URL https://dcc.ligo.org/LIGO-P1900040/public.

[91] LIGO Scientific Collaboration, Virgo Collaboration. Power Spectral Densities (PSD) release for GWTC-1, 2019. URL https://dcc.ligo.org/LIGO-P1900011/public.

[92] Craig Cahillane, Joe Betzwieser, Duncan A. Brown, Evan Goetz, Evan D. Hall, Kiwamu Izumi, Shivaraj Kandhasamy, Sudarshan Karki, Jeff S. Kissel, Greg Mendell, Richard L. Savage, Darkhan Tuyenbayev, Alex Urban, Aaron Viets, Madeline Wade, and Alan J. Weinstein. Calibration uncertainty for Advanced LIGO's

first and second observing runs. *Physical Review D*, 96(10):102001, 2017. doi: 10.1103/PhysRevD.96.102001.

[93] Aaron Viets et al. Reconstructing the calibrated strain signal in the Advanced LIGO detectors. *Class. Quant. Grav.*, 35(9):095015, 2018. doi: 10.1088/1361-6382/aab658.

[94] C. Cahillane, M. Hulko, J. S. Kissel, et al. O2 C02 Calibration Uncertainty. Technical Report LIGO-G1800319, LIGO Scientific Collaboration, 2018. URL https://dcc.ligo.org/LIGO-G1800319/public.

[95] Katerina Chatziioannou et al. On the properties of the massive binary black hole merger GW170729. *Phys. Rev.*, D100(10):104015, 2019. doi: 10.1103/PhysRevD.100.104015.

[96] Ethan Payne, Colm Talbot, and Eric Thrane. Higher order gravitational-wave modes with likelihood reweighting. *Phys. Rev.*, D100(12):123017, 2019. doi: 10.1103/PhysRevD.100.123017.

[97] Tim Dietrich, Sebastiano Bernuzzi, and Wolfgang Tichy. Closed-form tidal approximants for binary neutron star gravitational waveforms constructed from high-resolution numerical relativity simulations. *Phys. Rev. D*, 96:121501, Dec 2017. doi: 10.1103/PhysRevD.96.121501. URL https://link.aps.org/doi/10.1103/PhysRevD.96.121501.

[98] Tim Dietrich, Anuradha Samajdar, Sebastian Khan, Nathan K. Johnson-McDaniel, Reetika Dudi, and Wolfgang Tichy. Improving the NRTidal model for binary neutron star systems. *Phys. Rev.*, D100(4):044003, 2019. doi: 10.1103/PhysRevD.100.044003.

[99] Jonathan E. Thompson, Edward Fauchon-Jones, Sebastian Khan, Elisa Nitoglia, Francesco Pannarale, Tim Dietrich, and Mark Hannam. Modeling the gravitational wave signature of neutron star black hole coalescences: PhenomNSBH. *ArXiv e-prints*, 2020.

[100] D. Brown, S. Fairhurst, B. Krishnan, R.A. Mercer, R.K. Kopparapu, L. Santamaria, and J.T. Whelan. Data formats for numerical relativity waves. *ArXiv e-prints*, 9 2007.

[101] Luc Blanchet, Guillaume Faye, Bala R. Iyer, and Siddhartha Sinha. The Third post-Newtonian gravitational wave polarisations and associated spherical harmonic modes for inspiralling compact binaries in quasi-circular orbits. *Class. Quant. Grav.*, 25:165003, 2008. doi: 10.1088/0264-9381/25/16/165003,10.1088/0264-9381/29/23/239501. [Erratum: Class. Quant. Grav.29,239501(2012)].

[102] LIGO Scientific Collaboration. LALSimulation: Inspiral Simulation Packages. https://lscsoft.docs.ligo.org/lalsuite/lalsimulation/group__lalsimulation__inspiral.html, 2020.

[103] David M. Beazley. SWIG: An Easy to Use Tool for Integrating Scripting Languages with C and C++. In *Proc. 4th Conf. USENIX Tcl/Tk Workshop*, pages 15–15, Berkeley, CA, USA, 1996. USENIX Association. URL http://dl.acm.org/citation.cfm?id=1267498.1267513.

[104] David M. Beazley et al. SWIG - Simplified Wrapper and Interface Generator. https://www.swig.org, 2019.

[105] Karl Wette. SWIGLAL: Python and Octave interfaces to the LALSuite gravitational-wave data analysis libraries. *in preparation*, 2020. https://dcc.ligo.org/P2000094/.

Chapter 6

Conclusions

In this thesis, I have presented two new phenomenological models that describe the gravitational wave emission both for non-precessing and precessing black-hole binaries including the effect of several subdominant harmonics. I also presented the technique of multibanding for accelerating the evaluation of waveform models with adapted grids. While this is a general technique that can be applied to any Fourier domain model and extended to the time domain, we applied it to the two models presented here: IMRPhenomXHM and IMRPhenomXPHM. As part of the thesis, we implemented the two models together with the multibanding technique in the LSC Algorithm Library Suite (LALSuite) and after an exhaustive review of the code implementation and performance by members of the LSC the two models were approved and made available to the whole collaboration to be used in future official studies. With the recent improvements in the sensitivity of LIGO detectors the events where higher harmonics modes and precession are relevant are more likely to happen, therefore is crucial to incorporate waveform models that accurately describe these effects. With the addition of this new physics, the PE studies become also more complex and need more detailed analysis. Consequently, dispose of computationally efficient waveform models is crucial to carry out this task. The two new models presented in this thesis significantly outperform both in accuracy and computational efficiency the previous analogous models IMRPhenomHM and IMRPhenomPv3HM. They are also the most efficient models when compared to the analogous models of the other waveform families: EOB and Surrogate models. For these reasons, we expect that the models presented in this thesis will play a very important role in the PE studies of the upcoming gravitational wave events. In the following, I summarize in more detail the main results and contributions of the three studies presented in this thesis.

IMRPhenomXHM

This is a new phenomenological waveform model for the gravitational wave signal originating from non-precessing binary black-hole systems. Several higher spherical harmonics beyond the dominant mode are included: $(l, m) = (2, \pm 2), (2, \pm 1), (3, \pm 3), (3, \pm 2), (4, \pm 4)$. The previous model IMRPhenomHM was based on a PN scaling of the amplitude and phase of the dominant $(2, 2)$ mode given by IMRPhenomD what approximately reproduces the amplitude and phases of the higher modes. Nevertheless, IMRPhenomXHM is calibrated with the higher modes data from NR simulations including waveforms in the EMR limit. This improves the accuracy of the model in several scenarios. In the first place, the amplitude and phase of every individual mode are more accurately modelled, but also the relative phases between modes are now more accurate and they do not suffer from the dephasing introduced by the PN expressions during the merger. This allows us for a much better estimate of the final black hole recoil quantity. In addition, IMRPhenomXHM does not neglect the contribution of the odd modes in the equal mass limit. Finally, we include the description of the sharp features of the *mode-mixing* that appears for the $(3, 2)$ mode by modelling the ringdown part of the waveform in the spheroidal basics and performing a rotation back to the spherical. This technique can be straightforwardly extended to other modes with mixing like the $(4, 3)$ which will be incorporated in future updates of the model.

The calibration of the model to NR simulations is performed separately for the amplitude and for the phase. I carried out the calibration for the amplitude while Marta Colleoni did the corresponding for the phase. The amplitude is fully calibrated to NR in the three frequency regions: inspiral, intermediate and ringdown; while the phase only needs calibration in the intermediate one. In the inspiral, the phase employs the same PN scaling than IMRPhenomHM but using the improved model IMRPhenomXAS instead of IMRPhenomD and for the ringdown, it uses a suitable scaling heuristically determined. For the calibration of both amplitude and phase we used NR simulations from the publicly available SXS catalogue [1] as well as some private ones performed with the BAM [2–4] and ET [5] codes. We refined our pipeline to process the data from the different NR codes and we produced them in a standard HDF5 format [6]. This is used then to build the hybrid waveforms by plugging to the NR waveform an inspiral part described by EOB.

Focusing on the calibration of the amplitude, we first obtained the PN ansatz for the inspiral part of the higher modes. We put together the different PN orders present in the literature, correctly accounting for the different conventions in the several peer-reviewed articles and transformed them into the Fourier domain employing the SPA. Comparing these results with those in the literature [7] we realized that there was a mistake

in the aforementioned article which was afterwards avowed by the authors. The IMRPhenomHM model used to employ the wrong expressions from [7], as a member of the review team I flagged this issue and the error was corrected improving the performance of the model.

Next step consisted in obtaining the adequate cutting frequencies that allow us for a correct division of the frequency range across parameter space both for comparable and for EMR cases. Once the direct fits were done, the calibration of the coefficients over parameter space required intense human work. We had to adapt the hierarchical fitting procedure presented in [8] to incorporate the new features and new symmetries introduced by the higher modes. During this stage, inaccurate NR waveforms can be easily spotted as outliers since they show off from the smooth surfaces depicted by the "well behaved" data. Once the parameter space fits were finished we checked that the reconstructed model reproduces the input NR data that we used for the calibration. Then we passed to study the behaviour of the model outside the calibration region, i.e. for cases for which we lack NR data to compare with. We observed then that for cases where the amplitude of the higher modes was close to zero the accuracy of the fits was not enough to produce well-behaved collocation points. For that reason, we carried out an intense study across parameter space and developed a series of vetoes that removed ill-behaved collocation points and adapted the reconstruction of the model accordingly. This issue will be revisited in the future and we expect that the inclusion of more NR waveforms, mainly from the recent release of the new SXS catalogue [9], can help to properly solve this issue. Finally, we carried out a modular implementation of the model in LALSuite which allows one to easily incorporate these and other new updates to the model.

Multibanding

We presented a modified version of the multibanding technique introduced in [10] applied to accelerate the evaluation of waveform models for data analysis applications. While the technique can also be applied in the time domain, we focused on the Fourier domain and particularly to the IMRPhenomXHM model. In the time domain, the inspiral part is slowly varying since the two black holes are far apart while in the merger they are so close that the frequency is much higher and the waveform much more oscillating. In the Fourier domain, the behaviour is exactly the opposite, the inspiral is very oscillating and the merger-ringdown slowly varying. This motivated the use of a coarser non-uniform frequency grid, where the model is evaluated, then this set of points is interpolated into the final uniform grid. Since the interpolation is a much cheaper operation than the evaluation of the model this supposes a great speed up in the calculation of the waveform. We modified the criteria of [10] to choose the coarser grid and extend it to the merger-ringdown and for higher harmonics beyond the dominant one. Since the mode-mixing

of the $(3, 2)$ mode happened precisely in the merger-ringdown where the multibanding provides less points, we applied the algorithm of multibanding to the merger-ringdown waveform in the basis of spheroidal harmonics where the mixing is not present, and then applied a rotation back to spherical to obtain the final waveform. The accuracy and speed of the multibanding are controlled with a threshold value that represents the error in the interpolation. The lower this value the more restrictive the algorithm becomes. This translates into a higher accuracy at the cost of lower speed up. We asserted the robustness and accuracy of the algorithm by performing an exploration of one million points across parameter space and comparing waveforms without multibanding to waveforms with four different thresholds of multibanding. We also carried out PE studies which returned consistent results between thresholds. Benchmarks studies against other waveform models showed that even with a conservative choice of the multibanding threshold both the IMRPhenomXHM and IMRPhenomXPHM models are the fastest models currently available. We left for future work the extension to the time domain that will be applied to the recently developed IMRPhenomTP model [11], and a more precise application of the algorithm for the Euler angles We presented a modified version of the multibanding technique introduced in [10] applied to accelerate the evaluation of waveform models for data analysis applications. While the technique can also be applied in the time domain, we focused to the Fourier domain and particularly to the IMRPhenomXHM model. In time domain the inspiral part is slowly varying since the two black holes are far apart while in the merger they are so close that the frequency is much higher and the waveform far more oscillating. In the Fourier domain the behaviour is exactly the opposite, the inspiral is very oscillating and the merger-ringdown slowly varying. This motivated the use of a coarser non-uniform frequency grid, where the model is evaluated, then this set of points is interpolated into the final uniform grid. Since the interpolation is a much cheaper operation than the evaluation of the model this supposes a great speed up in the calculation of the waveform. We modified the criteria of [10] to choose the coarser grid and extend it to the merger-ringdown and for higher harmonics beyond the dominant one. Since the mode-mixing of the $(3, 2)$ mode happened precisely in the merger-ringdown where the multibanding provides less points, we applied the algorithm of multibanding to the merger-ringdown waveform in the basis of spheroidal harmonics where the mixing is not present, and then applied a rotation back to spherical to obtain the final waveform. The accuracy and speed of the multibanding is controlled with a threshold value that represents the error in the interpolation. The lower this value the more restrictive the algorithm becomes. This translates into a higher accuracy at the cost of lower speed up. We asserted the robustness and accuracy of the algorithm by performing an exploration of one million of points across parameter space and comparing waveforms without multibanding to waveforms with four different thresholds of multibanding. We also carried out PE studies which returned consistent results between

thresholds. Benchmarks studies against other waveform models showed that even with a conservative choice of the multibanding threshold both the IMRPhenomXHM and IMRPhenomXPHM models are the fastest models currently available. We left for future work the extension to the time domain that will be applied to the recently developed IMRPhenomTP model [11], and a more precise application of the algorithm for the Euler angles that takes into account the double spin effects of precessing systems.

IMRPhenomXPHM

Finally, we presented the extension of the IMRPhenomXHM model to include precession effects. Apart from some modifications to treat the higher modes, we followed the standard procedure of the twisting-up by which non-precessing modes described in the co-precessing frame are transformed into precessing modes in the inertial frame. The transformation consists in a Euler rotation between the two frames. The time evolution of the Euler angles can be obtained by two prescriptions: the PN next-to-next-to-leading order (NNLO) and the Multi-Scale-Analysis (MSA). Following the modular philosophy of the IMRPhenomX models both prescriptions were implemented, together with different options to choose the description of the final spin. Special care was put in obtaining all the precessing conventions correctly, in particular the transformations between frames. We derived all the conventions from end to end for a frequency domain model and properly documented them. The multibanding is already present when computing the non-precessing modes given by IMRPhenomXHM, but we also incorporated this technique for the evaluation of the Euler angles using, in a first approach, the same coarse grid we used for the non-precessing modes. Similarly to what we did for IMRPhenomXHM, we tested the multibanding of the Euler angles across the parameter space for four different thresholds, we performed PE studies that showed consistent results between thresholds and carried out benchmark tests which demonstrated that IMRPhenomXPHM is by far the fastest precessing model available. Regarding the accuracy, IMRPhenomXPHM clearly outperforms the previous analogous model IMRPhenomPv3HM. Its speed, its accuracy and its flexibility make IMRPhenomXPHM a great laboratory for testing physics in the current and future PE studies.

Outlook and future research

The work presented in this thesis constitutes the first release of a new family of computationally efficient waveform models including subdominant effects. These models are thought not to be static but to be easily updated as new data and techniques become available. In this regard, the most immediate improvement of the model is the recalibration to new and more accurate NR simulations. The reduction of the numerical noise

of the simulations will allow us to include more subdominant harmonics like the $(4, 3)$ and $(5, 5)$ and also to improve the performance of the model for those regions where the subdominant harmonics are diminished. A more detailed study of the EMR waveforms produced by solving the Teukolsky equations will indeed improve the understanding of the waveform phenomenology in this region and will help to fill the gap between the NR region $q \sim 18$ and the EMR region $q \sim 1000$.

From the analytical point of view, further developments in PN theory, in particular the inclusion of spin effects in the subdominant harmonics up to 3.5 PN order, would highly benefit our inspiral ansatz and would help to reach a smooth transition between the comparable and EMR regimes.

A near-future extension of the model, for which work has already been started, is to include the effects of tidal deformations [12] to describe binary neutron star systems. This would take into account only the dominant quadrupole part but plans to include subdominant harmonics are being considered too.

For other extensions of the precessing model, we consider developing an ansatz for the Euler angles in the Fourier domain such that its description does not rely on the SPA transformation which is invalid in the merger-ringdown. As discussed in [13] our treatment of mode-mixing in the non-precessing case can not strictly be extended to precession since the mode-mixing happens in the inertial frame instead of in the co-precessing frame, further improvements of the model will tackle this subject. Also, it would be desirable to have a numerical fit for the final spin of precessing systems instead of using an approximate formula as it is currently done. Some of these challenges will be easier to address in the time domain, and I thus foresee synergies with the IMRPhenomTP model. Finally, the computational efficiency of the model can be further optimized by rewriting the code to be parallelizable, for example using the CUDA platform [14] and running on GPUs.

Bibliography

[1] SXS catalogue, 2019. URL https://data.black-holes.org/waveforms/catalog.html.

[2] Bernd Brügmann, José A. González, Mark Hannam, Sascha Husa, Ulrich Sperhake, and Wolfgang Tichy. Calibration of moving puncture simulations. *Phys. Rev. D*, 77:024027, Jan 2008. doi: 10.1103/PhysRevD.77.024027. URL https://link.aps.org/doi/10.1103/PhysRevD.77.024027.

[3] Bernd Brügmann, Wolfgang Tichy, and Nina Jansen. Numerical Simulation of Orbiting Black Holes. *Phys. Rev. Lett.*, 92:211101, May 2004. doi: 10.1103/PhysRevLett.92.211101. URL https://link.aps.org/doi/10.1103/PhysRevLett.92.211101.

[4] Bernd Brügmann. Binary black hole mergers in 3d numerical relativity. *Int. J. Mod. Phys. D8*, 85, 1999.

[5] Einstein Toolkit code, 2018. URL https://doi.org/10.5281/zenodo.3522086.

[6] The HDF Group. Hierarchical Data Format, version 5, 1997-NNNN. http://www.hdfgroup.org/HDF5/.

[7] Chandra Kant Mishra, Aditya Kela, K. G. Arun, and Guillaume Faye. Ready-to-use post-Newtonian gravitational waveforms for binary black holes with nonprecessing spins: An update. *Phys. Rev. D*, 93:084054, Apr 2016. doi: 10.1103/PhysRevD.93.084054. URL https://link.aps.org/doi/10.1103/PhysRevD.93.084054.

[8] Xisco Jiménez-Forteza, David Keitel, Sascha Husa, Mark Hannam, Sebastian Khan, and Michael Pürrer. Hierarchical data-driven approach to fitting numerical relativity data for nonprecessing binary black holes with an application to final spin and radiated energy. *Phys. Rev. D*, 95:064024, Mar 2017. doi: 10.1103/PhysRevD.95.064024. URL https://link.aps.org/doi/10.1103/PhysRevD.95.064024.

[9] Michael Boyle, Daniel Hemberger, Dante A B Iozzo, Geoffrey Lovelace, Serguei Ossokine, Harald P Pfeiffer, Mark A Scheel, Leo C Stein, et al. The SXS collaboration catalog of binary black hole simulations. *Classical and Quantum Gravity*, 36(19):195006, sep 2019. doi: 10.1088/1361-6382/ab34e2. URL https://doi.org/10.1088%2F1361-6382%2Fab34e2.

[10] Serena Vinciguerra, John Veitch, and Ilya Mandel. Accelerating gravitational wave parameter estimation with multi-band template interpolation. *Classical and Quantum Gravity*, 34(11):115006, may 2017. doi: 10.1088/1361-6382/aa6d44. URL https://doi.org/10.1088%2F1361-6382%2Faa6d44.

[11] Héctor Estellés, Antoni Ramos-Buades, Sascha Husa, Cecilio García-Quirós, Marta Colleoni, Leïla Haegel, and Rafel Jaume. IMRPhenomTP: A phenomenological time domain model for dominant quadrupole gravitational wave signal of coalescing binary black holes. *ArXiv: 2004.08302*, 4 2020.

[12] Tim Dietrich, Sebastian Khan, Reetika Dudi, Shasvath J. Kapadia, Prayush Kumar, Alessandro Nagar, Frank Ohme, et al. Matter imprints in waveform models for neutron star binaries: Tidal and self-spin effects. *Phys. Rev. D*, 99:024029, Jan 2019. doi: 10.1103/PhysRevD.99.024029. URL https://link.aps.org/doi/10.1103/PhysRevD.99.024029.

[13] Antoni Ramos-Buades, Patricia Schmidt, Geraint Pratten, and Sascha Husa. Validity of common modelling approximations for precessing binary black holes with higher-order modes. *ArXiv: 2001.10936*, 2020.

[14] CUDA Toolkit for GPU programming, 2007. URL https://developer.nvidia.com/cuda-toolkit.

Abbreviations

ACT Auto-Correlation Times

ADM Arnowitt Deser Misner

BAM Bifunctional Adaptive Mesh

BBH Binary Black Hole

BNS Binary Neutron Star

BSSN Baumgharte Shapiro Shibata Nakamura

CBC Compact Binary Coalescence

ECSK Einstein Cartan Sciama Kibble

EM ElectroMagnetic

EMRI Extreme Mass Ratio

EOB Effective One Body

EOS Equation Of State

ESA European Space Agency

ET Einstein Toolkit

GPU Graphics Processing Unit

GR General Relativity

GSL GNU Scientific Library

GW Gravitational Waves

GWOSC Gravitational Wave Open Science Center

HDF5 Hierarchical Data Format version 5

IMR Inspiral Merger Ringdown

ISCO Innermost Stable Circular Orbit

KAGRA KAmioka GRAvitational wave detector

LIGO Laser Interferometer Gravitational Wave Observatory

LISA Laser Interferometer Space Antenna

LSC LIGO Scientific Collaboration

LVC LIGO-Virgo Collaboration

MCMC Markow Chain MonteCarlo

MECO Minimal Energy Circular Orbit

MSA Multi-Scale Analysis

NNLO Next-to-Next-to-Leading Order

NR Numerical Relativity

NSBH Neutron Star Black Hole

O1 First Observing run of the LIGO gravitational wave detectors

O2 Second Observing run of the LIGO gravitational wave detectors

O3 Third Observing run of the LIGO gravitational wave detectors

PE Parameter Estimation

PN Post Newtonian

PSD Power Spectral Density

QNM Quasi Normal Mode

RMS Root Mean Square

ROM Reduced Order Models

ROQ Reduced Order Quadrature

SNR Signal to Noise Ratio

SPA Stationary Phase Approximation

SpEC Spectral Einstein Code

SWSH Spin-2 Weighted Spherical Harmonics

TT Transverse Traceless

Appendix A

Fourier domain polarizations in terms of individual modes

In this section I derive the expression of the Fourier domain polarizations $\tilde{h}_{+,\times}(f)$ in terms of the individual modes $\tilde{h}_{lm}(f)$ for the non-precessing case. These expressions are truly important for building the multimode waveform model, but can barely be found in the literature. The results are included in the publication presented in chapter 3 and here I show the explicit derivation of such expressions. We start from the basic multimode decomposition in time domain

$$h(t) = h_+(t) - i\, h_\times(t) = \sum_{\ell \geq 2} \sum_{m=-\ell}^{\ell} h_{\ell m}(t)\, {}_{-2}Y_{\ell m}. \tag{A.1}$$

The $h_{+,\times}(t)$ polarizations are related to the real and imaginary part of the strain

$$h_+(t) = \mathrm{Re}(h) = \frac{1}{2}\left(h(t) + h^*(t)\right), \tag{A.2}$$

$$h_\times(t) = -\mathrm{Im}(h) = \frac{i}{2}\left(h(t) - h^*(t)\right) \tag{A.3}$$

In terms of the individual modes the above expressions are written as

$$h_+(t) = \frac{1}{2} \sum_{\ell \geq 2} \sum_{m=-\ell}^{\ell} \left(h_{\ell m}(t)\, {}_{-2}Y_{\ell m} + h^*_{\ell m}(t)\, {}_{-2}Y^*_{\ell m}\right), \tag{A.4}$$

$$h_\times(t) = \frac{i}{2} \sum_{\ell \geq 2} \sum_{m=-\ell}^{\ell} \left(h_{\ell m}(t)\, {}_{-2}Y_{\ell m} - h^*_{\ell m}(t)\, {}_{-2}Y^*_{\ell m}\right), \tag{A.5}$$

The Fourier transform of a real function satisfies that the positive and negative frequency regimes are related by a complex conjugation. Since $h_{+,\times}(t)$ are real functions we have

$$\tilde{h}_+(f) = \tilde{h}^*_+(-f), \qquad \tilde{h}_\times(f) = \tilde{h}^*_\times(-f). \tag{A.6}$$

For this reason we will focus hereafter on the expressions for the polarizations just for the positive frequency regime. Performing the Fourier transform of A.4, A.5 we obtain

$$\tilde{h}_+(f>0) = \frac{1}{2}\sum_{\ell\geq 2}\sum_{m=-\ell}^{\ell}\left(\tilde{h}_{\ell m}(f)\,{}_{-2}Y_{\ell m} + \tilde{h}^*_{\ell m}(-f)\,{}_{-2}Y^*_{\ell m}\right), \tag{A.7}$$

$$\tilde{h}_\times(f>0) = \frac{i}{2}\sum_{\ell\geq 2}\sum_{m=-\ell}^{\ell}\left(\tilde{h}_{\ell m}(f)\,{}_{-2}Y_{\ell m} - \tilde{h}^*_{\ell m}(-f)\,{}_{-2}Y^*_{\ell m}\right). \tag{A.8}$$

Hereafter we drop from the derivation the special case $m = 0$ which is not an oscillatory mode and present some additional complications that are out of the scope in this section. For non-precessing systems the positive and negative modes are related in the time domain by Eq. 2.61, induced by the equatorial symmetry. In the Fourier domain this relation translates into

$$\tilde{h}_{lm}(f) = (-1)^l\,\tilde{h}^*_{l-m}(-f). \tag{A.9}$$

We adopt the conventions of LALSuite for the rotation of the modes such that positive modes ($m > 0$) rotate clockwise and negative modes ($m < 0$) counterclockwise and the convention for the Fourier transform

$$\tilde{h}(f) = \int_{-\infty}^{\infty} h(t)\,e^{-i\,2\pi f t}\,dt, \tag{A.10}$$

The definitions above imply that $\tilde{h}_{lm>0}(f)$ is concentrated in the negative frequency regime and $\tilde{h}_{lm<0}(f)$ in the positive frequency regime:

$$\tilde{h}_{lm>0}(f>0) = 0, \qquad \tilde{h}_{lm<0}(f<0) = 0. \tag{A.11}$$

With the above considerations, expressions A.7, A.8 lead to

$$\tilde{h}_+(f>0) = \frac{1}{2}\sum_{\ell\geq 2}\sum_{m>0}^{\ell}\left(\cancelto{0}{\tilde{h}_{\ell m}(f)}\,{}_{-2}Y_{\ell m} + \tilde{h}^*_{\ell m}(-f)\,{}_{-2}Y^*_{\ell m}\right. \tag{A.12}$$

$$\left. +\tilde{h}_{\ell -m}(f)\,{}_{-2}Y_{\ell -m} + \cancelto{0}{\tilde{h}^*_{\ell -m}(-f)}\,{}_{-2}Y^*_{\ell -m}\right), \tag{A.13}$$

$$\tilde{h}_\times(f>0) = \frac{i}{2}\sum_{\ell\geq 2}\sum_{m>0}^{\ell}\left(\cancelto{0}{\tilde{h}_{\ell m}(f)}\,{}_{-2}Y_{\ell m} - \tilde{h}^*_{\ell m}(-f)\,{}_{-2}Y^*_{\ell m}\right. \tag{A.14}$$

$$+\tilde{h}_{\ell-m}(f)\,{}_{-2}Y_{\ell-m} - \cancelto{0}{\tilde{h}^*_{\ell-m}(-f)}\,{}_{-2}Y^*_{\ell-m}\Big). \tag{A.15}$$

We now use A.9 to obtain the result in terms of the individual modes which have support for positive frequencies (negative m):

$$\tilde{h}_+(f>0) = \frac{1}{2}\sum_{\ell\geq 2}\sum_{m>0}^{\ell}\left((-1)^l\tilde{h}_{\ell-m}(f)\,{}_{-2}Y^*_{\ell m} + \tilde{h}_{\ell-m}(f)\,{}_{-2}Y_{\ell-m}\right), \tag{A.16}$$

$$\tilde{h}_\times(f>0) = \frac{i}{2}\sum_{\ell\geq 2}\sum_{m>0}^{\ell}\left(-(-1)^l\tilde{h}_{\ell-m}(f)\,{}_{-2}Y^*_{\ell m} + \tilde{h}_{\ell-m}(f)\,{}_{-2}Y_{\ell-m}\right), \tag{A.17}$$

and rearranging terms we arrive at the result

$$\tilde{h}_+(f>0) = \frac{1}{2}\sum_{\ell\geq 2}\sum_{m>0}^{\ell}\left({}_{-2}Y_{\ell-m} + (-1)^l\,{}_{-2}Y^*_{\ell m}\right)\tilde{h}_{\ell-m}(f), \tag{A.18}$$

$$\tilde{h}_\times(f>0) = \frac{i}{2}\sum_{\ell\geq 2}\sum_{m>0}^{\ell}\left({}_{-2}Y_{\ell-m} - (-1)^l\,{}_{-2}Y^*_{\ell m}\right)\tilde{h}_{\ell-m}(f). \tag{A.19}$$

From the above expressions we can straightforwardly extract which is the contribution to the polarizations of just a pair of positive and negative modes $(l,\pm m)$ (assuming m>0):

$$\tilde{h}^{l\pm m}_+(f>0) = \frac{1}{2}\left({}_{-2}Y_{\ell-m} + (-1)^l\,{}_{-2}Y^*_{\ell m}\right)\tilde{h}_{\ell-m}(f), \tag{A.20}$$

$$\tilde{h}^{l\pm m}_\times(f>0) = \frac{i}{2}\left({}_{-2}Y_{\ell-m} - (-1)^l\,{}_{-2}Y^*_{\ell m}\right)\tilde{h}_{\ell-m}(f). \tag{A.21}$$

One can also obtain the contribution of just a single (l,m) mode, in which case a distinction between positive and negative m would be needed in order to simplify the result. The expression for a general (l,m) mode is

$$\tilde{h}^{l,m}_+(f>0) = \frac{1}{2}\left(\tilde{h}_{\ell m}(f)\,{}_{-2}Y_{\ell m} + \tilde{h}^*_{\ell m}(-f)\,{}_{-2}Y^*_{\ell m}\right), \tag{A.22}$$

$$\tilde{h}^{l,m}_\times(f>0) = \frac{i}{2}\left(\tilde{h}_{\ell m}(f)\,{}_{-2}Y_{\ell m} - \tilde{h}^*_{\ell m}(-f)\,{}_{-2}Y^*_{\ell m}\right). \tag{A.23}$$

For $m>0$ we recall that modes are zero for positive frequencies, and we use the relation A.9 to write the result in terms of individual modes at positive frequencies:

$$\tilde{h}^{l,m>0}_+(f>0) = \frac{1}{2}\left(\cancelto{0}{\tilde{h}_{\ell m}(f)}\,{}_{-2}Y_{\ell m} + \tilde{h}^*_{\ell m}(-f)\,{}_{-2}Y^*_{\ell m}\right) = \frac{1}{2}\,(-1)^l\,\tilde{h}_{\ell-m}(f)\,{}_{-2}Y^*_{\ell m}, \tag{A.24}$$

$$\tilde{h}^{l,m>0}_\times(f>0) = \frac{i}{2}\left(\cancelto{0}{\tilde{h}_{\ell m}(f)}\,{}_{-2}Y_{\ell m} - \tilde{h}^*_{\ell m}(-f)\,{}_{-2}Y^*_{\ell m}\right) = -\frac{i}{2}\,(-1)^l\,\tilde{h}_{\ell-m}(f)\,{}_{-2}Y^*_{\ell m}. \tag{A.25}$$

For $m < 0$ the modes are zero for negative frequencies and we obtain

$$\tilde{h}_{+}^{l,m<0}(f > 0) = \frac{1}{2}\left(\tilde{h}_{\ell m}(f)\,{}_{-2}Y_{\ell m} + \cancelto{0}{\tilde{h}^{*}_{\ell m}(-f)}\,{}_{-2}Y^{*}_{\ell m}\right) = \frac{1}{2}\,\tilde{h}_{\ell m}(f)\,{}_{-2}Y_{\ell m}, \quad \text{(A.26)}$$

$$\tilde{h}_{\times}^{l,m<0}(f > 0) = \frac{i}{2}\left(\tilde{h}_{\ell m}(f)\,{}_{-2}Y_{\ell m} - \cancelto{0}{\tilde{h}^{*}_{\ell m}(-f)}\,{}_{-2}Y^{*}_{\ell m}\right) = \frac{i}{2}\,\tilde{h}_{\ell m}(f)\,{}_{-2}Y_{\ell m}. \quad \text{(A.27)}$$

Appendix B

Permissions Chapter 3

This appendix gathers all the permissions from the authors authorizing Cecilio García Quirós to include the article presented in Chapter 3 as part of this thesis.

FORMAT CRITERIA FOR DOCTORAL THESES IN THE UNIVERSITY OF THE ILLES BALEARS
Annex 4: Model document of agreement between the co-authors of articles when the thesis is presented as a compendium of publications

Universitat de les Illes Balears

Marta Colleoni, as co-author of the following article:

Title: IMRPhenomXHM: A multi-mode frequency-domain model for the gravitational wave signal from non-precessing black-hole binaries
Published in: arXiv:2001.10914 [gr-qc]
Authors: Cecilio García-Quirós, Marta Colleoni, Sascha Husa, Héctor Estellés, Geraint Pratten, Antoni Ramos-Buades, Maite Mateu-Lucena, Rafel Jaume,

accepts that Cecilio García Quirós presents the cited article as the principal author and as a part of his doctoral thesis and that said article cannot, therefore, form part of any doctoral thesis.

And for all intents and purposes, hereby signs this document.

Signature

Palma de Mallorca, 24/04/2020

FORMAT CRITERIA FOR DOCTORAL THESES IN THE UNIVERSITY OF THE ILLES BALEARS
Annex 4: Model document of agreement between the co-authors of articles when the thesis is presented as a compendium of publications

Universitat de les Illes Balears

Sascha Husa, as co-author of the following article:

Title: IMRPhenomXHM: A multi-mode frequency-domain model for the gravitational wave signal from non-precessing black-hole binaries
Published in: arXiv:2001.10914 [gr-qc]
Authors: Cecilio García-Quirós, Marta Colleoni, Sascha Husa, Héctor Estellés, Geraint Pratten, Antoni Ramos-Buades, Maite Mateu-Lucena, Rafel Jaume,

accepts that Cecilio García Quirós presents the cited article as the principal author and as a part of his doctoral thesis and that said article cannot, therefore, form part of any doctoral thesis.

And for all intents and purposes, hereby signs this document.

Signature

Palma de Mallorca, 24/04/2020

FORMAT CRITERIA FOR DOCTORAL THESES IN THE UNIVERSITY OF THE ILLES BALEARS
Annex 4: Model document of agreement between the co-authors of articles when the thesis is presented as a compendium of publications

Universitat de les Illes Balears

Héctor Estellés, as co-author of the following article:

Title: IMRPhenomXHM: A multi-mode frequency-domain model for the gravitational wave signal from non-precessing black-hole binaries
Published in: arXiv:2001.10914 [gr-qc]
Authors: Cecilio García-Quirós, Marta Colleoni, Sascha Husa, Héctor Estellés, Geraint Pratten, Antoni Ramos-Buades, Maite Mateu-Lucena, Rafel Jaume,

accepts that Cecilio García Quirós presents the cited article as the principal author and as a part of his doctoral thesis and that said article cannot, therefore, form part of any doctoral thesis.

And for all intents and purposes, hereby signs this document.

Signature

Palma de Mallorca, 24/04/2020

FORMAT CRITERIA FOR DOCTORAL THESES IN THE UNIVERSITY OF THE ILLES BALEARS
Annex 4: Model document of agreement between the co-authors of articles when the thesis is presented as a compendium of publications

Universitat de les Illes Balears

Geraint Pratten, as co-author of the following article:

Title: IMRPhenomXHM: A multi-mode frequency-domain model for the gravitational wave signal from non-precessing black-hole binaries
Published in: arXiv:2001.10914 [gr-qc]
Authors: Cecilio García-Quirós, Marta Colleoni, Sascha Husa, Héctor Estellés, Geraint Pratten, Antoni Ramos-Buades, Maite Mateu-Lucena, Rafel Jaume,

accepts that Cecilio García Quirós presents the cited article as the principal author and as a part of his doctoral thesis and that said article cannot, therefore, form part of any doctoral thesis.

And for all intents and purposes, hereby signs this document.

Signature

Palma de Mallorca, 24/04/2020

FORMAT CRITERIA FOR DOCTORAL THESES IN THE UNIVERSITY OF THE ILLES BALEARS
Annex 4: Model document of agreement between the co-authors of articles when the thesis is presented as a compendium of publications

Universitat de les Illes Balears

Antoni Ramos-Buades, as co-author of the following article:

Title: IMRPhenomXHM: A multi-mode frequency-domain model for the gravitational wave signal from non-precessing black-hole binaries
Published in: arXiv:2001.10914 [gr-qc]
Authors: Cecilio García-Quirós, Marta Colleoni, Sascha Husa, Héctor Estellés, Geraint Pratten, Antoni Ramos-Buades, Maite Mateu-Lucena, Rafel Jaume,

accepts that Cecilio García Quirós presents the cited article as the principal author and as a part of his doctoral thesis and that said article cannot, therefore, form part of any doctoral thesis.

And for all intents and purposes, hereby signs this document.

Signature

Palma de Mallorca, 24/04/2020

FORMAT CRITERIA FOR DOCTORAL THESES IN THE UNIVERSITY OF THE ILLES BALEARS
Annex 4: Model document of agreement between the co-authors of articles when the thesis is presented as a compendium of publications

Universitat de les Illes Balears

Maite Mateu Lucena, as co-author of the following article:

Title: IMRPhenomXHM: A multi-mode frequency-domain model for the gravitational wave signal from non-precessing black-hole binaries
Published in: arXiv:2001.10914 [gr-qc]
Authors: Cecilio García-Quirós, Marta Colleoni, Sascha Husa, Héctor Estellés, Geraint Pratten, Antoni Ramos-Buades, Maite Mateu-Lucena, Rafel Jaume,

accepts that Cecilio García Quirós presents the cited article as the principal author and as a part of his doctoral thesis and that said article cannot, therefore, form part of any doctoral thesis.

And for all intents and purposes, hereby signs this document.

Signature

Palma de Mallorca, 24/04/2020

FORMAT CRITERIA FOR DOCTORAL THESES IN THE UNIVERSITY OF THE ILLES BALEARS
Annex 4: Model document of agreement between the co-authors of articles when the thesis is presented as a compendium of publications

Universitat de les Illes Balears

Rafel Jaume, as co-author of the following article:

Title: IMRPhenomXHM: A multi-mode frequency-domain model for the gravitational wave signal from non-precessing black-hole binaries
Published in: arXiv:2001.10914 [gr-qc]
Authors: Cecilio García-Quirós, Marta Colleoni, Sascha Husa, Héctor Estellés, Geraint Pratten, Antoni Ramos-Buades, Maite Mateu-Lucena, Rafel Jaume,

accepts that Cecilio García Quirós presents the cited article as the principal author and as a part of his doctoral thesis and that said article cannot, therefore, form part of any doctoral thesis.

And for all intents and purposes, hereby signs this document.

Signature

Palma de Mallorca, 24/04/2020

Appendix C

Permissions Chapter 4

This appendix gathers all the permissions from the authors authorizing Cecilio García Quirós to include the article presented in Chapter 4 as part of this thesis.

FORMAT CRITERIA FOR DOCTORAL THESES IN THE UNIVERSITY OF THE ILLES BALEARS
Annex 4: Model document of agreement between the co-authors of articles when the thesis is presented as a compendium of publications

Universitat de les Illes Balears

Dr. Sascha Husa, as co-author of the following article

1) Accelerating the evaluation of inspiral-merger-ringdown waveforms with adapted grids

Preprint: arXiv:2001.10897 ***[gr-qc]***

Authors: Cecilio García-Quirós, Sascha Husa, Maite Mateu-Lucena, Angela Borchers.

I DECLARE:

Accepts that Mr. Cecilio García Quirós presents the cited articles as the principal author and as a part of his doctoral thesis and that said articles cannot, therefore, form part of any doctoral thesis.

And for all intents and purposes, hereby signs this document.

Signature

Palma de Mallorca, 24/04/2020

FORMAT CRITERIA FOR DOCTORAL THESES IN THE UNIVERSITY OF THE ILLES BALEARS
Annex 4: Model document of agreement between the co-authors of articles when the thesis is presented as a compendium of publications

Universitat de les Illes Balears

Ms. Maite Mateu Lucena, as co-author of the following article

1) Accelerating the evaluation of inspiral-merger-ringdown waveforms with adapted grids

Preprint: arXiv:2001.10897 ***[gr-qc]***

Authors: Cecilio García-Quirós, Sascha Husa, Maite Mateu-Lucena, Angela Borchers.

I DECLARE:

Accepts that Mr. Cecilio García Quirós presents the cited articles as the principal author and as a part of his doctoral thesis and that said articles cannot, therefore, form part of any doctoral thesis.

And for all intents and purposes, hereby signs this document.

Signature

Palma de Mallorca, 24/04/2020

FORMAT CRITERIA FOR DOCTORAL THESES IN THE UNIVERSITY OF THE ILLES BALEARS
Annex 4: Model document of agreement between the co-authors of articles when the thesis is presented as a compendium of publications

Universitat de les Illes Balears

Angela Borchers, as co-author of the following article:

Title: Accelerating the evaluation of inspiral-merger-ringdown waveforms with adapted grids
Published in: arXiv:2001.10897 [gr-qc]
Authors: Cecilio García-Quirós, Sascha Husa, Maite Mateu-Lucena, Angela Borchers,

accepts that Cecilio García Quirós presents the cited article as the principal author and as a part of his doctoral thesis and that said article cannot, therefore, form part of any doctoral thesis.

And for all intents and purposes, hereby signs this document.

Signature

Palma de Mallorca, 24/04/2020

Appendix D

Permissions Chapter 5

This appendix gathers all the permissions from the authors authorizing Cecilio García Quirós to include the article presented in Chapter 5 as part of this thesis.

FORMAT CRITERIA FOR DOCTORAL THESES IN THE UNIVERSITY OF THE ILLES BALEARS
Annex 4: Model document of agreement between the co-authors of articles when the thesis is presented as a compendium of publications

Universitat de les Illes Balears

Geraint Pratten, as co-author of the following article:

Title: Let's twist again: computationally efficient models for the dominant and sub-dominant harmonic modes of precessing binary black holes
Published in: arXiv:2004.06503 [gr-qc]
Authors: Geraint Pratten, Cecilio García-Quirós, Marta Colleoni, Antoni Ramos-Buades, Héctor Estellés, Maite Mateu-Lucena, Rafel Jaume, Maria Haney, David Keitel, Jonathan E. Thompson, Sascha Husa,

accepts that Cecilio García Quirós presents the cited article as the principal author and as a part of his doctoral thesis and that said article cannot, therefore, form part of any doctoral thesis.

And for all intents and purposes, hereby signs this document.

Signature

Palma de Mallorca, 24/04/2020

FORMAT CRITERIA FOR DOCTORAL THESES IN THE UNIVERSITY OF THE ILLES BALEARS
Annex 4: Model document of agreement between the co-authors of articles when the thesis is presented as a compendium of publications

Universitat de les Illes Balears

Marta Colleoni, as co-author of the following article:

Title: Let's twist again: computationally efficient models for the dominant and sub-dominant harmonic modes of precessing binary black holes
Published in: arXiv:2004.06503 [gr-qc]
Authors: Geraint Pratten, Cecilio García-Quirós, Marta Colleoni, Antoni Ramos-Buades, Héctor Estellés, Maite Mateu-Lucena, Rafel Jaume, Maria Haney, David Keitel, Jonathan E. Thompson, Sascha Husa,

accepts that Cecilio García Quirós presents the cited article as the principal author and as a part of his doctoral thesis and that said article cannot, therefore, form part of any doctoral thesis.

And for all intents and purposes, hereby signs this document.

Signature

Palma de Mallorca, 24/04/2020

FORMAT CRITERIA FOR DOCTORAL THESES IN THE UNIVERSITY OF THE ILLES BALEARS
Annex 4: Model document of agreement between the co-authors of articles when the thesis is presented as a compendium of publications

Universitat de les Illes Balears

Antoni Ramos-Buades, as co-author of the following article:

Title: Let's twist again: computationally efficient models for the dominant and sub-dominant harmonic modes of precessing binary black holes
Published in: arXiv:2004.06503 [gr-qc]
Authors: Geraint Pratten, Cecilio García-Quirós, Marta Colleoni, Antoni Ramos-Buades, Héctor Estellés, Maite Mateu-Lucena, Rafel Jaume, Maria Haney, David Keitel, Jonathan E. Thompson, Sascha Husa,

accepts that Cecilio García Quirós presents the cited article as the principal author and as a part of his doctoral thesis and that said article cannot, therefore, form part of any doctoral thesis.

And for all intents and purposes, hereby signs this document.

Signature

Palma de Mallorca, 24/04/2020

FORMAT CRITERIA FOR DOCTORAL THESES IN THE UNIVERSITY OF THE ILLES BALEARS
Annex 4: Model document of agreement between the co-authors of articles when the thesis is presented as a compendium of publications

Universitat de les Illes Balears

Héctor Estellés, as co-author of the following article:

Title: Let's twist again: computationally efficient models for the dominant and sub-dominant harmonic modes of precessing binary black holes
Published in: arXiv:2004.06503 [gr-qc]
Authors: Geraint Pratten, Cecilio García-Quirós, Marta Colleoni, Antoni Ramos-Buades, Héctor Estellés, Maite Mateu-Lucena, Rafel Jaume, Maria Haney, David Keitel, Jonathan E. Thompson, Sascha Husa,

accepts that Cecilio García Quirós presents the cited article as the principal author and as a part of his doctoral thesis and that said article cannot, therefore, form part of any doctoral thesis.

And for all intents and purposes, hereby signs this document.

Signature

Palma de Mallorca, 24/04/2020

FORMAT CRITERIA FOR DOCTORAL THESES IN THE UNIVERSITY OF THE ILLES BALEARS
Annex 4: Model document of agreement between the co-authors of articles when the thesis is presented as a compendium of publications

Universitat de les Illes Balears

Maite Mateu-Lucena, as co-author of the following article:

Title: Let's twist again: computationally efficient models for the dominant and sub-dominant harmonic modes of precessing binary black holes
Published in: arXiv:2004.06503 [gr-qc]
Authors: Geraint Pratten, Cecilio García-Quirós, Marta Colleoni, Antoni Ramos-Buades, Héctor Estellés, Maite Mateu-Lucena, Rafel Jaume, Maria Haney, David Keitel, Jonathan E. Thompson, Sascha Husa,

accepts that Cecilio García Quirós presents the cited article as the principal author and as a part of his doctoral thesis and that said article cannot, therefore, form part of any doctoral thesis.

And for all intents and purposes, hereby signs this document.

Signature

Palma de Mallorca, 24/04/2020

FORMAT CRITERIA FOR DOCTORAL THESES IN THE UNIVERSITY OF THE ILLES BALEARS
Annex 4: Model document of agreement between the co-authors of articles when the thesis is presented as a compendium of publications

Universitat de les Illes Balears

Rafel Jaume, as co-author of the following article:

Title: Let's twist again: computationally efficient models for the dominant and sub-dominant harmonic modes of precessing binary black holes
Published in: arXiv:2004.06503 [gr-qc]
Authors: Geraint Pratten, Cecilio García-Quirós, Marta Colleoni, Antoni Ramos-Buades, Héctor Estellés, Maite Mateu-Lucena, Rafel Jaume, Maria Haney, David Keitel, Jonathan E. Thompson, Sascha Husa,

accepts that Cecilio García Quirós presents the cited article as the principal author and as a part of his doctoral thesis and that said article cannot, therefore, form part of any doctoral thesis.

And for all intents and purposes, hereby signs this document.

Signature

Palma de Mallorca, 24/04/2020

FORMAT CRITERIA FOR DOCTORAL THESES IN THE UNIVERSITY OF THE ILLES BALEARS
Annex 4: Model document of agreement between the co-authors of articles when the thesis is presented as a compendium of publications

Universitat de les Illes Balears

Maria Haney, as co-author of the following article:

Title: Let's twist again: computationally efficient models for the dominant and sub-dominant harmonic modes of precessing binary black holes
Published in: arXiv:2004.06503 [gr-qc]
Authors: Geraint Pratten, Cecilio García-Quirós, Marta Colleoni, Antoni Ramos-Buades, Héctor Estellés, Maite Mateu-Lucena, Rafel Jaume, Maria Haney, David Keitel, Jonathan E. Thompson, Sascha Husa,

accepts that Cecilio García Quirós presents the cited article as the principal author and as a part of his doctoral thesis and that said article cannot, therefore, form part of any doctoral thesis.

And for all intents and purposes, hereby signs this document.

Signature

Zürich, 24/04/2020

FORMAT CRITERIA FOR DOCTORAL THESES IN THE UNIVERSITY OF THE ILLES BALEARS
Annex 4: Model document of agreement between the co-authors of articles when the thesis is presented as a compendium of publications

Universitat de les Illes Balears

David Keitel, as co-author of the following article:

Title: Let's twist again: computationally efficient models for the dominant and sub-dominant harmonic modes of precessing binary black holes
Published in: arXiv:2004.06503 [gr-qc]
Authors: Geraint Pratten, Cecilio García-Quirós, Marta Colleoni, Antoni Ramos-Buades, Héctor Estellés, Maite Mateu-Lucena, Rafel Jaume, Maria Haney, David Keitel, Jonathan E. Thompson, Sascha Husa,

accepts that Cecilio García Quirós presents the cited article as the principal author and as a part of his doctoral thesis and that said article cannot, therefore, form part of any doctoral thesis.

And for all intents and purposes, hereby signs this document.

Signature

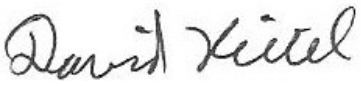

Palma de Mallorca, 24/04/2020

FORMAT CRITERIA FOR DOCTORAL THESES IN THE UNIVERSITY OF THE ILLES BALEARS
Annex 4: Model document of agreement between the co-authors of articles when the thesis is presented as a compendium of publications

Universitat de les Illes Balears

Jonathan E. Thompson, as co-author of the following article:

Title: Let's twist again: computationally efficient models for the dominant and sub-dominant harmonic modes of precessing binary black holes
Published in: arXiv:2004.06503 [gr-qc]
Authors: Geraint Pratten, Cecilio García-Quirós, Marta Colleoni, Antoni Ramos-Buades, Héctor Estellés, Maite Mateu-Lucena, Rafel Jaume, Maria Haney, David Keitel, Jonathan E. Thompson, Sascha Husa,

accepts that Cecilio García Quirós presents the cited article as the principal author and as a part of his doctoral thesis and that said article cannot, therefore, form part of any doctoral thesis.

And for all intents and purposes, hereby signs this document.

Signature

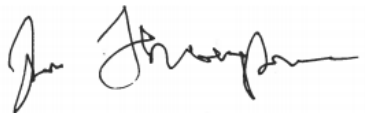

Palma de Mallorca, 24/04/2020

FORMAT CRITERIA FOR DOCTORAL THESES IN THE UNIVERSITY OF THE ILLES BALEARS
Annex 4: Model document of agreement between the co-authors of articles when the thesis is presented as a compendium of publications

Universitat de les Illes Balears

Sascha Husa, as co-author of the following article:

Title: Let's twist again: computationally efficient models for the dominant and sub-dominant harmonic modes of precessing binary black holes
Published in: arXiv:2004.06503 [gr-qc]
Authors: Geraint Pratten, Cecilio García-Quirós, Marta Colleoni, Antoni Ramos-Buades, Héctor Estellés, Maite Mateu-Lucena, Rafel Jaume, Maria Haney, David Keitel, Jonathan E. Thompson, Sascha Husa,

accepts that Cecilio García Quirós presents the cited article as the principal author and as a part of his doctoral thesis and that said article cannot, therefore, form part of any doctoral thesis.

And for all intents and purposes, hereby signs this document.

Signature

Palma de Mallorca, 24/04/2020